TUUVA KASTINEN

Molecular Level Understanding of Conjugated Organic Solar Cell Materials - a Computational Study

TUUVA KASTINEN

Molecular Level Understanding of Conjugated Organic Solar Cell Materials - a Computational Study

ACADEMIC DISSERTATION
To be presented, with the permission of
the Faculty of Engineering and Natural Sciences
of Tampere University,
for public discussion at Tampere University,
on 4 September 2020, at 12 o'clock.

ACADEMIC DISSERTATION
Tampere University, Faculty of Engineering and Natural Sciences
Finland

Responsible supervisor and Custos	Docent Terttu Hukka Tampere University Finland	
Supervisor	D.Sc. (Tech.) Oana Cramariuc Tampere University Finland	
Pre-examiners	Professor Anna Delin KTH Royal Institute of Technology Sweden	Professor Kari Laasonen Aalto University Finland
Opponent	Professor Fabrizia Negri University of Bologna Italy	

The originality of this thesis has been checked using the Turnitin OriginalityCheck service.

Cover design: Roihu Inc.

PREFACE

What a great journey this has been! Reaching this goal would have been impossible without various people. First and foremost, I would like to express my gratitude to my supervisor, University Lecturer, Docent Terttu Hukka for the opportunity to work as a doctoral student in her Academy of Finland project. I am very thankful for her guidance, patience, and never-ending support during these years. I would also like to thank my second supervisor Dr. Oana Cramariuc for all her advices.

I am very grateful to all my co-authors in the publications. My special thanks go to Dr. Mika Niskanen for all the instructions and help he gave in the first steps of this process. I would also like to express my gratitude to Prof. Demetrio A. da Silva Filho for the opportunity to visit his research group at Brasilia University. I would like to thank Dr. Chad Risko and Dr. Lassi Paunonen for their valuable help, as well. To Prof. Benjamin Lear, I am grateful for checking the language of this thesis.

Next, I would like to express my sincere thanks to all my colleagues for the warm and inspiring working environment. Especially, I thank Lauri Judin and Outi Kontkanen for your peer support and interesting conversations. I am also grateful to all fellow doctoral students that I have had a joy to get to known during these years.

Finally, I want to thank my family and friends for being there for me whenever I needed you. To my loving husband Mark, I am deeply grateful for your constant support during this (longish) project and listening to my occasional, work related ramblings. To my dear son Leo, I am ever thankful for your enthusiastic and honest way of viewing this world that brings great joy for me everyday.

Hämeenlinna, May 19th 2020
Tuuva Kastinen

ABSTRACT

Among different organic photovoltaic technologies, polymer solar cells (PSCs) have potential as light-weight, cost-effective, flexible, and transparent devices. A great amount of work has been carried out in developing and understanding the factors governing the efficiencies of PSCs. In the electronic structure studies of PSC systems, the careful selection of models and methods employed in theoretical calculations is essential for an accurate description of the π-conjugated PSC materials.

In this thesis, the efficient PSC systems have been examined with the density functional theory (DFT) methods. The studied compounds include fullerene-based PSCs, which combine donor–acceptor (D–A) copolymers as electron donor (eD) and fullerene derivatives as electron acceptor (eA) materials. Emerging non-fullerene (NF) devices, which make use of D–A copolymers or small-molecule acceptors, have been also studied. Both oligomeric and periodic copolymer models have been considered and the performance of global hybrid, non-tuned long-range corrected (LRC), and optimally tuned (OT) LRC functionals have been investigated. The aim has been to find suitable tools for modeling PSC systems, while gaining more understanding of the characteristics of PSC compounds and their interactions that impact the performance of PSCs.

The periodic DFT method is found to be a useful tool in modeling of the D–A copolymers. Both the functional and dispersion corrections impact greatly the results predicted for the studied PSC systems. The dispersion corrected OT-LRC functional gives the best description of the individual PSC compounds and their local interfaces. Both the multi-state treatment and dispersion corrected OT-LRC functional result in more constant electronic coupling values. The charge transfer rates are found to be strongly dependent on both the functional and relative orientation of the eD and eA compounds. These findings serve as guidelines for the selection of methods in future theoretical studies of PSC systems, but also provide beneficial information for designing and developing new materials for emerging NF PSCs.

TIIVISTELMÄ

Orgaanisista valosähköisistä sovelluksista polymeeriaurinkokennoilla (PSC) on potentiaalia kevyinä, kustannustehokkaina, joustavina ja läpinäkyvinä laitteina. Paljon työtä on tehty PSC:een tehokkuuksiin vaikuttavien tekijöiden tutkimiseksi ja ymmärtämiseksi. PSC-systeemien elektronirakennetutkimuksissa käytettävien mallien ja menetelmien huolellinen valitseminen on välttämätöntä π-konjugoituneiden PSC-materiaalien tarkkaan kuvaamiseen.

Tässä väitöskirjassa on tutkittu tehokkaita PSC-systeemejä tiheysfunktionaaliteoria (DFT) -menetelmillä. Tutkitut systeemit käsittävät fullereenipohjaiset PSC:t, joissa on käytetty donori–akseptori (D–A) -kopolymeerejä elektronidonoreina (eD) ja fullereenijohdannaisia elektroniakseptoreina (eA). Lisäksi on tutkittu uusia, ei-fullereeni (NF) -systeemejä, joissa on käytetty joko D–A-kopolymeerejä tai pienmolekyyliakseptoreja. Työssä on käytetty sekä oligomeerisia että periodisia malleja ja tutkittu globaalihybridisten, pitkän matkan korjattujen (LRC) ja optimaalisesti säädettyjen (OT) LRC funktionaalien soveltuvuutta. Työn tavoitteena on ollut löytää sopivat työkalut PSC-systeemien mallintamiseen saavuttaen samalla tarkempaa ymmärrystä PSC-yhdisteiden ominaisuuksista ja vuorovaikutuksista, joilla on merkitystä PSC:iden suorituskykyyn.

Periodisen DFT-menetelmän havaitaan olevan hyödyllinen työkalu D–A-kopolymeerien mallinnuksessa. Funktionaali ja dispersiokorjaukset vaikuttavat huomattavasti tutkittujen PSC-systeemien tuloksiin. Dispersiokorjattu OT-LRC funktionaali kuvaa parhaiten yksittäisiä PSC-yhdisteitä ja niiden paikallisia rajapintoja. Useamman viritystilan huomioiminen ja dispersiokorjatun OT-LRC funktionaalin käyttäminen johtavat vakioituneisiin sähköisen kytkennän arvoihin. Funktionaalilla ja molekyylien keskinäisellä sijainnilla on suuri vaikutus varauksensiirron nopeuksiin. Työstä saadut tiedot toimivat suuntaviivoina menetelmien valinnalle tulevissa PSC-systeemien laskennallisissa tutkimuksissa, mutta antavat myös hyödyllistä tietoa uusien NF PSC -materiaalien suunnittelussa.

CONTENTS

ABBREVIATIONS AND SYMBOLS

APSC	All-polymer solar cell
BDD	1,3-bis(thiophen-2-yl)-5,7-bis(2-ethylhexyl)benzo[1,2-*c*:4,5-*c*']dithiophene-4,8-dione
BDT	Benzo[1,2-*b*:4,5-*b*']dithiophene
BHJ	Bulk heterojunction
BLA	Bond-length alternation
C_{60}	Buckminsterfullerene
CAM	Coulomb-attenuation method
CPCM	Conductor-like polarizable continuum model
CR	Charge recombination
CRU	Constitutional repeating unit
CT	Charge transfer
D–A	Donor–acceptor
DFT	Density functional theory
EA	Electron affinity
eA	Electron acceptor
ED	Exciton dissociation
eD	Electron donor
ET	Electron transfer
ETL	Electron transport layer
FCD	Fragment charge difference
FMO	Frontier molecular orbital
GGA	Generalized gradient approximation

GMH	Generalized Mulliken–Hush
GS	Ground state
GTO	Gaussian-type orbital
HF	Hartree–Fock
HOMO	Highest occupied molecular orbital
HT	Hole transfer
HTL	Hole transport layer
ICT	Intramolecular charge transfer
IE	Ionization energy
IEFPCM	Integral equation formalism of the polarizable continuum model
INCN	2-(3-oxo-2,3-dihydroinden-1-ylidene)malononitrile
IT	Indacenodithieno[3,2-*b*]thiophene
LDA	Local density approximation
LR	Long-range
LRC	Long-range corrected
LSDA	Local spin-density approximation
LUMO	Lowest unoccupied molecular orbital
MD	Molecular dynamics
MO	Molecular orbital
MP	Møller–Plesset
MSIE	Many-electron self-interaction error
NDI	Naphthalene diimide
NF	Non-fullerene
NTO	Natural transition orbital
OT	Optimally-tuned
P(NDI2OD-T2)	Poly[(*N*,*N*'-bis(2-octyldodecyl)naphthalene-1,4,5,8-bis(di-carboximide)-2,6-diyl)-*alt*-5,5'-(2,2'-bithiophene)]

P3HT	Poly(3-hexylthiophene)
PBC	Periodic boundary conditions
PBDB-T-2F	Poly[(2,6-(4,8-bis(5-(2-ethylhexyl)-4-fluorothiophen-2-yl)-benzo[1,2-*b*:4,5-*b'*]dithiophene))-*alt*-(5,5-(1',3'-bis(thiophen-2-yl)-5,7-bis(2-ethylhexyl)benzo[1',2'-*c*:4,5-*c'*]dithiophene-4,8-dione))]
PBDT-TFQ	Poly[4,8-bis(2'-ethylhexyloxy)-benzo[1,2-*b*:4,5-*b'*]-dithiophene-*alt*-[5,8-bis(5'-thiophen-2'-yl)-6,7-difluoro-2,3-bis-(3"-hexyloxyphenyl)quinoxaline]]
PBDT-TPD	Poly(benzo[1,2-*b*:4,5-*b'*]dithiophene-*alt*-thieno-[3,4-*c*]pyrrole-4,6-dione)
PBDT-TzBI	Poly[4,8-bis(5-(2-ethylhexyl)-thiophen-2-yl)benzo[1,2-*b*:4,5-*b'*]dithiophene-*co*-4,8-di(thien-2-yl)-6-octyl-2-octyl-5H-pyrrolo[3,4-*f*]benzotriazole-5,7(6*H*)-dione]
$PC_{61}BM$	[6,6]-phenyl-C_{61}-butyric acid methyl ester
$PC_{71}BM$	[6,6]-phenyl-C_{71}-butyric acid methyl ester
PCE	Power conversion efficiency
PCM	Polarizable continuum model
PES	Potential energy surface
PET	Photoinduced electron transfer
PHT	Photoinduced hole transfer
PSC	Polymer solar cell
PTQ	Poly[2,3-bis-(3-octyloxyphenyl)quinoxaline-5,8-diyl-*alt*-thiophene-2,5-diyl]
RSH	Range-separated hybrid
SCF	Self-consistent-field
SMA	Small molecule acceptor
SP	Single point
SR	Short-range

TDA	Tamm–Dancoff approximation to time-dependent density functional theory
TDDFT	Time-dependent density functional theory
TPD	Thieno[3,4-*c*]pyrrole-4,6-dione
TzBI	Pyrrolo[3,4-*f*]benzotriazole-5,7-dione
XC	Exchange–correlation
$a_{i\mu}$	Molecular orbital coefficients
$\chi_i(\mathbf{x}_j)$	Spin orbital
ΔE_{Coul}	Coulombic attraction
ΔE_{ij}	Vertical excitation energy difference between the states i and j
ΔG°	Gibbs free energy of the reaction
$\Delta \mu_{\text{ij}}$	Electric dipole moment difference between the states i and j
Δq	Charge difference
$\mathbf{\Delta q}$	Charge difference matrix
E	Energy
ϵ_{HOMO}	Energy of the highest occupied molecular orbital
ϵ_{op}	Optical dielectric constant
ϵ_{s}	Static dielectric constant
$\widehat{F}$	Fock operator
$\hbar$	Reduced Planck's constant
$\widehat{H}$	Hamiltonian
$\widehat{H}_{\text{el}}$	Electronic hamiltonian
H_{if}	Electronic coupling
i	Imaginary unit
$\widehat{J}$	Coulomb operator
k	Charge transfer rate
k_0	Force constant of the isolated oscillator

k'	Force constant between N adjacent double bonds
$\widehat{K}$	Exchange operator
$\mathbf{k} = (k_x, k_y, k_z)$	Reciprocal-lattice vector
k_B	Boltzmann constant
λ_i	Inner reorganization energy
λ_{NTO}	Fraction of the hole–electron contribution to the transition
λ_s	External reorganization energy
M	Number of nuclei
μ	Dipole moment
m_A	Mass of the nucleus
μ_{ij}	Transition dipole moment between the states i and j
N	Number of double bonds
n	Number of repeating units
N_e	Number of electrons
∇^2	Laplacian operator
v_{XC}	Exchange–correlation potential
ω	Range-separation parameter
ω_i	Frequency
Ψ	N_e-electron wavefunction
ψ_i	Spatial orbital, i.e. molecular orbital
Q	Nuclear reaction coordinate
r_{ab}	Distance between particles a and b
$\rho(\mathbf{r})$	Electron density
T	Temperature
t	Time
$\widehat{T}$	Kinetic energy
$\mathbf{T}_v$	Translation vector

$\mathbf{U_1}$	Unitary transformation matrix
V_{ext}	External potential
$\widehat{V}$	Potential energy
V_i^{HF}	Hartree–Fock potential
φ	Basis function, i.e. atomic orbital
z	Scaling factor
Z_A	Atomic number of nucleus A

ORIGINAL PUBLICATIONS

Publication I T. Kastinen, M. Niskanen, C. Risko, O. Cramariuc, and T. I. Hukka, "Intrinsic Properties of Two Benzodithiophene-Based Donor–Acceptor Copolymers Used in Organic Solar Cells: A Quantum-Chemical Approach", *The Journal of Physical Chemistry A*, vol. 120, no. 7, pp. 1051–1064, 2016, DOI: `10.1021/acs.jpca.5b08465`.

Publication II T. Kastinen, M. Niskanen, C. Risko, O. Cramariuc, and T. I. Hukka, "On describing the optoelectronic characteristics of poly(benzodithiophene-*co*-quinoxaline)–fullerene complexes: the influence of optimally tuned density functionals", *Physical Chemistry Chemical Physics*, vol. 18, no. 39, pp. 27654–27670, 2016, DOI: `10.1039/c6cp04567g`.

Publication III T. Kastinen, D. A. da Silva Filho, L. Paunonen, M. Linares, L. A. Ribeiro Junior, O. Cramariuc, and T. I. Hukka, "Electronic couplings and rates of excited state charge transfer processes at poly(thiophene-*co*-quinoxaline)–$PC_{71}BM$ interfaces: two- versus multi-state treatments", *Physical Chemistry Chemical Physics*, vol. 21, no. 46, pp. 25606–25625, 2019, DOI: `10.1039/c9cp04837e`.

Publication IV T. Kastinen and T. I. Hukka, "Charge transfer characteristics of fullerene-free polymer solar cells via multi-state electronic coupling treatment", *Sustainable Energy & Fuels*, Advance Article 2020, DOI: `10.1039/D0SE00306A`.

Publication I   T. Kastinen chose the compounds modeled and planned and performed all the calculations. T. Kastinen set up and analyzed all the calculations with the help of M. Niskanen. M. Niskanen developed the equation for the scaled Kuhn fit. T. Kastinen wrote the manuscript with the comments provided by the other authors.

Publication II   T. Kastinen chose the systems modeled and planned and performed all the calculations. T. Kastinen set up and analyzed all the calculations with the help of M. Niskanen. T. Kastinen wrote the manuscript with the comments provided by the other authors.

Publication III   M. Linares and D. A. da Silva Filho chose the studied system and planned the initial plan for the study. M. Linares and L. A. Ribeiro Junior provided the initial structures of the studied compounds and complexes. T. Kastinen planned, set up, and performed the calculations. D. A. da Silva Filho wrote the code for analysing the molecular orbital composition, which was further developed by T. Kastinen. L. Paunonen wrote the Matlab code for the matrices used in the multi-state coupling calculations, which was further developed by T. Kastinen. T. Kastinen analyzed all the calculation results. T. Kastinen wrote the manuscript with the comments provided by the other authors.

Publication IV   T. Kastinen chose the studied systems and planned, set up, and performed all the calculations. Additionally, T. Kastinen analyzed all the calculation results. T. Kastinen wrote the manuscript with the comments provided by the co-author.

1 INTRODUCTION

Today's globally growing demand for energy, combined with environmental concerns related to fossil fuels, have motivated a search for alternative renewable energy sources that are clean, cost-effective, and high-performance [1, 2]. Solar energy offers practically limitless energy, which exceeds the total energy consumed in a year many times over [3]. Over the past several decades, great efforts have been made in developing photovoltaic technologies to harvest sunlight. So-far, commercial applications comprise inorganic crystalline silicon wafer-based devices or thin-film technologies [4]. Originally, the high price of silicon motivated the search for cheaper alternatives [5]. While the cost of silicon has dropped since then, alternative (still non-commercial) technologies including dye-sensitized, organic, quantum dot-sensitized, and perovskite solar cells are still continuously explored. This is due to promising features of these techniques that conventional, inorganic devices do not have. For example, organic solar cells based on conjugated polymers, i.e. polymer solar cells (PSCs), have potential for low-cost, light-weight, flexible, and large-scale processable applications, which make them a noteworthy candidate in solar cell market [6, 7].

In addition to extensive experimental work of PSCs, an enormous amount of theoretical studies have been carried out to achieve deeper understanding on PSC systems with the different levels of methods [3]. Various theoretical papers of intrinsic electronic and optical properties of existing PSC materials by means of quantum chemical methods have been published [8–13]. These findings have complemented experimental work, giving a better understanding to structure-function relations that define the efficiencies of PSC materials. Additionally, new materials have been effectively screened using joint experimental and theoretical studies to find new candidates with potential features [14]. Local interfacial charge transfer (CT) processes of the PSC compounds have also been exploited by means of excited state calculations and different CT rate models [8–12, 14]. The information of the blend morphology of a photoactive layer, which is one of the most important factors defining the efficiencies of the PSC, has been gained from atomistic molecular dynamics (MD)

simulations of bulk heterojunction (BHJ) systems, and can be used to better understand the impact of the structural properties of the PSC compounds on their packing and mixing tendency [15–19]. These studies have been typically multiscale calculations, which combine both the screening of the possible complex configurations with MD and further electronic structure calculations via quantum mechanical methods. There have been also Kinetic Monte Carlo simulations of charge transport in PSC systems [20]. Thus, theoretical modeling offers a wide scale of methods for studying the PSCs, which can be exploited alongside the experimental techniques.

While characterizing properties of PSC materials theoretically in conjunction with experimental measurements has become a routine work, careful consideration of the most suitable calculation method is often missing. Many of electronic structure calculations carried out with density functional theory (DFT) methods make use of such approximations for the exchange–correlation (XC) functional, which are popular but not necessarily optimal. Especially, global hybrid functionals with a fixed, global amount of exact Hartree–Fock (HF) exchange have been widely employed [8, 10, 11, 21–25], because they yield improved description of molecular properties (e.g. geometries, binding energies, vibrational frequencies, excitation energies, etc.) of conjugated, organic materials with respect to semi-local functionals [26]. However, because the global hybrids suffer from the many-electron self-interaction error (MSIE) [27, 28], which can lead to severe inaccuracies in several properties of interest in organic π-conjugated materials, the nature of the functional should be taken into account when modeling the electronic structure properties of PSC compounds [26].

Long-range corrected (LRC) functionals [29–32], which use different approximations for treating short-range (SR) and long-range (LR) interactions, are known to minimize the MSIE [28, 33]. Encouraging results have been achieved for predicting structural, optical, and electronic properties of organic conjugated materials when applying a non-empirical tuning procedure for range-separation parameter (ω) of the LRC functionals [9, 12, 14, 34]. The work described in this thesis examines the performance of several functionals, including common global hybrid functionals, non-tuned, and optimally-tuned (OT) LRC functionals for characterizing individual PSC compounds and their local interfacial systems by different DFT methods.

1.1   Research objectives

In this work, π-conjugated organic PSCs compounds were studied theoretically with DFT and time-dependent density functional theory (TDDFT) based methods. The main focus of the thesis is on the conjugated donor–acceptor (D–A) copolymers, which have been employed mainly as electron donor (eD) materials in the efficient PSCs, but also as electron acceptor (eA) materials in all-polymer solar cells (APSCs). Furthermore, two other types of eA materials are considered: fullerene derivatives and small molecule acceptors (SMAs). Fullerene derivatives have been typical eA materials in traditional polymer–fullerene devices, but lately SMAs have gained more attention in recent non-fullerene (NF) PSCs yielding the highest efficiencies among PSCs so far [25, 35]. To correctly describe these eD and eA materials and their local interactions theoretically, the models and methods used for calculations should be selected carefully. The purpose of this thesis was to establish how to make this selection while aiming for the understanding of CT processes in different PSC systems. The four following goals were set to achieve this objective.

Due to the limitations in size set by DFT-based methods, the conjugated polymers are typically modeled using their finite, oligomeric models [36, 37]. Optoelectronic properties of infinite polymers have been obtained as approximations from those of the corresponding finite monomers and oligomers, which range in the size from two to eight repeating units (i.e. constitutional repeating units, CRUs [38]) [8–10, 12, 14, 34]. The chain length of the oligomer should be sufficiently long to correctly describe the studied polymer, but short enough to be computationally accessible. However, there is no firm size associated with the convergence of oligomeric properties, as this may vary depending on the effective conjugation length of the studied system [36, 39]. An alternative method for the oligomeric studies is to model infinitely long polymer chains [14, 21, 22, 24, 37, 40] using one-dimensional periodic boundary conditions (PBC) within DFT [41, 42]. While this periodic method had been widely applied for other conjugated polymers, there existed only a few PBC-DFT studies of D–A copolymers. The first goal of this thesis was to investigate, how the results predicted by the oligomeric and periodic DFT methods for D–A copolymers differ [43]. Several extrapolation techniques including our modified version

of the Kuhn fit [44] were also evaluated for determining polymer properties at the infinite chain length.

The second goal of this work was to determine the applicability of various functionals for studying the properties of a set of D–A copolymers incorporated as active materials in the efficient PSCs. These functionals included commonly used global hybrid functionals and both non-tuned LRC and OT-LRC functionals. The purpose was to investigate, whether OT-LRC functionals can improve the description of the studied compounds with respect to the conventional global hybrid functionals. Furthermore, according to the previous theoretical studies, dispersion interactions should be taken into account when modeling eD–eA interfacial complexes, as they can have effect on the intermolecular interactions between the eD and eA compounds [3, 45]. Thus, the functionals including dispersion corrections were also considered in this work to see, what kind of effect they have in the studied complexes. During the time of this research, there existed only few studies [34, 46], where the effects of both the tuning of ω of a LRC functional and the inclusion of dispersion corrections on describing polymer–fullerene interfaces had been investigated. Thus, to investigate their combined effect on both the molecular and interfacial properties of the PSC systems, the OT-LRC functional including the dispersion corrections was also employed here.

The third, and one of the most important goals of this work was to investigate, what is the effect of the aforementioned functionals on the CT rate parameters and rates of the CT processes taking place at the polymer–fullerene interfaces. The main focus of this part of research was on the electronic coupling, which describes the strength of the interaction between the initial and final charge-localized states and is an important parameter in determining the CT rates of the PSC systems [47]. The eigenstate-based generalized Mulliken–Hush (GMH) [48, 49] and fragment charge difference (FCD) [50] schemes were selected, as they can be used to calculate electronic couplings for excited state CT processes and can be applied to large molecules, as well [48, 50, 51]. While typically two eigenstates have been used in these schemes at a time to form charge-localized diabatic states, sometimes multiple states are required. This is usually the case when local excitations are mixing with the lowest CT, i.e. CT_1, state, which may lead to overestimated couplings if only two states are employed [51–53]. Both the 2-state GMH [23, 54, 55] and FCD [15] schemes have been ap-

plied in the studies of PSC systems. However, the multi-state effects had not been considered yet with either of the schemes for these systems. Thus, the aim was to determine, whether the multi-state treatment would have an effect on the electronic couplings of the PSC systems with respect to the 2-state schemes.

Finally, the fourth goal of this thesis was to explore, whether the findings achieved for polymer–fullerene systems could be utilized in the studies of emerging type of NF PSC devices. While this field has gained much attention lately [7, 19, 56–58], systematic studies of the electronic structure–property relationships of the best performing compounds used in NF PSCs are still missing. Therefore, the aim was also to gain understanding on the characteristics of the selected NF PSC compounds, how the CT processes taking place on distinct NF PSC systems differ from each other, and whether these dissimilarities might explain the differences in the efficiencies of the studied systems. Additionally, the possible differences between NF PSC and conventional polymer–fullerene systems, as predicted by the calculations, were considered. The purpose was also to investigate, whether the multi-state FCD scheme is also applicable to the NF PSC systems and what is the effect of the inclusion of the dispersion corrections on the electronic coupling values.

1.2 Outline

The thesis is organized in five chapters as follows. Chapter 1 (this chapter) provides an introduction to the studied topic with the research objectives. In Chapter 2, the background and basic working principle of PSCs, typical photoactive eD and eA materials, and a brief summary of the theory behind the charge generation in PSCs and a CT rate model employed in this work, is given. In addition, the theoretical background of the DFT-based methods, which have been used in this thesis, is introduced.

In Chapter 3, the studied compounds are shortly introduced and theoretical models and methods employed in the calculations are reported. The details related to calculating the multi-state electronic couplings are given. Furthermore, the software used for calculations is shortly introduced.

Chapter 4 summarizes the main results of Publications I–IV. First, the OT ω values determined for all the studied eD and eA compounds and their interfaces are reported. After this, the structural and optoelectronic properties of the individual eD and eA compounds are presented. The effect of the functional and other calculation settings will also be discussed. Furthermore, the results from the extrapolations of the oligomeric values and PBC-DFT calculations are compared. Next, the structural characteristics and nature of excited states of the local interfacial complexes are described. Finally, the results of the multi-state electronic coupling calculations are presented together with the other CT rate parameters and resulting CT rates.

Finally, the conclusions of the thesis are given in Chapter 5. The guidelines and outlook for future computational studies of PSCs materials are discussed.

2   BACKGROUND

This chapter gives a brief background to PSCs covering their basic device structure, common PSC materials, and principles of the charge generation in the photoactive layer. The charge rate model, i.e. the Marcus theory, used in this work will be discussed. Moreover, a brief survey of the theory behind of the DFT methods applied in this thesis is given.

2.1   Polymer solar cells

Over the last two decades, organic solar cells using the π-conjugated polymers as eD materials have been a topic of interest [6, 7, 59]. This is due to their promising features, such as lightweight, transparency, thin film flexibility, low cost, solution processibility, and possibility of the large-scale processing, which make PSCs as strong candidates in the solar cell market. The most efficient PSCs make use of the BHJ architecture in a photoactive layer, where an eD material, i.e. polymer, is blended with an eA material. Fullerene derivatives have been a popular choice as the eA materials and the highest power conversion efficiencys (PCEs) achieved with a single-junction polymer–fullerene BHJ devices have been ca. 12% [60, 61]. However, due to limitations of fullerene derivatives (see Section 2.1.2), the PCEs of fullerene-based PSCs still lack behind those (> 20% [4]) of the commercialized, inorganic Si-based devices. Thus, alternative eA materials including conjugated polymers and A–D–A type SMAs have been developed to address these issues. The NF PSCs have reached promising PCEs of above 14% [25, 35] with better long-term stability compared to conventional fullerene-based devices.

The basic device structure of the PSC comprises interfacial layers that are deposited on each other (Figure 2.1). In general, the active layer, where the absorption of sunlight and generation of charge carriers take place, is sandwiched between two elec-
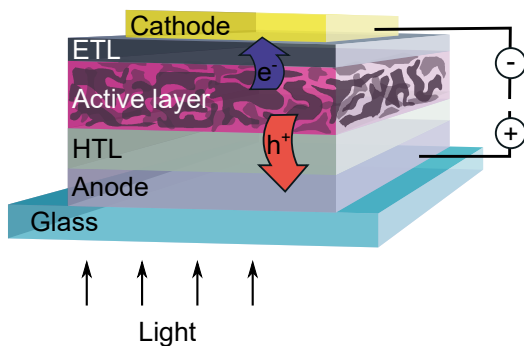
Figure 2.1 Schematic illustration of the PSC with a conventional layer structure. The directions of electrons (e$^-$) and holes (h$^+$) towards the electrodes are also presented with the arrows.

trodes [3]. Formation of an internal electric field and migration of electrons and holes from the active layer towards corresponding electrodes, i.e. a cathode and anode, respectively, is enabled by different work functions of the electrodes. Additional hole (HTL) and electron transport layers (ETLs) can be interposed between the active layer and electrodes to prevent the migration of the charge carriers in the wrong electrodes and thus improve the performance of the PSC. In the conventional architecture, the HTL, active layer, and ETL are deposited on an anode, whereas in an inverted PSC, the layers are deposited on a cathode in the opposite order.

Before going into more details about the PSCs, some of the terms relevant for this work will be defined. The words donor and acceptor are typically used in the literature to refer to the electron-donating and electron-accepting materials in the BHJ blend, respectively. However, the backbone units in constitutional repeating units (CRUs) of D–A copolymers (see Section 2.1.1) are also usually denoted by a donor and acceptor. Although D–A copolymers, which are characterized by small optical (and electronic) band gaps ($\leq$ 1.5 eV [6]), have been referred to as "low-bandgap" [6], "narrow-bandgap" [6], and "push–pull" [59] polymers in the literature, the term "D–A copolymer" will be used here, as it describes best the architecture of this particular class of conjugated materials. Thus, the word "electron" will be used in the context of the materials to distinguish them from the copolymer units: the material with the smallest ionization energy (IE) (often somewhat misleadingly [62] equated to the highest occupied molecular orbital (HOMO) energy) will be denoted by eD

8

and the material with the largest electron affinity (EA) (typically equated to the low-est unoccupied molecular orbital (LUMO) energy) will be denoted by eA [3].

2.1.1 Electron donor materials: conjugated polymers

The backbone of a semiconducting, π-conjugated polymer is composed of alternat-ing single and double bonds between carbon atoms with possible aromatic and het-eroaromatic rings. Due to conjugated backbones, this kind of polymers absorb in the visible spectral range, which make them suitable light absorbing material for so-lar cell applications [63]. Conjugated polymers used in PSCs can be classified by the type of their CRUs into homopolymers, D–A copolymers, quinoid polymers, and other types of polymers [6]. The first polymers employed in BHJ PSCs were polyphenylenevinylenes [64]. However, their limited light absorption due to the relatively large bandgaps (ca. 2.2 eV) and low carrier mobilities led to the PCEs of only 2–3%. Thus, the attention shifted towards polythiophenes, including a widely employed homopolymer poly(3-hexylthiophene) (P3HT), which had smaller band gap (ca. 1.9 eV), higher hole mobility, and broader spectral coverage compared to polyphenylenevinylenes [6, 65]. However, the PCEs of the P3HT–[6,6]-phenyl-C_{61}-butyric acid methyl ester ($PC_{61}BM$) system were still limited to 4–5% due to large IE of P3HT. Nevertheless, P3HT has been a subject of a tremendous amount of studies and a benchmark material in the many PSC studies [66].

Although the homopolymer P3HT had promising features, its performance could not be improved further and it did not meet all the requirements set for an "ideal" polymer. That is, a strong absorption in both the visible and near-infrared regions, IE and EA matching well with those of the eA material, and planar backbone to enable closely packed, parallel polymer chains [6, 59, 67]. In 1993, Havinga et al. [68, 69] introduced the concept of a D–A approach, where the CRU of a conjugated polymer consists of alternating electron-donating (donor) and electron-withdrawing (acceptor) units (Figures 2.2a and 2.2b). When considering this concept at the level of one-electron molecular orbitals (MOs), the MOs of the donor and acceptor units will interact leading to a set of hybridized MOs (Figure 2.2c), which are mainly de-termined by the corresponding energy levels of the individual donor and acceptor
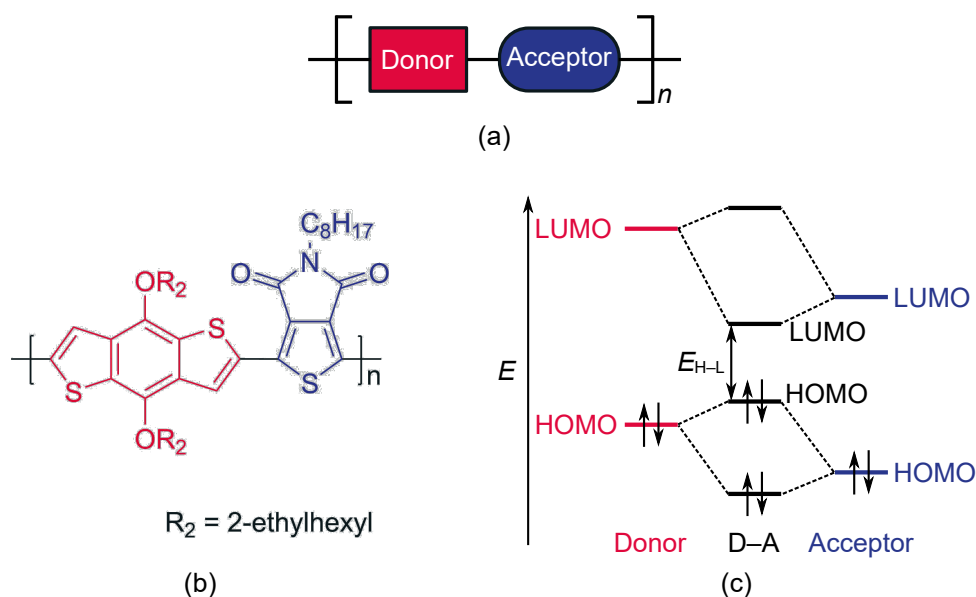
Figure 2.2 Schematic illustrations of (a) a CRU of a D–A copolymer, (b) a CRU of the PBDT-TPD copolymer, and (c) frontier molecular orbital (FMO) levels of separate donor and acceptor units and resulting hybridized FMO levels.

units. Thus, at the molecular level, the selection of the donor unit with a small IE (i.e. high-lying HOMO) and the acceptor unit with a large EA (i.e. low-lying LUMO) will lead to a smaller fundamental (HOMO–LUMO) gap than that of either unit. Consequently, the properties of the D–A copolymer, such as the IE, EA, band gap, optical gap, and transition dipole moments, can be fine-tuned by selecting the donor and acceptor units with suitable electron-donating and electron-withdrawing strengths [59, 70].

Different design strategies have been employed for obtaining D–A copolymers with desired characteristics. The optoelectronic properties, e.g. band gap, IE, EA, charge carrier mobility, and conductivity of the polymer are mainly governed by its conjugated backbone [59]. Typically, a planar backbone has been aimed at, as it enhances the delocalization of the electrons and π-stacking of the polymer chains. This has been achieved by using fused conjugated units consisting of three or more rings, such as benzene, thiophene, or other heterorings [6]. For example, benzo[1,2-*b*:4,5-*b'*]dithiophene (BDT) (see Figure 2.2b), which is included in most of the D–A copolymers studied in this work, has been a successful donor unit. Among the

acceptor units, thieno[3,4-*c*]pyrrole-4,6-dione (TPD) and quinoxaline, which have been employed also in the copolymers examined in this thesis, have been promising candidates. Even higher levels of fusion have been pursued via ladder-type donor units, where several adjacent aromatic units have been covalently fastened together. However, too rigid and coplanar backbones may lead to increased intermolecular π-π stacking interactions, which will hinder the solubility and processibility of the polymer and miscibility of the polymers with the eA materials, e.g. fullerenes [59]. This is also supported by MD simulations of Jackson et al. [13], where they have showed that some of the high-performing conjugated polymers do not necessarily have rigid, planar backbones, but rather disordered, twisted ones.

The side chains of the polymer may impact its molecular weight, solubility, and processibility [59]. They also control the intermolecular interactions, π–π stacking of polymer chains, and intercalation of fullerene derivatives between the polymer side chains [71]. However, they should be selected carefully, as long and branched side chains may improve solubility, but on the downside, introduce steric hindrance and increased torsional twists in the backbone leading to poorer photovoltaic properties of the polymer [6, 59]. This can be avoided by placing a spacer unit, e.g. thiophene, between the donor and acceptor units, which provides additional degree of freedom to the backbone [3].

Finally, the properties of the copolymer can be further fine-tuned by attaching different substituents, such as electron-donating methoxy groups and nitrogen or electron-withdrawing fluorine, chlorine, and cyano group, to its backbone units [6]. The inclusion of the electron-donating groups result in the decreased IEs (i.e. destabilized oxidation potentials), whereas the electron-withdrawing groups may increase both IEs and EAs (i.e. stabilize redox potentials), which has resulted in improved short-circuit current densities, open circuit voltages, fill-factors, and PCEs of the devices. Furthermore, it has been shown both experimentally [72, 73] and theoretically [15] that even small changes in these substituents can impact the blend morphology.

2.1.2 Electron acceptor materials

Since Heeger et al. observed [74] a photoinduced electron transfer (PET) between poly[2-methoxy-5-(2-ethylhexyloxy)-1,4-phenylenevinylene] and a buckminsterfullerene (C_{60}) in 1992, fullerene-based materials have been exploited as eAs in organic photovoltaics due to their high EAs and electron mobilities. However, as the solubility of C_{60} (and other fullerenes as well) is rather poor in organic solvents commonly used in PSCs (e.g. chloroform, chlorobenzene, etc.), more soluble fullerene derivatives have been employed instead. Especially, a C_{60} derivative $PC_{61}BM$ and its C_{70} analogous, [6,6]-phenyl-C_{71}-butyric acid methyl ester ($PC_{71}BM$), (see Figure 2.3) have been widely used fullerene derivatives in BHJ PSCs [3]. The present PCE records of ca. 12% for fullerene-based PSCs [60, 61] have been achieved with $PC_{71}BM$, which have broader absorption in the visible part of the spectrum and better solubility compared to $PC_{61}BM$. However, using $PC_{71}BM$ as the eA set restrictions to the choice of the polymer, as its properties (e.g. IE, EA, optical gap) should match with those of $PC_{71}BM$. While the structures of fullerenes do not enable further chemical tuning, the fullerene-based PSC are hindered by their poor light absorption in the visible and infrared spectra regions and morphological instabilities [7]. Therefore, the attention of the research community have shifted towards alternative NF eA materials.

Although the idea of incorporating conjugated polymers as both eD and eA materials in the BHJ tracks back in 1995 [75, 76], it has been only the past few years, during which conjugated D–A copolymers have emerged as potential eA materials. The APSCs have demonstrated improved light absorption, enhanced short-circuit current densities and open-circuit voltages, and better long-term stabilities compared to the conventional, fullerene-based PSCs [7]. Enhanced absorption is due to that in a polymer–polymer blend, both eD and eA can contribute to light harvesting (see Section 2.1.3). Moreover, polymer synthesis offer much higher versatility and flexibility than fullerene chemistry. Especially, the naphthalene diimide (NDI) based copolymers using thiophenes as the donor units have been promising candidates [77]. So far, the most successful NDI-based polymer has been poly[(*N,N'*-bis(2-octyldodecyl)naphthalene-1,4,5,8-bis(dicarboximide)-2,6-diyl)-*alt*-5,5'-(2,2'-bithiophene)] (P(NDI2OD-T2)) [78, 79], also referred to as N2200, which makes use of NDI
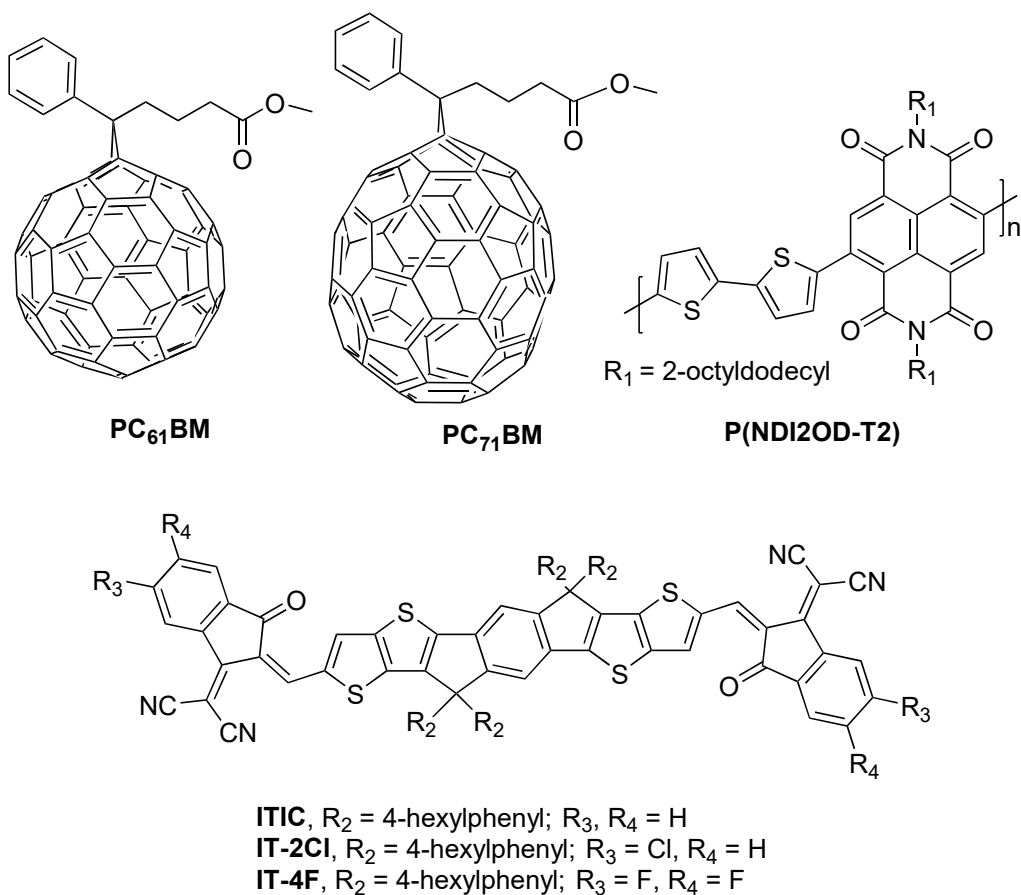
Figure 2.3 Structures of different types of eA materials employed in PSCs including fullerene derivatives PC$_{61}$BM and PC$_{71}$BM, D–A copolymer P(NDI2OD-T2), and SMA ITIC derivatives.

as the acceptor unit and bithiophene as the donor unit (Figure 2.3). P(NDI2OD-T2) has a small optical gap of ca. 1.5 eV [78], broad light absorption, and high electron mobility and EA. Furthermore, it matches well with a range of wide- (> 1.9 eV) and medium-bandgap (1.5–1.9 eV) copolymers [56]. The PCEs of 10% [80] have been obtained with the P(NDI2OD-T2)-based APSCs. Despite relative fast improvements in development of APSCs, the challenge is to balance between small phase separation and avoid interchain entanglement between two different polymers, which makes the development of APSCs more difficult [57].

The most successful NF PSCs so far have incorporated SMAs as eA materials. The fused-ring SMAs are based on a A–D–A structure, which enables strong intramolecu-

lar electron push-pulling effects similar to those of D–A copolymers [57]. A successful ITIC [81] consists of a ladder-type, electron-donating fused indacenodithieno[3,2-b]thiophene (IT) core end-capped with electron-deficient 2-(3-oxo-2,3-dihydroinden-1-ylidene)malononitrile (INCN) groups (Figure 2.3). In addition, four 4-hexylphenyl side groups are attached to the IT core, which control the accessibility of ITIC to the backbones of eD copolymers, as have been proven by theoretical MD studies [16] (see Section 4.5.1). The advantage of ITIC derivatives is that their optoelectronic properties can be easily tuned by molecular modifications, while keeping their key aspects of efficient eAs [57, 58, 81]. Furthermore, they have strong light absorption, high electron mobilities, and good miscibility with eD polymers. The SMA-based PSCs have shown the record braking PCEs of above 14% recently in single-junction devices [25, 35] and of above 17% in two-terminal tandem devices [82]. With these efficiencies, NF PSCs are one step closer to commercializing PSCs, as soon their issues related to use of green solvents, thickness tolerance, stability under different environmental factors, and relatively high cost are answered [57].

2.1.3 Charge generation in polymer solar cells

The performance of the PSC is controlled by the efficiencies of following main CT processes (Figure 2.4a): (i) light absorption by the eD material (Channel I in Figures 2.4a and 2.4b, the light absorption of the eA material would occur via Channel II) and formation of bound electron-hole pairs, i.e. excitons; (ii) exciton diffusion to the eD–eA interfaces; (iii) exciton dissociation (ED) into the free charge carries (holes and electrons) and formation of a CT state; (iv) charge-separation and migration toward the electrodes, and (v) charge collection at the electrodes. The optimization of all of these steps are crucial for efficient charge-generation in the PSC, especially those related to ED and formation of free charge carriers.

In contrast to the inorganic materials (e.g. crystalline silicon), where the electron and the hole separate immediately upon photoexcitation, generation of free charge carriers in organic solar cells is not spontaneous at room temperature. This is due to low dielectric constants ($\epsilon_s \approx 2$–4) [83] and the presence of strong electron-electron and electron-vibration interactions in organic π-conjugated materials [84], which leads
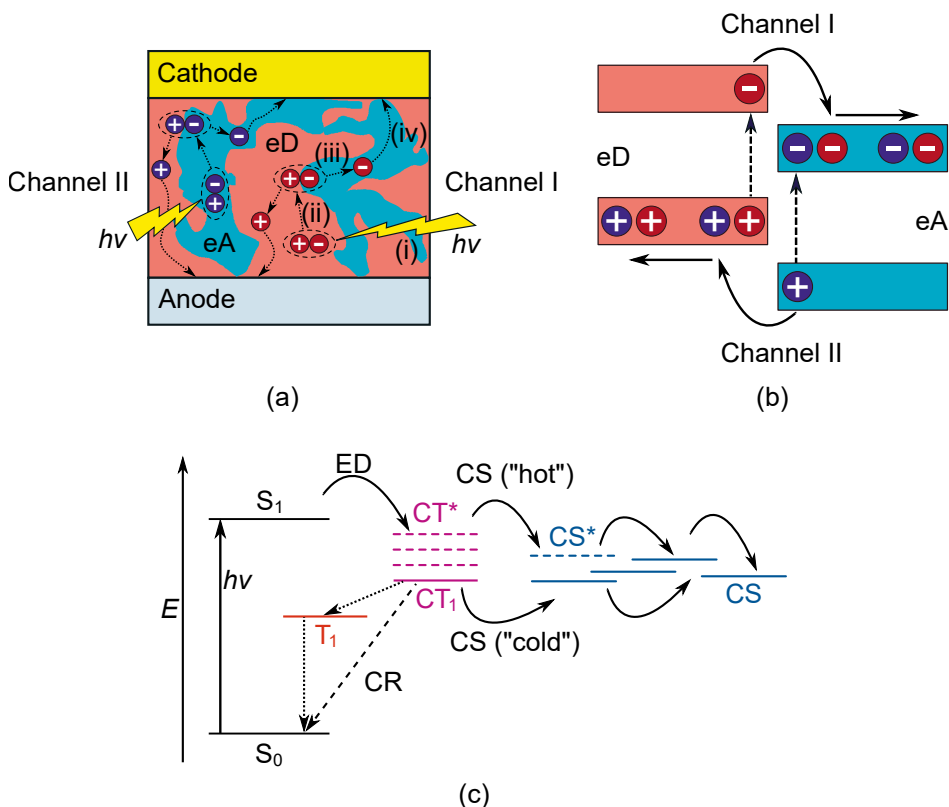
Figure 2.4 Schematic illustrations of (a) the basic CT processes taking place at the interfaces of the eD and eA compounds in the photoactive layer together with the (b) one-electron and (c) many-electron state descriptions of the charge generation in a PSC. The "cold" charge separation (CS) process refer to the CS via the CT_1 state, wheres the "hot" CS occur via higher-energy CT states.

to large exciton binding energies at room temperature (ca. 0.35–0.50 eV) [84, 85]. At the interfacial CT state, the hole and electron, which are localized on the eD and eA molecules, respectively, are still electrostatically bound to each other and have to overcome their Coulomb attraction to be able to separate to free charge carriers [84]. Otherwise, charges will recombine to the ground state (GS) [86]. Recombination via a triplet state is also one possible loss channel for PSCs (e.g. via the lowest triplet excited state, T_1, see Figure 2.4c) [83]. Thus, maximizing the ED and charge-separation, while preventing charge recombination (CR) are of the great importance [3]. In this work, the focus will be on theoretical examination of the excitation, ED, and CR processes.

In the PSCs, the ED can occur via two main channels referred to as Channels I and II [87]. In the Channel I, the eD compound is photoexcited followed by the electron transfer (ET) from the eD to eA compound, while in the Channel II, the eA compound is photoexcited followed by the hole transfer (HT) from the eA to eD (Figures 2.4a and 2.4b). In the conventional fullerene-based PSCs, the role of the Channel II has been usually neglected due to overlap of the absorption spectra of the individual eD and eA materials, i.e. polymers and fullerenes, respectively. However, in emerging NF PSCs, where the spectrum of eA is more easily separated from that of eD, the Channel II has been more focus of interest lately. Suitable energy offsets are required for the ED. In Channel I, the offsets between the excited electron on the eD compound and the EA of the eA compound in its GS (also approximated by the EAs of the eD and eA) provide a driving force for the PET [7, 87]. In Channel II, the excited eA compound oxidizes the eD compound, which is in the GS, and thus the efficiency of the photoinduced hole transfer (PHT) is governed by the offsets between the oxidation potential of the eD in its GS and the reduction potential of the excited eA (also approximated by the IEs of the compounds). Thus, for achieving efficient charge generation in PSCs, the eD and eA materials with the matching IEs and EAs should be selected.

In general, the mechanism of charge transport can be described by two different models depending on the material and temperature: a band transport model and localized hopping model [88, 89]. At very low temperature, the transport in inorganic crystals (or ultrapure organic crystals) occurs via coherent band transport, where charge carriers are fully delocalized at the valence or conduction band edges. At higher temperatures, e.g. room temperature, the charge transport of weakly coupled organic crystals and disordered solids, e.g. polymer melts is described with the hopping model: initially, the charge carrier is localized on one site in the solid, which, depending on the degree of the localization, can be a single molecular unit, larger part of molecule, or several molecules. From there, the charge carrier moves to another site by discrete jumps.

In a hopping regime, several theoretical approaches have been developed to describe charge transport, including CT rate models [88]. As the transfer of electron induces changes in the nuclear geometry of the system, the initial (i) and final (f) states of the CT processes can be represented by potential energy surface (PES) curves, i.e.
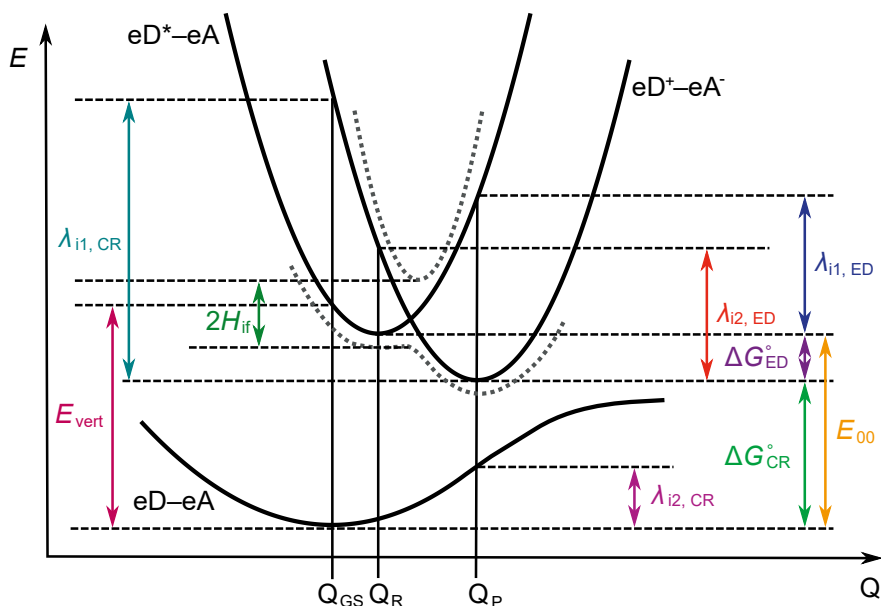
Figure 2.5 Schematic illustrations of changes in the potential energy of the system as a function of nuclear reaction coordinate Q of the states relevant to the ED and CR processes taking place at the interfacial eD–eA system. The black solid lines illustrate the diabatic potential energy curves, while the adiabatic ones are represented with gray, dashed lines. The equilibrium nuclear coordinates of the GS (i.e. eD–eA), reactants (i.e. eD*–eA), and products (i.e. eD$^+$–eA$^-$) are denoted by Q_{GS}, Q_R, and Q_P, respectively. The contributions to the CT parameters, i.e. inner reorganization energy (λ_i), Gibbs free energy of the reaction (ΔG°), and electronic coupling (H_{if}) are also indicated together with the lowest vertical excitation energy (E_{vert}) and energy difference between the GS and lowest excited state (E_{00}). Adapted from [90].

parabolas of the reactants and products as a function of nuclear coordinates Q (Figure 2.5) [83]. In the high-coupling limit, the Born–Oppenheimer approximation is valid and the electronic wave function changes slowly, i.e. adiabatically, when the system crosses the activation barrier between the initial and final charge localized states [88]. The degeneracy at the crossing of the states is removed (i.e. avoided crossing) leading to two new separate (adiabatic) PESs, where the CT proceeds along lower surface [47].

In the weak-coupling limit ($\hbar\omega_i \ll k_B T$; also denoted to as the high-temperature limit [91] or low-frequency regime), the CT is governed by the Franck–Condon principle, i.e. the ET occurs so fast (even on the femtosecond time scale) that the nuclear configuration will not have time to respond to it and remains unchanged

during the transfer. Thus, ET must take place at the intersection point of two cross-ing diabatic PES curves (Figure 2.5) [83]. On the basis of Fermi's golden rule, the hopping rate for the diabatic CT can be expressed by the semiclassical Marcus theory [92–94]:

$$k_{\text{ED/CR}} = \frac{|H_{\text{if}}|^2}{\hbar} \sqrt{\frac{\pi}{\lambda k_{\text{B}} T}} \exp\left[-\frac{(\Delta G^\circ + \lambda)^2}{4\lambda k_{\text{B}} T} \right] \qquad (2.1)$$

where H_{if} is the electronic coupling between the initial (i) and final (f) states of the particular CT process; k_{B} and $\hbar$ are the Boltzmann and reduced Planck's constants, respectively; λ is the reorganization energy (consisting of the inner, λ_{i}, and outer, λ_{s}, contributions); and ΔG° is the Gibbs free energy of the CT reaction.

The Marcus theory has been applied in several theoretical studies for calculating the CT rates of the PSC systems [23, 54, 55, 95]. While a variety of the computational methods have been developed for deriving the parameters present in Equation 2.1, i.e. H_{if}, λ, and ΔG°, their calculation is not so straightforward. The methods that have been applied for calculating the CT parameters in this work are presented in more detail under the methods, see Section 3.2.6. However, as one of the main fo-cuses of this work has been calculating the electronic couplings, different theoretical coupling schemes will be shortly discussed here.

The electronic coupling (also referred to as a transfer integral) is the off-diagonal matrix element of the electronic Hamiltonian of the system ($\widehat{H}$). The electronic coupling between the initial and final diabatic states $|\Psi_{\text{i}}>$ and $|\Psi_{\text{f}}>$ can be defined

$$H_{\text{if}} = < \Psi_{\text{i}} | \widehat{H} | \Psi_{\text{f}} > \qquad (2.2)$$

There exists different theoretical approaches for calculating electronic couplings, which differ in how they define the diabatic states [88]. In some of the schemes, e.g. constrained DFT [96], the diabatic states are constructed directly. Alternative, some schemes make use of the adiabatic eigenstates retrieved from the quantum me-chanical calculations in determining the diabatic ones. In the case of the symmetric systems, the simplest approach for the electronic coupling is to calculate it as half

the energy gap between the GS and excited state (see Figure 2.5). In the approaches based on Koopmans' theorem, the coupling is taken as half the splitting between the two HOMO (or two LUMO) levels of the interacting compounds [91]. As these schemes are not applicable for asymmetric systems, other approaches should be employed for them instead, such as a fragment orbital approach [97], which has been an efficient scheme for calculating the electronic couplings of the GS CT processes. Furthermore, it has also been employed to approximate the couplings for the excited state CT processes of the PSC systems [95]. There exist also several diabatization schemes, where the adiabatic states are transformed to the diabatic ones by using either the wave-function for example in Boys-localization [98], Edmiston–Ruedenberg localization [99], and block diagonalization [100, 101] or an additional operator, e.g. dipole moment (μ) in the GMH scheme [48, 49] or charge difference (Δq) in the FCD scheme [50].

As mentioned in Section 1.1, the eigenstate-based GMH and FCD have been employed in this work, as they are useful approaches for describing the electronic couplings of the CT processes involving excited states [48, 50, 51]. Importantly, they can be applied for large molecules like those employed in the PSC systems, where they have been popular schemes for calculating the electronic couplings of different CT processes. Furthermore, multiple states can be included simultaneously in both the GMH and FCD schemes [48–51].

2.2 Density functional theory calculations

This chapter will give a brief review of the theory behind the calculation methods used in this thesis. The idea is not to give a detailed account of the theory, but provide a context for the computational work carried out here. The focus will be mostly on quantum mechanics based DFT methods, especially on different approximate forms of the XC functional, as testing their performance in predicting the properties of PSC compounds has been one of the main cores for this work. However, as the foundation of DFT lies on the general electronic structure and HF theories, they will be shortly introduced first. Additionally, some of other relevant computational methods are discussed. In addition to the original texts of the theoretical approaches

presented here, the contents and notation used in this section is mainly based on the books of Jensen [102], Cramer [103], Atkins [104], and Foresman and Æleen [105] which provide more detailed background for these methods.

2.2.1 Electronic structure and Hartree–Fock theories

In quantum mechanics, one of the fundamental postulate is that the state and consequently all physical properties of a system can be fully described by a wavefunction Ψ. If a static system is considered, Ψ can by solved with the time-independent, non-relativistic form of the Schrödinger equation:

$$\widehat{H}\Psi = E\Psi \tag{2.3}$$

where $\widehat{H}$ and E are the Hamiltonian operator and its corresponding observable, the total energy of the system, respectively. The Hamiltonian operator for the N_e-electron and M-nuclei system have the following form in atomic units:

$$
\begin{aligned}
\widehat{H} &= \widehat{T}_e + \widehat{T}_n + \widehat{V}_{en} + \widehat{V}_{ee} + \widehat{V}_{nn} \\
&= -\sum_{i=1}^{N_e} \frac{\nabla_i^2}{2} - \sum_{A=1}^{M} \frac{\nabla_A^2}{2m_A} - \sum_{i=1}^{N_e}\sum_{A=1}^{M} \frac{Z_A}{r_{iA}} + \sum_{i=1}^{N_e}\sum_{j>i}^{N_e} \frac{1}{r_{ij}} + \sum_{A=1}^{M}\sum_{B>A}^{M} \frac{Z_A Z_B}{r_{AB}}
\end{aligned}
\tag{2.4}
$$

where i and j run over the electrons, A and B over the nuclei, m_A is the mass of the nucleus, ∇^2 is the Laplacian operator, Z_A is the atomic number of nucleus A, and r_{ab} is the distance between particles the a and b. In Equation 2.4, the first two terms, $\widehat{T}_e$ and $\widehat{T}_n$, are the kinetic energy of the electrons and nuclei, respectively, and the three last terms, $\widehat{V}_{en}$, $\widehat{V}_{ee}$, and $\widehat{V}_{nn}$, represent the potential energy due to the attraction between the electrons and nuclei, the electron-electron repulsions, and the nucleus-nucleus repulsions, respectively.

Analytical solving of Equation 2.4 is impossible for systems larger than two particles (i.e. the hydrogen atom) due to the complexity caused by pairwise attraction and repulsion terms. This problem can be addressed by adopting the Born–Oppenheimer approximation [106], which takes advantage of the fact that the nuclei are much heavier and move much slower than the electrons. Thus, the electrons can be assumed to respond instantaneously to the movement of the nuclei. Due to the different timescales of nuclear and electron motion, they can be decoupled and solve the Schrödinger equation for the molecular system at the fixed nuclear positions. Consequently, in Equation 2.4, the kinetic energy of the nuclei ($\widehat{T}_n$) is zero, correlation in $\widehat{V}_{en}$ is eliminated, and $\widehat{V}_{nn}$ becomes a constant that is easy to evaluate. The remaining terms account for the electronic Hamiltonian, $\widehat{H}_{el}$, which has the following form in atomic units:

$$\widehat{H}_{el} = -\sum_{i=1}^{N_e} \frac{\nabla_i^2}{2} - \sum_{i=1}^{N_e}\sum_{A=1}^{M} \frac{Z_A}{r_{iA}} + \sum_{i=1}^{N_e}\sum_{j>i}^{N_e} \frac{1}{r_{ij}} \tag{2.5}$$

When $\widehat{H}_{el}$ is employed in Equation 2.3 with an electronic wavefunction, Ψ_{el}, the electronic energy, E_{el}, is obtained. The total energy of the system (with the fixed nuclei) is obtained by adding E_{el} to a (classical) nucleus-nucleus repulsion energy: $E_{tot} = E_{el} + E_{nn}$.

Although Equation 2.5 has a simpler form than Equation 2.4, it is still insolvable for a many-electron system due to the remaining correlation between the individual electrons, and thus additional approximations are required. In independent-particle models, the electrons are assumed to move independently of each other. In the HF theory, this is achieved by treating the electron–electron repulsion in an averaged way, i.e. each electron moves in the electrostatic field of the nuclei and the average field generated by the other electrons. The many-electron problem reduces to the set of one-electron problems, where each electron in a molecule is described by a spin orbital, $\chi_i(\mathbf{x}_j)$, which is a product of a spatial orbital (also referred to as a MO), ψ_i, and an electron spin eigenfunction (α or β). The total, many-electron wavefunction is then expressed by a product of one-electron spin orbitals.

To obey the Pauli exclusion principle, the total wavefunction should be antisymmetric, which is ensured by writing it in the form of a single Slater determinant of spin orbitals. For a molecular system with N_e electrons, the wavefunction can be thus written in the form of

$$\Psi(\mathbf{x}_1, \mathbf{x}_2, ..., \mathbf{x}_{N_e}) = \frac{1}{\sqrt{N_e!}} \begin{vmatrix} \chi_1(\mathbf{x}_1) & \chi_2(\mathbf{x}_1) & \cdots & \chi_{N_e}(\mathbf{x}_1) \\ \chi_1(\mathbf{x}_2) & \chi_2(\mathbf{x}_2) & \cdots & \chi_{N_e}(\mathbf{x}_2) \\ \vdots & \vdots & \ddots & \vdots \\ \chi_1(\mathbf{x}_{N_e}) & \chi_2(\mathbf{x}_{N_e}) & \cdots & \chi_{N_e}(\mathbf{x}_{N_e}) \end{vmatrix} \tag{2.6}$$

where each row corresponds to an individual electron and each column to a spin orbital.

The MOs can be obtained as linear combinations of nuclei-centered basis functions, i.e. atomic orbitals, φ:

$$\psi_i = \sum_{\mu}^{\text{basis functions}} a_{i\mu} \varphi_\mu \tag{2.7}$$

where the set of basis functions φ_μ is also referred to as the basis set associated with a set of MO coefficients $a_{i\mu}$. In a basis set, a finite set of mathematical functions are used to represent the MOs and build the wavefunction. The quality of the quantum mechanical calculations depend on the size of the basis set, i.e. number of the basis functions it includes. Using an infinite, complete set of basis functions would be required to represent MOs exactly. However, this is impossible in practice and finite basis sets are used instead. In larger basis sets, fewer constraints have been set on electrons leading to more accurate description of the wavefunction, but also computationally more demanding calculations. Thus, suitable balance between the size of the basis set and accuracy should be found.

Current basis functions typically make use of the Gaussian-type orbitals (GTOs) as basis functions. Valence orbitals take part in the chemical bonding, while core orbitals are usually only weakly affected by it. In so-called split-valence basis sets,

this is utilized by representing core orbitals with a single (contracted) basis function, whereas valence orbitals are represented by two or more basis functions of different size. The Pople's split-valence basis sets have been generally popular and are also a common choice in the quantum chemical studies of PSC systems. While other type of basis sets, such as Dunning's, have also been employed for their modeling, only those of Pople's have been considered here, as the main focus of this work has been on comparison of different functionals.

In this thesis, the Pople's 6-31G** split-valence basis set, which consists of one core orbital basis function comprised from six primitive GTOs and two valence orbitals comprised from three and one primitive GTOs, has been mostly used. The 6-31G** basis set includes polarization functions for each atom (denoted by the asterisks), which allow more mathematical flexibility for description of MOs. The first "star" denotes to addition of six d-type polarization functions for each atom but hydrogen, whereas the second star refers to the addition of a set of three p-type polarization functions for each hydrogen atom. Furthermore, some calculations in this work have been carried out with the 6-31+G* basis set, which includes diffuse functions, i.e. large-size versions of the s- and p-type functions, which improve the description of molecules of lone pairs, e.g. anions.

As the MO coefficients, i.e. $a_{i\mu}$ in Equation 2.7 are not known, a trial wavefunction is used to solve the energy. The best set of MOs, which yield the lowest energy, will be obtained with a iterative self-consistent-field (SCF) approach. The minimized energy is defined by using the variational principle, according to which any approximate wavefunction will have an energy above or equal to the exact energy.

The HF equations that are solved self-consistently have the form

$$\widehat{F}\chi_i = (-\frac{1}{2}\nabla_i^2 - \sum_{A=1}^{M}\frac{Z_A}{r_{iA}} + V_i^{\mathrm{HF}})\chi_i = \epsilon_i\chi_i \qquad (2.8)$$

where $\widehat{F}$ is a one-electron Fock operator and V_i^{HF} is the HF potential, $\widehat{J} - \widehat{K}$, with the components of the Coulomb $(\widehat{J})$ and exchange $(\widehat{K})$ operators, which represent the Coulombic repulsion between the electrons and quantum effect procuded by interchanging two electrons, respectively.

The hindrance of the HF method is that it neglects the correlation between electrons, which leads to overestimation of electron localization [26]. Post-HF methods have been developed to account for the missing electron correlation. For example, in Configuration Interaction [107, 108] and Coupled Cluster methods [109], electron correlation is taken into account by using a multi-determinant wave function. In Møller–Plesset (MP) perturbation theory [110], the perturbation theory is applied to the Hamiltonian. These methods are computationally more demanding than HF, but have a high accuracy and offer results that systematically approach the exact solution of the Schrödinger equation. There are some approximations of these methods, e.g. the resolution of the identity MP2 (RI-MP2), which have lower computational cost, but produce the results nearly identical to those of full MP2 (i.e. the second order MP). In the theoretical studies of the PSC compounds, the RI-MP2 method has been used for example in calculating reference torsional potentials for monomers of D–A copolymers [111].

2.2.2 Density functional theory

Density functional theory provides an alternative method to account for electron correlation with significantly less computational cost compared to post-HF methods. The foundations of DFT were laid by Hohenberg and Kohn [112]. According to their first (existence) theorem, the GS electronic energy of a system is a unique functional of the electron density $\rho(\mathbf{r})$. Thus, the energy and associated GS properties of the system can be derived from $\rho(\mathbf{r})$. The second (variational) theorem proves that the GS energy can be obtained variationally, $\rho(\mathbf{r})$ that minimized the total energy is the exact GS density, ρ_0.

The modern DFT methods are based on the work of Kohn and Sham [113], who introduced a fictitious system of non-interacting electrons, which have the same ρ_0 as the real system of interest, to avoid the difficulties in deriving the electron–electron interactions. Using a non-interacting system makes the solving of the Schrödinger equation a trivial task, as the Hamiltonian is a sum of one-electron operators with eigenfunctions being the Slater determinants of the individual one-electron eigen-

functions and eigenvalues being the sum of the one-electron eigenvalues. In the Kohn–Sham formalism, the form of the general DFT energy functional is

$$E_{\text{DFT}}[\rho(\mathbf{r})] = T_s[\rho(\mathbf{r})] + V_{\text{ne}}[\rho(\mathbf{r})] + J[\rho(\mathbf{r})] + E_{\text{XC}}[\rho(\mathbf{r})] \qquad (2.9)$$

where $T_s[\rho(\mathbf{r})]$ is the kinetic energy, $V_{\text{ne}}[\rho(\mathbf{r})]$ is the nuclei-electron potential energy, and $J[\rho(\mathbf{r})]$ is the Coulomb integral, i.e. Hartree electron-electron repulsion. The last term, $E_{\text{XC}}[\rho(\mathbf{r})]$, contains the difference between the classical and quantum mechanical electron–electron repulsion and the difference in kinetic energy between the fictitious non-interacting and real systems. The term missing from Equation 2.9 is the HF exchange (K). The pure DFT functionals omit it completely, but in the global hybrid functionals, a small part of exact HF exchange is included in their energy expression. The exact form of E_{XC} is not known, and thus several approximations have been developed for it that will be reviewed below.

In the Kohn–Sham formalism [113], the exact GS electron density can be expressed in terms of a set of one-electron orbitals

$$\rho(\mathbf{r}) = \sum_{i=1}^{N_e} |\psi_i(\mathbf{r})|^2 \qquad (2.10)$$

where the sum runs over all the occupied Kohn–Sham orbitals, $\psi_i(\mathbf{r})$. The Kohn–Sham equations have the form

$$\left\{ -\frac{1}{2}\nabla^2 + \sum_{A=1}^{M} \frac{Z_A}{r_{1A}} + \int \frac{\rho(\mathbf{r}')}{|\mathbf{r}-\mathbf{r}'|} d\mathbf{r}' + v_{\text{XC}}(\mathbf{r}) \right\} \psi_i = \epsilon_i \psi_i \qquad (2.11)$$

where ϵ_i are the Kohn–Sham orbital energies and v_{XC} is the XC potential that is the functional derivative of E_{XC}:

$$v_{\text{XC}}(\rho) = \frac{\delta E_{\text{XC}}(\rho)}{\delta \rho}. \qquad (2.12)$$

The Kohn–Sham equations (Equation 2.11) are solved self-consistently starting by an initial guess of the electron density $\rho(\mathbf{r})$. Then v_{XC} is computed as a function of r with Equation 2.12 by using some approximation for E_{XC}, i.e. a XC functional (see below). The Kohn–Sham equations are then solved to obtain an initial set of ϵ_i, which are used to compute an improved ρ from Equation 2.10. This is repeated until $\rho(\mathbf{r})$ and E_{XC} have converged to within a certain tolerance and the total electronic energy is finally obtained with Equation 2.9.

In modern molecular quantum chemistry, DFT methods have become a main tool due to their accuracy and smaller computational cost compared to the post-HF methods. In the accurate MP and coupled cluster theory methods, the computational scaling is from N^5 to N^{10}, where N is the molecular size, which is typically the number of basis functions in the calculation. In DFT methods, the scaling is between N^2 and N^3, and developments of the linear-scaling algorithms have resulted in the scaling of N in some cases enabling the modeling of the systems consisting of thousands of atoms [42, 114]. The main disadvantage of DFT is that there is no systematic approach to improve the results towards the exact solution.

2.2.3   Time-dependent density functional theory

In the studies of excited-state properties of the system, a time-dependent Schrödinger equation is applied instead of Equation 2.3

$$\widehat{H}(t)\Psi(t) = i\,\hbar\,\frac{\Psi(t)}{dt} \qquad (2.13)$$

where $\widehat{H}(t)$ is the time-dependent Hamiltonian and $\Psi(t)$ is the electronic wavefunction as a function of time. Time-dependent extension of DFT, i.e. TDDFT is based on the Runge–Gross theorem [115], which, analogously to Hohenberg–Kohn theorems [112], states that the time-dependent external potential is a functional of the time-dependent electron density. Similarly to DFT, TDDFT simplifies the solving of Equation 2.13 for the many body system by replacing it with a set of time-dependent

single-electron orbitals. The TD Kohn–Sham equations in TDDFT have the form similar to Equation 2.11:

$$\left\{ -\frac{1}{2}\nabla^2 + v(\mathbf{r}, t) + \int \frac{\rho(\mathbf{r}', t)}{|\mathbf{r} - \mathbf{r}'|} d\mathbf{r}' + V_{\text{ext}}(t) + v_{\text{XC}}(\mathbf{r}, t) \right\} \psi_i(\mathbf{r}, t)$$

$$= i\hbar \frac{\partial}{\partial t} \psi_i(\mathbf{r}, t) \qquad (2.14)$$

where the external potential, V_{ext}, v_{XC}, the Kohn–Sham orbitals, and the density are now time-dependent. In TDDFT, the response of the molecular system to the varying V_{ext} (e.g. electric and magnetic fields) is studied, which enables the study of polarizabilities, hyper-polarizabilities, excitation energies, and absorption spectra.

In most quantum chemical codes, the linear response of TDDFT equation, i.e. the linear response of the time-independent GS density to a time-dependent V_{ext}, is used for calculating excitation energies instead of the full TDDFT. Moreover, the adiabatic approximation for the XC potential is usually applied, i.e. time-dependent $v_{\text{XC}}(\mathbf{r}, t)$ is replaced with time-independent $v_{\text{XC}}(\mathbf{r})$. This can be justified by an assumption that v_{XC} is local in time and only the present electron density is taken into account. Thus, the time-dependent density is used in the GS XC potential functionals, i.e. the same (semi)local XC functionals are employed as in DFT. In the Tamm–Dancoff approximation to time-dependent density functional theory (TDA) to TDDFT [116], the Hermitian eigenvalue equation of the full TDDFT is simplified to reduce the computational cost and address the issue of triplet instability, while leaving the excitation energies practically unchanged. In this work, both the linear-responsed TDDFT and TDA have been employed.

2.2.4   Density functional theory with periodic boundary conditions

Several different PBC codes have been developed to model extended, i.e. periodic systems, such as polymers, surfaces, and zeolites. Here, the focus will be on the PBC code developed by Kudin and Scuseria [41, 42], as it is implemented in the Gaussian

09 (and 16) suite of programs. It make use of localized GTOs that are transformed into crystalline orbitals, i.e. Bloch sums, with the following form

$$\Psi_{\mathbf{k}} = \sum_{\mathbf{g}} \left[\frac{1}{\sqrt{N}} e^{i\mathbf{k}\cdot\mathbf{g}} \right] \psi_{\mathbf{g}} \tag{2.15}$$

where $\mathbf{k} = (k_x, k_y, k_z)$ is the reciprocal-lattice vector, $\psi_{\mathbf{g}}$ is a GTO ψ centered in cell $\mathbf{g}$, and i is the imaginary unit. Periodic orbitals with different irreducible representations of the infinite translation group are classified by $\mathbf{k}$. Orbitals belonging to different $\mathbf{k}$ points do not interact with each other, and thus the SCF equations, which are similar as in the non-periodic case, can be solved separately for each $\mathbf{k}$ point.

Any orbital μ centered in the central cell (0) is coupled to any orbital ν centered in the gth neighbor cell by the Kohn–Sham Hamiltonian matrix elements.

$$F_{\mu\nu}^{0\mathbf{g}} = T_{\mu\nu}^{0\mathbf{g}} + U_{\mu\nu}^{0\mathbf{g}} + J_{\mu\nu}^{0\mathbf{g}} + V_{\mu\nu}^{0\mathbf{g}} \tag{2.16}$$

where $T_{\mu\nu}^{0\mathbf{g}}$ is the electronic kinetic energy, $U_{\mu\nu}^{0\mathbf{g}}$ is the electron-nuclear attraction term, $J_{\mu\nu}^{0\mathbf{g}}$ is the electron-electron repulsion term, and $V_{\mu\nu}^{0\mathbf{g}}$ is the contribution from the DFT XC potential. The first two terms in Equation 2.16 do not depend on the density matrix, whereas the latter two do. In general, the terms in Equation 2.16 are similar to those of the molecular case. However, one difference from the molecular case is that the electrostatic terms $U_{\mu\nu}^{0\mathbf{g}}$ and $J_{\mu\nu}^{0\mathbf{g}}$ include an infinite number of interactions between a given pair of basis functions and all the other charges of the system. The energy per unit cell are calculated as

$$E = \sum_{\mu \in 0} \sum_{\mathbf{g}} \sum_{\nu \in \mathbf{g}} (T_{\mu\nu}^{0\mathbf{g}} + U_{\mu\nu}^{0\mathbf{g}} + \frac{1}{2} J_{\mu\nu}^{0\mathbf{g}}) + E_{\text{XC}} + E_{\text{NR}} \tag{2.17}$$

where E_{NR} is the nuclear repulsion energy. The implementation of Kudin and Scuseria uses the fast multipole method for evaluation of the long-range electrostatic interactions, which enables high accuracy with the $O(N)$ computational cost.

2.2.5 Approximations to the exchange-correlation functional

In DFT, the exact form of the XC functional for E_{XC} is unknown, and thus numerous approximations have been developed. The choice of the functional defines the accuracy and efficiency of the DFT methods. Typically functionals are separated into an exchange and correlation part representing exchange and dynamic correlation energies, respectively. The simplest approximation, introduced by Kohn and Sham [113], is the local density approximation (LDA), where the density is a slowly varying function that is treated as a uniform electron gas with constant density. The spin-polarized formalism of LDA for the open-shell, i.e. unrestricted case is called as local spin-density approximation (LSDA). In the case of metals, alloys, and small-gap insulators, LDA and LSDA work well, especially in predicting structural properties.

However, as the electron density in a molecular system is typically far from spatially uniform, LDA and LSDA suffer from some limitations in predicting binding energies. This can be improved by making the correlation functional to depend on the extent to which the density is locally changing, i.e. the gradient of the density, instead of the local value of the density. In the generalized gradient approximation (GGA), a gradient correction term is included to the LDA functional. The first GGA-type exchange functional was developed by Becke [117, 118]. A popular GGA correlation functionals is LYP by Lee, Yang, and Parr [119], in which the correlation energy is computed totally instead of adding the correction term to LDA. The XC functionals are usually referred by combining the acronyms for the exchange and correlation functionals used in them in that order. For example, a BLYP functional combines the Becke's GGA exchange functional with the LYP GGA correlation functional.

Global hybrid functionals
The "pure" functionals based on LDA, LSDA, and GGA employ localized model for XC interaction but do not account for non-local effects. Thus, in the (global) hybrid functionals, a fixed amount of the exact HF exchange (typically 20–30%) is included to the pure DFT XC. A general form of the global hybrid functional based on the Becke's actual formulation [120], which separates the DFT exchange-correlation to

exchange and correlation parts (both local and non-local portions) with their own weighting factors c_1–c_5, is the following

$$E_{XC}[\rho(\mathbf{r})] = c_1 E_X^{HF} + c_2 E_X^{local} + c_3 E_X^{non\text{-}local} + c_4 E_C^{local} + c_5 E_C^{non\text{-}local}. \qquad (2.18)$$

Below, the formulas are given for some global hybrid functionals, which have been popular in the computational studies of PSC systems and have been also employed in this work. The popular three-parameter B3LYP [120, 121] implemented in the modern quantum mechanical software combines the exchange and correlation terms derived from LSDA, fraction of the exact HF exchange (20%), and the Becke's exchange functional B88 [118]. The non-local and local correlations in B3LYP are provided by the LYP and VWN [122] correlation functionals, respectively:

$$E_{XC}^{B3LYP} = 0.20 E_X^{HF} + 0.80 E_X^{LSDA} + 0.72 E_X^{B88} + 0.81 E_C^{LYP} + 0.19 E_C^{VWN} \qquad (2.19)$$

with the parameters ($c_1 = 0.20$, $c_2 = 1.00 - c_1$, $c_3 = 0.72$, $c_4 = 0.81$, and $c_5 = 1.00 - c_4$) being derived by a fit to the set of experimental data. B3LYP has been very popular functional and is commonly employed in the studies of PSC compounds even nowadays.

In the global hybrid functional PBE0 (also denoted by PBE1PBE1) [123, 124], which is mainly based on fundamental constants, the amount of the exact HF exchange (25%) has been defined on the basis of the perturbation theory rather than using empirically determined parameters:

$$E_{XC}^{PBE0} = \frac{1}{4} E_X^{HF} + \frac{3}{4}(E_X^{LSDA} + \Delta E_X^{PBE}) + E_C^{PW} + \Delta E_C^{PBE}. \qquad (2.20)$$

The PBE0 functional uses the PBE GGA exchange [125, 126] and PW correlation functionals [127]. Due to its single parameter ($c_2 = c_3 = 1.00 - c_1$) derived from the theoretical considerations, PBE0 is also said to be the parameter-free functional. It has resulted in relatively accurate electron densities for a set of the studied atomic

systems [128] and also for larger organic molecules including two to ten heavy atoms (e.g. carbon, oxygen, nitrogen, and sulfur) [129].

Despite the improved results provided by the global hybrid functionals due to the fragment of exact HF exchange when compared to the semilocal functionals, it is well known that they yield inaccurate description of some relevant molecular properties of the π-conjugated systems [26]. They tend to underestimate bond-length alternation (BLA) patterns [33], IEs [130], fundamental gaps [130, 131], and excited-state energies [9], while overestimating delocalization of the electron density [33], torsional barriers [132], and intermolecular electronic couplings [26]. These shortcomings are mainly due to the MSIE [27, 28] in these functionals, which leads to the incorrect dependence of the asymptotic region of v_{XC} with distance. Basically, the decay of the global hybrid functionals is proportional to the amount of the HF exchange in them ($-c_1/r$), while the correct decay should be $-1/r$. The inclusion of 100% HF exchange would correct these issues, but semi-local exchange is also required for the correct description of chemical bonding, etc. [26]. Thus, to utilize the advantages of HF and semi-local exchange, they should be both included in a functional.

Long-range corrected functionals
Restoring of the correct description of the asymptotic region of the v_{XC} can be achieved by partitioning the Coulomb operator $1/r_{12}$, which describes the interaction between electrons 1 and 2. In the class of so-called range-separated hybrid (RSH) functionals [29, 133, 134], the Coulomb operator is divided into SR and LR components with a standard error function (erf, or its modified version):

$$\frac{1}{r_{12}} = \underbrace{\frac{\mathrm{erf}(\omega r_{12})}{r_{12}}}_{\text{LR}} + \underbrace{\frac{1-\mathrm{erf}(\omega r_{12})}{r_{12}}}_{\text{SR}} \tag{2.21}$$

where ω is the range-separation parameter (with a dimension of inverse length). The general form of the RSH functional is

$$E_{\text{XC}}^{\text{RSH}} = c_{x,\text{SR}} E_{x,\text{SR}}^{\text{SR-HF}} + c_{x,\text{LR}} E_{x,\text{LR}}^{\text{LR-HF}} + (1 - c_{x,\text{SR}}) E_{x,\text{SR}}^{\text{DFT}}$$
$$+ (1 - c_{x,\text{LR}}) E_{x,\text{LR}}^{\text{DFT}} + E_c^{\text{DFT}}. \tag{2.22}$$

In the case of molecular systems, the RSH functionals referred to as LRC functionals are employed [29–32]. These functionals use the full non-local exchange and local correlation in the LR part, while treating the nonclassical interactions in the SR part by standard semi-local or global hybrid functionals. The idea is to take advantage of the semi-local or global hybrid functionals in the bonding region, while allowing for a correct treatment of the asymptotic region. In the calculations of solid-state systems, screened-exchange RSH functionals [135–137], where HF is used in SR and DFT in the LR, are employed instead. For the LRC functionals, $c_{x,\text{LR}}$ in Equation 2.22 equals one, while for the screened-exchange RSH functionals it equals zero.

The use of default values of ω in the LRC functionals is not recommended, as ω has proven to be a system-dependent parameter [130, 138]. Non-empirical tuning approaches for determining an optimal ω value for the studied system have been developed by Kronik et al. [131, 138], which are based on the DFT's analogous to the HF Koopman's theorem (see Section 3.2.3). In addition to tuning of ω, the mixing of a small amount of the HF exchange into the SR part has been observed to result in improved prediction of optoelectronic properties of compounds employed in organic light emitting diodes [139]. The LRC functional ωB97X consists of full (100%) HF exchange at the LR part and a small fraction of the SR HF exchange [30]:

$$E_{\text{XC}}^{\omega\text{B97X}} = E_{\text{X}}^{\text{LR-HF}} + c_x E_{\text{X}}^{\text{SR-HF}} + E_{\text{X}}^{\text{SR-B97}} + E_{\text{C}}^{\text{B97}} \tag{2.23}$$

with $c_x = 0.157706$. Both the ωB97X functional and its dispersion corrected version, ωB97X-D (see below), have been employed in this thesis.

In the LRC CAM-B3LYP functional [32], a generalized form of Equation 2.21, i.e. a Coulomb-attenuation method (CAM), is used for the splitting of the Coulomb

operator into the SR and LR parts. On the contrary to the most of the LRC functionals, which include the full HF exchange in the LR part, the amount of the exact HF in CAM-B3LYP is 65% in the LR. This smaller than 100% amount of the exact HF can have consequences on the calculated results. However, as the CAM-B3LYP functional has been a popular choice in the previous studies of excited state characteristics, electronic coupling, and CT rate calculations of copolymer–fullerene systems, it has been also used in this thesis for comparison.

Dispersion corrected functionals

Weak dispersion interactions, which are generated by the fluctuating changes in the charge distribution around the molecular system caused by the movement of electrons, are known to impact descriptions of eD–eA interfaces [3, 45]. Thus, they should be taken into account in the calculations of the eD–eA interfacial complexes. As both pure and global hybrid DFT functionals are not able to describe dispersion correctly, either new functionals including dispersion corrections have been developed or the empirical dispersion term have been added to the existing functionals. In the latter case, the general form of the total energy obtained with this kind of DFT-D scheme is [31]

$$E_{\text{DFT-D}} = E_{\text{KS-DFT}} + E_{\text{disp}} \tag{2.24}$$

where an empirical atomic-pairwise dispersion correction term (E_{disp}) is added to a Kohn-Sham (KS)-DFT part. For example, the form of the ωB97X-D functional is otherwise the same as that of ωB97X (Equation 2.23), but with the additional unscaled dispersion correction term added to the KS-DFT energy [31]. The dispersion corrected version of the global hybrid B3LYP, i.e. B3LYP-D, including the D3 version of Grimme's dispersion with the original D3 damping function has been also employed in this work.

3 COMPUTATIONAL MODELS AND METHODS

The theoretical models of the studied PSC compounds and details of the calculation methods employed in this thesis are presented in this chapter. In Section 3.1, the models of the isolated eD and eA compounds and their interfacial complexes are introduced. Section 3.2 summarizes the main details of computational methods and software. More detailed information and all the equations employed in the calculations can be found in the original publications.

3.1 Models

In this work, several different eD and eA compounds employed in efficient PSC were studied (Table 3.1). The eD compounds included different D–A copolymers (Figures 3.1 and 3.2), whereas the eA compounds comprised fullerene derivatives, a D–A copolymer, and A–D–A type SMAs (Figure 2.3). In most cases, the long alkyl side chains of the copolymers and SMAs were replaced by methyl groups (or hydrogens) to reduce the computational cost. However, it should be noted that the full-length side chains may have influence on torsions and conformational preferences in the backbones and solid-state packing of the studied compounds [13, 46].

3.1.1 Electron donor compounds

The eD compounds studied in this thesis are the D–A copolymers (Figures 3.1 and 3.2), which have donor and acceptor units and additional spacer units in their CRUs (i.e. repeating units, *n*). In the copolymers, which have donor and acceptor units in their CRUs, the left-most units in Figure 3.1 are the donor units and the right-most units are the acceptor units. These D–A copolymers include PBDCPDT-TPD [140], poly(benzo[1,2-*b*:4,5-*b*']dithiophene-*alt*-thieno-[3,4-*c*]pyrrole-4,6-dione) (PBDT-TPD)

Table 3.1 Studied eD and eA compounds in Publications I–IV.

eD		eA	
Compound	Publication	Compound	Publication
PBDCPDT-TPD	I	$PC_{61}BM$	II
PBDT-TPD	I	$PC_{71}BM$	II, III
PBDT-TFQ	II	P(NDI2OD-T2)	IV
PTQ	III	ITIC-4F	IV
PBDT-TzBI	IV	ITIC-2Cl	IV
PDTB-EF-T	IV		
PBDB-T-2F	IV		

[141], and poly[2,3-bis-(3-octyloxyphenyl)quinoxaline-5,8-diyl-*alt*-thiophene-2,5-diyl] (PTQ) [142]. In the other studied copolymers, i.e. poly[4,8-bis(2'-ethylhexyloxy)-benzo[1,2-*b*:4,5-*b*']-dithiophene-*alt*-[5,8-bis(5'-thiophen-2'-yl)-6,7-difluoro-2,3-bis(3"-hexyloxyphenyl)quinoxaline]] (PBDT-TFQ) [143], poly[4,8-bis(5-(2-ethylhexyl)-thio-phen-2-yl)benzo[1,2-*b*:4,5-*b*']dithiophene-*co*-4,8-di(thien-2-yl)-6-octyl-2-octyl-5H-pyr-rolo[3,4-*f*]benzotriazole-5,7(6*H*)-dione] (PBDT-TzBI) [144, 145], PDTB-EF-T [25], and poly[(2,6-(4,8-bis(5-(2-ethylhexyl)-4-fluorothiophen-2-yl)-benzo[1,2-*b*:4,5-*b*']dithio-phene))-*alt*-(5,5-(1',3'-bis(thiophen-2-yl)-5,7-bis(2-ethylhexyl)benzo[1',2'-*c*:4,5-*c*']dithio-phene-4,8-dione))] (PBDB-T-2F) [146, 147], there are additional thiophene spacers between them in the polymer backbones.

PBDT-TPD, PBDT-TFQ, PBDT-TzBI, PDTB-EF-T, and PBDB-T-2F have the same BDT donor unit. PBDCPDT-TPD has a heptacyclic ladder-type BDCPDT donor unit, which has been synthesized by covalently bridging two thiophenes with the central BDT unit, whereas PTQ has thiophene as the donor unit. Both PBDCPDT-TPD and PBDT-TPD have the TPD acceptor unit, whereas PTQ and PBDT-TFQ have a quinoxaline as the acceptor unit. The acceptors units in PBDT-TzBI and PBDB-T-2F are pyrrolo[3,4-*f*]benzotriazole-5,7-dione (TzBI) and 1,3-bis(thiophen-2-yl)-5,7-bis(2-ethylhexyl)benzo[1,2-*c*:4,5-*c*']dithiophene-4,8-dione (BDD), respectively, while in PDTB-EF-T, ester-substituted thiophenes will act as acceptors.

Within the CRU of a D–A copolymer, donor and acceptor units can be either in the *anti*-conformation, i.e. the neighboring heteroatoms (e.g. sulfur, nitrogen, or
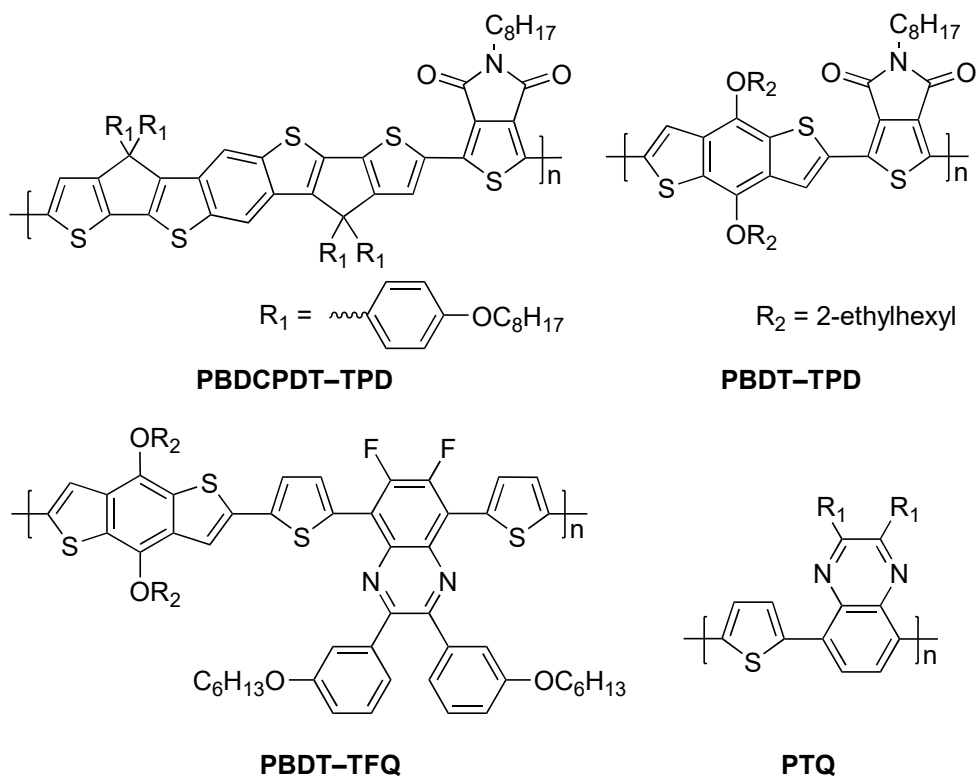
Figure 3.1 Structures of the D–A copolymers employed as the eD compounds in the fullerene-based PSCs.

oxygen) in them are on the opposite sides, or in the *syn*-conformation, i.e. the neighboring heteroatoms are on the same side of the conjugated backbone. The optimal dihedral angles between donor and acceptor units within a CRU were determined with relaxed PES scans of the monomers ($n = 1$, see Publications I, II, and IV). Furthermore, in the oligomers ($n \geq 2$), the neighboring CRUs can also have different orientations with the respect to each other. Thus, different conformational structures of the isolated oligomers of the D–A copolymers were constructed by using the optimized GS geometries of their monomers as the CRUs to determine the most stable conformers.

In Publications I and II, the periodic models of PBDCPDT-TPD, PBDT-TPD, and PBDT-TFQ were constructed in the same manner as those of the oligomers. How-
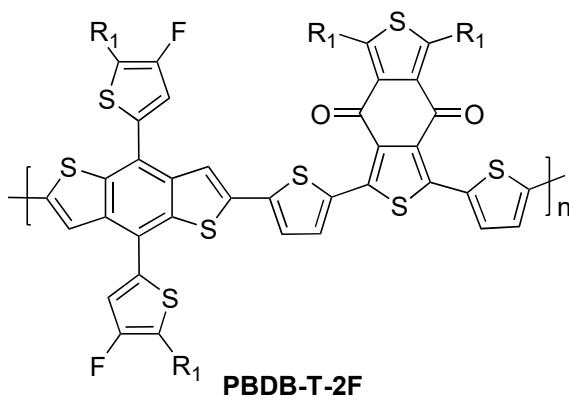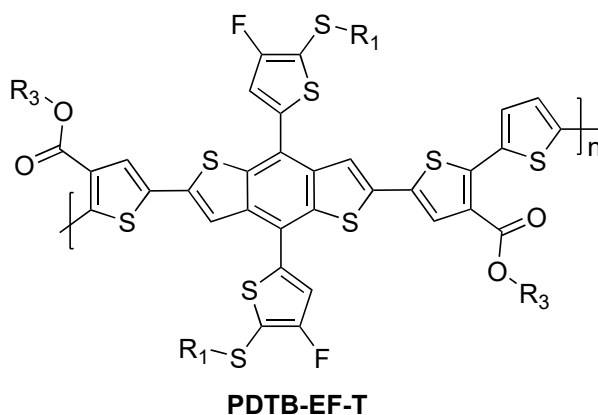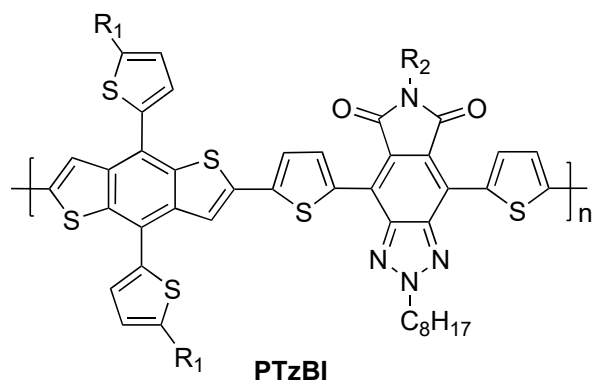
Figure 3.2 Structures of the D–A copolymers employed as the eD compounds in the NF PSCs.

ever, while building these models, it was noted that using one CRU, i.e. the monomer model, as the repeating unit was not enough for the correct repetition of the poly-

mer backbones leading to the convergence problems. Thus, two CRUs, i.e. dimer models were used instead to ensure repeatable structures. However, those conformations of PBDCPDT-TPD and PBDT-TPD, which had arch-shaped backbones, did not converge due to the incorrect repetition of the repeating unit. While using longer oligomers as the repeating unit could have solved this issue, these calculations would have been computationally too demanding. The oligomeric and periodic models of the studied D–A copolymers will be referred to as the acronyms presented in Table 3.1, but without the letter "P", which will be used only when referring to the real polymers. For example, the term BDCPDT-TPD will be used of the theoretical models of the copolymer PBDCPDT-TPD.

3.1.2 Electron acceptor compounds

Three different types of eA compounds were considered, namely the fullerene derivatives $PC_{61}BM$ and $PC_{71}BM$, D–A copolymer P(NDI2OD-T2), and D–A–D type SMAs ITIC, ITIC-4F, and ITIC-2Cl (Figure 2.3). In ITIC-4F, four hydrogen atoms of the INCN end groups of ITIC are replaced by fluorine atoms, whereas in ITIC-2Cl, two hydrogen atoms of the end groups are replaced by chlorine atoms [147]. Similarly to the models of the eD copolymers, the optimal dihedral angles between the backbone units of P(NDI2OD-T2) and ITIC derivatives were determined with relaxed PES scans (see Publication IV). The oligomeric models of P(NDI2OD-T2) will be referred to as NDI2OD-T2, hereafter.

In the recent study of Umeyama and Imahori [148], the different isomers of fullerene derivatives including [60]fullerene bisadducts, [70]fullerene bisadducts, and [70]fullerene monoadducts have been observed to have a notable effect on the miscibility of fullerene with eD polymers and thus consequently on the PCEs of the PSCs. For $PC_{71}BM$, the α isomer with (R)-, (S)-, and racemic enantiomer combinations and the β_2 isomer yielded better results than the β_1 isomer or the mixture of the α and β isomers. In this work, the (S)-enantiomer of the α isomer of $PC_{71}BM$ has been examined.

3.1.3 Local interfacial eD–eA complexes

In addition to the individual eD and eA compounds presented above, local interfacial complexes of some of them were constructed (Table 3.2). In all complexes, the isolated eD and eA compounds were first optimized separately at the levels of theory specified below, after which they were used to construct the complexes in the following manner.

In Publication II, the complexes of the polymer–fullerene system BDT-TFQ–PC$_{71}$BM were constructed from the B3LYP/6-31G** (vacuum) optimized GS geometries of the trimer of PBDT-TFQ and PC$_{71}$BM (Figure 3.3). To reduce the computational cost, a planarized trimer model of PBDT-TFQ, where the dihedral angles between the donor and acceptor units were constrained to 180°, while optimizing the geometry otherwise fully, was employed. Additionally, the hexyloxyphenyl side groups of the quinoxaline acceptor unit were replaced by hydrogens. Six different BDT-TFQ–PC$_{71}$BM complexes were constructed, where BDT-TFQ was oriented on the xy plane along the x axis, while PC$_{71}$BM was positioned either vertically or horizontally (with respect to the x axis) on the top of donor, thiophene, and acceptor units of BDT-TFQ. The intermolecular distance between the compounds, which was measured between the mass centers of the specific rings in BDT-TFQ and PC$_{71}$BM (Figures 3.3b and 3.3c), were varied from 3.0 Å to 5.0 Å (or 6.0 Å in some cases) by steps of 0.1 Å in the one-dimensional single point (SP) (rigid) potential energy scans. The following TDDFT calculations were carried out at both the optimized and constant (i.e. 3.5 Å) intermolecular distances to take the possible influence of a varying intermolecular distance on the excited state characteristics into account. The geometries of these complexes were not optimized.

In Publication III, the complexes of the polymer–fullerene type TQ–PC$_{71}$BM were built from the B3LYP/6-31G** (vacuum) optimized GS geometries of the oligomers of PTQ and PC$_{71}$BM (Figure 3.4). Two planar TQ oligomers were considered, where either thiophene (3T4Q) or quinoxaline (3Q4T) was the middlemost unit and the length of the oligomers was increased symmetrically by adding either thiophene or quinoxaline units to the chain ends. In the oligomers, the octyloxyphenyl side groups of the quinoxaline acceptor unit were replaced by hydrogens to ensure the pla-

Table 3.2 Studied eD–eA complexes.[1]

| Complex (eD–eA)	Geometry optimization[2]	Publication
BDT-TFQ–PC$_{71}$BM	no	II
TQ–PC$_{71}$BM	no	III
BDT-TzBI–NDI2OD-T2	yes	IV
DTB-EF-T–ITIC-4F	yes	IV
BDB-T-2F–ITIC-2Cl	yes	IV

[1] In the complexes, the length of the D–A oligomers was $n = 3$ for the planarized BDT-TFQ and $n = 1$ for BDT-TzBI, NDI2OD-T2, DTB-EF-T, and BDB-T-2F. The oligomers of TQ were seven units long, including either three thiophenes and four quinoxalines or three quinoxalines and four thiophenes.

[2] The GS geometry of the whole eD–eA complex.
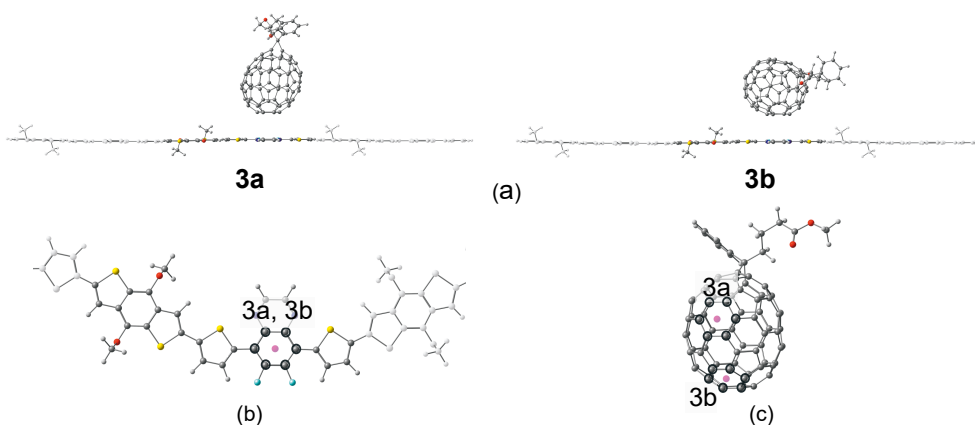
Figure 3.3 Studied BDT-TFQ–PC$_{71}$BM complexes, where PC$_{71}$BM was positioned (a) vertically (3a) or horizontally (3b) on the top of the acceptor unit of BDT-TFQ by superposing the centroids of the specific heterocycles in (b) BDT-TFQ (only the innermost CRU is presented wholly) and (c) PC$_{71}$BM. Adapted from [149] with permission from the PCCP Owner Societies.

nar backbones. It should be noted that the planarization of the helical TQ [150] and omission of its side groups might have consequences of the predicted results. However, the focus of this study was more on the multi-state treatment of the electronic couplings than on the correct description of the studied system. Furthermore, these approximations in the models led to the reduced computational cost in the coupling calculations. In the TQ–PC$_{71}$BM complexes, PC$_{71}$BM was positioned either on the middle thiophene unit (3T4Q) or the middle quinoxaline unit (3Q4T) of TQ with
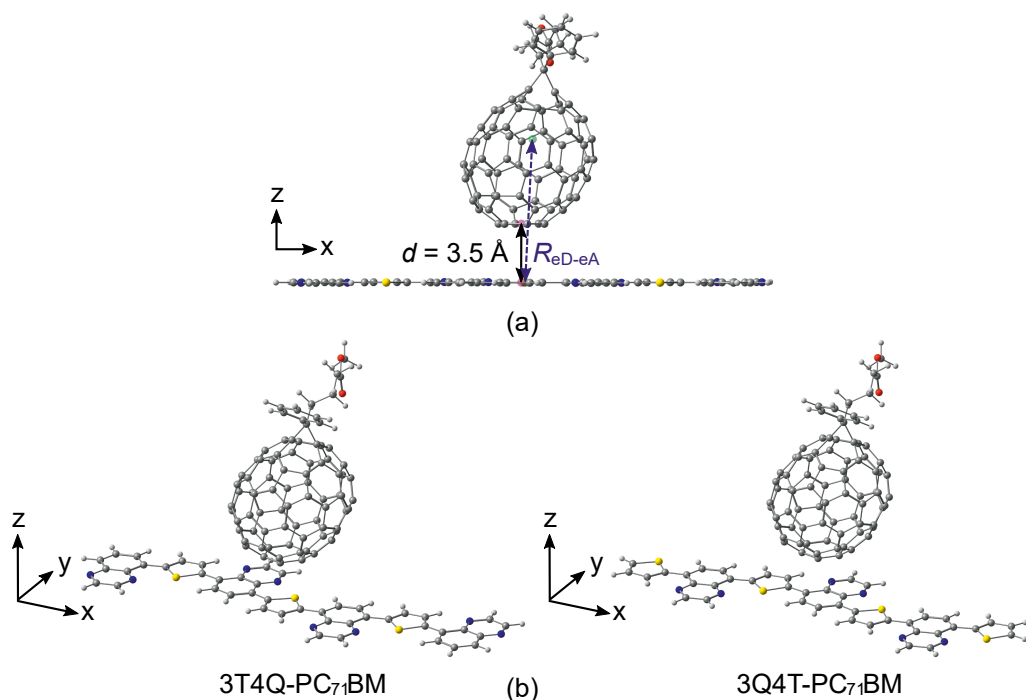
Figure 3.4 Illustrations of (a) intermolecular distance, d, and effective separation, R_{eD-eA}, between TQ and $PC_{71}BM$ in the studied TQ–$PC_{71}BM$ complexes, where $PC_{71}BM$ was (b) either above the middle thiophene (3T4Q–$PC_{71}BM$) or quinoxaline (3Q4T–$PC_{71}BM$) unit of TQ. The d and R_{eD-eA} were determined between the centers of mass of the specific rings (pink spheres) and those of the compounds (green spheres), respectively. Adapted from [151] with permission from the PCCP Owner Societies.

the fixed intermolecular distance, d, of 3.5 Å between the compounds (Figure 3.4a). The geometries of these complexes were not optimized.

In Publication IV, the complexes of the studied NF PSC systems, i.e. BDT-TzBI–NDI2OD-T2, DTB-EF-T–ITIC-4F, and BDB-T-2F–ITIC-2Cl, were built from the OT-ωB97X-D/6-31G** (blend) optimized GS geometries of the eD and eA compounds. In the case of the D–A copolymers, the monomer models were mostly employed, except for one complex configuration of BDT-TzBI–NDI2OD-T2, where the dimers were used instead. The eD compounds were oriented on the xy plane along the x axis. The eA compounds were positioned above the donor, thiophene, and acceptor units of the eD along the x axis with the initial intermolecular distance of 4 Å measured between the centers of mass of the superposed heterorings in the com-

pounds (see the original Publication IV for further information). The geometries of the complexes were then fully optimized without any constraints. The configurations, where the acceptor unit of the eA compound is located closest to the donor unit of the eD compound after the optimization, are referred to as the "DA" configurations. Similarly, those, where the acceptor unit of the eA compound is eventually closest to the acceptor unit of the eD compound, are referred to as the "AA" configurations. In BDT-TzBI–NDI2OD-T2, two different series were considered: (1), where the donor and acceptor units of both compounds were on the same direction and (2), where the donor and acceptor units of the compounds were on the opposite directions (see Publication IV for more detailed information).

3.2 Computational details

Here, the details related to the calculation methods and software are given. The calculations were carried out with the software installed on HP Proliant SL230s cluster (taito.csc.fi) at the CSC - IT Center for Science Ltd. In this thesis, only DFT-based methods were employed.

All the calculations in Publications I and II were carried out with the Gaussian 09 (Revisions C.01 and D.01) [152] suite of programs. In publication III, the calculations were carried out with the Q-Chem 4.2 software [153]. In publication IV, the Gaussian 16 (Revision B.01) [154] suite of programs was employed for all the calculations except for the electronic coupling calculations, which were carried out with the Q-Chem 4.2 software.

The eD–eA complexes were built using Materials Studio 8.0 [155] and 2017 R2 [156]. Pictorial presentations of the geometries, MOs, and natural transition orbitals (NTOs) were generated using ChemCraft 1.8 [157]. The data points for the graphical presentations of the UV-Vis absorption spectra were obtained also from ChemCraft 1.8 (see Section 3.2.2). The contributions of the backbone units to the NTOs were determined using the C-squared Population Analysis as implemented in the Orbital composition analysis module of Multiwfn 3.6 [158–160].

3.2.1 Ground state calculations

The GS geometries of the neutral D–A copolymer models, fullerene derivatives, and D–A–D type SMAs were fully optimized with DFT. With respect to the CT rate calculations carried out in Publications III and IV and the examination of the effect of ionization in Publication IV, the radical ions (i.e. cations and anions) of some of the models were optimized. The default calculation parameters were employed in the geometry optimizations, except for those carried with the Q-Chem 4.2 software in Publication III. There, the geometry optimizations of TQ and $PC_{71}BM$ were carried out with the EML(75,302) grid, SCF convergence criterion of 10^{-9}, and cutoff for neglect of two electron integrals of 10^{-14}.

The geometry optimizations of the eD and eA compounds and further calculations were carried out with the following functionals: the global hybrid functionals B3LYP (Publications I–III) and PBE0 (Publication III), the non-tuned (i.e. with the default ω) LRC functionals CAM-B3LYP (Publications I and III), ωB97X (Publication II), and ωB97X-D (Publication II), and the OT versions of LRC functionals ωB97X, and ωB97X-D, and BNL, denoted as OT-ωB97X (Publication II), OT-ωB97X-D (Publications II and IV), and OT-BNL (Publication III), respectively.

The 6-31G** basis set was used in all geometry optimizations, except for those related to the tuning of ωB97X and ωB97X-D in Publication II, where the 6-31G* basis set was used instead. In publications I and II, the structures of the monomers were confirmed as minima by the absence of the imaginary frequencies in the frequency calculations carried out at the B3LYP/6-31G** level of theory.

In Publications I and II, the periodic models of PBDCPDT-TPD, PBDT-TPD, and PBDT-TFQ were optimized using the default density of the **k** points. The length of the translation vector $\mathbf{T}_v$ determines the number of the **k** points: the longer $\mathbf{T}_v$, the fewer **k** points in the reciprocal space. The lengths of $\mathbf{T}_v$ were ca. 38, 24, and 58, which translated into 9, 14, and 6 **k** points in the periodic models of PBDCPDT-TPD, PBDT-TPD, and PBDT-TFQ, respectively.

3.2.2 Excited state calculations

The SP excited state calculations of the vertical excitation energies for the selected excited singlet (Publications I–IV) and triplet states (Publication I) and SP energy calculations related to the inner reorganization and Gibbs free energies were carried out with TDDFT. In Publication III, the Tamm–Dancoff approximation to TDDFT, i.e. TDA was also employed. The graphical illustrations of the UV-Vis absorption spectra were obtained via convolution of the calculated singlet vertical excitation energies and oscillator strengths using a Gaussian-shape broadening with a full width at half maximum of 0.30 eV. The nature of the electronic transitions was described using NTOs [161] as a representation of the transition density matrix.

Additionally, the geometry optimizations of the lowest excited singlet (S_1, in Publications I, III, and IV) and triplet (T_1, in Publication I) states of the selected compounds were carried out with TDDFT. The same levels of theory were employed in the excited state geometry optimizations as in the GS geometry optimizations.

3.2.3 Optimal tuning of long-range corrected functionals

In Publications II–IV, the range separation parameters of the LRC functionals ωB97X, ωB97X-D, and BNL were optimally tuned for the individual eD and eA compounds with the gap tuning procedure developed by Stein et al. [131, 138] by minimizing the following equation:

$$J_{\mathrm{gap}}(\omega)^2 = \sum_{i=0}^{1}\left[\epsilon_{\mathrm{HOMO}}^{\omega}(N+i) + \mathrm{IE}^{\omega}(N+i)\right]^2 \qquad (3.1)$$

where $\epsilon_{\mathrm{HOMO}}^{\omega}(N+i)$ and $\mathrm{IE}^{\omega}(N+i)$ are the HOMO energy and the (vertical) IE of the $N+i$ electron system, respectively, the N electron system corresponding to the neutral compound and the $N+1$ electron system to the anion.

For the eD–eA complexes, the modified version [162] of the gap tuning procedure was used:

$$J_{\text{gap}}(\omega) = \left| \epsilon_{\text{HOMO,eD}}^{\omega}(N) + \text{IE}_{\text{eD}}^{\omega}(N) \right| + \left| \epsilon_{\text{HOMO,eA}}^{\omega}(M+1) + \text{IE}_{\text{eA}}^{\omega}(M+1) \right| \quad (3.2)$$

where $\epsilon_{\text{HOMO}}^{\omega}(N)$ and $\text{IE}^{\omega}(N)$ are the HOMO energy and the (vertical) IE of the neutral eD, respectively, and $\epsilon_{\text{HOMO}}^{\omega}(M+1)$ and $\text{IE}^{\omega}(M+1)$ are the HOMO energy and the (vertical) IE of the anion of the eA, respectively.

In Publications II and IV, for each ω in the studied range, the vertical IE for the eD was calculated as the energy difference between the cation and the neutral both at the optimized geometry of the neutral system. Similarly, the vertical IE for the anion of the eA was calculated as the energy difference between the neutral and the anion both at the optimized geometry of the anion of the eA. However, in Publication III, the ω tuning was carried out as the SP calculations at the B3LYP/6-31G** -optimized geometries to keep the geometries consistent when employing different functionals in the electronic coupling and CT rate calculations.

Due to the issues known to arise when employing the polarizable continuum model (PCM) in the tuning of ω [163] (see Section 4.1 for further discussion), all the tuning calculations were carried out in vacuum. The OT ω values were determined with an accuracy of 0.01 bohr^{-1} and the 6-31G** basis set was used in all the tuning calculations, except for those carried out in Publication II, where the 6-31G* basis set was used.

3.2.4 Solution and blend environments

In addition to vacuum calculations, the effect of the surrounding medium was taken into account by means of the PCM. For the solution environment, either the integral equation formalism of the polarizable continuum model (IEFPCM) (Publications I and II) or the conductor-like polarizable continuum model (CPCM) (Publications III and IV) was employed. The default parameters, including static (ϵ_{s}) and optical (ϵ_{op},

i.e. dynamic) dielectric constants, of Gaussian were employed for the solvents, i.e. toluene (Publications I and II), 1,2-DCB (Publication II), and $CHCl_3$ (Publications I and IV). In Publication III, the ϵ_s and ϵ_{op} values of 10.1210 and 2.4072 (at 293.15 K), respectively, were employed for 1,2-DCB in the Q-Chem calculations instead.

For the solid state, i.e. the blend environment, the CPCM was employed with ϵ_s and ϵ_{op} of 3.6000 [20] and 3.2761, respectively, for TQ–PC_{71}BM (Publication III). The ϵ_s of the TQ–PC_{71}BM blend was calculated as the square of experimental refractive index (ca. 1.81 at 532 nm) [164]. In Publication IV, ϵ_s and ϵ_{op} of 4.00 [165, 166] and 2.55 [167], respectively, were used for the NF-PSC complexes. In this case, as experimental dielectric constants were not available for all the complexes, the given values employed also in the previous theoretical studies of organic solar cell systems were used instead.

3.2.5 Extrapolation techniques

In Publication I, the performance of different extrapolation techniques with respect to the periodic calculations was evaluated. The FMO, the HOMO–LUMO gap, and vertical transition energies at infinite length were determined by extrapolating from the oligomeric values, which were plotted against the reciprocal of the number of the double bonds ($1/N$). The extrapolation techniques, which were employed, included the linear fit, Kuhn fit, and our modified version of the Kuhn fit [44], i.e. scaled Kuhn fit. The number of double bonds for PBDCPDT-TPD ($N = 10$ per the CRU) and BDT-TPD ($N = 6$ per the CRU) were calculated along their conjugation paths.

In the Kuhn fit, a polymer chain is treated as a chain of linearly coupled N identical oscillators, i.e. C=C double bonds. Each of double bonds vibrates at an energy E_0 with a force constant of k_0. The N adjacent double bonds are coupled by the single bonds through a force constant k' resulting in N eigenmodes. The lowest excitation energy of the polymer is thus

$$E = E_0 \sqrt{1 + 2\frac{k'}{k_0}\cos\frac{\pi}{N+1}}. \tag{3.3}$$

Sometimes the Kuhn fit can result in inaccurate results due to its assumption for the constant k'/k_0 with increasing chain length. This applies for the homogeneous systems such as homopolymers, but does not take the chain end effects and intramolecular charge transfer (ICT) character present in the heterogeneous D–A copolymers into account [36, 168]. Furthermore, the energies for the larger D–A copolymers (i.e. with the larger N) locate closer to the infinite polymer region compared to the homopolymers, which have smaller CRUs. In Publication I, these issues were taking into account by adding a scaling factor, z, which multiplies the N, in the original Kuhn's equation (Equation 3.3):

$$E = E_0 \sqrt{1 + 2\frac{k'}{k_0} \cos \frac{\pi}{zN + 1}}.$$ (3.4)

The scaling factor z was iterated during the fitting procedure until the convergence was reached. Equation 3.4 will be referred to as the scaled Kuhn fit, hereafter.

3.2.6 Calculation of charge transfer rates

In Publications III and IV, the CT rates for the ED and CR processes were calculated with the Marcus theory (Equation 2.1) at a temperature of 293.15 K. The parameters used for calculating the rates were derived in the following manner. In organic systems, the intermolecular reorganization energy is typically divided into the inner (λ_i) and outer, i.e. external (λ_s) contributions. The inner contribution originates from the changes in the equilibrium geometries of the eD and eA compounds upon CT, whereas the external contribution is due to the changes in the electronic and nuclear polarizations and relaxation of the surrounding medium [91]. The inner reorganization energy can be determined either from a frequency analysis or by using the PESs of the molecular states involved in the CT processes considered [91]. The latter approach, where λ_i is calculated as the difference between the energy of the reactants (products) in the geometry of the products (reactants) and that of their equilibrium geometry (see Figure 2.5), has been a standard approach in the studies of the PSC systems and has been thus employed in this work, as well. The external reorganization

energy is usually determined by the classical dielectric continuum model of Marcus [169]. However, as the accurate description of λ_s is still rather challenging and is highly affected by the uncertainty of the calculated parameters used in this model, λ_s was kept as an adjusted parameter similarly to the previous studies [34, 170]. The CT rates were calculated with λ_s of 0.10–0.75 eV.

The Gibbs free energy ($\Delta G°$) is the energy difference between the complexes in their initial and final states (see Figure 2.5) [91]. Similarly to the previous studies of the PSC systems, the Weller's equation [171] was employed to calculate $\Delta G°$ from the energies of the individual eD and eA compounds, while taking the Coulombic attraction (ΔE_{Coul}) between their charged states into account [91, 167]. The full forms of the equations employed for calculating λ_i [91, 167, 172], $\Delta G°$ [91, 167], and ΔE_{Coul} [91, 167] can be found from the original Publications III and IV.

In Publication III, electronic couplings for the ED and CR processes of the eD–eA complexes were calculated with the two and multi-state GMH [48, 49] and FCD [50] schemes. In Publication IV, only the FCD schemes were employed. In GMH, the diabatic states localized at different sites (e.g. local and CT states) are assumed to have a zero transition dipole moment ($\mu_{\text{if}}^{\text{diab}}$) between them, whereas H_{if} between the diabatic states localized at the same sites is zero. In the limiting case of the 2-state GMH scheme, the coupling between the initial and final charge-localized, i.e. diabatic states is defined as

$$H_{\text{if}} = \frac{\mu_{12}\Delta E_{12}}{\Delta \mu_{\text{if}}^{\text{diab}}} = \frac{\mu_{12}\Delta E_{12}}{\sqrt{(\Delta \mu_{12})^2 + 4\mu_{12}{}^2}} \tag{3.5}$$

where diabatic H_{if} and the difference between the diabatic state dipole moments ($\Delta \mu_{\text{if}}^{\text{diab}}$) can be defined by the adiabatic terms, i.e. adiabatic transition dipole moment (μ_{12}), vertical excitation energy difference (ΔE_{12}), and the electric dipole moment difference ($\Delta \mu_{12} = \mu_1 - \mu_2$) between the adiabatic states $|1>$ and $|2>$.

The dipole moment vectors are typically projected either on the direction defined by $\Delta \mu_{12}$ (or the average of the electric dipole moment differences in the multi-state case) or the CT vector. Here, the latter manner was employed, i.e. the μ_{ii} and μ_{ij}

were projected along the CT vector, which is defined as the vector connecting the mass centers of the eD and eA, i.e. $\mathbf{e}R_{\text{eD}-\text{eA}}$:

$$\text{proj}_{R_{\text{eD}-\text{eA}}} \mu_{\text{ij}} = \frac{(\mu_{\text{ij}} \cdot R_{\text{eD}-\text{eA}})}{|R_{\text{eD}-\text{eA}}|^2} R_{\text{eD}-\text{eA}}. \tag{3.6}$$

Similarly to GMH, in FCD, the transition densities (Δq_{if}) between the diabatic states localized at different sites are zero.

The 2-state FCD has the similar form as the 2-state GMH:

$$H_{\text{if}} = \frac{|\Delta q_{12}| \Delta E_{12}}{\sqrt{(\Delta q_1 - \Delta q_2)^2 + 4\Delta q_{12}^2}}. \tag{3.7}$$

In FCD, the studied system is partitioned into two fragments corresponding to the eD and eA. An adiabatic eD–eA charge difference matrix, $\mathbf{\Delta q}^{\text{ad}}$, is defined by its elements

$$\Delta q_{\text{ij}}^{\text{ad}} = \int_{r \in \text{eD}} \rho_{\text{ij}}(r) \, dr - \int_{r \in \text{eA}} \rho_{\text{ij}}(r) \, dr \tag{3.8}$$

where $\rho_{\text{ij}}(r)$ is the one-particle density (if i = j) for the diagonal elements $\Delta q_{\text{ii}}^{\text{ad}}$ and $\Delta q_{\text{jj}}^{\text{ad}}$ defined as the eD–eA charge differences in the adiabatic states $|i\rangle$ and $|j\rangle$, respectively, or the transition density for the off-diagonal elements $\Delta q_{\text{ij}}^{\text{ad}}$ (if i≠j).

For calculating the multi-state electronic couplings, the approach proposed by Yang and Hsu [51], which is based on the similar 3-state approaches [52, 53], was followed. This method was selected, because it allows for calculating the multi-state GMH and FCD couplings without the need of manual selection and assignment for the states and has resulted in the couplings consistent with the experimental ones for the complexes of small and medium sized organic compounds and donor–bridge–acceptor systems [51]. Here, the equations will be presented only for the multi-state FCD scheme, but those of the multi-state GMH scheme are similar and have been presented in Publication III. First, $\mathbf{\Delta q}^{\text{ad}}$, (or similarly the adiabatic dipole moment

matrix μ^{ad} in GMH) was diagonalized with a unitary transformation matrix $\mathbf{U}_1$, which is composed of the eigenvectors of $\Delta\mathbf{q}^{ad}$ (or similarly to μ^{ad}):

$$\mathbf{U}_1^T\Delta\mathbf{q}^{ad}\mathbf{U}_1 = \mathbf{U}_1^T \begin{pmatrix} \Delta q_{11} & \Delta q_{12} & \Delta q_{13} & \cdots \\ \Delta q_{21} & \Delta q_{22} & \Delta q_{23} & \cdots \\ \Delta q_{31} & \Delta q_{32} & \Delta q_{33} & \cdots \\ \vdots & \vdots & \vdots & \ddots \end{pmatrix} \mathbf{U}_1$$

$$= \begin{pmatrix} \Delta q_l & 0 & 0 & \cdots \\ 0 & \Delta q_m & 0 & \cdots \\ 0 & 0 & \Delta q_n & \cdots \\ \vdots & \vdots & \vdots & \ddots \end{pmatrix} \tag{3.9}$$

The same transformation was applied to the corresponding adiabatic Hamiltonian, i.e. the diagonal adiabatic energy matrix $\mathbf{E}$, to obtain the Hamiltonian ($\mathbf{H}$):

$$\mathbf{U}_1^T\mathbf{E}\mathbf{U}_1 = \mathbf{U}_1^T \begin{pmatrix} E_1 & 0 & 0 & \cdots \\ 0 & E_2 & 0 & \cdots \\ 0 & 0 & E_3 & \cdots \\ \vdots & \vdots & \vdots & \ddots \end{pmatrix} \mathbf{U}_1 = \begin{pmatrix} H_{ll} & H_{lm} & H_{lm} & \cdots \\ H_{ml} & H_{mm} & H_{mn} & \cdots \\ H_{nl} & H_{nm} & H_{nn} & \cdots \\ \vdots & \vdots & \vdots & \ddots \end{pmatrix} \tag{3.10}$$

In the limiting case of the 2-state schemes, the diabatic charge difference matrix, $\Delta\mathbf{q}^{diab}$, (or similarly the diabatic dipole moment matrix, μ^{diab}) and diabatic Hamiltonian ($\mathbf{H}^{diab}$) can be obtained already from Equations 3.9 and 3.10, respectively. However, in the multi-state schemes, there may exist several states localized on the same site, i.e. with the same nature, and thus $\mathbf{H}$ should be localized within the same-site states. The states obtained in this manner are adiabatic within one block, but diabatic with respect to the states localized at different sites.

Thus, in the next step, the states are classified as the local or CT states according to their eigenvalues in the diagonalized $\Delta\mathbf{q}$ (or μ) matrix (obtained from Equation 3.9).

According to Yang and Hsu [51], in the FCD scheme, the Δq values for the ideal CT states should be 2 or -2, while those of the local states should be zero. Similarly, in GMH, the local states should have small μ values, whereas those of the CT states should approach the ideal dipole moment defined as $\Delta \mu_{if}^{id} = eR_{eD-eA}$, where R_{eD-eA} is the distance between the mass centers of eD and eA. Similarly to the work of Yang and Hsu, the averages of the Δq values of the ideal local (zero) and CT states (± 2), i.e. ± 1, were used as the thresholds for Δq to assign the local and CT subspaces in Publications III and IV. However, in the case of the multi-state GHM schemes, instead of using the half of the ideal dipole moment for assigning the states like suggested by Yang and Hsu, the threshold of 10.0 D was used in Publication III, because otherwise there would not have been any CT states in some cases.

After assigning the states, $\mathbf{H}$ (obtained from Equation 3.10) is re-diagonalized within each block (i.e. local and CT) to define the $\mathbf{H}^{diab}$:

$$\mathbf{U}_2^T \begin{pmatrix} \mathbf{H}_{LS} & \mathbf{H}_{LS,CT} \\ \mathbf{H}_{CT,LS} & \mathbf{H}_{CT} \end{pmatrix} \mathbf{U}_2 = \begin{pmatrix} \mathbf{E}_{CT1} & \widetilde{\mathbf{H}}_{CT1,LS} & \widetilde{\mathbf{H}}_{CT1,CT2} \\ \widetilde{\mathbf{H}}_{LS,CT1} & \mathbf{E}_{LS} & \widetilde{\mathbf{H}}_{LS,CT2} \\ \widetilde{\mathbf{H}}_{CT2,CT1} & \widetilde{\mathbf{H}}_{CT2,LS} & \mathbf{E}_{CT2} \end{pmatrix} \tag{3.11}$$

where each bold letter refers to a matrix in the local and CT subspaces defined by the subscript, $\mathbf{E}$ is a diagonal matrix, and the final coupling values (H_{if}) are obtained as the corresponding off-diagonal matrix elements in $\widetilde{\mathbf{H}}_{LS,CT}$. Furthermore, $\Delta \mathbf{q}^{diab}$ can be obtained by applying the same transformation $\mathbf{U}_2$ to the diagonalized $\Delta \mathbf{q}$ (or μ) matrix obtained from Equation 3.9:

$$\mathbf{U}_2^T \begin{pmatrix} \Delta q_l & 0 & 0 & \dots \\ 0 & \Delta q_m & 0 & \dots \\ 0 & 0 & \Delta q_n & \dots \\ \vdots & \vdots & \vdots & \ddots \end{pmatrix} \mathbf{U}_2 = \begin{pmatrix} \Delta \mathbf{q}_{CT1}^{diab} & 0 & \Delta \mathbf{q}_{CT1,CT2}^{diab} \\ 0 & \Delta \mathbf{q}_{LS}^{diab} & 0 \\ \Delta \mathbf{q}_{CT2,CT1}^{diab} & 0 & \Delta \mathbf{q}_{CT2}^{diab} \end{pmatrix} \tag{3.12}$$

The adiabatic electronic and transition dipole moments and charge differences for the GS and selected number of the singlet excited states were calculated by using the GMH and FCD schemes as implemented in Q-Chem 4.2. The Q-Chem software yields the 2-state couplings between each state, but only the 2-state FCD couplings were used as such. In Publication IV, the coupling calculations were carried out with the grid of 99 Euler–Maclaurin radial grid points and 302 Lebedev angular grid points, SCF convergence criterion of 10^{-6}, and the cutoff for neglect of two electron integrals of 10^{-12} to keep the calculations carried out with Gaussian 16 and Q-Chem consistent. Moreover, the radii from the Universal Force Field with a scaling factor of 1.1 were employed in conjunction with CPCM. Due to the SCF convergence problems of larger SMA-based complexes, the iterative conjugate gradient solver was employed together with the Precond, NoMatrix, and UseMultipole keywords.

4 RESULTS AND DISCUSSION

This chapter will summarize the key findings of this work, which have been presented in more detail in Publications I–IV. First, the OT ω values determined for all the studied compounds and their interfacial complexes are presented. After this, structural and optoelectronic properties of the individual PSC compounds will be examined to understand better their functionality and performance in the PSCs. Then, a step towards understanding of the interactions between the eD and eA compounds at their local interfaces will be taken by examining the structures and CT characteristics of the selected eD–eA complexes. Finally, the results of the multistate electronic coupling calculations together with the other CT rate parameters and rates for the ED and CR processes taking place in the eD–eA complexes are presented. In all cases, the effect of the functional and dispersion corrections on the features is closely examined. Furthermore, the effect of other calculation parameters and models used will be also considered.

4.1 Optimally tuned range-separation parameters

All the OT ω values determined for the individual eD and eA compounds and their complexes in Publications II–IV are represented in Table 4.1. In general, the OT ω values are smaller than the default ones in the ωB97X (0.3 bohr^{-1}), ωB97X-D (0.2 bohr^{-1}), and BNL (0.5 bohr^{-1}) functionals. This is consistent with the previous findings that the original ω values of the LRC functionals are too large for the systems with the extended π-conjugation [130], such as the polyenes and oligoacenes [130] and the D–A copolymers [9, 12, 14], leading to a large localization error [26]. Thus, the tuning of ω is required for better description of photoactive systems, when employing the LRC functionals.

Table 4.1 Optimally tuned (OT) range-separation parameters (ω, in bohr^{-1}) of the LRC-functionals determined in vacuum.[1]

Model	OT-ωB97X	OT-ωB97X-D	OT-BNL	Publication
eD				
BDT-TFQ	0.10 (0.11)[2]	0.09 (0.10)[2]	-	II
TQ	-	-	0.15	III
BDT-TzBI	-	0.09 (0.12)[2]	-	IV
DTB-EF-T	-	0.09 (0.11)[2]	-	IV
BDB-T-2F	-	0.10 (0.11)[2]	-	IV
eA				
PC$_{61}$BM	0.16	0.15	-	II
PC$_{71}$BM	0.14	0.13	0.18	II&III
NDI2OD-2T	-	0.12 (0.16)[2]	-	IV
ITIC	-	0.09	-	IV
ITIC-4F	-	0.09	-	IV
ITIC-2Cl	-	0.09	-	IV
eD–eA				
BDT-TFQ–PC$_{71}$BM	0.13	0.12	-	II
TQ–PC$_{71}$BM	-	-	0.17	III
BDT-TzBI–NDI2OD-T2	-	0.14	-	IV
DTP-EF-T–ITIC-4F	-	0.10	-	IV
BDB-T-2F–ITIC-2Cl	-	0.10	-	IV

[1] The OT ω values of the individual compounds and complexes were obtained with the Equation 3.1 and Equation 3.2, respectively. In Publications II and III, the 6-31G* basis set was employed in the tuning of ω, whereas in Publication IV, the 6-31G** basis set was employed.

[2] The OT ω values of the oligomeric models employed in the eD–eA complexes, i.e. the planarized trimer for BDT-TFQ and the monomer for other compounds.

In OT-ωB97X and OT-ωB97X-D, the OT ω values for the oligomers of the eD D–A copolymers are generally the same, which indicates the similar extent of π-conjugation in their backbone with the characteristic length scales (1/ω) [173] of ca. 9–11 bohr (i.e. 5–6 Å). The SMAs ITIC and its derivatives have the same OT ω values as the D–A oligomers, whereas fullerene derivatives and the tetramer of the eA-type D–A copolymer P(NDI2OD-2T) have somewhat larger values due to a

smaller degree of π-conjugation in them [130]. Overall, the OT ω values of the eD and eA compounds are in line with those (0.10–0.20 bohr^{-1}) determined for other D–A copolymers [9, 12, 14] and fullerene derivatives, i.e. $PC_{61}BM$ and $PC_{71}BM$ [174, 175]. The OT ω values determined for the eD–eA complexes are between those of the individual molecules, although somewhat closer to those of the eA compounds.

When comparing different LRC functionals, it can be seen that the OT ω values for OT-ωB97X and OT-ωB97X-D are almost the same, those of OT-ωB97X being only 0.01 bohr^{-1} larger. As the only difference between these functionals is the empirical dispersion corrections included in ωB97X-D, it can be concluded that the dispersion corrections do not have a significant effect on the OT ω values and consequently the characteristic length scales. The OT ω values for OT-BNL are generally slightly larger than those for OT-ωB97X and OT-ωB97X-D. This is most probably due to a partial SR HF exchange in ωB97X and ωB97X-D that is not included in BNL, leading to the larger characteristic length of the SR/LR transition for OT-ωB97X and OT-ωB97X-D [130]. Moreover, in the case of OT-BNL, the tuning of the ω has been carried out with the SP calculations using the B3LYP-optimized geometries, which may have some influence, as well (see Section 3.2.3 for the further information). However, the differences in the semilocal approximations to exchange and correlation between different LRC functionals should not affect the overall picture too much and similar results have been predicted when describing the conjugation of the system [130] and the optical properties of the D–A oligomers [9] regardless of the OT-LRC functional. Although the use of dispersion corrections can have a notable influence, as will be seen for the eD–eA complexes later on.

While OT-LRC functionals have yielded improved IEs and vertical excitation energies for the D–A copolymers compared to the global hybrid and non-tuned LRC functionals, as is observed in both this work and other theoretical studies [9, 12, 14], it should be noted that in some cases the OT tuning can lead to inconsistent results. For example, the BLA values predicted for highly conjugated polymers, such as polyenes [33] and a planar cyclopentadithiophene-*co*-benzothiadiazole based D–A copolymer [9], do not saturate with the increasing chain length, as should be expected with the increasing conjugation. In their study, Körzdörfer et al. explained this by the lack of the size consistency in the OT-LRC functionals, which is a direct

consequence of tuning ω with system size [33]. In other words, the OT-LRC functional approaches the semilocal functional with the increasing chain length, while losing size consistency of standard LRC functionals.

Another shortcoming of the OT-LRC functionals is the failure in combining the tuning of ω with a continuum solvation model [163]. Namely, carrying out the tuning in the presence of CPCM have resulted in unreasonable small values of ω and consequently too low excitation energies for oligothiophenes [176]. This is because the PCM affects the total energies, but not the DFT eigenvalues, i.e. the HOMO energies. One option to overcome this problem would be using an explicit solvent in the tuning calculations. While this method has potential, it has several challenges, such as large computational cost, difficulty in finding the right structure for solvent, and delocalization of the HOMO over the solvent [163, 177]. The latter problem can be overcome by using a locally projected self-consistent field [177], large computational cost caused by the explicit solvent still remains. Thus, in the absence of more accurate methods at the moment, the tuning for large systems is recommended to be carried out in vacuum and use the resulting ω values in the PCM calculations [163], as has been also done in this work.

## 4.2 Structural properties of polymer solar cell compounds

In this thesis, the structural characteristics of several PSC compounds have been examined with the DFT methods. Especially for the D–A copolymers, the structure of the polymer backbone can have a significant impact on their ordering and packing tendencies in the solvent [13] and solid state [17]. Thus, the GS geometries of the studied D–A copolymer models have been compared to better understand those structure-function relations, which may determine their efficiencies. Furthermore, for some of the compounds, the geometries of the corresponding radical ions, i.e. cations and anions, and the excited states have been also optimized to investigate their structural changes taken place upon ionization or excitation. The results of these studies have been published in Publications I, II, and IV.

4.2.1   Ground-state structural properties

The shapes and curvatures of the backbones of the D–A copolymers and SMAs are controlled by the sizes and shapes of the donor and acceptor units, conformational preferences, and resulting torsions between the neighboring units [111, 178]. Among the studied compounds, the GS geometries of the D–A oligomers have indeed different shapes and degrees of the curvature (Figures 4.1 and 4.2). Most of them have the sine wave-shaped backbones, except for eD-type DTB-EF-T, whose backbone have a zigzag-shape, and for eD-type BDT-TFQ and eA-type NDI2OD-T2 (Figure 4.3), which have helical structures. The backbone of the eD copolymer PTQ including the phenyl side groups in the quinoxaline unit has been observed to have a helical shape, as well [150]. However, in this work, the phenyl groups in the studied TQ oligomers have been replaced by hydrogen atoms to ensure the planar backbones (see Section 3.1.3).

In addition to the shapes of the backbone units, the weak non-bonding intramolecular interactions between particular atoms (e.g. oxygen, sulfur, nitrogen, hydrogen) of the neighboring backbone units impact the planarity and define the conformational preferences of the D–A copolymers [111]. In Publication I, the global hybrid functional B3LYP predicts that BDCPDT-TPD and BDT-TPD, which consist of only alternating donor and acceptor units, have planar (0–3°) or nearly planar (1–11°) backbones, respectively (Figure 4.1). The results obtained with the non-tuned LRC functional CAM-B3LYP for these oligomers are the same. Both compounds prefer the *syn*-conformation due to non-traditional hydrogen bonding [111] predicted between the carbonyl oxygen of the TPD acceptor unit and hydrogen of the neighboring donor unit, which enhances the planarity of the backbones. Furthermore, the ladder-type donor unit in BDCPDT-TPD increases the planarity compared with BDT-TPD, which includes smaller BDT donor unit. In the case of these eD oligomers, the conformation of backbone is not observed to have much effect on their planarity or optoelectronic properties. The GS geometry of BDT-TPD predicted here is inline with the previous theoretical studies of the same compound [8, 9].
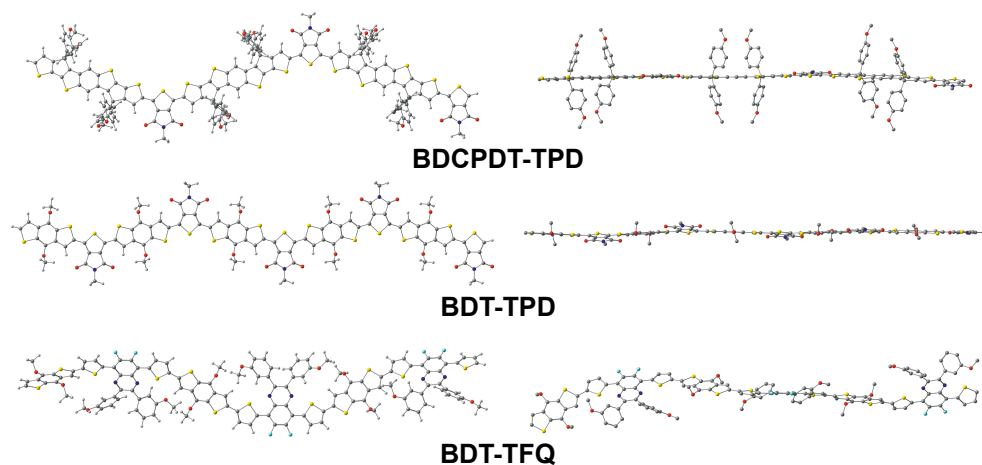
Figure 4.1 Optimized GS geometries of the most stable conformations of the oligomeric models of the eD-type PSC copolymers calculated at the B3LYP/6-31G** level of theory in vacuum. The hydrogens are not shown in the side-view figures (on the right) for the clarity.

As mentioned in Section 2.1.1, the planar backbones of the D–A copolymers have been originally aimed for to ensure the high efficiencies of the corresponding PSCs. In the case of BDT-TPD, high PCEs (ca. 8.5%) have been predicted for the PSCs based on the corresponding copolymer and $PC_{71}BM$. However, this is not the case with the ladder-type BDCPDT-TPD, as the PCEs predicted for the device incorporating the corresponding copolymer and $PC_{71}BM$ have been only ca. 6.6%. Thus, the backbone of BDCPDT-TPD might be too rigid leading to the poorer performance compared to BDT-TPD. However, it should be noted that the efficiency of a PSC and optimal morphology of the active layer are not governed entirely by the backbones of the D–A copolymers, but the choice of the side chains, processing conditions, and eA compound may play role, as well.

The backbones of the eD-type oligomers consisting of additional thiophene spacers between the donor and acceptor units, i.e. BDT-TFQ, BDT-TzBI, DTB-EF-T, and BDB-T-2F, have larger torsional twists (3–41° in vacuum, see the original Publications II and IV for the definitions of the dihedral angles) between the units as predicted by B3LYP and the non-tuned LRC and OT-LRC functionals (Figures 4.1 and 4.2). This is due to the larger degrees of freedom between the units induced by the thiophene spacers. In these compounds, the BDT donor and thiophene units are *anti* to each other due to steric repulsion between the neighboring sulfur atoms,
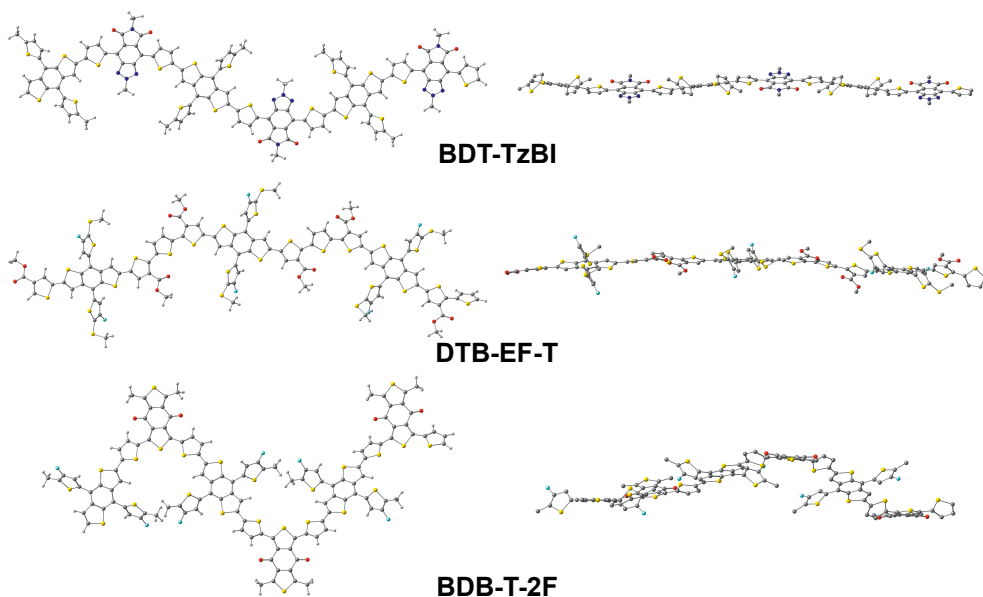
Figure 4.2 Optimized GS geometries of the most stable conformations of the oligomeric models of the eD-type NF PSC copolymers calculated at the OT-ωB97X-D/6-31G** level of theory in blend. The hydrogens are not shown in the side-view figures (on the right) for the clarity.

while the thiophene and acceptor units can be either *syn* (BDT-TFQ , BDT-TzBI, and BDB-T-2F) or *anti* (DTB-EF-T) to each other depending on the possible attractive and repulsive interactions between the neighboring heteroatoms (i.e. sulfur, nitrogen, oxygen, and fluorine). In line with similar TQ [150], a helical backbone is predicted for BDT-TFQ, which is most probably due to the relative orientations of the backbone units and metoxyphenyl side groups in the quinoxaline acceptor units. The GS geometry of BDB-T-2F is also consistent with the previous theoretical characterizations [16, 19]. As the PSCs employing the corresponding D–A copolymers have had high PCEs of ca. 8.0% for PBDT-TFQ–PC$_{71}$BM [179] and 9.2–14.2% for the NF PSCs [25, 145, 147], it can be concluded that this type of twisted backbone with thiophene spacers may be more beneficial for the performance of the PSC than the planar, rigid backbone predicted for BDCPDT-TPD.

Among the studied eA compounds, the SMA compounds ITIC and its derivatives, ITIC-2Cl and ITIC-4F, are planar (0°, see the original Publications I, II, and IV for the definitions of the dihedral angles), as can be expected from their rigid central cores (only the optimized geometry of ITIC is presented in Figure 4.3). The OT-ωB97X-

NDI2OD-T2

ITIC
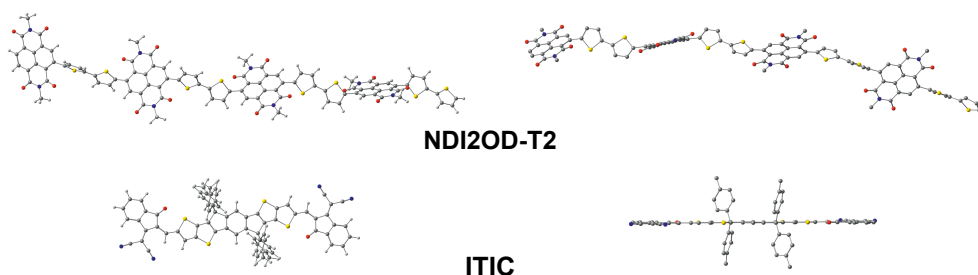
Figure 4.3 Optimized GS geometries of the most stable conformations of the eA-type NF PSC compounds calculated at the OT-ωB97X-D/6-31G** level of theory in blend. The hydrogens are not shown in the side-view figures (on the right) for the clarity.

Table 4.2 Dihedral angles (in degrees)[1] and BLA values (in Å)[2] of the GS geometries of the oligomeric and periodic (in parenthesis) models of PBDT-TFQ predicted with different functionals.

Functional	α	β_1	β_2	BLA
B3LYP	163 (158)	-10 (-15)	-7 (-10)	0.036 (0.039)
B3LYP-D	160 (-)	-12 (-)	-10 (-)	0.037 (-)
ωB97X	157 (155)	-16 (-18)	-20 (-19)	0.059 (0.060)
ωB97X-D	156 (-)	-15 (-)	-17 (-)	0.052 (-)
OT-ωB97X	161 (160)	-21 (-21)	-21 (-19)	0.043 (0.044)
OT-ωB97X-D	159 (-)	-18 (-)	-13 (-)	0.042 (-)

[1] Between the donor and first thiophene (α), first thiophene and acceptor (β_1), and acceptor and second thiophene (β_2) in the CRU of BDT-TFQ. See Publication II for the definitions of the dihedral angles.

[2] The oligomeric BLA values were calculated from the innermost CRU of the trimer.

D functional predicts that the *syn*-conformation is the most stable for ITIC, i.e. the sulfurs of the IT donor core unit and neighboring carbonyl oxygen of the INCN end-groups prefer to be on the same side. The similar findings have been observed in the previous theoretical calculations with the B3LYP/6-31G** level of theory [180] and experiments [181], although in the latter case, somewhat larger torsions (4–5°) have been predicted for the crystal structures of ITIC by X-ray diffraction analysis. The differences between the calculated and experimental results may be due to the truncated side chains used here, as the full side chains and the presence of neighboring molecules in the solid state most probably induce additional torsion between the backbone units.

On the contrary, the backbone of eA-type oligomer NDI2OD-2T calculated with ωB97X-D has relatively large twists (ca. 29–60°, see the original Publications I, II, and IV for the definitions of the dihedral angles) from planarity (Figure 4.3). This is consistent with the previous findings, although the dihedral angles between the donor thiophene and acceptor NDI units (ca. 60°) predicted here are somewhat larger than those obtained both theoretically at the B3LYP/6-31G** level of theory (42° and 138°) and experimentally (37° and 142°) via IR and reflection–absorption IR spectroscopy measurements [182]. The differences in the calculated results may be due to the different functionals, while similar to the ITIC derivatives, the differences between the calculations and experiments may originate from the absence of the full side chains in the NDI acceptor and neighboring molecules. Like for ITIC, the *syn*-conformation is observed also for NDI2OD-2T, i.e. sulfur atoms of the thiophene donors and the carbonyl oxygens of the neighboring acceptor units are on the same side. This is opposite to some of previous theoretical studies using the global hybrid functionals [182]. However, the *syn*-conformation has been predicted also by the (non-tuned) LRC CAM-B3LYP [183].

So far, the GS structural properties of the studied PSC compounds have been presented in the general level without discussing the effect of the functional. The dihedral angles of the GS geometries of BDT-TFQ predicted by the different functionals are in the same range, although the functional has some effect on them (Table 4.2). The global hybrid functional B3LYP predicts the deviations of 7–17° from planarity. The inclusion of the dispersion corrections in B3LYP-D, increases the torsions slightly up to 10–20°. Both the non-tuned LRC and OT-LRC functionals predict the similar deviations from planarity of 15–24° and 13–21°, respectively, which are also slightly larger than those of B3LYP. The BLA (middle) values increases in the order of the global hybrid < OT-LRC < non-tuned LRC functionals indicating that the non-tuned LRC functionals predict the less delocalized backbone for BDT-TFQ than other functionals due to the larger amount of HF exchange in them [14]. Similar trends in the effect of the functional on the dihedral angles and BLA values have been predicted by Niskanen and Hukka [14].

4.2.2 Structural changes induced by ionization and excitation

To better understand the ionization and excitation characteristics of the studied PSC compounds, different structural parameters including BLAs and bond length differences of their neutral, ionized, and excited states have been compared in Publications I and IV. For the NF PSC oligomers, smaller BLA values (calculated for the innermost CRUs) are observed for the radicals due to the shortened single bonds and lengthened double bonds compared to the neutral compounds. The trimers of the studied eD copolymers have relatively similar BLA values, although smaller BLA is predicted for the cation of DTB-EF-T indicating slightly larger delocalization for it upon oxidation compared to other trimers. The BLA values of the anions of DTB-EF-T and BDT-TzBI are smaller than those of BDB-T-2F indicating that their delocalization increases more upon reduction compared to BDB-T-2F. For the neutral eA compound NDI2OD-T2, similar BLA values are observed as for the neutral eD trimers. Depending on the number of the units used for calculating BLA, the cation of NDI2OD-T2 has either smaller or slightly larger BLA values than the eD trimers. However, the BLA values of the anion of NDI2OD-T2 are mostly larger than those of the eD trimers. The BLA values for the optimized S_1 geometries of the eD-type trimers are close or equal to zero indicating delocalized structures, except that for DTB-EF-T predicted in vacuum, which is slightly larger. Overall, the surrounding medium does not have large effect on the BLA values.

The corresponding bond length differences between the radical ions and neutral compounds give more insight into the regions that are the most affected by ionization and excitation. Generally, the relaxation of the oligomer geometry taking place upon both ionization and excitation processes shortens the single bonds and lengthens the double bonds resulting in the inverse single–double C–C bond patterns with respect to the GS geometry (Figure 4.4). The largest changes in the bond lengths are observed inside or in the close region of the middle CRUs of the oligomers. For the eD trimers BDT-TzBI and BDB-T-2F, the OT-ωB97X-D functional predicts that the structural reformations induced by oxidation take place in the middlemost BDT donor unit and neighboring thiophenes. The largest changes caused by reduction are observed in the middlemost acceptor unit for BDT-TzBI, while for BDB-T-2F, reduction affects mostly thiophene (in vacuum) and donor units (in CHCl$_3$ and blend
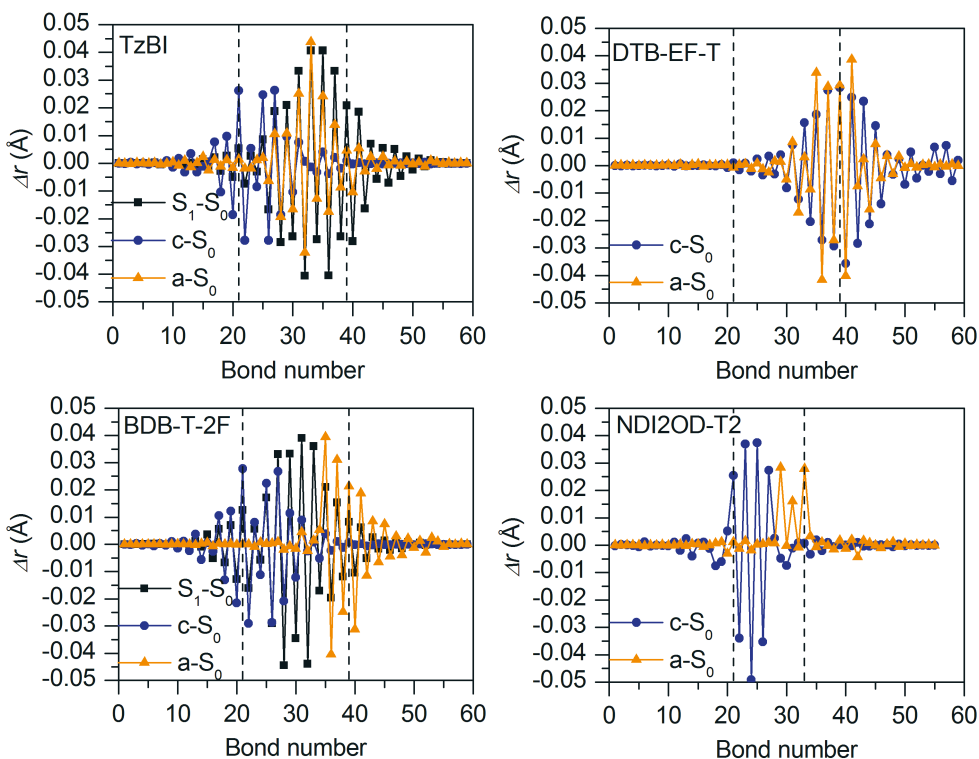
Figure 4.4 Bond length differences (Δr) between the OT-ωB97X-D/6-31G**-optimized (in CHCl$_3$) radical (c = cation and a = anion)/S$_1$ and the neutral GS, i.e. S$_0$ geometries of the eD and eA compounds with respect to the bond lengths along the conjugation paths. The regions corresponding to the middle CRUs (or middlemost donor and acceptor units in the case of NDI2OD-T2) have been marked with the dashed lines in the graphs. Adapted from Publication IV [184] - Published by The Royal Society of Chemistry.

environments) instead of the acceptor units. In DTB-EF-T, both oxidation and reduction induce the largest changes mostly in the substituted (i.e. acceptors) and unsubstituted thiophenes, whereas the BDT donor units are affected only in few cases. In the eA compound NDI2OD-T2, oxidation and reduction cause similar changes in the bond lengths as for BDT-TzBI and BDB-T-2F, namely the oxidation takes place in the thiophene donor units and reduction in the NDI acceptor unit (with additional thiophene units). This is inline with the results predicted by Fazzi et al. with the non-tuned CAM-B3LYP [183].

According to OT-ωB97X-D, the excitations and following vibrational relaxations of the eD trimers BDT-TzBI, DTB-EF-T, and BDB-T-2F occur mostly in the same

regions as their reduction, i.e. in the acceptor and neighboring thiophenes of the middle CRU, although for BDB-T-2F, the structural changes are observed in the BDT donor, as well. For BDCPDT-TPD and BDT-TPD, B3LYP predicts that the largest structural changes upon excitation to the S_1 state occur in the middlemost donor and acceptor unit, wheres the relaxation to the T_1 state is more localized on the donor units. Even thought no direct conclusions can be drawn from these results obtained with different functionals, as they are for different compounds, the global hybrid B3LYP seems to yield more delocalized description, which could be expected based on the previous results [183] and its tendency for delocalized description of other properties, as well.

4.3 Oligomeric versus periodic approaches

Finding of the good trade-off between the system size and computational level is essential when modeling the conjugated PSC polymers. Many properties, such as FMO energies, gap energies, IEs, and EAs are inversely proportional to chain length, i.e. their values decrease with increasing conjugation length [36, 37]. The properties of a polymer at the infinite chain length can be extrapolated from those of the corresponding oligomers. However, care must be taken in extrapolating these values, as most of them are method dependent and do not necessarily scale linearly with the inverse of the chain length $(1/n)$ [36, 37]. Thus, the linear fit, which is sometimes chosen as an extrapolation method in the studies of PSC polymers, is not always the best choice for all the properties. Alternatively, periodic values can be obtained with the PBC-DFT method, but unfortunately it cannot be yet employed for calculating all of the polymer properties (e.g. reorganization energies, IEs, excitation energies, etc.).

In Publication I, the FMO and HOMO–LUMO gap energies at the infinite chain length for BDCPDT-TPD and BDT-TPD have been obtained by both extrapolating the oligomeric values and calculating the periodic ones with the PBC-DFT method. Additionally, vertical excitation energies (for the $S_0 \rightarrow S_1$ transition) at the infinite chain length have been also determined with different extrapolation techniques. The oligomeric and periodic values predicted by B3LYP with respect to either $1/n$ or the
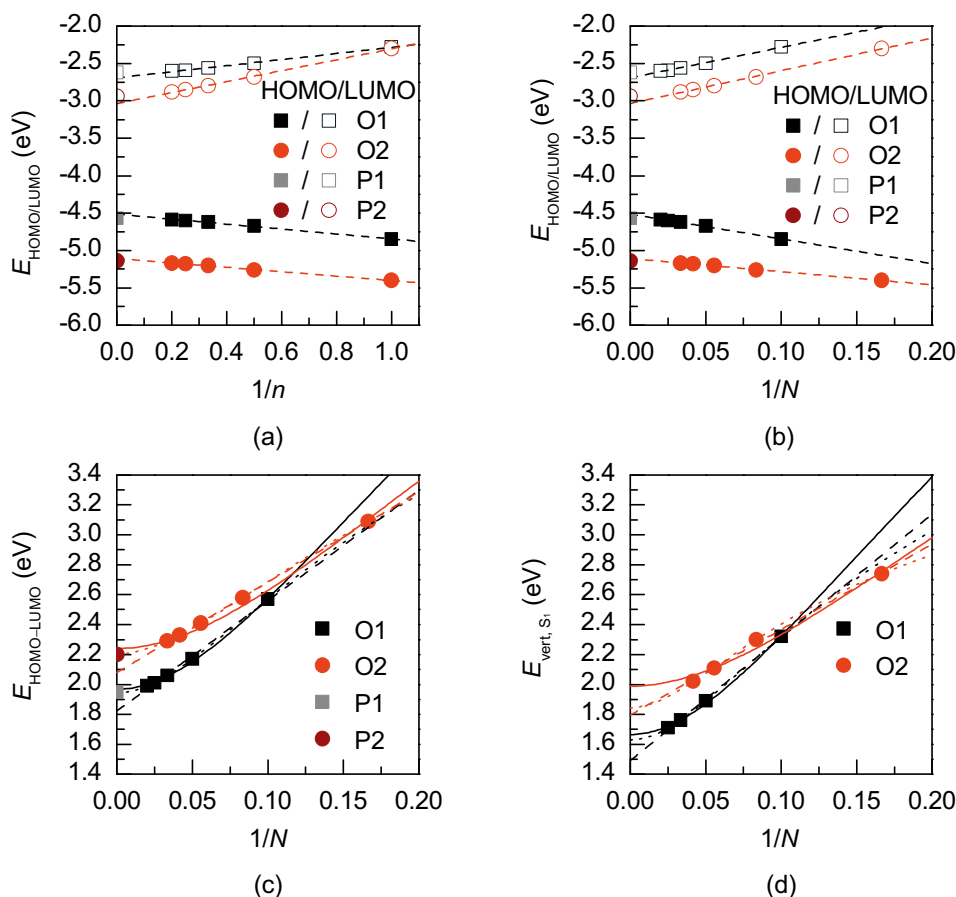
Figure 4.5 Extrapolations of the oligomeric HOMO and LUMO energies with respect to the reciprocals of both (a) n and (b) N, and the extrapolations of the oligomeric (c) HOMO–LUMO gap and (d) vertical $S_0 \rightarrow S_1$ excitation energies with respect to the reciprocal of N for BDCPDT-TPD (O1) and BDT-TPD (O2) calculated at the B3LYP/6-31G** level of theory in vacuum. The periodic values for BDCPDT-TPD (P1) and BDT-TPD (P2) are also presented in the graphs (a)–(c). The extrapolations to the infinite chain lengths were carried out with the linear (dashed lines), Kuhn (solid lines), and scaled Kuhn fits (dotted lines).

inverse of the number of the double bonds ($1/N$) are illustrated in Figure 4.5. For both compounds, the linear fit slightly overestimates the HOMO energies and underestimates the LUMO and HOMO–LUMO gap energies compared to the periodic values. For the HOMO–LUMO gap energies, both the Kuhn and scaled Kuhn fit yield very similar values that are almost identical to the periodic ones. The scaled Kuhn fit follows the data points even more closely than the original Kuhn fit. The

similar trends are observed for the extrapolated vertical $S_0 \rightarrow S_1$ transition energies, namely the linear fit yields the smallest values, while the Kuhn fit yields the largest.

All the techniques predict smaller gap energies and excitation energies for the ladder-type BDCPDT-TPD than for BDT-TPD, which is most probably due to the extended conjugation and more planar structure of BDCPDT-TPD. The LRC functional CAM-B3LYP predicts the same trends, although the HOMO energies are energetically-destabilized and the LUMO energies are energetically-stabilized with respect to the B3LYP values leading to the notable larger gap values. The conformation of the polymer backbone does not have much effect on these trends and the values predicted for different conformational models either by extrapolating or with periodic calculations are rather similar.

When comparing the GS geometries of the oligomeric and periodic models of PBDT-TFQ in Publication II, it is observed that the periodic models have dihedral angles close to the oligomeric ones, although the periodic calculations predict slightly less planar backbone (Table 4.2). The similar dihedral angles for the oligomeric and periodic models of the different D–A copolymers have been predicted previously [14]. The BLA (middle) values of the oligomers and the corresponding periodic values are also close to each other. In Publication I, the oligomeric and periodic HOMO and LUMO predicted for BDCPDT-TPD and BDT-TPD are observed to resemble also each other, but due to the absence of the chain end effects in the periodic models, the periodic HOMO and LUMO are delocalized along entire backbone, wheres the oligomeric ones are localized mostly on the middle CRUs.

4.4 Optoelectronic properties of polymer solar cell compounds

Characterization of the electronic and optical properties, i.e. FMO energies, gap energies, IEs, and EAs, vertical excitation energies, and corresponding spectra, is one of the main areas for the theoretical studies of the D–A copolymers and other PSC compounds. However, the functional may have a large effect on the calculated values and nature of the studied transitions. In this section, the effect of the functional on

these features will be discussed. The results of these studies have been published in Publications I, II, and IV.

4.4.1 Electronic properties

In Publications I and II, the HOMO, LUMO, and HOMO–LUMO gap energies of the oligomers of the D–A copolymers employed as the eD compounds in the polymer–fullerene systems have been examined. As mentioned above in Section 4.3, due to the extended conjugation of the ladder-type BDCPDT-TPD, both the global hybrid B3LYP and LRC functional CAM-B3LYP predict smaller HOMO–LUMO gap energies for it compared to the similar BDT-TPD with the smaller BDT donor unit. However, CAM-B3LYP predicts destabilized HOMO energies and stabilized LUMO energies and thus larger HOMO–LUMO gaps for both compounds compared with those predicted by the B3LYP. Similar trends have been observed for BDT-TFQ in Publication II. Namely, the HOMO energies of BDT-TFQ decrease in the order of the global hybrid > OT-LRC > non-tuned LRC functionals, whereas the LUMO energies increase in the order of the global hybrid < OT-LRC < non-tuned LRC functionals. Consequently, the LRC functionals yield larger HOMO–LUMO gap energies than the global hybrids. Similar trends, i.e. the stabilized HOMO energies, destabilized LUMO energies, and larger HOMO–LUMO gaps predicted by the LRC functionals with respect to the global hybrids, are also observed for the fullerene derivatives $PC_{61}BM$ and $PC_{71}BM$ in Publication II. The results in Publications I and II also show that the conformation of D–A copolymer and inclusion of the solvent environment do not have large effect on the calculated HOMO, LUMO, and HOMO–LUMO gap energies of the studied compounds.

The FMO energies and HOMO–LUMO gaps of the PSC compounds calculated with DFT are commonly compared to the experimental values derived from the oxidation and reduction potentials, which have been determined with electrochemical, e.g. cyclic voltammetry measurements. However, it should be noted that both of these methods yield only approximate values of IE and EA of the studied system from the different point of views [62]. Thus, the direct comparison of the values obtained with these methods is misleading. More precise manner would be

to calculate the IE and EA theoretically as the total energy differences between the neutral and charged states and compare these results with the experimental values obtained with gas-phase ultraviolet photoelectron spectroscopy and electron attachment spectroscopy or inverse photoemission spectroscopy. In DFT, the exact functional should yield the HOMO energy equal and opposite to the vertical IE. As mentioned in Section 2.2.5, the OT-LRC functionals are designed to fulfill this relation, and thus they should provide IEs (and consequently HOMO energies) closer to the experimental ones [131, 138]. Unfortunately, experimental reference values of IE (and EA) are not always available for PSC materials.

In Publication II, it is observed that for $PC_{71}BM$, the OT-ωB97X-D functional yield the HOMO energy (-7.05 eV) closest to the (negative of) experimental IE determined in the gas phase with the ultraviolet photoelectron spectroscopy [185]. The global hybrid functionals yield the destabilized HOMO for $PC_{71}BM$, whereas the non-tuned LRC functionals yield stabilized HOMO compared to the experiments. Similarly, in Publication IV, the IEs of the eD and eA compounds employed in the NF PSCs are close to the experimental values. While the OT-LRC functionals have been observed to provide the EAs of pentacene close to the experimental ones [45], here it is noted that the EAs calculated in Publication IV are notable underestimated compared to the experimental ones. This could be due to the inaccuracies in deriving EA from the IE of the anionic system (see Equation 3.1). A basis set including diffuse functions might yield more accurate EAs [8]. However, the effect of the extended basis set has not been verified here, as such calculations would have been computationally too demanding for the studied systems.

4.4.2 Vertical excitation energies and absorption spectra

The vertical transition maxima, i.e. the transitions with the largest oscillator strength, of the studied compounds are collected in Table 4.3. For the oligomers of the studied D–A copolymers and ITIC derivatives, this is the lowest vertical excitation, i.e. $S_0 \rightarrow S_1$ transition, whereas for the fullerene derivatives, higher-energy transition is the maximum. Generally, B3LYP underestimates the vertical excitation energies by 0.1–0.4 eV with respect to the experimental values, which are also presented in Ta-

Table 4.3 Vertical excitation energies (in eV) for the transition maxima[1] of the eD and eA compounds calculated with different functionals in vacuum and solvent (in parentheses).[2,3]

| Model	B3LYP	ωB97X	ωB97X-D	OT-ωB97X	OT-ωB97X-D	Exp.
eD						
BDCPDT-TPD[4]	1.76	-	-	-	-	1.96
BDT-TPD[4]	1.97	-	-	-	-	2.03
BDT-TFQ	1.82	3.09	2.82	2.27 (2.28)	2.28 (2.28)	2.24
BDT-TzBI	-	-	-	-	2.43 (2.48)	2.27
DTB-EF-T	-	-	-	-	2.56 (2.57)	2.28
BDB-T-2F	-	-	-	-	2.49 (2.49)	2.25
eA						
$PC_{61}BM$	3.50	4.82	4.51	4.18 (4.13)	4.26 (4.21)	3.75
$PC_{71}BM$	2.37	2.97	2.77	2.59 (2.58)	2.64 (2.63)	2.68
NDI2OD-2T	-	-	-	-	2.38 (2.41)	1.85
ITIC	-	-	-	-	2.20 (2.07)	1.83
ITIC-4F	-	-	-	-	2.16 (2.03)	1.72
ITIC-2Cl	-	-	-	-	2.17 (2.04)	1.73

[1] The transitions with the largest oscillator strengths, i.e. the $S_0 \rightarrow S_1$ transitions for the oligomers of the D–A copolymers.

[2] The 6-31G** basis set was employed in all calculations.

[3] Experimental UV-Vis spectra were measured in toluene for BDCPCT-TPD, $PC_{61}BM$, and $PC_{71}BM$, in $CHCl_3$ for BDT-TPD, BDT-TzBI, BDB-T-2F, and ITIC, in 1,2-DCB for BDT-TFQ, and in CB for DTB-EF-T. For ITIC-2Cl and ITIC-4F, the experimental absorption was measured from thin films. The solvents used in the calculations were chosen accordingly, except for DTB-EF-T, ITIC-2Cl, and ITIC-4F, for which $CHCl_3$ was used.

[4] The vertical excitation energies calculated with CAM-B3LYP were 2.47 eV for BDCPDT-TPD and 2.70 eV for BDT-TPD.

ble 4.3. The non-tuned LRC functionals overestimate excitation energies by 0.1–1.1 eV compared to the experiments, which is due to the larger amount of the explicit HF in them compared to the global hybrids. The OT-LRC functionals yield excitation energies between those of B3LYP and non-tuned LRC functionals and in some cases, e.g. for BDT-TFQ and $PC_{71}BM$, the excitation energies obtained with OT-ωB97X and OT-ωB97X-D are almost equal to the experimental values.
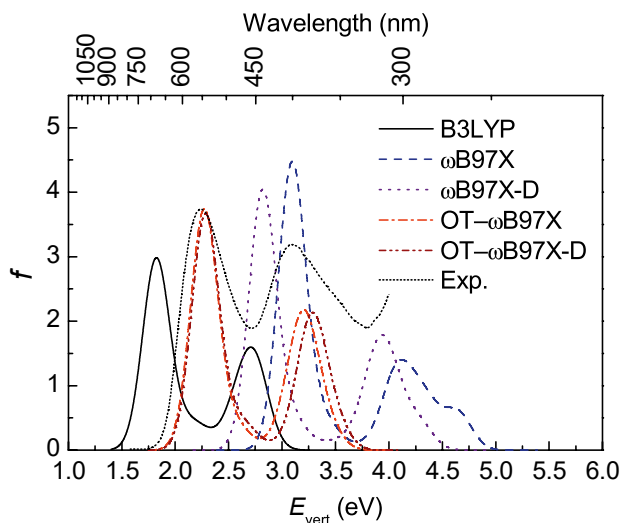
Figure 4.6 UV-Vis absorption spectra of BDT-TFQ (n = 3) calculated in 1,2-DCB using TDDFT with different functionals and the 6-31G** basis set. The digitized experimental spectrum of the PBDT-TFQ copolymer is also presented (the vertical axis has been scaled to match the maximum of the calculated OT-ωB97X spectrum. Reproduced from [149] with permission from the PCCP Owner Societies.

The corresponding UV-Vis spectra of the studied D–A copolymers are characterized by two bands: a dominant one at the lower-energy with large oscillator strength and a second one at the higher energy with smaller oscillator strength. In all cases, the dominating peak originates from the $S_0 \rightarrow S_1$ transition, which has an ICT nature (see the corresponding NTOs below). The overall shapes of the calculated spectra correspond well with those of experimental ones. However, as observed for the excitation energies reported in Table 4.3, the functional has a large effect on the relative position of the spectra with respect to the experiments [143].

The UV-Vis absorption spectra of eD-type trimer BDT-TFQ calculated with several functionals are presented in Figure 4.6 together with the experimental reference spectrum [143]. As is observed for the $S_0 \rightarrow S_1$ excitation energies predicted by different functionals in Table 4.3, the OT-ωB97X and OT-ωB97X-D yields the spectra closest to the experimental one. The oscillator strengths for the main peak increase in the order of B3LYP (B3LYP-D) < OT-LRC < non-tuned LRC functionals. The same trend is observed [9] also by Pandey et al.

Overall, these results are inline with the previous findings on the effect of the functional and improved description of the excitation energies and spectra of the D–A oligomers with the OT-LRC functionals [9, 12, 14]. However, this does not apply for all the studied compounds, as OT-ωB97X-D overestimates the excitation energies of PC$_{61}$BM and the NF PSC compounds by 0.2–0.5 eV with respect to the experiment.

4.4.3 Intramolecular charge transfer in the donor–acceptor copolymers

The nature of the S$_0$ → S$_1$ transition for the studied D–A copolymers can be examined by illustrating the corresponding NTOs obtained for their oligomers. Overall, all the studied oligomers have ICT from the donor units to the acceptor units with a varying degree depending on the torsions between the units and functional used. The contributions of the backbone units to the corresponding NTOs (the dominant pair) of the studied eD and eA compounds are presented in Table 4.4.

Table 4.4 Contributions (%) of the electron densities of the donor (D), thiophene (T), and acceptor (A) backbone units to the NTOs[1] of the studied eD and eA compounds.

Compound	Functional	λ_{NTO}	hole			electron		
			D	T	A	D	T	A
BDCPDT-TPD	B3LYP	0.92	81	-	19	67	-	33
	CAM-B3LYP	0.61	81	-	19	67	-	33
BDT-TPD	B3LYP	0.88	75	-	25	50	-	50
	CAM-B3LYP	0.57	74	-	26	52	-	48
BDT-TFQ	B3LYP	0.91	47	38	15	16	25	59
	OT-ωB97X-D	0.66	38	44	18	17	24	59
BDT-TzBI	OT-ωB97X-D	0.64	42	40	18	24	28	48
DTB-EF-T	OT-ωB97X-D	0.64	36	23	41	33	17	50
BDB-T-2F	OT-ωB97X-D	0.61	40	39	21	30	33	37
NDI2OD-2T	OT-ωB97X-D	0.60	78	-	22	13	-	87
ITIC	OT-ωB97X-D	0.87	79	-	21	54	-	46
ITIC-4F/ITIC-2Cl	OT-ωB97X-D	0.87	78	-	22	53	-	47

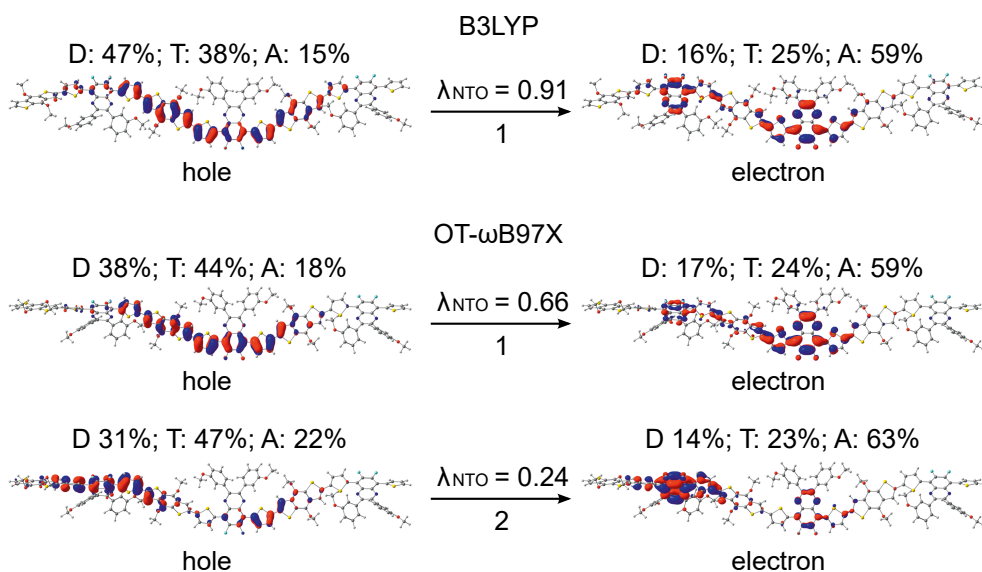[1] For the S$_0$ →S$_1$ transitions as calculated in vacuum with TDDFT.

For BDCPDT-TPD, BDT-TPD, and BDT-TFQ, B3LYP yields one dominating NTO pair ($\lambda_{\text{NTO}} > 0.9$), which indicates a partial CT from the donor units to the acceptor units (see Figure 4.7 for BDT-TFQ). As the $S_0 \rightarrow S_1$ transition is mainly HOMO $\rightarrow$ LUMO in nature for these compounds, their NTOs resemble closely to the FMOs (see Publication I for the illustration of the FMOs for BDCPDT-TPD and BDT-TPD). The similar shapes of the main NTO pair for the $S_0 \rightarrow S_1$ transition and FMOs have been observed for the other D–A copolymers also in the previous studies [8, 9]. In BDCPDT-TPD, the contribution of the donor units to both the hole and electron NTOs are larger than that of the acceptor units, whereas in BDT-TPD, the donor units contribute more to the hole NTO than the acceptor units, but in the electron NTO, they have equal contribution.

In the case of the other eD oligomers, a partial CT is observed as well (Table 4.4), but on the contrary to BDCPDT-TPD and BDT-TPD, which consisted of only donor and acceptor units, there are additional thiophene spacers in the backbones of BDT-TFQ, BDT-TzBI, DTB-EF-T, and BDB-T-2F. Based on the calculated contributions of the backbone units to the NTOs, these thiophenes act as donors transferring charge density to acceptor units as well. In the case of BDT-TFQ (see Figure 4.7), all functionals predict that the hole NTO is delocalized along the backbone with larger amount of charge density on the donor units than on the thiophenes or acceptor units, whereas the electron NTO is localized mainly on the acceptor units with a small amount of charge density on the donor units and thiophenes, as well. Similar CT character is predicted also by OT-ωB97X-D for BDT-TzBI and BDB-T-2F. The amount of the charge density transferred from the donor and thiophene units to the acceptor units is somewhat larger in BDT-TzBI (ca. 30 percentage points, i.e. pp) than in BDB-T-2F (16 pp). As the copolymers of these oligomers have been employed in the efficient fullerene-based [179] and NF PSCs [145, 147], their CT character seems to be beneficial for the performance of the corresponding PSC. However, no direct conclusions can be drawn merely on the amount of transferred charge density, as a relatively small amount (9 pp) of charge density is observed to transfer in DTB-EF-T, the corresponding copolymer of which has been incorporated in the one of the most efficient NF PSC so far [25].

In general, the LRC functionals tend to yield somewhat different description for the NTOs of the $S_0 \rightarrow S_1$ transitions of the D–A oligomers compared to the global hy-

Figure 4.7 NTOs (the dominant pairs) and the contributions of the donor (D), thiophene spacer (T), and acceptor (A) units to the NTOs calculated in vacuum using TDDFT with different functionals and 6-31G** basis set for the $S_0 \rightarrow S_1$ vertical transition of BDT-TFQ (isodensity contour = 0.025). The fractions of the hole–electron contribution to the transition, λ_{NTO}, are also presented. Adapted from [149] with permission from the PCCP Owner Societies.

brids. As mentioned above, the global hybrid B3LYP tends to yield one dominating NTO pair, which is typically mainly HOMO $\rightarrow$ LUMO in nature, whereas the LRC functionals predict additional electronic configurations and consequently additional NTO pairs that can contribute to the lowest electronic transition [9]. For the eD oligomers BDCPDT-TPD and BDT-TPD, the LRC CAM-B3LYP functional yields slightly more localized description of the main NTO pair compared with B3LYP. However, the overall contributions of the backbone units to the main NTOs are close to those predicted by B3LYP. For both compounds, the second NTO pair contributes also to their $S_0 \rightarrow S_1$ transition. In the case of the eD oligomer BDT-TFQ, the OT-LRC functionals yield also the similar CT character for the main NTO pair of the $S_0 \rightarrow S_1$ transition as B3LYP (1 in Figure 4.7). However, the contributions of thiophene spacers to the hole NTO are larger with OT-ωB97X than with B3LYP. The electron NTO is almost the same with both the functionals. In the second NTO pair (2 in Figure 4.7), OT-ωB97X predicts also a partial CT from the donor and thiophene units to the acceptor units with similar contributions to the first NTO pair, but the NTOs are now localized in the different parts of the backbone.

4.5 Local interfacial eD–eA complexes

The morphology, i.e. the molecular order and microstructure of the active layer is one of the key factors defining the efficiency of charge generation in PSCs [87]. While information regarding the molecular packing behavior in the blend can be obtained via atomistic MD simulations, the quantum mechanical calculations of the local complex structures yield insight into electronic-level phenomena taking place at the interfaces of the participating molecules. In this section, structural and CT characteristics of the local interfacial complexes of the studied eD–eA systems are discussed. They comprise both conventional polymer–fullerene and emerging NF, i.e. polymer–polymer and polymer–SMA type blend systems. The results of these studies have been published in Publications II–IV.

4.5.1 Structural characteristics of eD–eA complexes

In Publication II, the effect of the functional on the optimal intermolecular distance between the planarized oligomeric model of the D–A copolymer PBDT-TFQ and PC$_{71}$BM has been examined. Furthermore, energetically the most favorable position (donor vs. thiophene vs. acceptor unit) and orientation (vertical vs. horizontal) of PC$_{71}$BM on the top of BDT-TFQ have been considered. The global hybrid B3LYP and the OT-LRC functional OT-ωB97X yield the largest distances between the compounds of 4.0–5.3 Å, whereas other functionals predict the similar distances of 3.3–3.7 Å, which are consistent with the previous MD simulations of the BDT-TPD–PC$_{71}$BM system [18]. Inclusion of the dispersion corrections in B3LYP-D and OT-ωB97X-D decrease the predicted distances with respect to B3LYP and OT-ωB97X, respectively. The interaction energies follow the opposite trend than the optimal distances. The relatively large intermolecular distances (and small interaction energies) predicted with OT-ωB97X may be due to a too small ω for describing these complexes for which reason the OT-ωB97X functional is closer to a pure density functional (B97X with a limiting case of $\omega = 0.00$ bohr^{-1}) than to a LRC functional.

Table 4.5 Optimal intermolecular distances (d_{opt}) and interaction energies (E_{int}) between BDT-TFQ and PC$_{71}$BM in the BDT-TFQ–PC$_{71}$BM complexes[1] calculated with different functionals and the 6-31G* basis set.

| | Orientation of PC$_{71}$BM | | | |
| | Vertical | | Horizontal | |
Functional	d_{opt} (Å)	E_{int} (kJ mol^{-1})	d_{opt} (Å)	E_{int} (kJ mol^{-1})
B3LYP	4.0	-1.0	4.0	-1.3
B3LYP-D	3.3	-55.5	3.3	-63.7
ωB97X	3.4	-19.5	3.4	-22.7
ωB97X-D	3.3	-58.0	3.3	-66.1
OT-ωB97X	4.7	-0.5	4.7	-0.9
OT-ωB97X-D	3.4	-42.0	3.3	-47.0

[1] The results are only for the complexes, where PC$_{71}$BM is on the top of the acceptor unit of BDT-TFQ. For the other complexes, see the original Publication II.

Overall, the orientation of PC$_{71}$BM does not have a significant effect on the optimal intermolecular distances, i.e. they are practically the same whether PC$_{71}$BM is vertically or horizontally oriented with respect to BDT-TFQ, see Table 4.5. However, the (absolute) interaction energies are somewhat larger for the horizontal models. In Publication II, all the functionals are observed to predict the smallest intermolecular distances and largest interaction energies, when PC$_{71}$BM locates on the top of the quinoxaline acceptor unit of BDT-TFQ. In most cases, the largest distances and smallest interaction energies are obtained when PC$_{71}$BM is on the top of the donor unit of BDT-TFQ, except for the vertical models, where the smallest interaction energies are observed, when PC$_{71}$BM is on the top of the thiophene unit. The stronger interaction between the acceptor unit of the D–A copolymer and PC$_{71}$BM has been observed also by a previous experimental study [186] and it may play a role in the preferred binding sites of some copolymer–fullerene systems. However, this does not apply to all systems, as opposite results have been obtained experimentally [186] and theoretically [34], as well.

As the intermolecular distances between BDT-TFQ and PC$_{71}$BM has been studied via rigid SP PES scans, their geometries have not been optimized. In Publication IV, somewhat different approach has been taken, as the geometries of polymer–polymer

and polymer–SMA systems have been optimized to obtain their relaxed (GS) structures. Similarly to the BDT-TFQ–PC$_{71}$BM complexes, several relative orientations of these compounds have been considered to see whether they have some preferences. In the most stable configuration predicted for the polymer–polymer type BDT-TzBI–NDI2OD-T2 complexes, the acceptor units of BDT-TzBI and NDI2OD-T2 prefer to be face-to-face, while their donor units are also face-to-face (i.e. the AA(1) configuration). This supports previous experimental findings for the face-to-face stacking between the similar PTzBI-Si copolymer and P(NDI2OD-T2) [80]. In the alternative configuration (with the energy difference of 0.9 kJ mol^{-1} to the most stable one), the donor and acceptor units of BDT-TzBI and NDI2OD-T2 prefer to be face-to-face, respectively, whereas the acceptor and donor units of BDT-TzBI and NDI2OD-T2 are face-to-face, respectively (the DA(2) configuration). These kind of face-to-face orientations between the copolymers are important for forming strong π-orbital overlap at their interfaces, which will reduce the binding energy of the excitons and promote the free charge carrier generation [7]. The intermolecular distances predicted here between the backbones of BDT-TzBI and NDI2OD-T2 are ca. 3.4–4.0 Å with the average of 3.7 Å, which is in line with the experimental π–π stacking distance (3.7 Å) for this system [187].

In the polymer–SMA type complexes, DTB-EF-T–ITIC-4F and BDB-T-2F–ITIC-2Cl, the electron-withdrawing INCN end groups of the ITIC derivatives have been positioned above different backbone units of DTB-EF-T and BDB-T-2F, as these kinds of relative orientations have been predicted in the MD simulations of other polymer–ITIC systems [16]. This tendency for locating the end-groups of the ITIC on the polymer backbone has been explained by the steric hindrance caused by the hexylphenyl side groups in the IT core unit of ITIC, which prevent the approach of the polymer chains. In Publication IV, the DA configuration of DTB-EF-T–ITIC-4F, where the electron-withdrawing end-group of ITIC-4F is on the top of the BDT donor unit of DTB-EF-T, is predicted to be the energetically more favorable conformation than the AA configuration. In the AA configuration, the end-group of ITIC-4F has been positioned initially on the top of the acceptor unit, i.e. one of the substituted thiophenes of DTB-EF-T, but is eventually located above the bond connecting the acceptor unit and the neighboring BDT donor unit after the geometry optimization of the complex. In the BDB-T-2F–ITIC-2Cl complexes, the opposite result has been obtained, namely the AA configuration, where the end-group
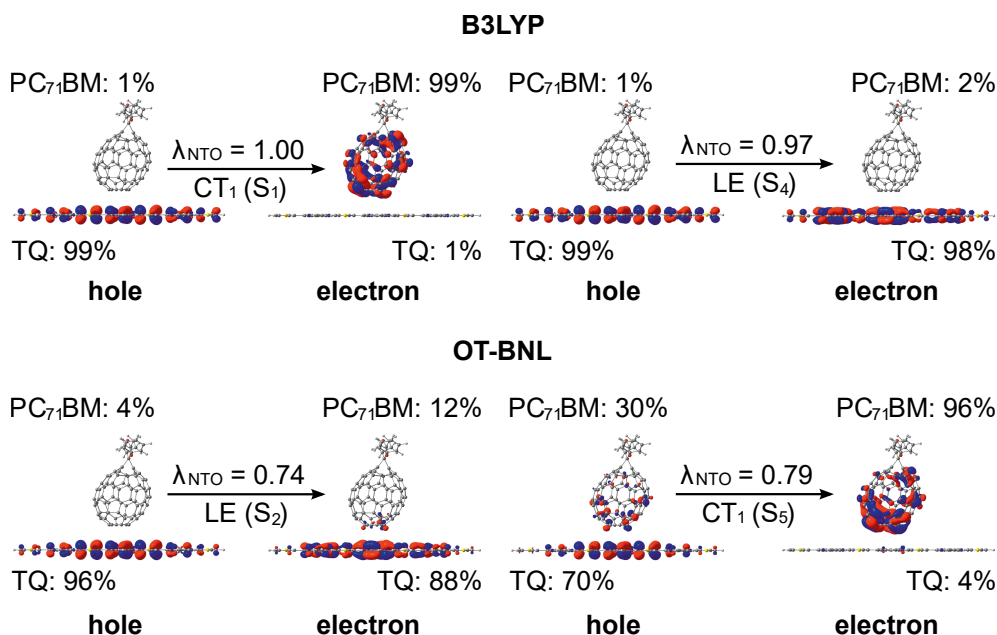
of ITIC-2Cl is on the top of the acceptor unit of BDB-T-2F is predicted to be energetically more favorable than the DA configuration, where the end-group is on the top of the donor unit. This is inline with the previous MD simulations of the BDB-T-2F–ITIC systems [16, 19].

Alongside the interaction strength between the compounds, the length and degree of branching of the polymer side chains control the accessibility of the backbone and possible intercalation of fullerene derivatives between the side chains [71, 186]. As the full-length side chains have not been included here, the studied complexes do not take these factors into account, but rather give an idea of the mutual interactions between the eD and eA compounds.

4.5.2 Nature of the excited states in the eD–eA complexes

The functional has a great influence on the ordering and nature of the excited states of the eD–eA complexes. In general, for the studied polymer–fullerene systems, BDT-TFQ–$PC_{71}BM$ and TQ–$PC_{71}BM$, the global hybrid functionals tend to predict a intermolecular CT character for the (two or three) lowest excited singlet states with a complete CT from the D–A oligomer to $PC_{71}BM$ (see Figure 4.8 for the NTOs of TQ–$PC_{71}BM$). In the higher energy, there is the main vertical transition with the largest oscillator strength that corresponds to the intramolecular excitation of the D–A oligomer, i.e. the LE state. Above these states in energy, there are additional CT states or local excitations of $PC_{71}BM$. This ordering of the states, i.e. the lowest CT (CT_1) state being at the lower energy than the LE state, is consistent with the experimental findings for PTQ–$PC_{71}BM$ [188, 189].

However, both the non-tuned and OT-LRC functionals predict the opposite ordering of the states for the polymer–fullerene systems compared with the global hybrids and experiments, namely the LE state is at the lower energy than the CT_1 state. The OT-LRC functional tends to predict the mixing of the local excitations of $PC_{71}BM$ with the CT_1 state, whereas the non-tuned LRC functionals either yield the CT_1 state with the similar mixed character as the OT-LRC functionals or do not detect any CT states among the ten lowest excited singlet states (see below). Similar dependence between the functional and nature of the excited state was predicted for

B3LYP

PC$_{71}$BM: 1% PC$_{71}$BM: 99% PC$_{71}$BM: 1% PC$_{71}$BM: 2%

λ_{NTO} = 1.00
CT$_1$ (S$_1$)

λ_{NTO} = 0.97
LE (S$_4$)

TQ: 99% TQ: 1% TQ: 99% TQ: 98%

hole **electron** **hole** **electron**

OT-BNL

PC$_{71}$BM: 4% PC$_{71}$BM: 12% PC$_{71}$BM: 30% PC$_{71}$BM: 96%

λ_{NTO} = 0.74
LE (S$_2$)

λ_{NTO} = 0.79
CT$_1$ (S$_5$)

TQ: 96% TQ: 88% TQ: 70% TQ: 4%

hole **electron** **hole** **electron**

Figure 4.8 NTOs (the dominant pairs) of the CT$_1$ and LE states of the TQ–PC$_{71}$BM complexes calculated in vacuum with TDDFT using different functionals and the 6-31G* basis set (isodensity contour = 0.025). The contributions (%) of the compounds and the λ_{NTO} values are also presented. Adapted from [151] with permission from the PCCP Owner Societies.

pentacene–C$_{60}$ by Zhang et al. [45], namely B3LYP yielded a complete CT character for the S$_2$ state, whereas OT-LC-BLYP predicted the CT state with admixture of the excitation of C$_{60}$. The non-tuned LC-BLYP predicted S$_2$ state to be a local excitation of C$_{60}$ and CT state was at the higher energy. The previous experimental and theoretical studies have hinted for the possibility of the delocalized CT excitations at or near the eD–eA interface of the PSC systems, which would have an important role in decreasing the Coulomb binding energy due to the reduced electrostatic attraction between the hole and electron [3, 190]. Thus, the OT-LRC functional including the dispersion corrections appear to be the best choice for the correct description of the intermolecular distances (see Section 4.5.1) and nature of the CT states at the local interfaces of PSC systems.

In the polymer–fullerene system BDT-TFQ–PC$_{71}$BM, the tuning of ω seem to affect the appearance of the CT states, as the corresponding non-tuned LRC functionals ωB97X and ωB97X-D do not predict any CT states among the ten lowest excited
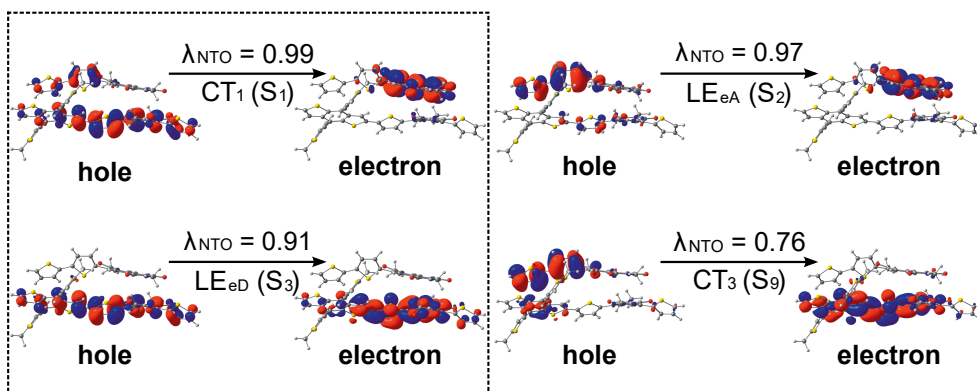
Figure 4.9 NTOs (the dominant pairs) of the different excited states of the BDT-TzBI–NDI2OD-T complex (the AA(1) configuration) calculated in blend with TDDFT at the OT-ωB97X-D/6-31G** level of theory (isodensity contour = 0.025). The λ_{NTO} values are also presented. The states relevant for the ED and CR processes, i.e. the CT_1 and LE states are highlighted with the dashed rectangle. Reproduced from Publication IV [184] - Published by The Royal Society of Chemistry.
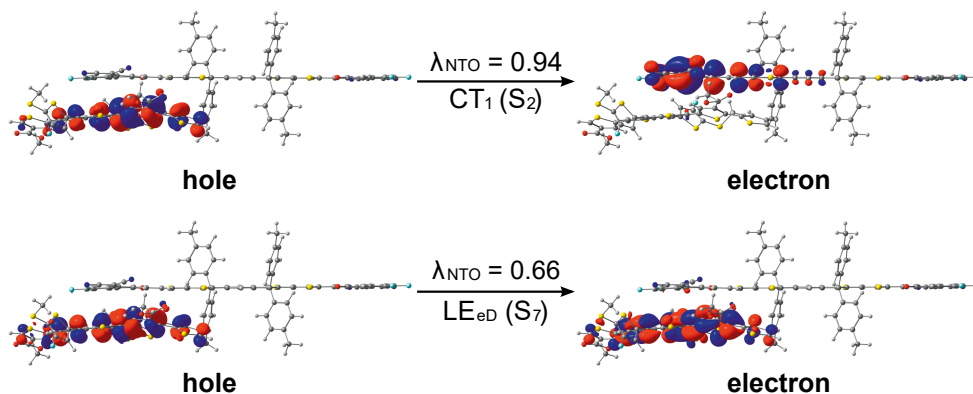
Figure 4.10 NTOs (the dominant pairs) of the CT_1 and LE states of the DTB-EF-T–ITIC-4F complex (the DA configuration) calculated in blend with TDDFT at the OT-ωB97X-D/6-31G** level of theory (isodensity contour = 0.025). The λ_{NTO} values are also presented. Reproduced from Publication IV [184] - Published by The Royal Society of Chemistry.

singlet states at the constant intermolecular distance of 3.5 Å (Publication II). However, this is not a common trait for all non-tuned LRC functionals, as the non-tuned CAM-B3LYP predicts CT states for TQ–PC$_{71}$BM among the ten lowest excited singlet states (e.g. the CT_1 state at the fifth lowest singlet excited state, see Publication III). As the default values of ω in these functionals are rather similar (ωB97X: 0.30 bohr^{-1}, ωB97X-D: 0.20 bohr^{-1}, CAM-B3LYP: 0.33 bohr^{-1}), the appearance of the

CT states are more likely governed by the differences between the studied systems and the underlying approximations in these LRC functionals. The intermolecular distance plays also a notably role on the appearance of the CT states for BDT-TFQ–PC$_{71}$BM, as no CT states are observed at the optimal distance of 4.7 Å with OT-ωB97X, but at the smaller distance of 3.5 Å, the CT states can be observed.

In the case of the studied NF PSC systems, OT-ωB97X-D predicts the same ordering of the states as the global hybrids do for the polymer–fullerene systems, i.e. the CT$_1$ state is in the lower energy than the LE state. Interestingly, this is the opposite to that predicted by OT-ωB97X-D for BDT-TFQ–PC$_{71}$BM, i.e. the CT$_1$ state is in the higher energy than the LE state. While differences in the OT ω values predicted for these systems might explain the different ordering of the states [45], the more likely explanation is the different type of systems, as the OT ω value for BDT-TFQ–PC$_{71}$BM (0.12 bohr^{-1}, see Table 4.1) is larger than those of the polymer–SMA systems (0.10 bohr^{-1}), but smaller than that of the polymer–polymer system (0.14 bohr^{-1}).

Similarly to the polymer–fullerene systems, a small amount of a local excitation of the eA compound NDI2OD-T2 is mixed with the CT$_1$ state in the polymer–polymer system BDT-TzBI–NDI2OD-T2 (the AA(1) configuration, Figure 4.9). However, in the polymer–SMA systems, i.e. DTB-EF-T–ITIC-4F (the DA configuration, Figure 4.10) and BDB-T-2F–ITIC-2Cl (see Publication IV for the illustration of the NTOs) no contributions of the local excitations to the CT$_1$ state are observed. In the AA(1) configuration of BDT-TzBI–NDI2OD-T2, the CT occurs from entire backbone of BDT-TzBI to the acceptor unit of NDI2OD-T2. In the polymer–SMA systems, the nature of CT is quite similar and CT occurs from the eD compound to the end-group of the ITIC derivative, although in DTB-EF-T, the hole NTO is more evenly distributed along the backbone, while in BDB-T-2F, it is mainly localized on the acceptor unit. Interestingly, in BDT-TzBI–NDI2OD-T2, a "backward" CT process is observed to take place from the thiophene donor units of the eA compound NDI2OD-T2 to the several backbone units of the eD compound BDT-TzBI (the CT$_3$ state in Figure 4.9). This kind of CT could correspond to the hole transfer from the eA compound to eD, i.e. Channel II CT process, that may participate in the ET process from the eD compound to eA compound during exciton generation [87].

4.6 Calculating the charge transfer rates at local eD–eA interfaces

Finally, the calculated CT parameters and rates for the studied eD–eA systems are presented in this section. Here, the findings for applying the multi-state treatments for calculating the electronic couplings, which have been originally presented in Publications III and IV, are also presented.

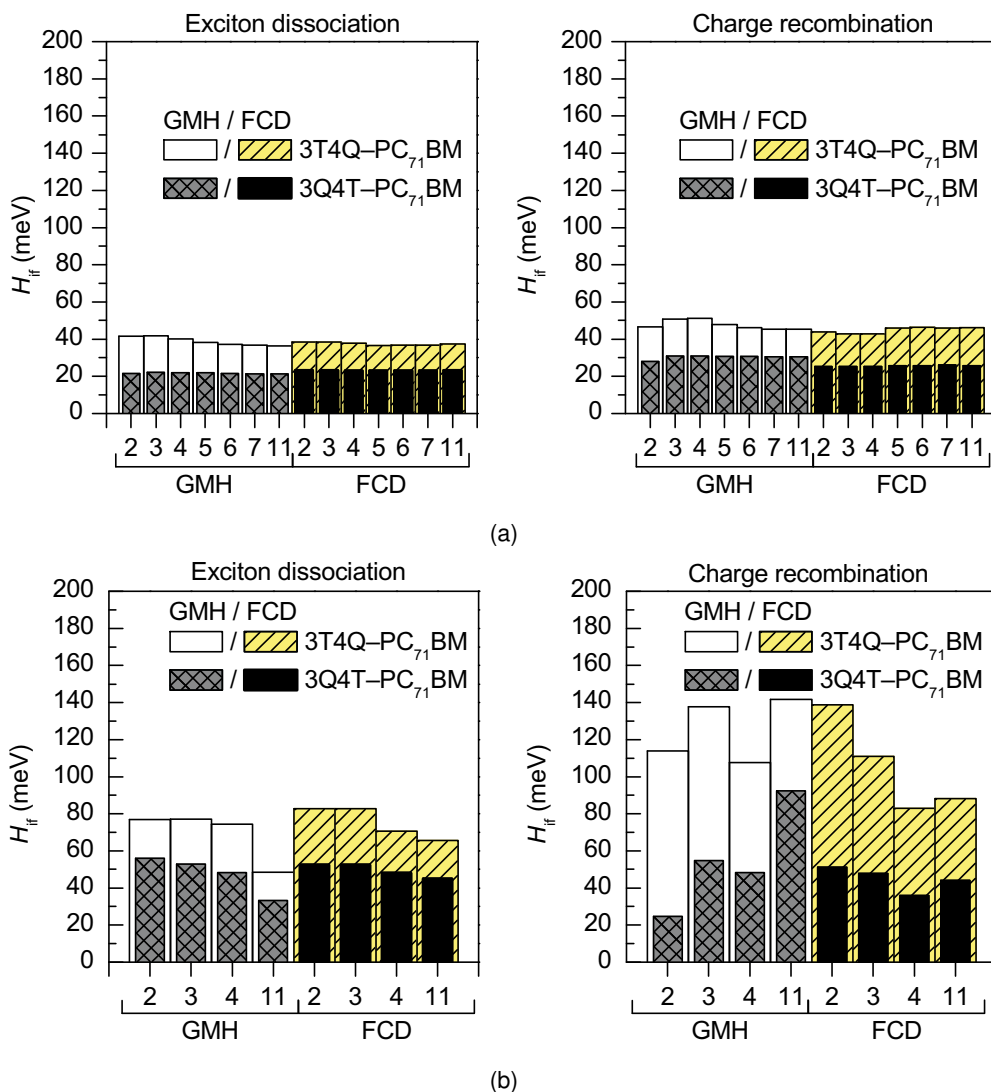### 4.6.1 Electronic couplings with the multi-state treatments

Before going into the calculated CT rates of the studied PSC systems, the results of the multi-state electronic coupling calculations carried out in Publications III and IV, are discussed in closer detail. In most cases, the ED couplings are predicted to be smaller than the CR couplings, although the opposite results are observed, as well. For the polymer–fullerene system TQ–PC$_{71}$BM, the choice of the functional has an influence on the size of the electronic coupling values, especially when employing the GMH scheme (Figure 4.11, see Publication III for the results of PBE0 and CAM-B3LYP). In general, both the GMH and FCD couplings increase in the order of B3LYP (20% HF) < PBE0 (25% HF) < CAM-B3LYP ≤ OT-BNL. Sini et al. have observed [191] the similar linear correlation between the coupling values and the percentage of the explicit HF exchange, i.e. larger couplings with the functionals including larger amount of the HF exchange. While the LRC functionals employed here can be expected to include the greater amount of HF exchange than the global hybrids, this percentage cannot be directly assigned, as it depends on the amount of HF exchange included in the LR (and SR) component, the ω value, and studied system. However, the amount of effective HF exchange can be used as an estimation of the exact exchange instead [14, 191]. Although the effective percentages of exact exchange in CAM-B3LYP and OT-BNL cannot be verified with the number of the functionals used in this work, the couplings are excepted to increase with the increasing amount of the effective HF exchange in the functional, as well.

Furthermore, the functional has a clear effect on the relation between the coupling values and the number of excited states used for forming the diabatic states. With the global hybrid functionals, B3LYP (Figure 4.11a) and PBE0, both the GMH and FCD scheme yield very constant couplings for the TQ–PC$_{71}$BM that decrease only slightly with the increasing number of states. This can be explained by the tendency of the global hybrids to predict only a small or negligible mixing of the adiabatic states (see Figure 4.8). Thus, as the adiabatic CT states are already well localized, the diabatization does not change their nature much even with larger number of the states.

However, with the LRC functionals, CAM-B3LYP and OT-BNL (Figure 4.11b), the number of the states has more notable effect on the electronic couplings. Generally, the GMH and FCD ED couplings predicted with the LRC functionals decrease with the increasing number of the states, with the exception of some multi-state results, which are slightly higher than the 2-state ones. Additionally, the FCD CR couplings mainly decrease with the increasing number of the states, but the GMH CR couplings do not follow such a clear trend and rather oscillate when the number of states increases. These differences in the coupling values obtained with the different number of states can be attributed to the tendency of the LRC functionals used here to predict the mixing of the local excitation with the CT$_1$ state (see Figure 4.8).

As the sizes of the studied TQ–PC$_{71}$BM complexes set limitations to the computational time, it is not possible to determine whether the couplings predicted by the LRC functionals have converged already to the certain values or whether more excited states would have been required. Nevertheless, based on the Δq^{diab} values of the CT$_1$ state (see the original Publication III), which are closer to the ideal value of 2 with the 11-state FCD scheme (1.8–1.9) than with the 2–4-state schemes (0.7–1.7), the 11-state FCD couplings are excepted to be more reliable. Similarly, while not reaching the ideal dipole moments calculated for the studied TQ–PC$_{71}$BM complexes (41.1 D and 41.3 D for 3T4Q–PC$_{71}$BM and 3Q4T–PC$_{71}$BM, respectively), the μ^{diab} values of the CT$_1$ state are closer to the ideal ones with the 11-state GMH scheme (24.5–27.9 D) than with the 2–4-state schemes (11.4–21.8 D).

Alongside the functional, other calculation settings can influence the couplings. In Publication III, the basis set, excited state method, and surrounding medium are

Figure 4.11 Electronic couplings obtained using the GMH and FCD schemes with different number of states (2–11) for the TQ–PC$_{71}$BM complexes. The calculations were carried out in vacuum with TDDFT using (a) B3LYP and (b) OT-BNL with the 6-31G* basis set. Adapted from [151] with permission from the PCCP Owner Societies.

found to have a notable effect on the GMH CR couplings when employing the LRC functionals, whereas no significant changes in the values are observed with the global hybrid functionals. When comparing the excited state methods, TDA predicts larger couplings with the LRC functionals than TDDFT. The same applies for the larger

6-31G** basis set, which predicts larger couplings than the smaller 6-31G*. Furthermore, the GMH CR couplings calculated either in $CHCl_3$ or blend are larger than those obtained in vacuum. Thus, the GMH scheme is more sensitive to the different calculation settings and number of the states than the FCD scheme is, especially when using the LRC functionals. Based on these results, the use of FCD is more recommended for calculating the multi-state couplings of the PSC systems when applying the LRC functionals.

This study has been extended in Publication IV, where the effect of the dispersion corrections on the prediction of the multi-state electronic couplings has been examined for the polymer–polymer system BDT-TzBI–NDI2OD-T2. Both the ED and CR couplings calculated with the FCD scheme and OT-ωB97X-D are very constant regardless of the number of states. In other words, the 2-state and multi-state (for 3–26 states) values are almost the same. While the reference calculations both without the dispersion corrections and with the default ω values have not been carried out to see, whether this is due to the dispersion corrections, OT-LRC functional used, or the studied system, the dispersion corrections are expected to be beneficial for the calculating the FCD electronic couplings for the PSC systems with the OT-LRC functionals. Similar trends are observed also for the polymer–SMA systems in Publication IV, as the 2-state and multi-state (i.e. 11-state) electronic couplings predicted for them are close to each other. However, in these systems, the effect of the inclusion of more states could not be verified, as these calculations would have been computationally too demanding.

It is well known that the electronic couplings are highly sensitive to the relative orientations of the studied compounds [34, 91, 165, 192]. In Publication III, both the ED and CR couplings of the polymer–fullerene system TQ–PC$_{71}$BM are predicted to be stronger (by ca. 21–83 meV for ED and 25–252 meV for CR) when PC$_{71}$BM is on the top of the thiophene donor unit of TQ than when it is on the top of quinoxaline acceptor unit. Similarly, stronger ED and CR couplings have been predicted by Wang et al. with the fragment orbital approach [97] and the non-tuned ωB97X-D, when PC$_{71}$BM is closer to the donor unit of PBDT-TPD [18]. They have also predicted stronger CR couplings with the 2-state FCD scheme and the OT ωB97X-D functional when PC$_{71}$BM is on the donor unit of benzothiadiazole-quaterthiophene

-based copolymers [15]. However, opposite results, i.e. stronger couplings on the top of the acceptor units of the copolymers, have been observed, as well [34].

The relative orientation of the eD and eA compounds in the NF PSC systems is also observed to have a notable effect on the calculated couplings. In the case of the polymer–SMA systems, the strongest electronic couplings are predicted for the most stable, i.e. DA and AA configurations of the DBT-EF-T–ITIC-4F and BDB-T-2F–ITIC-2Cl, respectively (see Publication IV and Table 4.7). However, the most stable, i.e. AA(1) configuration of the polymer–polymer system BDT-TzBI–NDI2OD-T2 has smaller couplings than the DA(2) configuration, which is energetically (by 0.9 kJ mol^{-1}) very close to the AA(1) one. These findings highlight the previously stated fact that electronic couplings can change even by minor displacements of the interacting compounds [91]. It should be noted that, unlike for example in the studies of Wang et al. [15, 18], the full side chains have not been included here in the coupling calculations. While the long alkyl side chains can be expected to impact the preferred relative orientations and the resulting interactions between the eD and eA compounds in the real blend systems [18], the electronic couplings predicted here yield insight into the interactions between different units of the studied compounds.

4.6.2   Charge transfer parameters and rates

The parameters, i.e. electronic couplings, inner reorganization energies, and Gibbs free energies, used for calculating the ED and CR rates at the local interfacial eD–eA complexes are presented in Tables 4.6 and 4.7. The electronic couplings have been discussed in the previous section, so they will not be considered here. Only the results obtained in the blend environments will be presented. However, the values predicted for TQ–PC$_{71}$BM in CHCl$_3$ (Publication III) will be also briefly discussed.

Overall, the global hybrid functionals predict smaller inner reorganization energies than the LRC functionals. In the case of polymer–fullerene system TQ–PC$_{71}$BM, the polarity of the medium does not have much influence on the λ_i values and they are similar in both CHCl$_3$ and blend. The studied system seems to affect, whether the λ_i values predicted for the ED processes are larger than those of the CR processes. For both TQ–PC$_{71}$BM and polymer–SMA system DTB-EF-T–ITIC-4F, the

Table 4.6 Parameters for calculating the charge transfer rates for the ED and CR processes of the TQ–PC$_{71}$BM complexes calculated with different functionals and the 6-31G** basis set in blend.

Functional	Pos. of PC$_{71}$BM	$H_{if,ED}$ (meV)	$H_{if,CR}$ (meV)	$\lambda_{i,ED}$ (eV)	$\lambda_{i,CR}$ (eV)	ΔG°_{ED} (eV)	ΔG°_{CR} (eV)
B3LYP	donor	41.8	50.2	0.14	0.22	0.03	-1.75
	acceptor	29.4	27.7	0.14	0.22	-0.08	-1.64
PBE0	donor	45.5	51.9	0.15	0.23	-0.10	-1.73
	acceptor	32.6	28.9	0.15	0.23	-0.22	-1.65
CAM-B3LYP	donor	63.1	89.5	0.21	0.32	-0.15	-2.12
	acceptor	49.4	41.6	0.21	0.32	-0.24	-2.08
OT-BNL	donor	69.1	95.8	0.19	0.28	-0.08	-1.87
	acceptor	48.3	47.3	0.19	0.28	-0.21	-1.81

$\lambda_{i,ED}$ values are smaller than the $\lambda_{i,CR}$ ones. The opposite, i.e. larger $\lambda_{i,ED}$ values is observed for the polymer–polymer system BDT-TzBI–NDI2OD-T2 and polymer–SMA system BDB-T-2F–ITIC-2Cl. As the contributions of the geometrical changes of the eA compounds to λ_i are the same in both the ED and CR processes (ED: eA → eA$^-$, CR: eA$^-$ → eA), the eD compounds define the differences in the λ_i values for these processes. Thus, it can be concluded that the eD compounds TQ and DTB-EF-T undergo larger geometrical changes upon CR, i.e. going from the cation geometry to that of the neutral compound, than upon ED, i.e. going from the S$_1$ geometry to that of the cation. The opposite applies for BDT-TzBI and BDB-2F-T, which undergo larger changes during ED than CR. The λ_i values predicted for BDB-T-2F–ITIC-2C are quite consistent to those ($\lambda_{i,ED}$ of ca. 0.20 eV and $\lambda_{i,CR}$ of ca. 0.25–0.29 eV) predicted by Wang et al. [19] for the similar systems of BDB-T-2F and methoxy-substituted ITIC (ITIC-OM).

The ED and CR processes of the studied eD–eA systems are predicted to be spontaneous ($\Delta G^\circ < 0$) in the most cases. Within the studied range of the external reorganization energy, the ED processes of TQ–PC$_{71}$BM are predicted to occur in the Marcus normal region ($|\Delta G^\circ_{ED}| < \lambda_{ED}$) in blend, whereas in CHCl$_3$, PBE0 and CAM-B3LYP predict that the ED process takes place in the normal region when $\lambda_s \geq$ 0.14 eV. For the NF PSC systems, there are more variations and only the ED process

Table 4.7 Parameters for calculating the CT rates for the ED and CR processes of the studied NF PSC systems[1] calculated at the OT-ωB97X-D/6-31G** level of theory in blend.

Complex	Configuration	$H_{if,ED}$ (meV)	$H_{if,CR}$ (meV)	$\lambda_{i,ED}$ (eV)	$\lambda_{i,CR}$ (eV)	ΔG°_{ED} (eV)	ΔG°_{CR} (eV)
BDT-TzBI–NDI2OD-T2	DA(2)	37.54	72.74	0.43	0.30	-0.81	-1.70
	AA(1)	16.55	47.76	0.43	0.32	-0.68	-1.81
DBT-EF-T–ITIC-4F	DA	110.91	99.80	0.22	0.30	-0.56	-2.03
	AA	0.35	24.38	0.23	0.32	-0.59	-2.01
BDB-T-2F–ITIC-2Cl	DA	6.87	70.37	0.28	0.24	-0.36	-2.00
	AA	33.82	131.83	0.32	0.30	-0.50	-1.83

[1] For BDT-TzBI–NDI2OD-T2, the configuration, where the donor and acceptor units of the both compounds have been oriented in the same direction, are labeled with (1). The configuration, where the donor and acceptor units have been oriented in the opposite directions, are labeled with (2). See Section 3.1.3 and Publication IV for more detailed information.

of the DA configuration of BDB-T-2F–ITIC-2Cl occurs in the Marcus normal region for the studied range of λ_s. The CR process, in turn, is predicted to take place deep in the Marcus inverted region ($|\Delta G^{\circ}_{CR}| \gg \lambda_{CR}$) for all the studied systems. The ΔG°_{ED} values predicted for BDB-T-2F–ITIC-2Cl are in line with those (-0.45–(-0.11) eV) obtained by Wang et al. [19] for the BDB-T-2F–ITIC-OM systems.

The ED and CR rates for the polymer–fullerene and NF systems calculated as a function of the outer reorganization energy are presented in Figures 4.12 and 4.13 respectively. Generally, all the systems have larger ED rates (up to $10^{12} - 10^{14}$ s^{-1}) than the CR rates ($< 10^{12}$ s^{-1}), although competing CR rates are predicted for TQ–PC$_{71}$BM with larger λ_s (> ca. 0.66 eV). In general, the calculated ED rates are in the same range as those obtained in previous experimental and theoretical studies of similar PSC systems. For example, experimental ED rates of the order of $10^{11} - 10^{12}$ s^{-1} have been observed for TQ–PC$_{61}$BM [193] and other copolymer–PC$_{61}$BM systems [194], whereas theoretical ED rates of the order of $10^{8} - 10^{12}$ s^{-1} have been predicted for the complexes of BDB-T-2F and different ITIC derivatives [19, 195, 196]. With certain values of λ_s (> 0.20–0.40 eV depending on the system), the calculated CR rates are consistent with the previously predicted values for the systems of BDB-T-2F and ITIC derivatives, i.e. $10^{2} - 10^{10}$ s^{-1} [19, 195, 196], whereas vanishing small
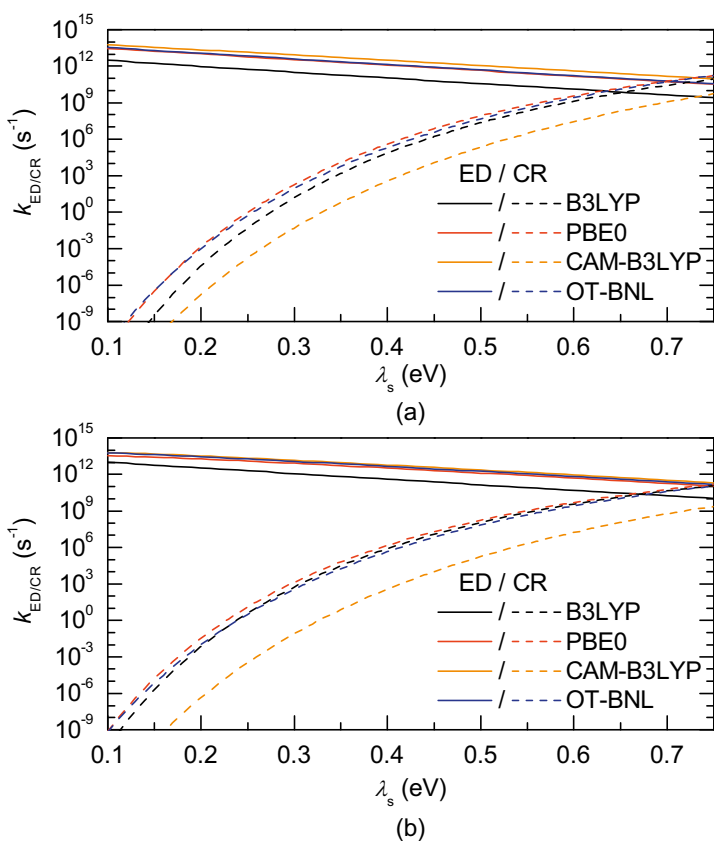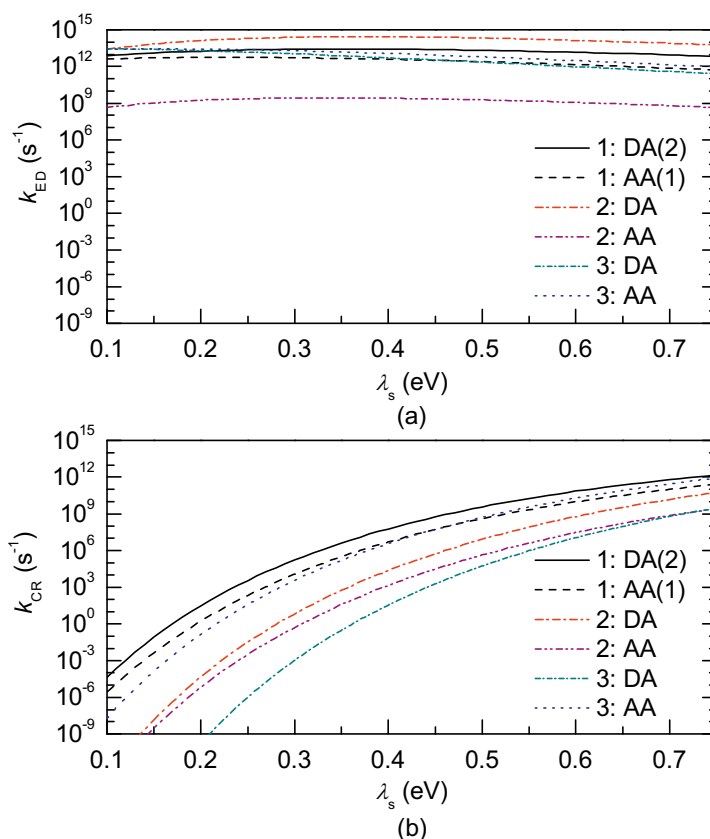
Figure 4.12 Evolutions of the ED and CR rates as the function of λ_s for the TQ–PC$_{71}$BM complexes calculated at the OT-ωB97X-D/6-31G** level of theory in blend. PC$_{71}$BM is either on the top of (a) the donor (3T4Q–PC$_{71}$BM) or (b) acceptor unit of TQ (3Q4T–PC$_{71}$BM). Adapted from [151] with permission from the PCCP Owner Societies.

CR rates are obtained here with smaller λ_s. While both the ED and CR rates are affected by the value of λ_s, it has clearly more pronounced effect on the CR rates. Relatively slow CR rates might be due to that the CR processes of all the studied systems take place deep in the Marcus inverted region ($|\Delta G^\circ_{CR}| \gg \lambda_{CR}$) [167], which may indicate that another CT rate model like the Marcus–Levich–Jortner one [197] would be more suitable for predicting the CR rates of these systems, as the Marcus theory may lead to the underestimated values [19, 194].

In the case of polymer–fullerene system TQ–PC$_{71}$BM, the functional has some effect on the calculated rates: the ED rates increase in the order of B3LYP < PBE0 < OT-BNL < CAM-B3LYP (Figure 4.12). With the CR rates, there is not so clear trend

Figure 4.13 Evolutions of (a) the ED and (b) CR rates as the function of λ_s for the BDT-TzBI–NDI2OD-T2 (1), DTB-EF-T–ITIC-4F (2), and BDB-T-2F–ITIC-2Cl (3) complexes calculated at the OT-ωB97X-D/6-31G** level of theory in blend. Adapted from Publication IV [184] - Published by The Royal Society of Chemistry.

between the global hybrids and LRC functionals and the rates increase in the order of CAM-B3LYP < B3LYP < OT-BNL < PBE0. The rates predicted in 1,2-DCB are slightly faster than those predicted in blend. The effect of the position of $PC_{71}BM$ above TQ on the rates is different in different medium: in 1,2-DCB, faster rates are predicted when $PC_{71}BM$ is on the top of the donor unit of TQ, whereas in the blend, the faster rates are obtained when $PC_{71}BM$ is on the top of the acceptor unit.

In the NF PSC systems, the impact of the relative orientations of the eD and eA compounds can be observed more clearly, as completely different rates are predicted for the different configurations of the same system (Figure 4.13). For example, DBT-EF-T–ITIC-4F is predicted to have the fastest ED rates among the studied fullerene-free

91

eD–eA complexes, when the electron-withdrawing INCN end-group of ITIC-4F is on the top of the BDT donor unit of DTB-EF-T (the DA configuration), whereas the same system has the lowest ED rates, when the end-group of ITIC-4F is on the top of the acceptor unit (the AA configuration). This can be attributed to the different electronic couplings of these configurations, as their other CT parameters are rather similar (Table 4.7). In general, energetically the most stable configurations have the fastest ED and CR rates, the trend similar to the electronic couplings. However, this does not always apply, as the most stable configuration of BDT-TzBI–NDI2OD-T2, i.e. the AA(1) configuration (see Publication IV), has (mostly) the slowest ED and CR rates among the studied configurations of this system. This can be explained by the smaller $|\Delta G^{\circ}_{\text{ED}}|$ value of the AA(1) configuration compared to those of the other configurations of BDT-TzBI–NDI2OD-T2, which together with the moderate ED coupling lead to the slower k_{ED}. Additionally, the larger $|\Delta G^{\circ}_{\text{CR}}|$ value of the AA(1) configuration leads to the slower k_{CR} compared to the other configurations of BDT-TzBI–NDI2OD-T2, because the CR process of AA(1) will occur deeper in the Marcus inverted region.

While no clear conclusions can be drawn from the ED rates of different NF PSC systems, the CR rates predicted for the polymer–SMA systems are slower than those of the polymer–polymer system. Generally, the slower CR rates are observed in those polymer–SMA systems, where the CR occurs deeper in the Marcus inverted region. This could contribute to higher efficiencies predicted for the studied polymer–SMA systems compared to that of the polymer–polymer system. The full-length side groups, which are known to control the interfacial orientations and stacking distances of the eD and eA compounds, have not been considered here. Nevertheless, these results complement the experimental findings for the importance of optimal molecular orientation at the eD–eA interfaces [7]. Furthermore, more insight into the effect of the functional on the CT rates for polymer–fullerene systems has been gained.

5   CONCLUSIONS

In this thesis, a comprehensive set of organic π-conjugated PSC compounds and their interfacial eD–eA complexes were examined by means of DFT and TDDFT methods. The studied systems were based on both the efficient conventional, fullerene-based PSCs and the emerging NF PSCs including the APSC and polymer–SMA systems. The main focus was on the eD compounds incorporated in these devices, i.e. π-conjugated D–A copolymers, but various π-conjugated eA compounds were considered as well. Method-wise, the focus was on defining the performance of the global hybrid, non-tuned LRC, and OT-LRC functionals in predicting the structural and optoelectronic properties of the studied eD and eA compounds and the CT characteristics of their local interfacial complexes. This chapter will highlight all the key findings presented in this work and give some considerations for the future studies.

First, the calculated results on the electronic and structural properties were compared between the finite oligomeric and infinite D–A copolymer models. Among the extrapolation techniques employed for the oligomers, both the original and scaled Kuhn fit yielded HOMO–LUMO gap energies almost identical to the periodic values. The backbones of the oligomeric and periodic models of the D–A copolymer PBDT-TFQ were rather similar, although the periodic model was slightly less planar than the oligomeric one. Overall, the periodic DFT method is a useful tool for determining the structural and electronic properties of infinite D–A copolymers, although the repeating unit should be constructed carefully to ensure its correct repetition. As the periodic method is not yet available for the excited state calculations, the original and scaled Kuhn fits offer suitable alternatives for determining the vertical excitation energies of the infinite copolymers.

Second, the applicability of the global hybrid, non-tuned LRC, and OT-LRC functionals in modeling of the PSC systems was examined. For the individual PSC compounds, the functional had the largest effects on their optoelectronic and intramolecular CT characteristics. In most cases, the OT-LRC functionals improved

the description of IEs, excitation energies, and absorption spectra with respect to the experiments when compared to the other functionals employed. Thus, these results are in line with the previous findings on advantages of the OT-LRC functionals with respect to the global hybrid and non-tuned LRC functionals in describing the PSC compounds.

Furthermore, the combined effect of the functional and dispersion corrections were considered in the local interfacial eD–eA complexes. In the polymer–fullerene systems, the ordering and nature of the excited states relevant to the ED and CR processes were clearly affected by the functional. The global hybrid functionals predicted a complete CT from the eD to eA, while the local excitation was mixing with the CT_1 state when using the the non-tuned LRC and OT-LRC functionals. The inclusion of the dispersion corrections led to the reasonable intermolecular distances between the polymer and fullerene regardless of the functional. In accordance with both the present calculated results and the previous theoretical and experimental evidence of delocalized CT excitation at or near the polymer–fullerene interface, the dispersion corrected OT-LRC functional appears to give the most reasonable prediction of the interfacial characteristics of the PSC systems.

As the third goal of this thesis, the effect of the functional was considered in the CT rate calculations of the polymer–fullerene PSC system. Furthermore, the multi-state treatment was exploited in the electronic coupling calculations of the PSC systems. In most cases, larger electronic couplings and faster CT rates were predicted by the non-tuned LRC and LRC functionals compared to the global hybrids. Inclusion of multiple states led to the more localized description of the CT states by reducing the mixing of the local excitation predicted by the LRC functionals. As the electronic couplings calculated with the GMH scheme seemed to be more sensitive to the calculation method, especially with both the non-tuned LRC and OT-LRC functionals, the FCD scheme is recommended instead.

Finally, the findings on the conventional polymer–fullerene systems were utilized for modeling the recent NF PSC systems. The backbones of the studied NF PSC compounds were governed by the shapes of the backbone units and their conformational preferences. In the eD–eA complexes, the relative position of the eA compound above the eD depended on the studied NF PSC system and had a large effect

on the electronic couplings and the CT rates. In the polymer–polymer system, the CT from the eA compound to the eD compound indicated that the eA compound could contribute to the charge generation in this system. Similar to the polymer-fullerene system, the calculated ED rates were faster than the CR rates for all the NF PSC systems, which is desirable for the efficient charge-generation. No clear trends were observed in the ED rates, but the slower CR rates of the polymer–SMA systems compared to the polymer–polymer system could be one explanation for the higher PCEs in the SMA containing devices. In addition, the OT-LRC functional including the dispersion corrections provided constant electronic coupling values for the studied NF PSC systems regardless of the number of states. Thus, the dispersion corrected OT-LRC functional is recommended when applying the FCD scheme in the studies of PSC systems.

To summarize, the OT-LRC functionals offer a noteworthy alternative for the common global hybrid functionals in theoretical studies of PSC systems. The inclusion of the dispersion corrections is essential for the correct description of the interfacial eD–eA complexes. Thus, the dispersion corrected OT-LRC is highly recommended for the DFT studies of the PSC systems. Moreover, the multi-state treatment should be considered with the GMH and FCD schemes for the electronic coupling calculations when employing either the non-tuned LRC or OT-LRC functionals. While the inclusion of the dispersion corrections seems to provide constant coupling values for the studied NF PSC systems regardless of the number of the states, more calculations would be required to determine, whether this applies to other PSC systems. These findings can be used as guidelines for future theoretical examinations of similar PSC systems. Furthermore, information about the structural and CT characteristics of the individual PSC compounds and their interfaces can be exploited in designing and developing new, more efficient systems. Especially the emerging NF PSCs, which have shown encouraging efficiencies during the past few years, could benefit from the results presented in this thesis.

BIBLIOGRAPHY

[1] S. Chu and A. Majumdar, "Opportunities and challenges for a sustainable energy future", *Nature*, vol. 488, no. 7411, pp. 294–303, 2012, DOI: `10.1038/nature11475`.

[2] O. Krishan and S. Suhag, "An updated review of energy storage systems: Classification and applications in distributed generation power systems incorporating renewable energy resources", *International Journal of Energy Research*, vol. 43, no. 12, pp. 6171–6210, 2019, DOI: `10.1002/er.4285`.

[3] B. Rand and H. Richter, *Organic Solar Cells: Fundamentals, Devices, and Upscaling*, Taylor & Francis Group, LLC, 2014, ISBN: 9789814463669.

[4] M. H. Shubbak, "Advances in solar photovoltaics: Technology review and patent trends", *Renewable and Sustainable Energy Reviews*, vol. 115, p. 109383, 2019, DOI: `https://doi.org/10.1016/j.rser.2019.109383`.

[5] O. Inganäs, "Organic Photovoltaics over Three Decades", *Advanced Materials*, vol. 30, no. 35, p. 1800388, 2018, DOI: `10.1002/adma.201800388`.

[6] H. Zhou, L. Yang, and W. You, "Rational Design of High Performance Conjugated Polymers for Organic Solar Cells", *Macromolecules*, vol. 45, no. 2, pp. 607–632, 2012, DOI: `10.1021/ma201648t`.

[7] C. Lee, S. Lee, G.-U. Kim, W. Lee, and B. J. Kim, "Recent Advances, Design Guidelines, and Prospects of All-Polymer Solar Cells", *Chemical Reviews*, vol. 119, no. 13, pp. 8028–8086, 2019.

[8] C. Risko, M. D. McGehee, and J.-L. Brédas, "A quantum-chemical perspective into low optical-gap polymers for highly-efficient organic solar cells", *Chemical Science*, vol. 2, no. 7, pp. 1200–1218, 2011, DOI: `10.1039/C0SC00642D`.

[9] L. Pandey, C. Doiron, J. S. Sears, and J.-L. Brédas, "Lowest excited states and optical absorption spectra of donor-acceptor copolymers for organic photovoltaics: a new picture emerging from tuned long-range corrected density func-

tionals.", *Physical Chemistry Chemical Physics*, vol. 14, no. 41, pp. 14243–14248, 2012, DOI: `10.1039/c2cp41724c`.

[10]   L. Pandey, C. Risko, J. E. Norton, and J.-L. Brédas, "Donor–Acceptor Copolymers of Relevance for Organic Photovoltaics: A Theoretical Investigation of the Impact of Chemical Structure Modifications on the Electronic and Optical Properties", *Macromolecules*, vol. 45, no. 16, pp. 6405–6414, 2012, DOI: `10.1021/ma301164e`.

[11]   N. Banerji, E. Gagnon, P.-Y. Morgantini, S. Valouch, A. R. Mohebbi, J.-H. Seo, M. Leclerc, and A. J. Heeger, "Breaking Down the Problem: Optical Transitions, Electronic Structure, and Photoconductivity in Conjugated Polymer PCDTBT and in Its Separate Building Blocks", *The Journal of Physical Chemistry C*, vol. 116, no. 21, pp. 11456–11469, 2012, DOI: `10.1021/jp301639e`.

[12]   I. T. Lima, C. Risko, S. G. Aziz, D. A. da Silva Filho, and J.-L. Brédas, "Interplay of alternative conjugated pathways and steric interactions on the electronic and optical properties of donor–acceptor conjugated polymers", *J. Mater. Chem. C*, vol. 2, no. 42, pp. 8873–8879, 2014, DOI: `10.1039/C4TC01264J`.

[13]   N. E. Jackson, K. L. Kohlstedt, B. M. Savoie, M. Olvera de la Cruz, G. C. Schatz, L. X. Chen, and M. A. Ratner, "Conformational Order in Aggregates of Conjugated Polymers", *Journal of the American Chemical Society*, vol. 137, no. 19, pp. 6254–6262, 2015, DOI: `10.1021/jacs.5b00493`.

[14]   M. Niskanen and T. I. Hukka, "Modeling of photoactive conjugated donor-acceptor copolymers: the effect of the exact HF exchange in DFT functionals on geometries and gap energies of oligomer and periodic models.", *Physical chemistry chemical physics*, vol. 16, no. 26, pp. 13294–13305, 2014, DOI: `10.1039/c4cp01165a`.

[15]   T. Wang, X.-K. Chen, A. Ashokan, Z. Zheng, M. K. Ravva, and J.-L. Brédas, "Bulk Heterojunction Solar Cells: Impact of Minor Structural Modifications to the Polymer Backbone on the Polymer–Fullerene Mixing and Packing and on the Fullerene–Fullerene Connecting Network", *Advanced Functional Materials*, vol. 28, no. 14, p. 1705868, 2018, DOI: `10.1002/adfm.201705868`.

[16]   G. Han, Y. Guo, X. Ma, and Y. Yi, "Atomistic Insight Into Donor/Acceptor Interfaces in High-Efficiency Nonfullerene Organic Solar Cells", *Solar RRL*, vol. 2, no. 11, p. 1800190, 2018, DOI: `10.1002/solr.201800190`.

[17]   S. E. Root, N. E. Jackson, S. Savagatrup, G. Arya, and D. J. Lipomi, "Modelling the morphology and thermomechanical behaviour of low-bandgap conjugated polymers and bulk heterojunction films", *Energy Environ. Sci.* Vol. 10, pp. 558–569, 2 2017, DOI: `10.1039/C6EE03456J`.

[18]   T. Wang, M. K. Ravva, and J.-L. Brédas, "Impact of the Nature of the Side-Chains on the Polymer-Fullerene Packing in the Mixed Regions of Bulk Heterojunction Solar Cells", *Advanced Functional Materials*, vol. 26, no. 32, pp. 5913–5921, 2016, DOI: `10.1002/adfm.201601134`.

[19]   T. Wang and J.-L. Brédas, "Organic Solar Cells Based on Non-fullerene Small-Molecule Acceptors: Impact of Substituent Position", *Matter*, vol. 2, no. 1, pp. 119–135, 2020, DOI: `https://doi.org/10.1016/j.matt.2019.10.025`.

[20]   A. Melianas, F. Etzold, T. J. Savenije, F. Laquai, O. Inganäs, and M. Kemerink, "Photo-generated carriers lose energy during extraction from polymer-fullerene solar cells", *Nature Communications*, vol. 6, no. 1, p. 8778, 2015, DOI: `10.1038/ncomms9778`.

[21]   S. S. Zade and M. Bendikov, "From oligomers to polymer: convergence in the HOMO–LUMO gaps of conjugated oligomers.", *Organic letters*, vol. 8, no. 23, pp. 5243–6, 2006, DOI: `10.1021/ol062030y`.

[22]   T. M. Pappenfus, J. A. Schmidt, R. E. Koehn, and J. D. Alia, "PBC-DFT Applied to Donor–Acceptor Copolymers in Organic Solar Cells: Comparisons between Theoretical Methods and Experimental Data", *Macromolecules*, vol. 44, no. 7, pp. 2354–2357, 2011, DOI: `10.1021/ma1026498`.

[23]   Y. Li, T. Pullerits, M. Zhao, and M. Sun, "Theoretical Characterization of the $PC_{60}BM$:PDDTT Model for an Organic Solar Cell", *The Journal of Physical Chemistry C*, vol. 115, no. 44, pp. 21865–21873, 2011, DOI: `10.1021/jp2040696`.

[24]   L. Zhang, M. Yu, H. Zhao, Y. Wang, and J. Gao, "Theoretical investigations on the electronic and optical characteristics of fused-ring homopolymers: Comparison of oligomer method and PBC-DFT method", *Chemical Physics Letters*, vol. 570, pp. 153–158, 2013, DOI: `http://dx.doi.org/10.1016/j.cplett.2013.03.068`.

[25]   S. Li, L. Ye, W. Zhao, H. Yan, B. Yang, D. Liu, W. Li, H. Ade, and J. Hou, "A Wide Band Gap Polymer with a Deep Highest Occupied Molecular Orbital Level Enables 14.2% Efficiency in Polymer Solar Cells", *Journal of the American Chemical Society*, vol. 140, no. 23, pp. 7159–7167, 2018, DOI: `10.1021/jacs.8b02695`.

[26]   T. Körzdörfer and J.-L. Brédas, "Organic electronic materials: recent advances in the DFT description of the ground and excited states using tuned range-separated hybrid functionals.", *Accounts of chemical research*, vol. 47, no. 11, pp. 3284–3291, 2014, DOI: `10.1021/ar500021t`.

[27]   A. Ruzsinszky, J. P. Perdew, G. I. Csonka, O. A. Vydrov, and G. E. Scuseria, "Spurious fractional charge on dissociated atoms: Pervasive and resilient self-interaction error of common density functionals", *The Journal of Chemical Physics*, vol. 125, no. 19, p. 194112, 2006, DOI: `10.1063/1.2387954`.

[28]   P. Mori-Sánchez, A. J. Cohen, and W. Yang, "Many-electron self-interaction error in approximate density functionals.", *The Journal of chemical physics*, vol. 125, no. 20, p. 201102, 2006, DOI: `10.1063/1.2403848`.

[29]   H. Iikura, T. Tsuneda, T. Yanai, and K. Hirao, "A long-range correction scheme for generalized-gradient-approximation exchange functionals", *The Journal of Chemical Physics*, vol. 115, no. 8, p. 3540, 2001, DOI: `10.1063/1.1383587`.

[30]   J.-D. Chai and M. Head-Gordon, "Systematic optimization of long-range corrected hybrid density functionals", *The Journal of Chemical Physics*, vol. 128, no. 8, p. 084106, 2008, DOI: `10.1063/1.2834918`.

[31]   J.-D. Chai and M. Head-Gordon, "Long-range corrected hybrid density functionals with damped atom-atom dispersion corrections.", *Physical chemistry chemical physics*, vol. 10, no. 44, pp. 6615–6620, 2008, DOI: `10.1039/b810189b`.

[32]   T. Yanai, D. P. Tew, and N. C. Handy, "A new hybrid Exchange–Correlation functional using the Coulomb-attenuating method (CAM-B3LYP)", *Chemical Physics Letters*, vol. 393, no. 1-3, pp. 51–57, 2004, DOI: `10.1016/j.cplett.2004.06.011`.

[33]   T. Körzdörfer, R. M. Parrish, J. S. Sears, C. D. Sherrill, and J.-L. Brédas, "On the relationship between bond-length alternation and many-electron self-interaction error.", *The Journal of chemical physics*, vol. 137, no. 12, p. 124305, 2012, DOI: `10.1063/1.4752431`.

[34] L. Pandey, "Theoretical studies of the structure-property relationships of hole- and electron-transport materials for organic photovoltaic applications.", PhD thesis, Georgia Institute of Technology, 2013, p. 155.

[35] Z. Zheng, Q. Hu, S. Zhang, D. Zhang, J. Wang, S. Xie, R. Wang, Y. Qin, W. Li, L. Hong et al., "A Highly Efficient Non-Fullerene Organic Solar Cell with a Fill Factor over 0.80 Enabled by a Fine-Tuned Hole-Transporting Layer", *Advanced Materials*, vol. 30, no. 34, p. 1801801, 2018, DOI: `10.1002/adma.201801801`.

[36] J. Gierschner, J. Cornil, and H.-J. Egelhaaf, "Optical Bandgaps of π-Conjugated Organic Materials at the Polymer Limit: Experiment and Theory", *Advanced Materials*, vol. 19, no. 2, pp. 173–191, 2007, DOI: `10.1002/adma.200600277`.

[37] S. S. Zade, N. Zamoshchik, and M. Bendikov, "From Short Conjugated Oligomers to Conjugated Polymers. Lessons from Studies on Long Conjugated Oligomers", *Accounts of Chemical Research*, vol. 44, no. 1, pp. 14–24, 2011, DOI: `10.1021/ar1000555`.

[38] A. D. McNaught and A. Wilkinson, *IUPAC. Compendium of Chemical Terminology, 2nd ed. (the "Gold Book")*, Oxford, 1997, Online version (2019-), URL: `https://doi.org/10.1351/goldbook`.

[39] H. Meier, U. Stalmach, and H. Kolshorn, "Effective conjugation length and UV/vis spectra of oligomers", *Acta Polymerica*, vol. 48, no. 9, pp. 379–384, 1997, DOI: `10.1002/actp.1997.010480905`.

[40] V. Manninen, M. Niskanen, T. I. Hukka, F. Pasker, S. Claus, S. Höger, J. Baek, T. Umeyama, H. Imahori, and H. Lemmetyinen, "Conjugated donor-acceptor (D-A) copolymers in inverted organic solar cells - a combined experimental and modelling study", *Journal of Materials Chemistry A*, vol. 1, no. 25, pp. 7451–7462, 2013, DOI: `10.1039/C3TA10686A`.

[41] K. N. Kudin and G. E. Scuseria, "A fast multipole algorithm for the efficient treatment of the Coulomb problem in electronic structure calculations of periodic systems with Gaussian orbitals", *Chemical Physics Letters*, vol. 289, no. 5, pp. 611–616, 1998, DOI: `https://doi.org/10.1016/S0009-2614(98)00468-0`.

[42]   K. N. Kudin and G. E. Scuseria, "Linear-scaling density-functional theory with Gaussian orbitals and periodic boundary conditions: Efficient evaluation of energy and forces via the fast multipole method", *Physical Review B*, vol. 61, no. 24, pp. 16440–16453, 2000, DOI: `10.1103/PhysRevB.61.16440`.

[43]   T. Kastinen, M. Niskanen, C. Risko, O. Cramariuc, and T. I. Hukka, "Intrinsic Properties of Two Benzodithiophene-Based Donor–Acceptor Copolymers Used in Organic Solar Cells: A Quantum-Chemical Approach", *The Journal of Physical Chemistry A*, vol. 120, no. 7, pp. 1051–1064, 2016, DOI: `10.1021/acs.jpca.5b08465`.

[44]   W. Kuhn, "Über das Absorptionsspektrum der Polyene", *Helvetica Chimica Acta*, vol. 31, no. 6, pp. 1780–1799, 1948, DOI: `10.1002/hlca.19480310644`.

[45]   C.-R. Zhang, J. S. Sears, B. Yang, S. G. Aziz, V. Coropceanu, and J.-L. Brédas, "Theoretical Study of the Local and Charge-Transfer Excitations in Model Complexes of Pentacene-C_{60} Using Tuned Range-Separated Hybrid Functionals", *Journal of Chemical Theory and Computation*, vol. 10, no. 6, pp. 2379–2388, 2014, DOI: `10.1021/ct500259m`.

[46]   D. Niedzialek, I. Duchemin, T. B. De Queiroz, S. Osella, A. Rao, R. Friend, X. Blase, S. Kümmel, and D. Beljonne, "First Principles Calculations of Charge Transfer Excitations in Polymer-Fullerene Complexes: Influence of Excess Energy", *Advanced Functional Materials*, vol. 25, no. 13, pp. 1972–1984, 2015, DOI: `10.1002/adfm.201402682`.

[47]   A. Farazdel, M. Dupuis, E. Clementi, and A. Aviram, "Electric-field induced intramolecular electron transfer in spiro π-electron systems and their suitability as molecular electronic devices. A theoretical study", *Journal of the American Chemical Society*, vol. 112, no. 11, pp. 4206–4214, 1990, DOI: `10.1021/ja00167a016`.

[48]   R. J. Cave and M. D. Newton, "Generalization of the Mulliken-Hush treatment for the calculation of electron transfer matrix elements", *Chemical Physics Letters*, vol. 249, no. 1-2, pp. 15–19, 1996, DOI: `10.1016/0009-2614(95)01310-5`.

[49]   R. J. Cave and M. D. Newton, "Calculation of electronic coupling matrix elements for ground and excited state electron transfer reactions: Comparison of the generalized Mulliken-Hush and block diagonalization methods", *Journal*

of Chemical Physics, vol. 106, no. 22, pp. 9213–9226, 1997, DOI: `10.1063/1.474023`.

[50]   A. A. Voityuk and N. Rösch, "Fragment charge difference method for estimating donor–acceptor electronic coupling: Application to DNA π-stacks", *The Journal of Chemical Physics*, vol. 117, no. 12, pp. 5607–5616, 2002, DOI: `10.1063/1.1502255`.

[51]   C.-H. Yang and C.-P. Hsu, "A multi-state fragment charge difference approach for diabatic states in electron transfer: Extension and automation", *Journal of Chemical Physics*, vol. 139, no. 15, p. 154104, 2013, DOI: `10.1063/1.4824906`.

[52]   M. Rust, J. Lappe, and R. J. Cave, "Multistate effects in calculations of the electronic coupling element for electron transfer using the generalized Mulliken-Hush method", *Journal of Physical Chemistry A*, vol. 106, no. 15, pp. 3930–3940, 2002, DOI: `10.1021/jp0142886`.

[53]   S.-J. Lee, H.-C. Chen, Z.-Q. You, K.-L. Liu, T. J. Chow, I.-C. Chen, and C.-P. Hsu, "Theoretical characterization of photoinduced electron transfer in rigidly linked donor-acceptor molecules: the fragment charge difference and the generalized Mulliken-Hush schemes", *Molecular Physics*, vol. 108, no. 19-20, pp. 2775–2789, 2010, DOI: `10.1080/00268976.2010.525538`.

[54]   Y. Li, Y. Feng, and M. Sun, "Photoinduced Charge Transport in a BHJ Solar Cell Controlled by an External Electric Field", *Scientific Reports*, vol. 5, p. 13970, 2015, DOI: `10.1038/srep13970`.

[55]   D. Qian, Z. Zheng, H. Yao, W. Tress, T. R. Hopper, S. Chen, S. Li, J. Liu, S. Chen, J. Zhang et al., "Design rules for minimizing voltage losses in high-efficiency organic solar cells", *Nature Materials*, vol. 17, no. 8, pp. 703–709, 2018, DOI: `10.1038/s41563-018-0128-z`.

[56]   P. Cheng, G. Li, X. Zhan, and Y. Yang, "Next-generation organic photovoltaics based on non-fullerene acceptors", *Nature Photonics*, vol. 12, no. 3, pp. 131–142, 2018, DOI: `10.1038/s41566-018-0104-9`.

[57]   J. Hou, O. Inganas, R. H. Friend, and F. Gao, "Organic solar cells based on non-fullerene acceptors", *Nature Materials*, vol. 17, no. 2, pp. 119–128, 2018, DOI: `10.1038/NMAT5063`.

[58]   H. Sun, F. Chen, and Z.-K. Chen, "Recent progress on non-fullerene acceptors for organic photovoltaics", *Materials Today*, vol. 24, pp. 94–118, 2019, DOI: `https://doi.org/10.1016/j.mattod.2018.09.004`.

[59]   L. Lu, T. Zheng, Q. Wu, A. M. Schneider, D. Zhao, and L. Yu, "Recent Advances in Bulk Heterojunction Polymer Solar Cells", *Chemical Reviews*, vol. 115, pp. 12666–12731, 2015, DOI: `10.1021/acs.chemrev.5b00098`.

[60]   J. Zhao, Y. Li, G. Yang, K. Jiang, H. Lin, H. Ade, W. Ma, and H. Yan, "Efficient organic solar cells processed from hydrocarbon solvents", *Nature Energy*, vol. 1, no. 2, p. 15027, 2016, DOI: `10.1038/NENERGY.2015.27`.

[61]   Y. Jin, Z. Chen, M. Xiao, J. Peng, B. Fan, L. Ying, G. Zhang, X.-F. Jiang, Q. Yin, Z. Liang et al., "Thick Film Polymer Solar Cells Based on Naphtho[1,2-c:5,6-c]bis[1,2,5]thiadiazole Conjugated Polymers with Efficiency over 11%", *Advanced Energy Materials*, vol. 7, no. 22, p. 1700944, 2017, DOI: `10.1002/aenm.201700944`.

[62]   J.-L. Brédas, "Mind the gap!", *Materials Horizons*, vol. 1, no. 1, pp. 17–19, 2014, DOI: `10.1039/c3mh00098b`.

[63]   A. Kohler and H. Bassler, *Electronic Processes in Organic Semiconductors*, John Wiley & Sons, Ltd, 2015, ISBN: 9783527685172.

[64]   G. Yu, J. Gao, J. C. Hummelen, F. Wudl, and A. J. Heeger, "Polymer Photovoltaic Cells: Enhanced Efficiencies via a Network of Internal Donor-Acceptor Heterojunctions", *Science*, vol. 270, no. 5243, pp. 1789–1791, 1995, DOI: `10.1126/science.270.5243.1789`.

[65]   L. Dou, Y. Liu, Z. Hong, G. Li, and Y. Yang, "Low-Bandgap Near-IR Conjugated Polymers/Molecules for Organic Electronics", *Chemical Reviews*, vol. 115, no. 23, pp. 12633–12665, 2015, DOI: `10.1021/acs.chemrev.5b00165`.

[66]   A. T. Kleinschmidt, S. E. Root, and D. J. Lipomi, "Poly(3-hexylthiophene) (P3HT): fruit fly or outlier in organic solar cell research?", *J. Mater. Chem. A*, vol. 5, pp. 11396–11400, 23 2017, DOI: `10.1039/C6TA08317J`.

[67]   M. C. Scharber, D. Mühlbacher, M. Koppe, P. Denk, C. Waldauf, A. J. Heeger, and C. J. Brabec, "Design Rules for Donors in Bulk-Heterojunction Solar Cells–Towards 10 % Energy-Conversion Efficiency", *Advanced Materials*, vol. 18, no. 6, pp. 789–794, 2006, DOI: `10.1002/adma.200501717`.

[68] E. E. Havinga, W. ten Hoeve, and H. Wynberg, "A new class of small band gap organic polymer conductors", *Polymer Bulletin*, vol. 29, no. 1-2, pp. 119–126, 1992, DOI: `10.1007/BF00558045`.

[69] E. Havinga, W. ten Hoeve, and H. Wynberg, "Alternate donor-acceptor small-band-gap semiconducting polymers; Polysquaraines and polycroconaines", *Synthetic Metals*, vol. 55, no. 1, pp. 299–306, 1993, DOI: `https://doi.org/10.1016/0379-6779(93)90949-W`.

[70] D. Beljonne and J. Cornil, *Molecular Quantum Mechanics*, Berlin Heidelberg: Springer-Verlag, 2014, ISBN: 9783662438749.

[71] N. C. Miller, E. Cho, R. Gysel, C. Risko, V. Coropceanu, C. E. Miller, S. Sweetnam, A. Sellinger, M. Heeney, I. McCulloch et al., "Factors Governing Intercalation of Fullerenes and Other Small Molecules Between the Side Chains of Semiconducting Polymers Used in Solar Cells", *Advanced Energy Materials*, vol. 2, no. 10, pp. 1208–1217, 2012, DOI: `10.1002/aenm.201200392`.

[72] S. C. Price, A. C. Stuart, L. Yang, H. Zhou, and W. You, "Fluorine substituted conjugated polymer of medium band gap yields 7% efficiency in polymer-fullerene solar cells", *Journal of the American Chemical Society*, vol. 133, no. 12, pp. 4625–4631, 2011, DOI: `10.1021/ja112595`.

[73] H. J. Son, W. Wang, T. Xu, Y. Liang, Y. Wu, G. Li, and L. Yu, "Synthesis of fluorinated polythienothiophene-*co*-benzodithiophenes and effect of fluorination on the photovoltaic properties", *Journal of the American Chemical Society*, vol. 133, no. 6, pp. 1885–1894, 2011, DOI: `10.1021/ja108601g`.

[74] N. S. Sariciftci, L. Smilowitz, A. J. Heeger, and F. Wudl, "Photoinduced electron transfer from a conducting polymer to buckminsterfullerene", *Science*, vol. 258, no. 5087, pp. 1474–1476, 1992, DOI: `10.1126/science.258.5087.1474`.

[75] J. J. Halls, C. A. Walsh, N. C. Greenham, E. A. Marseglia, R. H. Friend, S. C. Moratti, and A. B. Holmes, "Efficient photodiodes from interpenetrating polymer networks", *Nature*, vol. 376, no. 6540, pp. 498–500, 1995, DOI: `10.1038/376498a0`.

[76]   G. Yu and A. J. Heeger, "Charge separation and photovoltaic conversion in polymer composites with internal donor/acceptor heterojunctions", *Journal of Applied Physics*, vol. 78, no. 7, pp. 4510–4515, 1995, DOI: `10.1063/1.359792`.

[77]   M. Sommer, "Conjugated polymers based on naphthalene diimide for organic electronics", *J. Mater. Chem. C*, vol. 2, pp. 3088–3098, 17 2014, DOI: `10.1039/C3TC31755B`.

[78]   X. Guo and M. D. Watson, "Conjugated Polymers from Naphthalene Bisimide", *Organic Letters*, vol. 10, no. 23, pp. 5333–5336, 2008, DOI: `10.1021/ol801918y`.

[79]   H. Yan, Z. Chen, Y. Zheng, C. Newman, J. R. Quinn, F. Dötz, M. Kastler, and A. Facchetti, "A high-mobility electron-transporting polymer for printed transistors", *Nature*, vol. 457, no. 7230, pp. 679–686, 2009, DOI: `10.1038/nature07727`.

[80]   B. Fan, L. Ying, P. Zhu, F. Pan, F. Liu, J. Chen, F. Huang, and Y. Cao, "All-Polymer Solar Cells Based on a Conjugated Polymer Containing Siloxane-Functionalized Side Chains with Efficiency over 10%", *Advanced Materials*, vol. 29, no. 47, p. 1703906, 2017, DOI: `10.1002/adma.201703906`.

[81]   Y. Lin, J. Wang, Z.-G. Zhang, H. Bai, Y. Li, D. Zhu, and X. Zhan, "An Electron Acceptor Challenging Fullerenes for Efficient Polymer Solar Cells", *Advanced Materials*, vol. 27, no. 7, pp. 1170–1174, 2015, DOI: `10.1002/adma.201404317`.

[82]   L. Meng, Y. Zhang, X. Wan, C. Li, X. Zhang, Y. Wang, X. Ke, Z. Xiao, L. Ding, R. Xia et al., "Organic and solution-processed tandem solar cells with 17.3% efficiency", *Science*, vol. 361, no. 6407, pp. 1094–1098, 2018, DOI: `10.1126/science.aat2612`.

[83]   T. M. Clarke and J. R. Durrant, "Charge Photogeneration in Organic Solar Cells", *Chemical Reviews*, vol. 110, no. 11, pp. 6736–6767, 2010, DOI: `10.1021/cr900271s`.

[84]   J.-L. Brédas, "When Electrons Leave Holes in Organic Solar Cells", *Science*, vol. 343, no. 6170, pp. 492–493, 2014, DOI: `10.1126/science.1249230`.

[85] M. C. Scharber and N. S. Sariciftci, "Efficiency of bulk-heterojunction organic solar cells", *Progress in Polymer Science*, vol. 38, no. 12, pp. 1929–1940, 2013, DOI: `10.1016/j.progpolymsci.2013.05.001`.

[86] K. M. Pelzer and S. B. Darling, "Charge generation in organic photovoltaics: a review of theory and computation", *Mol. Syst. Des. Eng.* Vol. 1, no. 1, pp. 10–24, 2016, DOI: `10.1039/C6ME00005C`.

[87] D. M. Stoltzfus, J. E. Donaghey, A. Armin, P. E. Shaw, P. L. Burn, and P. Meredith, "Charge Generation Pathways in Organic Solar Cells: Assessing the Contribution from the Electron Acceptor", *Chemical Reviews*, vol. 116, no. 21, pp. 12920–12955, 2016, DOI: `10.1021/acs.chemrev.6b00126`.

[88] H. Oberhofer, K. Reuter, and J. Blumberger, "Charge Transport in Molecular Materials: An Assessment of Computational Methods", *Chemical Reviews*, vol. 117, no. 15, pp. 10319–10357, 2017, DOI: `10.1021/acs.chemrev.7b00086`.

[89] C. Wang, F. Wang, X. Yang, Q. Li, and Z. Shuai, "Theoretical comparative studies of charge mobilities for molecular materials: Pet versus bnpery", *Organic Electronics*, vol. 9, no. 5, pp. 635–640, 2008, DOI: `https://doi.org/10.1016/j.orgel.2008.04.003`.

[90] P. Song, Y. Li, F. Ma, T. Pullerits, and M. Sun, "Photoinduced Electron Transfer in Organic Solar Cells", *The Chemical Record*, vol. 16, no. 2, pp. 734–753, 2016, DOI: `10.1002/tcr.201500244`.

[91] J. L. Brédas, D. Beljonne, V. Coropceanu, and J. Cornil, "Charge-transfer and energy-transfer processes in π-conjugated oligomers and polymers: A molecular picture", *Chemical Reviews*, vol. 104, no. 11, pp. 4971–5003, 2004, DOI: `10.1021/cr040084k`.

[92] R. A. Marcus, "On the Theory of Oxidation-Reduction Reactions Involving Electron Transfer. I", *The Journal of Chemical Physics*, vol. 24, no. 5, pp. 966–978, 1956, DOI: `10.1063/1.1742723`.

[93] R. A. Marcus and N. Sutin, "Electron Transfers in Chemistry and Biology", *BBA Reviews On Bioenergetics*, vol. 811, no. 3, pp. 265–322, 1985, DOI: `10.1016/0304-4173(85)90014-X`.

[94] R. A. Marcus, "Electron transfer reactions in chemistry. Theory and experiment", *Rev. Mod. Phys.* Vol. 65, pp. 599–610, 3 1993, DOI: `10.1103/RevModPhys.65.599`.

[95] C. Leng, H. Qin, Y. Si, and Y. Zhao, "Theoretical Prediction of the Rate Constants for Exciton Dissociation and Charge Recombination to a Triplet State in PCPDTBT with Different Fullerene Derivatives", *The Journal of Physical Chemistry C*, vol. 118, no. 4, pp. 1843–1855, 2014, DOI: `10.1021/jp410562u`.

[96] Q. Wu and T. Van Voorhis, "Extracting electron transfer coupling elements from constrained density functional theory", *Journal of Chemical Physics*, vol. 125, no. 16, p. 164105, 2006, DOI: `10.1063/1.2360263`.

[97] E. F. Valeev, V. Coropceanu, D. A. da Silva Filho, S. Salman, and J.-L. Brédas, "Effect of Electronic Polarization on Charge-Transport Parameters in Molecular Organic Semiconductors.", *Journal of the American Chemical Society*, vol. 128, no. 30, pp. 9882–9886, 2006, DOI: `10.1021/ja061827h`.

[98] J. M. Foster and S. F. Boys, "Canonical configurational interaction procedure", *Reviews of Modern Physics*, vol. 32, no. 2, pp. 300–302, 1960, DOI: `10.1103/RevModPhys.32.300`.

[99] C. Edmiston and K. Ruedenberg, "Localized atomic and molecular orbitals", *Reviews of Modern Physics*, vol. 35, no. 3, pp. 457–465, 1963, DOI: `10.1103/RevModPhys.35.457`.

[100] T. Pacher, L. S. Cederbaum, and H. Köppel, "Approximately diabatic states from block diagonalization of the electronic Hamiltonian", *The Journal of Chemical Physics*, vol. 89, no. 12, pp. 7367–7381, 1988, DOI: `10.1063/1.455268`.

[101] Y. Mo, J. Gao, and S. D. Peyerimhoff, "Energy decomposition analysis of intermolecular interactions using a block-localized wave function approach", *Journal of Chemical Physics*, vol. 112, no. 13, pp. 5530–5538, 2000, DOI: `10.1063/1.481185`.

[102] F. Jensen, *Introduction to Computational Chemistry*, England: John Wiley & Sons, Ltd., 2007, ISBN: 9780470011867.

[103] C. Cramer, *Essentials of Computational Chemistry: Theories and Models*, Wiley, 2005, ISBN: 9780470091838.

[104] P. Atkins and R. Friedman, *Molecular Quantum Mechanics*, New York: Oxford University Press Inc., 2005, ISBN: 0199274983.

[105] J. B. Foresman and Æ. Frisch, *Exploring Chemistry with Electronic Structure Methods, 3rd ed.* Wallingford, CT: Gaussian, Inc., 2015, ISBN: 978-1-935522-03-4.

[106] M. Born and R. Oppenheimer, "Zur Quantentheorie der Molekeln", *Annalen der Physik*, vol. 389, no. 20, pp. 457–484, 1927, DOI: `10.1002/andp.19273892002`.

[107] J. A. Pople, R. Seeger, and R. Krishnan, "Variational configuration interaction methods and comparison with perturbation theory", *International Journal of Quantum Chemistry*, vol. 12, no. S11, pp. 149–163, 1977, DOI: `10.1002/qua.560120820`.

[108] R. Krishnan, H. B. Schlegel, and J. A. Pople, "Derivative studies in configuration–interaction theory", *The Journal of Chemical Physics*, vol. 72, no. 8, pp. 4654–4655, 1980, DOI: `10.1063/1.439708`.

[109] R. J. Bartlett and G. D. Purvis, "Many-body perturbation theory, coupled-pair many-electron theory, and the importance of quadruple excitations for the correlation problem", *International Journal of Quantum Chemistry*, vol. 14, no. 5, pp. 561–581, 1978, DOI: `10.1002/qua.560140504`.

[110] C. Møller and M. S. Plesset, "Note on an Approximation Treatment for Many-Electron Systems", *Phys. Rev.* Vol. 46, pp. 618–622, 7 1934, DOI: `10.1103/PhysRev.46.618`.

[111] N. E. Jackson, B. M. Savoie, K. L. Kohlstedt, M. Olvera de la Cruz, G. C. Schatz, L. X. Chen, and M. A. Ratner, "Controlling Conformations of Conjugated Polymers and Small Molecules: The Role of Nonbonding Interactions", *Journal of the American Chemical Society*, vol. 135, no. 28, pp. 10475–10483, 2013, DOI: `10.1021/ja403667s`.

[112] P. Hohenberg and W. Kohn, "Inhomogeneous electron gas", *Physical Review*, vol. 136, no. 3B, B864–B871, 1964, DOI: `10.1103/PhysRev.136.B864`.

[113] W. Kohn and L. J. Sham, "Self-consistent equations including exchange and correlation effects", *Physical Review*, vol. 140, no. 4A, A1133–A1138, 1965, DOI: `10.1103/PhysRev.140.A1133`.

[114]   G. E. Scuseria, "Linear Scaling Density Functional Calculations with Gaussian Orbitals", *The Journal of Physical Chemistry A*, vol. 103, no. 25, pp. 4782–4790, 1999, DOI: `10.1021/jp990629s`.

[115]   E. Runge and E. K. U. Gross, "Density-Functional Theory for Time-Dependent Systems", *Phys. Rev. Lett.* Vol. 52, pp. 997–1000, 12 1984, DOI: `10.1103/PhysRevLett.52.997`.

[116]   S. Hirata and M. Head-Gordon, "Time-dependent density functional theory within the Tamm–Dancoff approximation", *Chemical Physics Letters*, vol. 314, no. 3, pp. 291–299, 1999, DOI: `https://doi.org/10.1016/S0009-2614(99)01149-5`.

[117]   A. D. Becke, "Density functional calculations of molecular bond energies", *The Journal of Chemical Physics*, vol. 84, no. 8, pp. 4524–4529, 1986, DOI: `10.1063/1.450025`.

[118]   A. D. Becke, "Density-functional exchange-energy approximation with correct asymptotic behavior", *Physical Review A*, vol. 38, pp. 3098–3100, 6 1988, DOI: `10.1103/PhysRevA.38.3098`.

[119]   C. Lee, W. Yang, and R. G. Parr, "Development of the Colle-Salvetti correlation-energy formula into a functional of the electron density", *Physical Review B*, vol. 37, pp. 785–789, 1988, DOI: `10.1103/PhysRevB.37.785`.

[120]   A. D. Becke, "Density-functional thermochemistry. III. The role of exact exchange", *The Journal of Chemical Physics*, vol. 98, no. 7, pp. 5648–5652, 1993, DOI: `10.1063/1.464913`.

[121]   P. J. Stephens, F. J. Devlin, C. F. Chabalowski, and M. J. Frisch, "Ab Initio Calculation of Vibrational Absorption and Circular Dichroism Spectra Using Density Functional Force Fields", *The Journal of Physical Chemistry*, vol. 98, no. 45, pp. 11623–11627, 1994, DOI: `10.1021/j100096a001`.

[122]   S. H. Vosko, L. Wilk, and M. Nusair, "Accurate spin-dependent electron liquid correlation energies for local spin density calculations: a critical analysis", *Canadian Journal of Physics*, vol. 58, no. 8, pp. 1200–1211, 1980, DOI: `10.1139/p80-159`.

[123]   C. Adamo and V. Barone, "Toward reliable density functional methods without adjustable parameters: The PBE0 model", *The Journal of Chemical Physics*, vol. 110, no. 13, pp. 6158–6170, 1999, DOI: `10.1063/1.478522`.

[124]   M. Ernzerhof and G. E. Scuseria, "Assessment of the Perdew–Burke–Ernzerhof exchange-correlation functional", *The Journal of Chemical Physics*, vol. 110, no. 11, pp. 5029–5036, 1999, DOI: `10.1063/1.478401`.

[125]   J. P. Perdew, K. Burke, and M. Ernzerhof, "Generalized Gradient Approximation Made Simple", *Phys. Rev. Lett.* Vol. 77, pp. 3865–3868, 18 1996, DOI: `10.1103/PhysRevLett.77.3865`.

[126]   J. P. Perdew, K. Burke, and M. Ernzerhof, "Generalized Gradient Approximation Made Simple [Phys. Rev. Lett. 77, 3865 (1996)]", *Phys. Rev. Lett.* Vol. 78, pp. 1396–1396, 7 1997, DOI: `10.1103/PhysRevLett.78.1396`.

[127]   J. P. Perdew and W. Yue, "Accurate and simple density functional for the electronic exchange energy: Generalized gradient approximation", *Phys. Rev. B*, vol. 33, pp. 8800–8802, 12 1986, DOI: `10.1103/PhysRevB.33.8800`.

[128]   M. G. Medvedev, I. S. Bushmarinov, J. Sun, J. P. Perdew, and K. A. Lyssenko, "Density functional theory is straying from the path toward the exact functional", *Science*, vol. 355, no. 6320, pp. 49–52, 2017.

[129]   P. Bleiziffer, K. Schaller, and S. Riniker, "Machine Learning of Partial Charges Derived from High-Quality Quantum-Mechanical Calculations", *Journal of Chemical Information and Modeling*, vol. 58, no. 3, pp. 579–590, 2018, DOI: `10.1021/acs.jcim.7b00663`.

[130]   T. Körzdörfer, J. S. Sears, C. Sutton, and J.-L. Brédas, "Long-range corrected hybrid functionals for π-conjugated systems: dependence of the range-separation parameter on conjugation length.", *The Journal of chemical physics*, vol. 135, no. 20, p. 204107, 2011, DOI: `10.1063/1.3663856`.

[131]   T. Stein, H. Eisenberg, L. Kronik, and R. Baer, "Fundamental gaps in finite systems from eigenvalues of a generalized Kohn-Sham method.", *Physical review letters*, vol. 105, no. 26, p. 266802, 2010, DOI: `10.1103/PhysRevLett.105.266802`.

[132]   C. Sutton, T. Körzdörfer, M. T. Gray, M. Brunsfeld, R. M. Parrish, C. D. Sherrill, J. S. Sears, and J.-L. Brédas, "Accurate description of torsion potentials in conjugated polymers using density functionals with reduced self-interaction error.", *The Journal of chemical physics*, vol. 140, no. 5, p. 054310, 2014, DOI: `10.1063/1.4863218`.

[133]   A. Savin and H.-J. Flad, "Density functionals for the Yukawa electron-electron interaction", *International Journal of Quantum Chemistry*, vol. 56, no. 4, pp. 327–332, 1995, DOI: `10.1002/qua.560560417`.

[134]   T. Leininger, H. Stoll, H.-J. Werner, and A. Savin, "Combining long-range configuration interaction with short-range density functionals", *Chemical Physics Letters*, vol. 275, no. 3-4, pp. 151–160, 1997, DOI: `10.1016/S0009-2614(97)00758-6`.

[135]   J. Heyd, G. E. Scuseria, and M. Ernzerhof, "Hybrid functionals based on a screened Coulomb potential", *The Journal of Chemical Physics*, vol. 118, no. 18, p. 8207, 2003, DOI: `10.1063/1.1564060`.

[136]   J. Heyd, G. E. Scuseria, and M. Ernzerhof, "Erratum: "Hybrid functionals based on a screened Coulomb potential" [J. Chem. Phys. 118, 8207 (2003)]", *The Journal of Chemical Physics*, vol. 124, no. 21, p. 219906, 2006, DOI: `10.1063/1.2204597`.

[137]   A. V. Krukau, O. A. Vydrov, A. F. Izmaylov, and G. E. Scuseria, "Influence of the exchange screening parameter on the performance of screened hybrid functionals.", *The Journal of chemical physics*, vol. 125, no. 22, p. 224106, 2006, DOI: `10.1063/1.2404663`.

[138]   T. Stein, L. Kronik, and R. Baer, "Reliable prediction of charge transfer excitations in molecular complexes using time-dependent density functional theory.", *Journal of the American Chemical Society*, vol. 131, no. 8, pp. 2818–2820, 2009, DOI: `10.1021/ja8087482`.

[139]   M. Alipour and Z. Safari, "Photophysics of OLED Materials with Emitters Exhibiting Thermally Activated Delayed Fluorescence and Used in Hole/-Electron Transporting Layer from Optimally Tuned Range-Separated Density Functional Theory", *Journal of Physical Chemistry C*, vol. 123, no. 1, pp. 746–761, 2019, DOI: `10.1021/acs.jpcc.8b11681`.

[140] Y.-L. Chen, C.-Y. Chang, Y.-J. Cheng, and C.-S. Hsu, "Synthesis of a New Ladder-Type Benzodi(cyclopentadithiophene) Arene with Forced Planarization Leading to an Enhanced Efficiency of Organic Photovoltaics", *Chemistry of Materials*, vol. 24, no. 20, pp. 3964–3971, 2012, DOI: `10.1021/cm3024082`.

[141] Y. Zou, A. Najari, P. Berrouard, S. Beaupré, B. Réda Aïch, Y. Tao, and M. Leclerc, "A Thieno[3,4-c]pyrrole-4,6-dione-Based Copolymer for Efficient Solar Cells", *Journal of the American Chemical Society*, vol. 132, no. 15, pp. 5330–5331, 2010, DOI: `10.1021/ja101888b`.

[142] E. Wang, L. Hou, Z. Wang, S. Hellström, F. Zhang, O. Inganäs, and M. R. Andersson, "An easily synthesized blue polymer for high-performance polymer solar cells", *Advanced Materials*, vol. 22, no. 46, pp. 5240–5244, 2010, DOI: `10.1002/adma.201002225`.

[143] H.-C. Chen, Y.-H. Chen, C.-C. Liu, Y.-C. Chien, S.-W. Chou, and P.-T. Chou, "Prominent Short-Circuit Currents of Fluorinated Quinoxaline-Based Copolymer Solar Cells with a Power Conversion Efficiency of 8.0%", *Chemistry of Materials*, vol. 24, no. 24, pp. 4766–4772, 2012, DOI: `10.1021/cm302861s`.

[144] L. Lan, Z. Chen, Q. Hu, L. Ying, R. Zhu, F. Liu, T. P. Russell, F. Huang, and Y. Cao, "High-Performance Polymer Solar Cells Based on a Wide-Bandgap Polymer Containing Pyrrolo[3,4-f]benzotriazole-5,7-dione with a Power Conversion Efficiency of 8.63%", *Advanced Science*, vol. 3, no. 9, p. 1600032, 2016, DOI: `10.1002/advs.201600032`.

[145] B. Fan, L. Ying, Z. Wang, B. He, X. F. Jiang, F. Huang, and Y. Cao, "Optimisation of processing solvent and molecular weight for the production of green-solvent-processed all-polymer solar cells with a power conversion efficiency over 9%", *Energy and Environmental Science*, vol. 10, no. 5, pp. 1243–1251, 2017, DOI: `10.1039/c7ee00619e`.

[146] M. Zhang, X. Guo, W. Ma, H. Ade, and J. Hou, "A Large-Bandgap Conjugated Polymer for Versatile Photovoltaic Applications with High Performance", *Advanced Materials*, vol. 27, no. 31, pp. 4655–4660, 2015, DOI: `10.1002/adma.201502110`.

[147] H. Zhang, H. Yao, J. Hou, J. Zhu, J. Zhang, W. Li, R. Yu, B. Gao, S. Zhang, and J. Hou, "Over 14% Efficiency in Organic Solar Cells Enabled by Chlori-

nated Nonfullerene Small-Molecule Acceptors", *Advanced Materials*, vol. 30, no. 28, p. 1800613, 2018, DOI: `10.1002/adma.201800613`.

[148] T. Umeyama and H. Imahori, "Isomer Effects of Fullerene Derivatives on Organic Photovoltaics and Perovskite Solar Cells", *Accounts of Chemical Research*, vol. 52, no. 8, pp. 2046–2055, 2019, DOI: `10.1021/acs.accounts.9b00159`.

[149] T. Kastinen, M. Niskanen, C. Risko, O. Cramariuc, and T. I. Hukka, "On describing the optoelectronic characteristics of poly(benzodithiophene-*co*-quinoxaline)–fullerene complexes: the influence of optimally tuned density functionals", *Physical Chemistry Chemical Physics*, vol. 18, no. 39, pp. 27654–27670, 2016, DOI: `10.1039/c6cp04567g`.

[150] S. Hedström and P. Persson, "Quantum Chemical Calculations of Side-Group Stacking and Electronic Properties in Thiophene–Quinoxaline Polymers", *The Journal of Physical Chemistry C*, vol. 116, no. 51, pp. 26700–26706, 2012, DOI: `10.1021/jp308063u`.

[151] T. Kastinen, D. A. da Silva Filho, L. Paunonen, M. Linares, L. A. Ribeiro Junior, O. Cramariuc, and T. I. Hukka, "Electronic couplings and rates of excited state charge transfer processes at poly(thiophene-*co*-quinoxaline)–PC$_{71}$BM interfaces: two- versus multi-state treatments", *Physical Chemistry Chemical Physics*, vol. 21, no. 46, pp. 25606–25625, 2019, DOI: `10.1039/c9cp04837e`.

[152] M. J. Frisch, G. W. Trucks, H. B. Schlegel, G. E. Scuseria, M. A. Robb, J. R. Cheeseman, G. Scalmani, V. Barone, B. Mennucci, G. A. Petersson et al., *Gaussian 09 Revisions C.01 and D.01*, Wallingford CT, 2009.

[153] Y. Shao, Z. Gan, E. Epifanovsky, A. T. Gilbert, M. Wormit, J. Kussmann, A. W. Lange, A. Behn, J. Deng, X. Feng et al., "Advances in molecular quantum chemistry contained in the Q-Chem 4 program package", *Molecular Physics*, vol. 113, no. 2, pp. 184–215, 2015, DOI: `10.1080/00268976.2014.952696`.

[154] M. J. Frisch, G. W. Trucks, H. B. Schlegel, G. E. Scuseria, M. A. Robb, J. R. Cheeseman, G. Scalmani, V. Barone, G. A. Petersson, H. Nakatsuji et al., *Gaussian 16 Revision B.01*, Wallingford CT, 2016.

[155] *Dassault Systèmes BIOVIA, Materials Studio 8.0, v8.0.0.843*, San Diego, 2014.

[156]   *Dassault Systèmes BIOVIA, Materials Studio 2017 R2, v17.2.0.1626*, San Diego, 2016.

[157]   G. A. Zhurko, *Chemcraft - graphical program for visualization of quantum chemistry computations. Ivanovo, Russia, 2005.* URL: `http://www.chemcraftprog.com`.

[158]   *Multiwfn 3.6*, URL: `http://sobereva.com/multiwfn/` (visited on 01/05/2020).

[159]   T. Lu and F. Chen, "Multiwfn: a multifunctional wavefunction analyzer.", *Journal of Computational Chemistry*, vol. 33, no. 5, pp. 580–592, 2012, DOI: `10.1002/jcc.22885`.

[160]   T. Lu and F. Chen, "Calculation of Molecular Orbital Composition", *Acta Chimica Sinica*, vol. 69, pp. 2393–2406, 2011.

[161]   R. L. Martin, "Natural transition orbitals", *The Journal of Chemical Physics*, vol. 118, no. 11, pp. 4775–4777, 2003, DOI: `10.1063/1.1558471`.

[162]   B. Yang, Y. Yi, C.-R. Zhang, S. G. Aziz, V. Coropceanu, and J.-L. Brédas, "Impact of Electron Delocalization on the Nature of the Charge-Transfer States in Model Pentacene/C_{60} Interfaces: A Density Functional Theory Study", *The Journal of Physical Chemistry C*, vol. 118, no. 48, pp. 27648–27656, 2014, DOI: `10.1021/jp5074076`.

[163]   L. Kronik and S. Kummel, "Dielectric Screening Meets Optimally Tuned Density Functionals", *Advanced Materials*, vol. 30, no. 41, p. 1706560, 2018, DOI: `10.1002/adma.201706560`.

[164]   M. Campoy-Quiles, C. Müller, M. Garriga, E. Wang, O. Inganäs, and M. I. Alonso, "On the complex refractive index of polymer:Fullerene photovoltaic blends", *Thin Solid Films*, vol. 571, pp. 371–376, 2014, DOI: `10.1016/j.tsf.2014.02.096`.

[165]   X.-K. Chen, M. K. Ravva, H. Li, S. M. Ryno, and J.-L. Brédas, "Effect of Molecular Packing and Charge Delocalization on the Nonradiative Recombination of Charge-Transfer States in Organic Solar Cells", *Advanced Energy Materials*, vol. 6, no. 24, p. 1601325, 2016, DOI: `10.1002/aenm.201601325`.

[166] G. Han and Y. Yi, "Local Excitation/Charge-Transfer Hybridization Simultaneously Promotes Charge Generation and Reduces Nonradiative Voltage Loss in Nonfullerene Organic Solar Cells", *Journal of Physical Chemistry Letters*, vol. 10, no. 11, pp. 2911–2918, 2019, DOI: `10.1021/acs.jpclett.9b00928`.

[167] V. Lemaur, M. Steel, D. Beljonne, J.-L. Brédas, and J. Cornil, "Photoinduced Charge Generation and Recombination Dynamics in Model Donor/Acceptor Pairs for Organic Solar Cell Applications: A Full Quantum-Chemical Treatment", *Journal of the American Chemical Society*, vol. 127, no. 16, pp. 6077–6086, 2005, DOI: `10.1021/ja042390l`.

[168] M. Wykes, B. Milian-Medina, and J. Gierschner, "Computational engineering of low bandgap copolymers.", *Frontiers in chemistry*, vol. 1, pp. 1–12, 2013, DOI: `10.3389/fchem.2013.00035`.

[169] R. A. Marcus, "On the Theory of Electron-Transfer Reactions. VI. Unified Treatment for Homogeneous and Electrode Reactions", *The Journal of Chemical Physics*, vol. 43, no. 2, pp. 679–701, 1965, DOI: `10.1063/1.1696792`.

[170] T. Liu and A. Troisi, "Absolute Rate of Charge Separation and Recombination in a Molecular Model of the P3HT/PCBM Interface", *The Journal of Physical Chemistry C*, vol. 115, no. 5, pp. 2406–2415, 2011, DOI: `10.1021/jp109130y`.

[171] D. Rehm and A. Weller, "Kinetics of Fluorescence Quenching by Electron and H-Atom Transfer", *Israel Journal of Chemistry*, vol. 8, no. 2, pp. 259–271, 1970, DOI: `10.1002/ijch.197000029`.

[172] L. Cupellini, P. Wityk, B. Mennucci, and J. Rak, "Photoinduced electron transfer in 5-bromouracil labeled DNA. A contrathermodynamic mechanism revisited by electron transfer theories", *Physical Chemistry Chemical Physics*, vol. 21, no. 8, pp. 4387–4393, 2019, DOI: `10.1039/c8cp07700b`.

[173] S. Refaely-Abramson, R. Baer, and L. Kronik, "Fundamental and excitation gaps in molecules of relevance for organic photovoltaics from an optimally tuned range-separated hybrid functional", *Physical Review B*, vol. 84, no. 7, p. 075144, 2011, DOI: `10.1103/PhysRevB.84.075144`.

[174] M. E. Foster, J. D. Azoulay, B. M. Wong, and M. D. Allendorf, "Novel Metal–Organic framework linkers for light harvesting applications", *Chemical Science*, vol. 5, no. 5, pp. 2081–2090, 2014, DOI: `10.1039/c4sc00333k`.

[175] N. R. Tummala, Z. Zheng, S. G. Aziz, V. Coropceanu, and J.-L. Brédas, "Static and Dynamic Energetic Disorders in the C_{60}, $PC_{61}BM$, C_{70}, and $PC_{71}BM$ Fullerenes", *The Journal of Physical Chemistry Letters*, vol. 6, no. 18, pp. 3657–3662, 2015, DOI: `10.1021/acs.jpclett.5b01709`.

[176] T. B. de Queiroz and S. Kümmel, "Charge-transfer excitations in low-gap systems under the influence of solvation and conformational disorder: Exploring range-separation tuning", *The Journal of Chemical Physics*, vol. 141, no. 8, p. 084303, 2014, DOI: `10.1063/1.4892937`.

[177] T. B. de Queiroz and S. Kümmel, "Tuned range separated hybrid functionals for solvated low bandgap oligomers", *The Journal of Chemical Physics*, vol. 143, no. 3, p. 034101, 2015, DOI: `10.1063/1.4926468`.

[178] C.-F. Huang, S.-L. Wu, Y.-F. Huang, Y.-C. Chen, S.-T. Chang, T.-Y. Wu, K.-Y. Wu, W.-T. Chuang, and C.-L. Wang, "Packing Principles for Donor-Acceptor Oligomers from Analysis of Single Crystals", *Chemistry of Materials*, vol. 28, no. 15, pp. 5175–5190, 2016, DOI: `10.1021/acs.chemmater.6b00671`.

[179] C. Cabanetos, A. El Labban, J. A. Bartelt, J. D. Douglas, W. R. Mateker, J. M. J. Fréchet, M. D. McGehee, and P. M. Beaujuge, "Linear side chains in Benzo[1,2-b:4,5-b']dithiophene-Thieno[3,4-c]pyrrole-4,6-dione polymers direct self-assembly and solar cell performance.", *Journal of the American Chemical Society*, vol. 135, no. 12, pp. 4656–4659, 2013, DOI: `10.1021/ja400365b`.

[180] Z. Zhang, J. Yu, X. Yin, Z. Hu, Y. Jiang, J. Sun, J. Zhou, F. Zhang, T. P. Russell, F. Liu, and W. Tang, "Conformation Locking on Fused-Ring Electron Acceptor for High-Performance Nonfullerene Organic Solar Cells", *Advanced Functional Materials*, vol. 28, no. 11, p. 1705095, 2018, DOI: `10.1002/adfm.201705095`.

[181] T. J. Aldrich, M. Matta, W. Zhu, S. M. Swick, C. L. Stern, G. C. Schatz, A. Facchetti, F. S. Melkonyan, and T. J. Marks, "Fluorination Effects on Indacenodithienothiophene Acceptor Packing and Electronic Structure, End-Group Redistribution, and Solar Cell Photovoltaic Response", *Journal of the Amer-*

ican Chemical Society, vol. 141, no. 7, pp. 3274–3287, 2019, DOI: `10.1021/jacs.8b13653`.

[182] E. Giussani, D. Fazzi, L. Brambilla, M. Caironi, and C. Castiglioni, "Molecular Level Investigation of the Film Structure of a High Electron Mobility Copolymer via Vibrational Spectroscopy", *Macromolecules*, vol. 46, no. 7, pp. 2658–2670, 2013, DOI: `10.1021/ma302664s`.

[183] D. Fazzi, M. Caironi, and C. Castiglioni., "Quantum-Chemical Insights into the Prediction of Charge Transport Parameters for a Naphthalenetetracarboxydiimide-Based Copolymer with Enhanced Electron Mobility", *Journal of the American Chemical Society*, vol. 133, no. 47, pp. 19056–19059, 2011, DOI: `10.1021/ja208824d`.

[184] T. Kastinen and T. I. Hukka, "Charge transfer characteristics of fullerene-free polymer solar cells via multi-state electronic coupling treatment", *Sustainable Energy & Fuels*, Advance Article 2020, DOI: `10.1039/D0SE00306A`.

[185] K. Akaike, K. Kanai, H. Yoshida, J. Tsutsumi, T. Nishi, N. Sato, Y. Ouchi, and K. Seki, "Ultraviolet photoelectron spectroscopy and inverse photoemission spectroscopy of [6,6]-phenyl-$C_6$1-butyric acid methyl ester in gas and solid phases", *Journal of Applied Physics*, vol. 104, p. 023710, 2008, DOI: `10.1063/1.2957588`.

[186] K. R. Graham, C. Cabanetos, J. P. Jahnke, M. N. Idso, A. El Labban, G. O. Ngongang Ndjawa, T. Heumueller, K. Vandewal, A. Salleo, B. F. Chmelka et al., "Importance of the Donor:Fullerene Intermolecular Arrangement for High-Efficiency Organic Photovoltaics", *Journal of the American Chemical Society*, vol. 136, no. 27, pp. 9608–9618, 2014, DOI: `10.1021/ja502985g`.

[187] A. Yin, D. Zhang, S. H. Cheung, S. K. So, Z. Fu, L. Ying, F. Huang, H. Zhou, and Y. Zhang, "On the understanding of energetic disorder, charge recombination and voltage losses in all-polymer solar cells", *J. Mater. Chem. C*, vol. 6, pp. 7855–7863, 29 2018, DOI: `10.1039/C8TC02689K`.

[188] D. H. K. Murthy, A. Melianas, Z. Tang, G. Juška, K. Arlauskas, F. Zhang, L. D. A. Siebbeles, O. Inganäs, and T. J. Savenije, "Origin of reduced bimolecular recombination in blends of conjugated polymers and fullerenes", *Advanced Functional Materials*, vol. 23, no. 34, pp. 4262–4268, 2013, DOI: `10.1002/adfm.201203852`.

[189]   A. A. Bakulin, Y. Xia, H. J. Bakker, O. Inganäs, and F. Gao, "Morphology, Temperature, and Field Dependence of Charge Separation in High-Efficiency Solar Cells Based on Alternating Polyquinoxaline Copolymer", *Journal of Physical Chemistry C*, vol. 120, no. 8, pp. 4219–4226, 2016, DOI: `10.1021/acs.jpcc.5b10801`.

[190]   A. A. Bakulin, A. Rao, V. G. Pavelyev, P. H. M. van Loosdrecht, M. S. Pshenichnikov, D. Niedzialek, J. Cornil, D. Beljonne, and R. H. Friend, "The Role of Driving Energy and Delocalized States for Charge Separation in Organic Semiconductors", *Science*, vol. 335, no. 6074, pp. 1340–1344, 2012, DOI: `10.1126/science.1217745`.

[191]   G. Sini, J. S. Sears, and J.-L. Brédas, "Evaluating the performance of DFT functionals in assessing the interaction energy and ground-state charge transfer of donor/acceptor complexes: Tetrathiafulvalene-tetracyanoquinodimethane (TTF-TCNQ) as a model case", *Journal of Chemical Theory and Computation*, vol. 7, no. 3, pp. 602–609, 2011, DOI: `10.1021/ct1005517`.

[192]   Y. Yi, V. Coropceanu, and J.-L. Brédas, "A comparative theoretical study of exciton-dissociation and charge-recombination processes in oligothiophene/-fullerene and oligothiophene/perylenediimide complexes for organic solar cells", *Journal of Materials Chemistry*, vol. 21, no. 5, pp. 1479–1486, 2011, DOI: `10.1039/c0jm02467h`.

[193]   D. A. Vithanage, E. Wang, Z. Wang, F. Ma, O. Inganäs, M. R. Andersson, A. Yartsev, V. Sundström, and T. Pascher, "Charge carrier dynamics of polymer:fullerene blends: From geminate to non-geminate recombination", *Advanced Energy Materials*, vol. 4, no. 8, p. 1301706, 2014, DOI: `10.1002/aenm.201301706`.

[194]   T. Unger, S. Wedler, F.-J. Kahle, U. Scherf, H. Bässler, and A. Köhler, "The Impact of Driving Force and Temperature on the Electron Transfer in Donor-Acceptor Blend Systems", *The Journal of Physical Chemistry C*, vol. 121, no. 41, pp. 22739–22752, 2017, DOI: `10.1021/acs.jpcc.7b09213`.

[195]   Q.-Q. Pan, S.-B. Li, Y.-C. Duan, Y. Wu, J. Zhang, Y. Geng, L. Zhao, and Z.-M. Su, "Exploring what prompts ITIC to become a superior acceptor in organic solar cell by combining molecular dynamics simulation with quantum

chemistry calculation", *Phys. Chem. Chem. Phys.* Vol. 19, pp. 31227–31235, 46 2017, DOI: `10.1039/C7CP05938H`.

[196]   Q.-Q. Pan, S.-B. Li, Y. Wu, Y. Geng, M. Zhang, and Z.-M. Su, "Exploring more effective polymer donors for the famous non-fullerene acceptor ITIC in organic solar cells by increasing electron-withdrawing ability", *Organic Electronics*, vol. 53, pp. 308–314, 2018, DOI: `https://doi.org/10.1016/j.orgel.2017.11.002`.

[197]   J. Jortner, "Temperature dependent activation energy for electron transfer between biological molecules", vol. 64, no. 12, pp. 4860–4867, 1976, DOI: `10.1063/1.432142`.

PUBLICATIONS

PUBLICATION

I

"Intrinsic Properties of Two Benzodithiophene-Based Donor–Acceptor
Copolymers Used in Organic Solar Cells: A Quantum-Chemical Approach"

T. Kastinen, M. Niskanen, C. Risko, O. Cramariuc, and T. I. Hukka

Intrinsic Properties of Two Benzodithiophene-Based Donor–Acceptor Copolymers Used in Organic Solar Cells: A Quantum-Chemical Approach

Tuuva Kastinen,*[,†] Mika Niskanen,[†,‡] Chad Risko,[§] Oana Cramariuc,[∥] and Terttu I. Hukka*[,†]

[†]Department of Chemistry and Bioengineering, Tampere University of Technology, P.O. Box 541, FI-33101 Tampere, Finland

[‡]Department of Physics, Imperial College London, South Kensington Campus, London SW7 2AZ, U.K.

[§]Department of Chemistry and Center for Applied Energy Research, University of Kentucky, Lexington, Kentucky 40511, United States

[∥]Department of Physics, Tampere University of Technology, P.O. Box 692, FI-33101 Tampere, Finland

ⓢ *Supporting Information*

ABSTRACT: Conjugated donor–acceptor (D–A) copolymers show tremendous promise as active components in thin-film organic bulk heterojunction solar cells and transistors, as appropriate combinations of D–A units enable regulation of the intrinsic electronic and optical properties of the polymer. Here, the structural, electronic, and optical properties of two D–A copolymers that make use of thieno[3,4-*c*]pyrrole-4,6-dione as the acceptor and differ by their donor unit—benzo[1,2-b:4,5-b′]dithiophene (BDT) vs the ladder-type heptacyclic benzodi(cyclopentadithiophene)—are compared using density functional theory methods. Our calculations predict some general similarities, although the differences in the donor structures lead also to clear differences. The extended conjugation of the stiff ladder-type donor destabilizes both the highest occupied and lowest unoccupied molecular orbital energies of the ladder copolymer and results in smaller gap energies compared to its smaller counterpart. However, more significant charge transfer nature is predicted for the smaller BDT-based copolymer by natural transition orbitals than for the ladder copolymer. That is, the influence of the acceptor on the copolymer properties is "diluted" to some extent by the already extended conjugation of the ladder-type donor. Thus, the use of stronger acceptor units with the ladder-type donors would benefit the future design of new D–A copolymers.
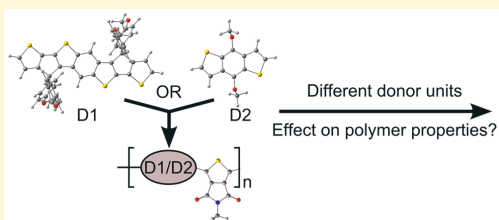
INTRODUCTION

Among molecules used as hole-transport (donor) materials in solution-processed organic solar cells, π-conjugated polymers have shown great potential owing to their favorable optoelectronic, mechanical, and processing characteristics. So-called polymer solar cells (PSCs), when compared to conventional inorganic silicon-based devices, offer the potential of devices that are lightweight with enhanced flexibility and lower manufacturing costs due to large-scale processability.[1,2] Most successful PSCs make use of an active layer that takes on the so-called bulk heterojunction (BHJ) structure,[3] where the polymer donor material is typically codeposited with a fullerene derivative, e.g., [6,6]-phenyl-C₆₁-butyric acid methyl ester (PC₆₁BM) or [6,6]-phenyl-C₇₁-butyric acid methyl ester (PC₇₁BM).[3,4] The BHJ architecture maximizes the interfacial contact and surface area and has generally improved performance when compared to bilayer heterojunction devices;[3] power conversion efficiencies (PCEs) for PSCs can now typically range from 5% to 9%, with some materials pushing past this range;[5–8] combining two or more single cells in tandem structures has led to devices with PCEs over 10%.[9]

In addition to the use of the BHJ structure, significant device efficiency enhancements have arisen from the use of donor–acceptor (D–A) copolymers, where an electron-rich donor unit is coupled to an electron-deficient acceptor unit to form a comonomer.[10] The coupling of the donor and acceptor units defines the intrinsic electronic and optical properties of the polymer. As substituted fullerenes are typically used as acceptors, the ionization energies (IE, i.e., the ionization potential, often associated with the highest-occupied molecular orbital, HOMO), electron affinities (EA, often associated with the lowest-unoccupied molecular orbital, LUMO), and optical gaps of D–A copolymers are tuned through chemical functionality to ensure both large open-circuit voltages and short-circuit currents in thin-film material blends.[2,11,12]

Electron-rich donor units typically consist of fused heterocycles. Over the past few years, benzo[1,2-b:4,5-b′]dithiophene (BDT), where one benzene is fused with two thiophene rings,
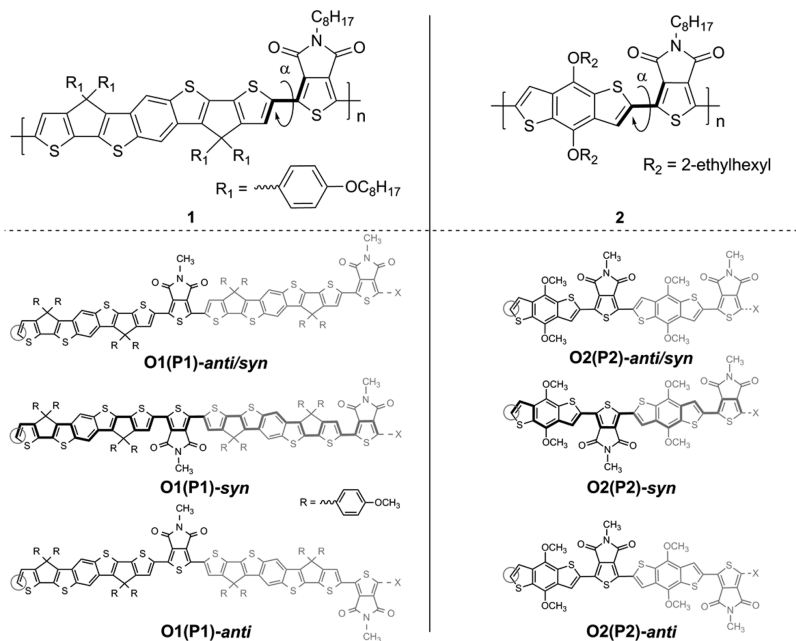
Figure 1. Constitutional repeating units (CRUs)[63] representing the ladder D−A copolymer **1** and the shorter analogue **2**. Donors are the leftmost and acceptors the rightmost units. Below **1** and **2** are the repeating patterns for the oligomeric (O1 and O2) and periodic (P1 and P2) models presenting three different conformational structures of the copolymers. In the periodic structures, the models are translated from the circled carbon atoms to the atoms marked by an X. The dihedral angle (α) between the donor and acceptor units determined with the potential energy surface (PES) scans is in bold in the representations of **1** and **2**. The conjugation paths used for calculating the BLAs and the number of the double bonds (N) are in bold in the representations of O1(P1)-*syn* and O2(P2)-*syn*.

has been widely used as the donor moiety in D−A copolymers.[5,8,13−16] Acceptor unit thieno[3,4-*c*]pyrrole-4,6-dione (TPD), which is symmetric, planar, and has a large EA, has been used in some of the most successful single-junction BHJ PSCs incorporating BDT as the donor unit.[15,17−19]

Longer, ladder-type donor units have also been used in PSCs with some success.[20−24] The increased planarization and conjugation length[25] of the ladder-type donor tend to decrease the electrochemical and optical gaps, in turn having an impact on material performance.[26,27] For instance, the ladder-type heptacyclic benzodi(cyclopentadithiophene) donor, where BDT is covalently bridged with two thiophenes, was introduced by Chen and co-workers[28] in combination with TPD. The resulting ladder copolymer **1** (see Figure 1) was employed in PSCs with efficiencies of 6.6%.

In order to provide a deeper understanding into the intrinsic properties of ladder copolymers, we make use of density functional theory (DFT) and its time-dependent formalism (TDDFT) to compare the intrinsic structural, electronic, and optical properties of the ladder D−A copolymer **1**[28] with copolymer **2**,[17−19] both of which contain the TPD acceptor (see Figure 1); while **2** has previously been studied via DFT[29−31] methods, the ladder copolymer **1** has not been previously considered. Our purpose is to compare the impact of the donor units on critical aspects of the ground (S_0) and excited (S_1 and T_1) state properties of the copolymers to shed light onto possible future polymer design considerations.

■ COMPUTATIONAL DETAILS

The intrinsic properties of conjugated D−A copolymers have been widely investigated through computational approaches at the DFT level, as it allows for detailed connections to be made between chemical/structural design[32−34] and the resulting electronic and optical properties,[29,35−42] e.g., ground[29,35−41] and excited state[42] geometries [including bond-length alternation (BLA)[41−47]], MO energies and distributions,[29,35−38,40,41] electrochemical and optical gaps, and UV−vis spectra.[29,35−42] The electronic and optical energies of (infinite) polymers have been approximated by extrapolating the properties of oligomers to infinite length.[41,42,48−51] In addition to oligomer-based studies, periodic boundary condition (PBC)[52,53] calculations can provide insight into structure−function relationships;[34,50,51,54−60] however, to the best of our knowledge, there exist only a few studies[33,40,41,61] of D−A copolymers using the PBC−DFT method.

Models. Oligomeric (O1 and O2, n = 2−5) and periodic models (P1 and P2, n = ∞) of **1** and **2** (Figure 1) were constructed by repeating the monomer models M1 and M2 (n = 1) [see Figure S1 of the Supporting Informaton (SI)]. The octyl and 2-ethylhexyl chains of the copolymers were replaced by methyl groups to reduce the computational cost. We note, however, that long alkyl side chains will have a great impact on solid-state packing.[62]

The donor and acceptor units within monomers can be either in an *antiperiplanar* conformation, i.e., the neighboring

sulfur atoms of the units are on the opposite sides (α is from 150° to 180°), or in a *synperiplanar* conformation, i.e., the neighboring sulfur atoms of the units are on the same side (α is from 0° to 30°). For the sake of simplicity, these two conformations are referred to as *anti* and *syn* hereafter. The exact orientations of the donor and acceptor units with respect to the dihedral angle α were determined on the basis of the relaxed potential energy surface (PES) scans of the monomer models M1 and M2 (see the Methods section).

Three different conformational structures of isolated oligomers (O1 and O2, $n = 2-5$) were constructed: (i) the *anti/syn*-conformations of O1/O2 consist of the repeating M1/M2-*anti* units, respectively. The repetition of the M1/M2-*syn* units would yield the same structures. (ii) In the *syn*-conformations, the M1/M2-*syn* units are *syn* to each other. (iii) Finally, in the *anti*-conformations, the M1/M2-*anti* units are *anti* to each other. The conformational structures of the periodic models P1 and P2 were constructed in the same manner as those of the oligomers, but using two M1 and M2 monomer models, i.e., dimers as the repeating units to ensure the repeatable structures. The arch-shaped *anti/syn*-conformations of both P1 and P2 did not converge, because of the incorrect repetition of the repeating unit during the calculations. Use of a longer oligomer as the repeating unit could have solved the problem, but would have also been computationally more demanding. Thus, only the results for the *syn*- and *anti*-conformations of P1 and P2 are presented here.

Methods. All DFT, PBC−DFT,[52,53] and TDDFT calculations were carried out in vacuum with the Gaussian 09 (Revision C.01) suite of programs.[64] In addition, single point (SP) TDDFT calculations were carried out in solvents for selected oligomers; see below. The global hybrid functional B3LYP[65,66] and the long-range-corrected (LRC) hybrid functional CAM-B3LYP[67] [with the default range-separation parameter (ω) of 0.33 b^{-1}] were used in all monomeric, oligomeric, and periodic DFT calculations with the 6-31G** basis set, unless specified otherwise. The LRC functional ωB97X-D[68] (with the default ω of 0.20 b^{-1}), which includes the empirical dispersion correction, was also used in the monomeric DFT calculations. Frequency calculations were carried out for monomers and dimers on the B3LYP/6-31G**-optimized geometries to ensure the absence of the imaginary frequencies and to confirm the minimized structures. Pictorial presentations of the geometries and the frontier MOs (FMOs) of the oligomeric and periodic models and the natural transition orbitals (NTOs) of the oligomeric models were generated using ChemCraft 1.7.[69] The contributions of the electron densities to the FMOs and the NTOs of the donor and acceptor units were determined with C-squared population analysis (C-SPA)[70] as implemented in Multiwfn 3.3.6.[71−73]

Relaxed PES Scans. Dihedral angles α between the donor and acceptor units of models M1 and M2 (see Figure S1, SI) were determined with the relaxed PES scans, where the geometry of a model was optimized at constrained α intervals of 5° between 0° and 360°. In addition, the effect of the replacement of the longer alkyl chains by methyl chains on the monomer properties was checked by optimizing M1 and M2 with full lengths of the alkyl chains (see Figure 1) at the B3LYP/6-31G** level of theory.

PBC−DFT Calculations. The periodic models (P1 and P2) were optimized using the default density of the k-points. The length of the translation vector $\mathbf{T}_v$ determines the number of the k-points; i.e., the longer the vector, the fewer k-points in the reciprocal space. The lengths of $\mathbf{T}_v$ were ca. 38 and 24 Å and translated into 9 and 14 k-points in P1 and P2, respectively.

TDDFT Calculations. The energies of the vertical electronic transitions for the first 20 singlet and triplet excited states were determined in vacuum for all monomeric and oligomeric models ($n = 2-4$ for O1 and $n = 2-5$ for O2) using TDDFT, except for the O1 pentamers, which were computationally too demanding for TDDFT. The graphical presentations of the UV−vis absorption spectra of O1 ($n = 3$) and O2 ($n = 5$) were created via convolution of the vertical singlet transition energies and oscillator strengths using a Gaussian-shape broadening with a full width at half-maximum (fwhm) of 0.30 eV. The nature of the $S_0 \rightarrow S_1$ electronic transitions for O1 ($n = 3$) and O2 ($n = 5$) was described using NTOs[74] as a representation for the transition density matrix. The SP TDDFT calculations were also carried out for the first 20 singlet excited states of the O1 ($n = 3$) and O2 ($n = 5$) in toluene and chloroform, respectively. Solvation effects were included by means of the integral equation formalism of the polarizable continuum model (IEFPCM)[75,76] using dielectric constants of 2.37 and 4.71 for toluene and chloroform, respectively. Moreover, the excited state (S_1 and T_1) geometries of the *syn*-conformations of O1 ($n = 3$) and O2 ($n = 5$) were optimized at the TDDFT/B3LYP/6-31G** level of theory.

Bond-Length Alternations. The BLAs were calculated for the optimized S_0, S_1, and T_1 geometries of the oligomer models and the optimized S_0 geometries of the periodic models, as follows. Each BLA value was determined as the average difference in length between the adjacent C−C single and C═C double bonds within the conjugation path in a molecule (see Figure 1), i.e., within the shortest path between the terminal carbon atoms.[42,47,77] The total BLA values of the S_0 geometries of the oligomers ($n = 1-5$) were compared to the BLA$_{middle}$ values taken from one innermost CRU of the trimers, two innermost CRUs of the tetramers, and both one and three innermost CRUs of the pentamers of O1 and O2. In the case of the S_1 and T_1 geometries of O1 ($n = 3$) and O2 ($n = 5$), the BLA$_{middle}$ values were calculated in the same manner as described above. In addition, some BLA$_{middle}$ values, which are defined in more detail in the Supporting Information, were calculated for these geometries.

Extrapolation Techniques. The FMO energies, differences between the HOMO and LUMO energies, i.e., the HOMO−LUMO gaps, and the vertical transition energies at infinite length were extrapolated from the oligomer values plotted against the reciprocal of the number of the double bonds ($1/N$) using the linear, Kuhn, and scaled Kuhn fits. The number of the double bonds (e.g., 10 for the CRU of **1** and 6 for that of **2**) was calculated along the conjugation path (see Figures 1 and S1, SI). The absorption wavelengths at infinite length and effective conjugation lengths were also determined from the oligomeric absorption wavelengths plotted against the reciprocal of n, i.e. $1/n$, using the Meier fit.

The Kuhn fit, introduced by Kuhn[78] in 1948, is based on the statement made by Lewis and Calvin[79] that the double bonds of a polyene can be presented as N identical oscillators, each having a vibrational energy of E_0. Kuhn developed the model further by including a coupling force constant, k', of the N adjacent double bonds. The resulting minimum energy can be written as
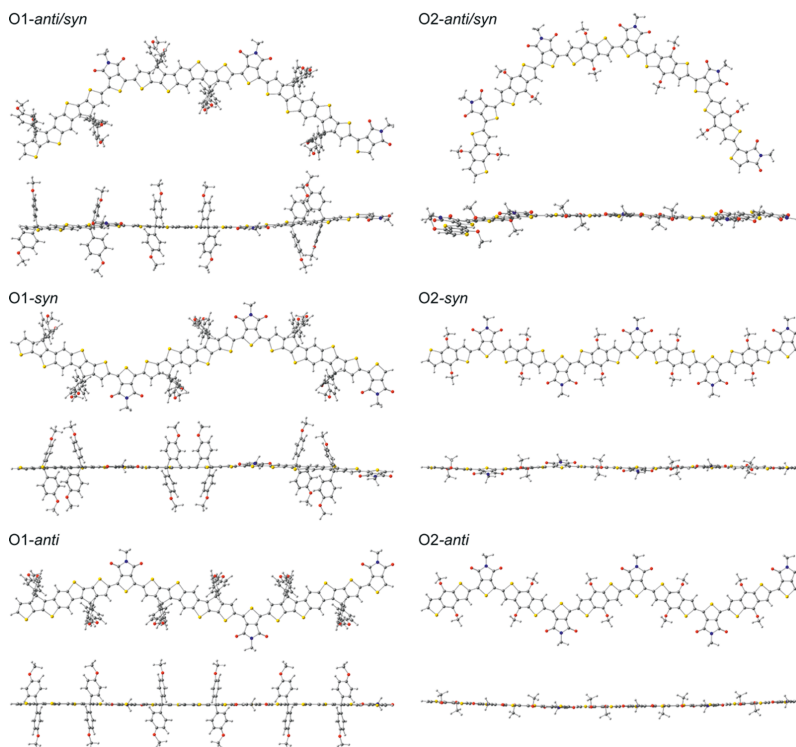
Figure 2. Optimized ground-state structures of the *anti/syn*-, *syn*-, and *anti*-conformational models of O1 ($n = 3$) and O2 ($n = 5$) calculated at the B3LYP/6-31G** level of theory. The *syn*-conformers of the monomers, oligomers, as well as of the periodic structures were found to be energetically the most favorable.

$$E = E_0 \sqrt{1 + 2\frac{k'}{k_0} \cos \frac{\pi}{N+1}} \tag{1}$$

where k_0 is the force constant of an isolated oscillator unit. The value of k'/k_0 is usually on the order of ca. −0.45.[48]

The original Kuhn fit can sometimes yield unsatisfactory results due to its assumption of a constant k'/k_0 in spite of the increasing chain length, which holds for the homogeneous systems (e.g., homopolymers) but does not take chain end effects arising in heterogeneous systems into account. For example, the Kuhn fit neglects the intramolecular charge transfer (ICT) occurring in D−A copolymers.[48,49] Additionally, in the case of the D−A copolymers, the energy values of longer polymers, which have larger number of N, locate closer to the infinite polymer region. Thus, a modification of eq 1 is required.[48] Here, we suggest an addition of a scaling factor, z, which multiplies the N:

$$E = E_0 \sqrt{1 + 2\frac{k'}{k_0} \cos \frac{\pi}{zN+1}} \tag{2}$$

The scaling factor z is iterated during the fitting procedure using the Levenberg−Marquardt algorithm until convergence is reached.

According to Meier et al.,[80] the dependence of the absorption wavelength on the number of repeating units n can be described by the following exponential function

$$\lambda(n) = \lambda_\infty - (\lambda_\infty - \lambda_1)e^{-b(n-1)} \tag{3}$$

where λ_1 is the wavelength of the monomer, λ_∞ is the wavelength at infinite chain length ($n = \infty$), and b is a parameter indicating how fast the limit of convergence is approached. Meier et al. also defined the term "effective conjugation length" as the conjugation length at which the wavelength of the oligomer series is equal to or 1 nm smaller than that of the infinitely long polymer, i.e., λ_∞.

RESULTS AND DISCUSSION

To establish the influence of the ladder-type construction of the donor on the electronic and optical properties of D−A copolymers, we begin by detailing the geometric structure of the ground state as a function of the donor unit. This is then followed by a description of the FMOs, excited-state transitions, UV−vis spectra, and NTOs. Finally, we explore the relaxation of the S_1 and T_1 excited states through TDDFT.

Ground-State (S_0) Structural Properties of the Oligomeric and Periodic Models. The results and further discussion for the monomeric calculations are presented in the Supporting Information. In summary, the PES scans indicate

that the ladder-type monomer M1 is planar and the smaller monomer M2 nearly planar. Moreover, the *syn*-conformation is energetically more favorable than the *anti*-conformation for both M1 and M2.

With the monomer properties established, one can now turn to larger oligomer models ($n = 2-5$) to examine effects of the length of the donor unit and the backbone conformation. The B3LYP/6-31G**-optimized ground-state structures of the trimers of O1 and the pentamers of O2 are presented in Figure 2. These oligomer sizes are used hereafter to keep the relative conjugation lengths (i.e., the number of the double bonds) of O1 and O2 consistent. As with the monomers, the ladder copolymer models O1/P1 are planar ($0°-3°$) and the O2/P2 copolymers nearly planar ($1°-11°$) (see Figures S3 and S4 and Tables S2 and S3 of the SI for further details). The *anti*/*syn*-conformations of O1 and O2 have clear arch shapes, while both the *syn*- and *anti*-conformations have zigzag patterns. The *syn*-conformation of O1 is more curved than the *anti*-conformation of O1, whereas O2-*syn* is less curved than O2-*anti*. Furthermore, O1-*syn* is more curved than O2-*syn*. These differences are a direct consequence of the lengths of the donor units. The CAM-B3LYP-optimized ground-state structures show the same degrees of curvature as the B3LYP-optimized structures in all conformations. Additionally, the curvatures of the *syn*- and *anti*-conformations of the periodic models are the same as those of the corresponding oligomeric models. It is worth noting that the polymer backbone curvature has been shown to influence the solubility and charge-carrier mobility:[81−83] polymers with a higher degree of curvature are more soluble but tend to have smaller charge-carrier mobilities; in addition, thin films formed with curved polymers have less-ordered structures. On the basis of these factors, the highly curved backbones of the *anti*/*syn*-conformations of O1 and O2 may hinder polymer chain packing and result in low-ordered films with lower charge-carrier mobilities when compared to the *syn*- and *anti*-conformations of O1 and O2. However, the structure of O2-*syn* is less curved than that of O1-*syn*, according to our calculations, which does not seem to correlate with the experimental hole carrier mobilities[19,28,84] and the earlier experimental statement.[81−83] One possible reason for the better hole carrier mobility of **1** could be the more planar structure of **1** predicted by our calculations.

The *syn*-conformations of the O1 (Table S4, SI) and O2 (Table S5, SI) oligomers are energetically the most stable. The relative energies between the conformations, notably, increase systematically with the increasing number of the CRUs ($n = 1-5$), i.e., for the ladder oligomers O1 from 4.3 to 20.3 kJ·mol^{-1} (between O1-*syn* and O1-*anti*/*syn*) and from 4.3 to 35.9 kJ·mol^{-1} (between O1-*syn* and O1-*anti*) and twice as much for the smaller oligomers O2 from 7.7 to 40.0 kJ·mol^{-1} (between O2-*syn* and O2-*anti*/*syn*) and from 7.7 to 66.8 kJ·mol^{-1} (between O2-*syn* and O2-*anti*). If the relative energy per CRU is considered, the O1-*syn* oligomers are ca. 4.1 kJ·mol^{-1} more stable than the O1-*anti*/*syn* oligomers and 4.3−7.2 kJ·mol^{-1} more stable than the O1-*anti* oligomers, and again, the O2-*syn* oligomers are twice as stable with respect to the other oligomers, i.e., ca. 8.0 kJ·mol^{-1} more stable than the O2-*anti*/*syn* oligomers and 7.7−13.4 kJ·mol^{-1} more stable than the O1-*anti* oligomers. For both O1 and O2, the relative energies between the *syn*- and *anti*-conformations per CRU are the largest, as their structures differ most (see below). The energies of the *anti*-conformations are closer to those of the *anti*/*syn*-conformations than to those of the *syn*-conformations. Energy

profiles derived with the CAM-B3LYP-optimized oligomers (Tables S4 and S5, SI) provide similar general trends; i.e., the *syn*-conformations of both O1 and O2 are the most stable.

On the basis of the computed distances (∼2.2 Å) between carbonyl oxygen of the acceptor and C−H hydrogen of the donor, nontraditional hydrogen bonding appears to be present in the most stable *syn*-conformations of the oligomers as was the case with the monomers (see Supporting Information). This C−H⋯O interaction is absent in the energetically least stable *anti*-conformers (see Tables S4 and S5, SI). In the second most stable *anti*/*syn*-conformations, half of the bonding C−H⋯O interactions present in the *syn*-conformations are replaced by the weaker but potentially still bonding[31] C−H⋯S interactions with distances of ∼2.8 Å. On the basis of the computed distances (∼3.0 Å), the S⋯O interactions, which are present in the *anti*/*syn*- and *anti*-conformers of the oligomers, might be slightly bonding, planarizing the *anti*/*syn*- and *anti*-conformers with respect to the *syn*-conformers due to the symmetrical interactions. The S⋯S interactions (with computed distances ∼3.3 Å) that exist only in the *syn*- and *anti*/*syn*-conformers might be slightly repulsive (the reported equilibrium distance is larger, i.e., 4.0 Å[31]), increasing the dihedral angles, especially in O2-*syn*, where there are three neighboring S atoms interacting. However, in O1-*syn*, where there are five S atoms neighboring each other, the S⋯S interactions do not increase the dihedral angles, as the long ladder-type donor unit hinders the rotational freedom in the backbone more than the smaller BDT donor unit in O2-*syn* (Tables S2 and S3, SI).

The evolutions of the BLA values with the O1 and O2 chain lengths are depicted in Figure 3; the corresponding numerical
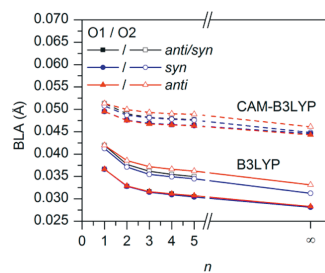
Figure 3. Evolution of BLA for the oligomers O1 and O2 ($n = 1-5$) and periodic models P1 and P2 ($n = \infty$) as a function of n determined at the B3LYP/6-31G** (solid lines) and CAM-B3LYP/6-31G** (dashed lines) levels of theory.

BLA values are presented in Table S6 of the SI. The BLA values decrease when the number of CRUs increases, due to the improved delocalization of the π electrons along the backbone.[47] Both O1 and O2 have positive BLA values, which indicate highly alternated structures, and are therefore classified as having "aromatic" character.[42] The patterns of the graphs in Figure 3 are similar for both O1 and O2, though the O2 oligomers have slightly larger BLA values. However, the length of the donor barely affects the BLA: the BLA values at infinite chain length (periodic models P1 and P2 for both *syn* and *anti*) are 0.028 and 0.031−0.033 Å, respectively. Moreover, the conformation does not affect the BLAs significantly, especially in the case of O1. The chain lengths of the oligomeric models are too short for the BLA to converge to the periodic values. However, if only the middle CRUs are used for calculating the

BLAs of the oligomers ($n = 3-5$), the values are close to those of the periodic models (see Table S6, SI). These differences in the BLAs are due to the chain end effects.[47] The values closest to the BLAs of the periodic models are obtained with tetramers, where the two innermost CRUs are considered. This is not surprising, as the repeating units of the periodic models were constructed using two CRUs. Thus, the BLA at the infinite chain length for the *anti/syn*-conformation of the models of **1** and **2** can be evaluated from the two innermost CRUs of tetramers of O1 and O2, yielding ca. 0.029 and 0.032 Å, respectively. These results are similar to the values (0.033 Å) reported elsewhere[41] for a D–A copolymer incorporating BDT as the donor unit.

Here it is important to keep in mind the effect of multielectron self-interaction errors (MSIE),[46] i.e., the tendency of the global hybrid functionals, e.g., B3LYP, to overestimate conjugation and thus to predict too small BLA values. In previous work, the LRC CAM-B3LYP functional yielded more reliable BLA results than B3LYP for π-conjugated quasilinear chains, compared to the BLA reference values calculated with the coupled-cluster single double (triple) CCSD(T) method, which is known[46,47] to give reliable BLA values for conjugated systems. However, due to the computational cost of this level of theory, it can be only used for small systems. The BLA values derived here with the CAM-B3LYP functional are subtly larger than those given by B3LYP for both the oligomeric and periodic models of **1** and **2**, e.g., 0.044−0.046 Å; this is due to the larger amount of the exact HF exchange[41] in CAM-B3LYP than in B3LYP. LRC hybrid functionals are able to minimize MSIE and have been employed in calculating BLAs of conjugated, organic systems.[46] While tuning the range-separation parameter ω of a LRC functional can yield accurate BLAs, it has also resulted in increased MSIE and poorly described BLA. The extent of conjugation affects the optimal ω value and, hence, the BLA. For strongly π-conjugated systems (e.g., polyenes), the optimally tuned ω and BLA decrease almost linearly with the increasing chain length and do not saturate at large numbers of repeat units. One possible explanation for the failure of optimally tuned LRC functionals is the lack of size-consistency as a result of ω tuning of the functional with system size.[46,85] The lack of saturation has also been observed[35] for a planar[29] D–A copolymer consisting of cyclopentadithiophene and benzothiadiazole units. On the basis of these facts, it can be expected that for planar O1, ω will not saturate either, leading to too small ω values and eventually to pure density functional. Hence, we did not carry out the tuning procedure for CAM-B3LYP, although it is otherwise highly recommended to be checked.[85] While promising for the more accurate description of conjugated systems, the LRC functionals still require further development to eliminate this problem. Because we do not have high-level computational (or experimental[47]) reference data for comparison, the BLAs calculated with the selected methods here should not be taken as the exact values of the studied systems but, rather, as relative values that enable the comparison of these copolymers and of other copolymers studied with the corresponding methods.

Ground-State (S$_0$) Electronic Properties of the Oligomeric and Periodic Models. The HOMO and LUMO energies and HOMO−LUMO gaps of the oligomeric and periodic models are presented in Table S7 of the SI; additionally, the evolutions of the HOMO and LUMO energies of O1 and O2 as a function of $1/N$ are illustrated in Figure S6

of the SI. As a point of reference, the HOMO−LUMO gap, due to the extended conjugation, of the ladder-type donor is smaller than that of the BDT donor (see Figure S5, SI), as expected. This will have consequences on the oligomer/polymer electronic and optical properties, as shown below.

In the case of O1, the different conformations do not affect the HOMO energies of the oligomers of the same length (n), whereas the LUMO energies decrease in the order *syn* < *anti/syn* < *anti*. For O2, both the HOMO and LUMO energies decrease as *anti* < *anti/syn* < *syn*. However, the overall differences in the HOMO and LUMO energies between different conformational models are very small (ca. 0.01−0.04 eV). There is a linear relationship between the HOMO and LUMO energies and the inverse of N for all oligomeric conformations (Figure S6, SI), as expected.[29,86] In addition to the linear fit, we also tested the Kuhn (eq 1) and scaled Kuhn (eq 2) fits for the extrapolation of the FMO energies. The scaled Kuhn fit works rather well and yields values either identical with or close to those obtained with PBC-DFT, whereas the Kuhn fit suffers some limitations in extrapolating the LUMO energies (see the Supporting Information for further discussion). The comparison of the HOMO and LUMO energies at the polymer limit, both extrapolated from the oligomeric values using the linear fit and obtained with PBC-DFT method (Table S7, SI), is presented in Figure 4. The
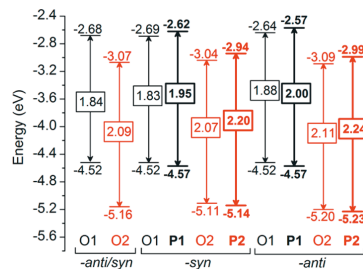
Figure 4. HOMO (lower values) and LUMO (upper values) energies of the conformational models of **1** (in black) and **2** (in red) extrapolated from the oligomeric values of O1 and O2 ($n = 1-5$) using the linear fit and the corresponding periodic values of P1 and P2 ($n = \infty$, in bold) obtained with PBC-DFT at the B3LYP/6-31G** level of theory. The differences between the HOMO and LUMO energies, i.e., the HOMO−LUMO gaps, are presented in the boxes. The experimental HOMO and LUMO energies estimated with CV are −5.36 and −3.20 eV for **1**[28] and −5.43 and −3.40 eV for **2**,[19] respectively.

HOMO energies of the periodic *syn*- and *anti*-conformers are only slightly stabilized (0.0−0.1 eV) with respect to the HOMO energies at the polymer limit derived from the extrapolations for the corresponding oligomeric conformers. On the other hand, the LUMO energies of P1 and P2 are destabilized by ca. 0.1 eV with respect to those of O1 and O2 at the polymer limit. According to the extrapolated and PBC values, both the HOMO (0.6−0.7 eV) and the LUMO (0.3−0.5 eV) of **1** are destabilized with respect to the HOMO and LUMO of **2**. This is an interesting consequence, as the extended conjugation typically destabilizes the HOMO and stabilizes the LUMO in homopolymers to close the gap. However, here **1** and **2** are D–A copolymers, not homopolymers, which may explain this phenomenon. These

Table 1. HOMO–LUMO Gaps (eV) of 1 and 2 Extrapolated from the Oligomeric Values (*n* = 1−5) of O1 and O2 Using the Linear, Kuhn (eq 1), and Scaled Kuhn Fits (eq 2) and Calculated from the Periodic PBC-DFT Results of P1 and P2 at the B3LYP/6-31G** and CAM-B3LYP/6-31G** (in parentheses) Levels of Theory[a]

	anti/syn		syn		anti	
method	O1	O2	O1	O2	O1	O2
linear fit	1.84 (4.10)	2.09 (4.33)	1.82 (4.09)	2.08 (4.32)	1.88 (4.13)	2.11 (4.34)
Kuhn fit	1.99 (4.27)	2.27 (4.55)	1.97 (4.25)	2.26 (4.54)	2.02 (4.29)	2.30 (4.56)
scaled Kuhn fit	1.97 (4.25)	2.22 (4.49)	1.94 (4.23)	2.21 (4.48)	2.00 (4.26)	2.23 (4.50)
	P1	**P2**	**P1**	**P2**	**P1**	**P2**
PBC-DFT	–	–	1.95 (4.23)	2.21 (4.48)	2.00 (4.27)	2.24 (4.50)

[a]Electrochemical gaps are 2.16 eV[28] for **1** and 2.03 eV[19] for **2**, as determined by CV. According to the ref 28, **1** showed stable and reversible processes in CV. Reference 19 did not comment about reversibility of the process for **2**.
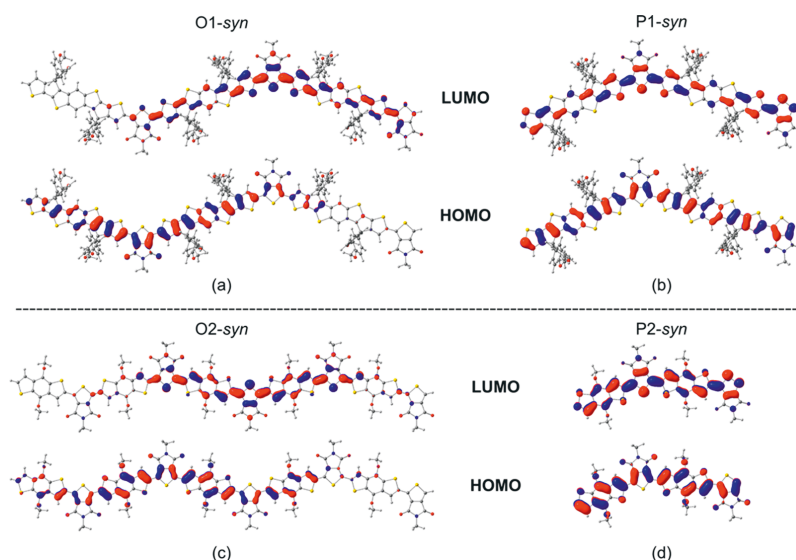
Figure 5. FMOs of (a) O1-*syn* (*n* = 3), (b) P1-*syn* (*n* = ∞), (c) O2-*syn* (*n* = 5), and (d) P2-*syn* (*n* = ∞) calculated at the DFT/B3LYP/6-31G** level of theory (isodensity contour = 0.025).

trends are also in good agreement with the redox potentials measured with cyclic voltammetry (CV).[19,28] While IEs have not been evaluated, the calculated HOMO and LUMO energies suggest that the ladder copolymer **1** should be easier to oxidize but more difficult to reduce than **2** (for the same number of D and A units). The CAM-B3LYP functional predicts the same trends (Table S7, SI) as B3LYP.

The HOMO–LUMO gaps of the copolymer models at the polymer limit, determined by the three extrapolation methods, are presented in Table 1 together with the PBC-DFT values; see the Supporting Information for the extrapolations (Figure S7 and Table S8) and more detailed discussion of the differences between the extrapolation methods. Regardless of the method used, the conformation does not significantly affect the gap energies. The gap energies of the ladder copolymer **1** are ca. 0.2−0.3 eV smaller than those of the smaller copolymer **2**. CAM-B3LYP predicts approximately twice as large gaps as B3LYP. The electrochemical gaps determined experimentally with CV[19,28] show an opposite order. However, here we should keep in mind that due to the differences between the methods[87] the theoretical and experimental values cannot be compared

directly. Additionally, the DFT calculations have been performed in vacuum and are therefore not taking the solvent effects into account. Moreover, only one isolated oligomer has been considered, and the solid-state effects have been omitted.[48]

The FMOs of the *syn*-conformations of both the oligomeric and periodic models of **1** and **2** calculated with B3LYP are shown in Figure 5. The CAM-B3LYP-calculated FMOs are almost the same and are thus not presented here. The conformation does not affect the shapes of the FMOs much and therefore the FMOs of the *anti/syn*- and *anti*-conformations are not illustrated. The HOMOs of the oligomeric models O1 and O2 are delocalized on several donor and acceptor units, which is typical for the D−A copolymers.[29,35] The LUMOs of both O1 and O2 are also delocalized over several donor and acceptor units in the right-hand-side regions of the models in Figure 5. The LUMO delocalization is due to a good match between the LUMO levels of the donors and acceptors, especially in the case of **1** (see Figure S5, SI). In addition, the planar backbone of O1 enhances the mixing and delocalization of the FMOs even

Table 2. Vertical $S_0 \rightarrow S_1$, $S_0 \rightarrow S_2$, and $S_0 \rightarrow T_1$ Transition Energies (eV) and Exchange Energies, ΔE_{ST} (eV), of O1 ($n = 3$) and O2 ($n = 5$) Calculated with TDDFT at the B3LYP/6-31G and CAM-B3LYP/6-31G** (in parentheses) Levels of Theory Using the Geometries Optimized at the Corresponding Theory Levels**

	$S_0 \rightarrow S_1$		$S_0 \rightarrow S_2$		$S_0 \rightarrow T_1$		$\Delta E_{ST}{}^a$	
conformation	O1	O2	O1	O2	O1	O2	O1	O2
anti/syn	1.78	1.98	2.03	2.17	1.23	1.41	0.55	0.57
	(2.49)	(2.71)	(2.70)	(2.89)	(1.36)	(1.53)	(1.13)	(1.18)
syn	1.76	1.97	2.01	2.17	1.21	1.40	0.55	0.57
	(2.47)	(2.70)	(2.68)	(2.88)	(1.34)	(1.54)	(1.13)	(1.16)
anti	1.79	1.99	2.04	2.18	1.25	1.42	0.54	0.57
	(2.50)	(2.71)	(2.71)	(2.89)	(1.39)	(1.53)	(1.11)	(1.18)

$^a\Delta E_{ST} = E(S_1) - E(T_1)$

Table 3. Vertical $S_0 \rightarrow S_1$ Transition Energies (eV) of 1 and 2 Extrapolated from the Oligomeric Values ($n = 1-4$) of O1 and O2, with TDDFT at the B3LYP/6-31G and CAM-B3LYP/6-31G** (in parentheses) Levels of Theory, Using the Linear, Kuhn (eq 1), and Scaled Kuhn Fits (eq 2)^a**

	anti/syn		*syn*		*anti*	
method	O1	O2	O1	O2	O1	O2
linear fit	1.50	1.80	1.49	1.80	1.52	1.81
	(2.25)	(2.51)	(2.24)	(2.52)	(2.27)	(2.52)
Kuhn fit	1.68	1.99	1.67	1.99	1.70	2.01
	(2.40)	(2.69)	(2.39)	(2.69)	(2.42)	(2.69)
scaled Kuhn fit	1.64	1.87	1.63	1.84	1.66	1.88
	(2.39)	(2.63)	(2.37)	(2.62)	(2.41)	(2.63)

^{a}Experimental absorption maxima of **1** and **2** are 1.96 eV (in toluene)[28] and 2.03 eV (in chloroform),[19] respectively, and the optical gaps estimated from the onset wavelengths of the UV−vis spectra of **1** and **2** (in films) are 1.88[28] and 1.82 eV,[19] respectively.

more.[35] In the periodic models, the FMOs are delocalized over the entire backbones, which results from the geometrically identical CRUs and the absence of the chain end effects. In the oligomeric models, the chain end effects together with the geometrically nonidentical CRUs yield more localized FMOs. Thus, the PBC models describe the FMOs of the middle parts of the oligomers. Altogether, the delocalizations of the FMOs in the periodic models are similar to those in the oligomeric models and the FMOs of **1** and **2** are very similar.

Excited-State Optical Properties of the Oligomeric Models. We now turn to how the structural properties influence the optical characteristics. The $S_0 \rightarrow S_1$ vertical transition energies, wavelengths, and oscillator strengths and the main transition configurations of O1 ($n = 1-4$) and O2 ($n = 1-5$) are summarized in Tables S9 and S10 of the SI. When comparing the oligomers of the same size (n), it is seen that incorporation of a ladder-type donor unit into O1 decreases the $S_0 \rightarrow S_1$ transition energies by 0.3−0.5 eV and increases the oscillator strengths by 0.9−3.4 in comparison to O2, as expected due to the extended conjugation. The $S_0 \rightarrow S_1$ transitions are mainly HOMO → LUMO in character for all oligomers, though increasing the number of CRUs increases the contribution of the additional electronic configurations. The oligomer conformation has a rather minor effect on the transition energies (wavelengths) and oscillator strengths.

The energies of the vertical $S_0 \rightarrow S_1$, $S_0 \rightarrow S_2$, and $S_0 \rightarrow T_1$ transitions of O1 ($n = 3$) and O2 ($n = 5$) are summarized in Table 2. The energies of the S_1, S_2, and T_1 states of the calculated O2 conformations are ca. 0.1−0.2 eV higher than those of the O1 conformations. The $S_0 \rightarrow S_1$ transition energies in toluene and chloroform for O1 ($n = 3$) and O2 ($n = 5$, Table S11, SI), respectively, are slightly smaller (i.e., red-shifted) than the ones calculated in vacuum (Table 2). The exchange energy (ΔE_{ST}), i.e., the difference between the S_1 and T_1 energies,

gives insight into the relative positioning and intersystem crossing between these two excited states in the polymer.[29,88] For O1 and O2, ΔE_{ST} are almost the same, ca. 0.5−0.6 eV with B3LYP, and are in line with the literature values (~0.6 eV) for conjugated polymers.[29,88] The modestly smaller ΔE_{ST} value of O1 can be explained by its more rigid backbone compared to O2, since ΔE_{ST} has been attributed to the level of the overlap between electron and hole wave functions and a smaller ΔE_{ST} is achieved for more planar polymers.[88] The corresponding CAM-B3LYP results are also presented in Table 2. In all cases, the CAM-B3LYP values are somewhat larger than the B3LYP values, but the trend is the same; i.e., the vertical transition energies of O1 are smaller than those of O2. Additionally, both functionals yield the smallest transition energies for the *syn*-conformations of O1 and O2 (with an exception of the T_1 energy of O2-*syn* calculated with CAM-B3LYP), though these differences are minimal (0.01−0.03 eV).

The extrapolated vertical transition energies reported in Table 3 are ca. 0.3 eV smaller than the HOMO−LUMO gaps (Table 1). However, they follow the same trend; i.e., the vertical transition energies of O1 are smaller than those of O2. Again, the conformation does not significantly affect the values; see the Supporting Information for the extrapolations (Figure S8 and Table S12) and more detailed discussion of the differences between the extrapolation methods. The effective conjugation lengths[80] (Figure S9 and Table S13, SI) calculated from the B3LYP wavelengths of the oligomeric models predict that a limiting conjugation length is reached with $n = 7$ and 9−11 for O1 and O2, respectively. This indicates that the longest oligomers used in this study, i.e., pentamers, would be too short to predict the properties of the polymer chains of **1** and **2** accurately enough. However, the effective conjugation lengths calculated from the CAM-B3LYP values are 5 for O1 and 6 or 7 for O2, which are almost the same as the oligomer sizes used

here. Unfortunately, using longer oligomers in calculations would have been too demanding computationally, and these results cannot be verified. Nevertheless, the experimental absorption maxima (634 nm for **1**[28] and 610 nm for **2**[19]) are already reached with the smaller oligomers (Tables S9−S11, SI), whereas the extrapolated values (Tables 3 and S13, SI) are red-shifted with B3LYP and blue-shifted with CAM-B3LYP when compared to the experimental values. These differences originate again from the MSIE and the different amounts of the exact HF exchange in the functionals.

Calculated absorption spectra of O1 ($n = 3$) and O2 ($n = 5$) are presented in Figure 6. All spectra are characterized by one
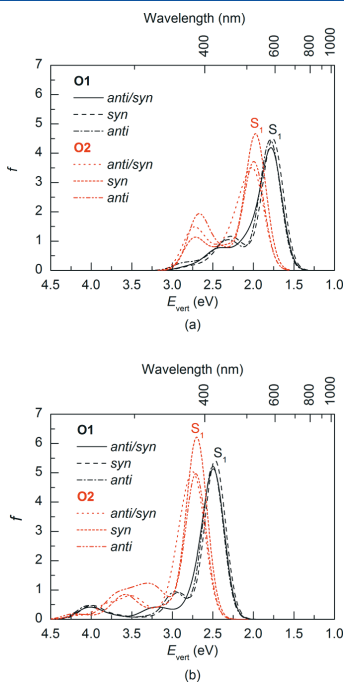
Figure 6. UV−vis absorption spectra of the conformational models of O1 (black, $n = 3$) and O2 (red, $n = 5$) in vacuum calculated with TDDFT at the (a) B3LYP/6-31G** and (b) CAM-B3LYP/6-31G** levels of theory. The spectra were created using a Gaussian-shape broadening with fwhm of 0.30 eV.

broad low-energy transition (at the longer wavelength) and additional smaller high-energy peaks. The overall shape of the calculated spectra resembles the corresponding experimental spectra[17−19,28] and have dual-band features characteristic of D−A copolymers.[89] In the experimental spectra of **1**[28] and **2**,[17−19] however, the dual-band feature is not as visible as in the spectra of other D−A copolymers,[32,89] and instead of two separate bands, merely one dominant low-energy absorption band with a shoulder and one significantly smaller high-energy peak are observed. In the calculated spectra, the first low-energy peaks, i.e., absorption maxima, originate from the $S_0 \rightarrow S_1$ transitions and are mainly HOMO → LUMO in nature for both O1 and O2 (see Tables S9 and S10, SI). The absorption maxima, ca. 1.8 eV for O1 and ca. 2.0 eV for O2, of the spectra calculated with

B3LYP are in good agreement with the experimental values[19,28] (Table 3). However, CAM-B3LYP yields absorption maxima at ca. 2.5 eV for O1 and ca. 2.7 eV for O2, which are somewhat blue-shifted with respect to the experimental values. The higher-energy peaks in the calculated spectra originate from transitions to the higher states (B3LYP, $S_5−S_9$ for O1 and $S_{15}−S_{20}$ for O2; CAM-B3LYP, S_3, $S_{10}−S_{16}$ for O1 and $S_3−S_{14}$ for O2) and are observed at ca. 2.3 eV for O1 and ca. 2.7 eV for O2 with B3LYP, whereas CAM-B3LYP predicts the peaks at ca. 3.0 and 4.0 eV for O1 and at ca. 3.5 eV for O2.

The nature of the electronic transitions was studied using NTOs, which provide a compact description of the electronic transition density matrix and simplify the analysis of the excited states consisting of mixed electronic configurations, which are usually difficult to characterize with MOs.[74] The NTOs reduce the description of an excited-state transition into a single hole− electron excitation whose fraction to the given transition is given by an eigenvalue λ, which is $0 \leq \lambda \leq 1$. The NTOs for the $S_0 \rightarrow S_1$ transition of the *syn*-conformations of O1 and O2 calculated with B3LYP are illustrated in Figure 7. The calculated contributions of the electron densities of the donor and acceptor units to these NTOs are presented in Table 4. Because the conformation does not significantly affect the shapes (or contributions) of the NTOs, the NTOs of the *anti/ syn*- and *anti*-conformations are not illustrated. As mentioned above, the $S_0 \rightarrow S_1$ transitions of O1 and O2 are mainly HOMO → LUMO in nature (see Tables S9 and S10, SI), and thus, the corresponding NTOs (1 in Figure 7) are similar to the FMOs (Figure 5). In O1, the hole and electron are delocalized on the donor and acceptor units in the middle part of the backbone. In the case of O2, two pairs of NTOs are used to describe the $S_0 \rightarrow S_1$ transition. Similar to O1, the dominant hole−electron pair (1 in Figure 7) is delocalized on the donor and acceptor units in the middle part of the backbone, whereas the second pair (2 in Figure 7) is localized on every other repeating unit.

The calculated contributions (Table 4) of the electron densities to the NTOs offer a more detailed account to their distributions over the acceptor and donor units. These results indicate partial charge transfer from the donor units to the acceptor units in the $S_0 \rightarrow S_1$ transitions of both O1 and O2, supporting previous statements[90,91] of the partial ICT nature of the low-energy band in the absorption spectra of the D−A copolymers. In addition, the second NTO pair of O2 shows also partial charge transfer character with almost the same contributions from the donor and acceptor units to NTOs as in the dominant NTOs. It is noteworthy that more electron density (25−29 percentage units) transfers from the donor to the acceptor in O2 than in O1 (15 percentage units). CAM-B3LYP yields contributions close to those predicted by B3LYP. However, the second NTO pair is now required for the description of $S_0 \rightarrow S_1$ transitions of both O1 and O2, as the transitions consist of several electronic configurations rather than just one dominant HOMO → LUMO transition.

Excited-State (S₁ and T₁) Structural Properties of the Oligomeric Models. The optimized S_1 and T_1 excited-state geometries of the *syn*-conformations of O1 ($n = 3$) and O2 ($n = 5$) were determined with TDDFT/B3LYP/6-31G** to investigate geometry relaxation in the low-lying excited states. The S_1 and T_1 geometries of O1 show only modest changes in dihedral angles vs S_0, resulting in only marginally more planarized backbones. For O2-*syn,* the dihedral angles are
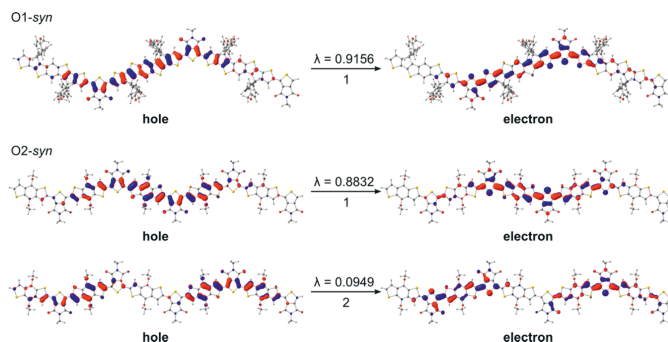
Figure 7. NTOs calculated at the TDDFT/B3LYP/6-31G** level of theory for the $S_0 \rightarrow S_1$ transition of the *syn*-conformations of O1 ($n = 3$) and O2 ($n = 5$) (isodensity contour = 0.025). The eigenvalue λ is the fraction of the hole−electron contribution to the given excitation.

Table 4. Contributions (%) of the Electron Densities of the Donor and Acceptors Units to the NTOs Corresponding to the $S_0 \rightarrow S_1$ Transition in the Oligomeric Models O1 ($n = 3$) and O2 ($n = 5$) As Calculated via C-SPA[70] ^{a}

				hole		electron	
conformation	compound	hole−electron pair	λ	D	A	D	A
anti/syn	O1	1	0.91 (0.61)	81 (81)	19 (19)	66 (67)	34 (33)
		(2)	(0.24)	(76)	(24)	(60)	(40)
	O2	1	0.89 (0.58)	74 (72)	26 (28)	50 (51)	50 (49)
		2	0.09 (0.24)	75 (73)	25 (27)	47 (51)	53 (49)
syn	O1	1	0.92 (0.61)	81 (81)	19 (19)	67 (67)	33 (33)
		(2)	(0.23)	(76)	(24)	(61)	(39)
	O2	1	0.88 (0.57)	75 (74)	25 (26)	50 (52)	50 (48)
		2	0.09 (0.23)	76 (74)	24 (26)	47 (52)	53 (48)
anti	O1	1	0.91 (0.61)	81 (81)	19 (19)	66 (67)	34 (33)
		(2)	(0.24)	(76)	(24)	(60)	(40)
	O2	1	0.88 (0.58)	74 (72)	26 (28)	49 (51)	51 (49)
		2	0.10 (0.23)	75 (72)	25 (28)	47 (50)	53 (50)

^{a}The NTOs were determined with TDDFT at the B3LYP/6-31G** and CAM-B3LYP/6-31G** (in parentheses) levels of theory.

between 6° and 8° in the S_1 geometry and between 4° and 11° in the T_1 geometry (compared with 8−11° in the S_0 geometry).

The differences between the bond lengths of the excited-state (S_1 and T_1) and ground-state (S_0) geometries of the O1-*syn* trimers and the O2-*syn* pentamers are given in Figure 8. The dashed vertical lines divide the CRUs into different sections for an easier comparison of the corresponding parts of O1 and O2. The largest changes occur in the middle of the oligomers. The relaxation in the S_1 state shortens the single bonds and lengthens the double bonds, resulting in an inverse single−double C−C bond pattern (see the graph) compared to that in the S_0 geometry. The bond pattern of the S_1 geometry is similar for O1 and O2. For T_1, the FMOs localize primarily on one donor, with some extension to the two neighboring acceptors; hence, T_1 is shown to be considerably more localized when compared to S_1 (Figure S10, SI). In addition, the T_1 relaxation energies of O1 and O2 differ somewhat, i.e., the ladder-type donor of O1 leads to a slightly larger relaxation energy (24.36 kJ·mol^{-1}) with respect to O2 (20.45 kJ·mol^{-1}), which has the smaller BDT donor.

The BLA values for the S_0, S_1, and T_1 geometries of the *syn*-conformations of O1 and O2 are presented in Table S14 of the SI for the whole backbones and the innermost CRUs (BLA$_{middle}$). Here, we will only focus on the BLA$_{middle}$ values, as this is where the FMOs of the excited states localize (see

Figure 8 and Figure S10, SI). The BLA$_{middle}$ values of the S_0 and S_1 geometries of O1 and O2 are very close to each other. Also, the S_1 relaxation energies are identical for O1 and O2 (10.63 kJ·mol^{-1}). The S_0 geometries of both O1 and O2 show aromatic nature, as discussed above, whereas the BLA$_{middle}$ values of the S_1 geometries are slightly negative, but close to zero, indicating a modest quinoid character. However, the BLA$_{middle}$ values for the T_1 geometries are ca. −0.019 and 0.011 Å for O1 and O2, respectively. In other words, the innermost CRUs in the excited states have more quinoid character than the terminal CRUs, as observed also in other studies.[42,77] However, if the BLA$_{middle}$ of O2 is calculated for the bonds 21−43 (12 double bonds) in order to keep the relative conjugation length (i.e., the number of the double bonds) of the oligomers as consistent as possible, the BLA of the S_0 geometry of O2 is again close to that of O1, but the BLAs of S_1 and T_1 are positive, indicating aromatic character.

■ CONCLUSIONS

In this work, we have theoretically compared the ladder-type BDT-based donor to its smaller counterpart, which has been more widely used in organic solar cells, to understand the structure−property relationships of two D−A copolymers, i.e., **1** and **2**, where these two donors have been used, respectively, together with a TPD acceptor. Our calculations predict some
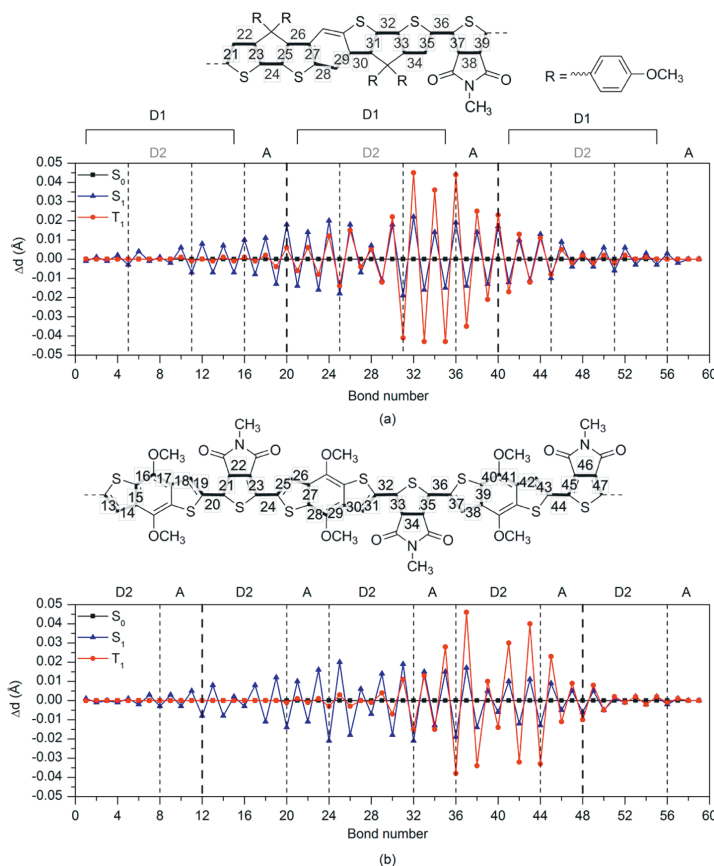
Figure 8. Differences of the bond lengths between the B3LYP/6-31G**-optimized excited-state (S_1 and T_1) and ground-state (S_0) geometries with respect to the bond numbers of (a) O1-*syn* ($n = 3$) and (b) O2-*syn* ($n = 5$) along the numbered conjugation paths marked with bold (only middle CRUs presented here). The dashed lines divide the CRUs into different sections: the ladder-type donor unit of O1 (D1), the BDT donor unit of O2 (D2), and the acceptor unit (A).

general similarities, although the differences in the donor structures also lead to clear differences, for example, in the charge transfer characteristics. The highly curved backbones predicted for the *anti/syn*-conformations of **1** and **2** may hinder polymer chain packing and result in low-ordered films with lower charge-carrier mobilities when compared to *syn*- and *anti*-conformations. The *syn*-conformations are energetically the most favorable structures for both copolymers. However, the *syn*-conformation of **2** is predicted to be less curved than that of **1**, which does not seem to correlate with the reported experimental hole carrier mobilities. One possible explanation for the better hole carrier mobility of **1** could be that the more planar structure predicted by our calculations helps the molecular packing. According to the calculated BLA values, the ground-state geometries of **1** and **2** are aromatic in nature, whereas the S_1 and T_1 geometries present some quinoid character. In addition, the extended conjugation of the stiff ladder-type donor destabilizes both the HOMO and LUMO energies of the ladder copolymer **1** and leads to a smaller gap energy with respect to the copolymer **2**, which has the smaller

BDT donor. Even though the shapes of the spectra of **1** and **2** are similar, the ladder-type donor unit of **1** reduces the transition energies (i.e., leads to red-shifted spectra) and increases the oscillator strengths compared to the smaller BDT donor unit of **2**. The more rigid backbone of **1** leads to a modestly smaller exchange energy. A more significant charge transfer nature is predicted for the less-curved copolymer **2**, which is in agreement with the better power conversion efficiency reported in the literature.

In the future studies, the influence of the more rigid, rodlike structure of the ladder copolymer on molecular packing and the resulting intra- and intermolecular interactions should be also examined. In addition, the use of stronger acceptor units with ladder-type donors should be investigated, because the influence of the acceptor on the charge transfer properties of copolymer **1** seems to be "diluted" by the extended conjugation of the longer ladder-type donor. Such studies would be beneficial in modifying the intrinsic properties and eventual materials performance of ladder copolymers.

Article

■ ASSOCIATED CONTENT

Ⓢ Supporting Information

The Supporting Information is available free of charge on the ACS Publications website at DOI: 10.1021/acs.jpca.5b08465.

Details concerning structural, electronic, and optical properties of the monomer, oligomer, and periodic models: PES scans, total and relative energies, dihedral angles, BLA values, HOMO, LUMO, and HOMO–LUMO gap energies, vertical transition energies, oscillator strengths, electronic configurations, and FMOs of the excited state geometries. Additionally, more detailed discussion of the differences between the extrapolation methods is provided. (PDF)

■ AUTHOR INFORMATION

Corresponding Authors

*T.K.: e-mail, tuuva.kastinen@tut.fi.

*T.I.H: e-mail, terttu.hukka@tut.fi; telephone, +358 40 198 1133.

Notes

The authors declare no competing financial interest.

■ ACKNOWLEDGMENTS

■ REFERENCES

(1) Blom, P. W. M.; Mihailetchi, V. D.; Koster, L. J. A.; Markov, D. E. Device Physics of Polymer:Fullerene Bulk Heterojunction Solar Cells. *Adv. Mater.* **2007**, *19*, 1551−1566.

(2) Thompson, B. C.; Fréchet, J. M. J. Polymer-Fullerene Composite Solar Cells. *Angew. Chem., Int. Ed.* **2008**, *47*, 58−77.

(3) Yu, G.; Gao, J.; Hummelen, J. C.; Wudl, F.; Heeger, A. J. Polymer Photovoltaic Cells: Enhanced Efficiencies via a Network of Internal Donor-Acceptor Heterojunctions. *Science* **1995**, *270*, 1789−1791.

(4) Wienk, M. M.; Kroon, J. M.; Verhees, W. J. H.; Knol, J.; Hummelen, J. C.; van Hal, P. A.; Janssen, R. A. J. Efficient Methano[70]fullerene/MDMO-PPV Bulk Heterojunction Photovoltaic Cells. *Angew. Chem., Int. Ed.* **2003**, *42*, 3371−3375.

(5) He, Z.; Zhong, C.; Su, S.; Xu, M.; Wu, H.; Cao, Y. Enhanced Power-Conversion Efficiency in Polymer Solar Cells Using an Inverted Device Structure. *Nat. Photonics* **2012**, *6*, 591−595.

(6) Ma, W.; Yang, C.; Gong, X.; Lee, K.; Heeger, A. J. Thermally Stable, Efficient Polymer Solar Cells with Nanoscale Control of the Interpenetrating Network Morphology. *Adv. Funct. Mater.* **2005**, *15*, 1617−1622.

(7) Chen, H.-Y.; Hou, J.; Zhang, S.; Liang, Y.; Yang, G.; Yang, Y.; Yu, L.; Wu, Y.; Li, G. Polymer Solar Cells with Enhanced Open-Circuit Voltage and Efficiency. *Nat. Photonics* **2009**, *3*, 649−653.

(8) Liang, Y.; Xu, Z.; Xia, J.; Tsai, S.-T.; Wu, Y.; Li, G.; Ray, C.; Yu, L. For the Bright Future—Bulk Heterojunction Polymer Solar Cells with Power Conversion Efficiency of 7.4%. *Adv. Mater.* **2010**, *22*, E135−E138.

(9) You, J.; Dou, L.; Yoshimura, K.; Kato, T.; Ohya, K.; Moriarty, T.; Emery, K.; Chen, C.-C.; Gao, J.; Li, G.; et al. A Polymer Tandem Solar Cell with 10.6% Power Conversion Efficiency. *Nat. Commun.* **2013**, *4*, 1446.

(10) Havinga, E. E.; ten Hoeve, W.; Wynberg, H. A New Class of Small Band Gap Organic Polymer Conductors. *Polym. Bull.* **1992**, *29*, 119−126.

(11) Soci, C.; Hwang, I.-W.; Moses, D.; Zhu, Z.; Waller, D.; Gaudiana, R.; Brabec, C. J.; Heeger, A. J. Photoconductivity of a Low-Bandgap Conjugated Polymer. *Adv. Funct. Mater.* **2007**, *17*, 632−636.

(12) Scharber, M. C.; Mühlbacher, D.; Koppe, M.; Denk, P.; Waldauf, C.; Heeger, A. J.; Brabec, C. J. Design Rules for Donors in Bulk-Heterojunction Solar Cells—Towards 10% Energy-Conversion Efficiency. *Adv. Mater.* **2006**, *18*, 789−794.

(13) Price, S. C.; Stuart, A. C.; Yang, L.; Zhou, H.; You, W. Fluorine Substituted Conjugated Polymer of Medium Band Gap Yields 7% Efficiency in Polymer−Fullerene Solar Cells. *J. Am. Chem. Soc.* **2011**, *133*, 4625−4631.

(14) Zhou, H.; Yang, L.; Stuart, A. C.; Price, S. C.; Liu, S.; You, W. Development of Fluorinated Benzothiadiazole as a Structural Unit for a Polymer Solar Cell of 7% Efficiency. *Angew. Chem., Int. Ed.* **2011**, *50*, 2995−2998.

(15) Cabanetos, C.; El Labban, A.; Bartelt, J. A.; Douglas, J. D.; Mateker, W. R.; Fréchet, J. M. J.; McGehee, M. D.; Beaujuge, P. M. Linear Side Chains in Benzo[1,2-*b*:4,5-*b′*]dithiophene-Thieno[3,4-*c*]pyrrole-4,6-dione Polymers Direct Self-Assembly and Solar Cell Performance. *J. Am. Chem. Soc.* **2013**, *135*, 4656−4659.

(16) Liu, C.; Wang, K.; Hu, X.; Yang, Y.; Hsu, C.-H.; Zhang, W.; Xiao, S.; Gong, X.; Cao, Y. Molecular Weight Effect on the Efficiency of Polymer Solar Cells. *ACS Appl. Mater. Interfaces* **2013**, *5*, 12163−12167.

(17) Zou, Y.; Najari, A.; Berrouard, P.; Beaupré, S.; Réda Aïch, B.; Tao, Y.; Leclerc, M. A Thieno[3,4-*c*]pyrrole-4,6-dione-Based Copolymer for Efficient Solar Cells. *J. Am. Chem. Soc.* **2010**, *132*, 5330−5331.

(18) Piliego, C.; Holcombe, T. W.; Douglas, J. D.; Woo, C. H.; Beaujuge, P. M.; Fréchet, J. M. J. Synthetic Control of Structural Order in *N*-alkylthieno[3,4-*c*]pyrrole-4,6-dione-Based Polymers for Efficient Solar Cells. *J. Am. Chem. Soc.* **2010**, *132*, 7595−7597.

(19) Zhang, Y.; Hau, S. K.; Yip, H.-L.; Sun, Y.; Acton, O.; Jen, A. K.-Y. Efficient Polymer Solar Cells Based on the Copolymers of Benzodithiophene and Thienopyrroledione. *Chem. Mater.* **2010**, *22*, 2696−2698.

(20) Chen, Y.-C.; Yu, C.-Y.; Fan, Y.-L.; Hung, L.-I.; Chen, C.-P.; Ting, C. Low-Bandgap Conjugated Polymer for High Efficient Photovoltaic Applications. *Chem. Commun.* **2010**, *46*, 6503−6505.

(21) Zheng, Q.; Jung, B. J.; Sun, J.; Katz, H. E. Ladder-Type Oligo-*p*-phenylene-Containing Copolymers with High Open-Circuit Voltages and Ambient Photovoltaic Activity. *J. Am. Chem. Soc.* **2010**, *132*, 5394−5404.

(22) Wang, J.-Y.; Hau, S. K.; Yip, H.-L.; Davies, J. A.; Chen, K.-S.; Zhang, Y.; Sun, Y.; Jen, A. K.-Y. Benzobis(silolothiophene)-Based Low Bandgap Polymers for Efficient Polymer Solar Cells. *Chem. Mater.* **2011**, *23*, 765−767.

(23) Yu, C.-Y.; Chen, C.-P.; Chan, S.-H.; Hwang, G.-W.; Ting, C. Thiophene/Phenylene/Thiophene-Based Low-Bandgap Conjugated Polymers for Efficient Near-Infrared Photovoltaic Applications. *Chem. Mater.* **2009**, *21*, 3262−3269.

(24) Chen, C.-H.; Cheng, Y.-J.; Chang, C.-Y.; Hsu, C.-S. Donor−Acceptor Random Copolymers Based on a Ladder-Type Nonacyclic Unit: Synthesis, Characterization, and Photovoltaic Applications. *Macromolecules* **2011**, *44*, 8415−8424.

(25) Roncali, J. Molecular Engineering of the Band Gap of π-Conjugated Systems: Facing Technological Applications. *Macromol. Rapid Commun.* **2007**, *28*, 1761−1775.

(26) He, F.; Wang, W.; Chen, W.; Xu, T.; Darling, S. B.; Strzalka, J.; Liu, Y.; Yu, L. Tetrathienoanthracene-Based Copolymers for Efficient Solar Cells. *J. Am. Chem. Soc.* **2011**, *133*, 3284−3287.

(27) Baek, N. S.; Hau, S. K.; Yip, H.-L.; Acton, O.; Chen, K.-S.; Jen, A. K.-Y. High Performance Amorphous Metallated π-Conjugated Polymers for Field-Effect Transistors and Polymer Solar Cells. *Chem. Mater.* **2008**, *20*, 5734−5736.

(28) Chen, Y.-L.; Chang, C.-Y.; Cheng, Y.-J.; Hsu, C.-S. Synthesis of a New Ladder-Type Benzodi(cyclopentadithiophene) Arene with

Forced Planarization Leading to an Enhanced Efficiency of Organic Photovoltaics. *Chem. Mater.* **2012**, *24*, 3964−3971.

(29) Risko, C.; McGehee, M. D.; Bredas, J.-L. A Quantum-Chemical Perspective into Low Optical-Gap Polymers for Highly-Efficient Organic Solar Cells. *Chem. Sci.* **2011**, *2*, 1200−1218.

(30) Pandey, L.; Doiron, C.; Sears, J. S.; Brédas, J.-L. Lowest Excited States and Optical Absorption Spectra of Donor-Acceptor Copolymers for Organic Photovoltaics: A New Picture Emerging from Tuned Long-Range Corrected Density Functionals. *Phys. Chem. Chem. Phys.* **2012**, *14*, 14243−14248.

(31) Jackson, N. E.; Savoie, B. M.; Kohlstedt, K. L.; Olvera de la Cruz, M.; Schatz, G. C.; Chen, L. X.; Ratner, M. A. Controlling Conformations of Conjugated Polymers and Small Molecules: The Role of Nonbonding Interactions. *J. Am. Chem. Soc.* **2013**, *135*, 10475−10483.

(32) Blouin, N.; Michaud, A.; Gendron, D.; Wakim, S.; Blair, E.; Neagu-Plesu, R.; Belletête, M.; Durocher, G.; Tao, Y.; Leclerc, M. Toward a Rational Design of Poly(2,7-Carbazole) Derivatives for Solar Cells. *J. Am. Chem. Soc.* **2008**, *130*, 732−742.

(33) Liu, X.; He, R.; Shen, W.; Li, M. Theoretical Design of Donor-Acceptor Conjugated Copolymers Based on Furo-, Thieno-, and Selenopheno[3,4-c] thiophene-4,6-dione and Benzodithiophene Units for Organic Solar Cells. *J. Mol. Model.* **2013**, *19*, 4283−4291.

(34) Zhang, L.; Yu, M.; Zhao, H.; Wang, Y.; Gao, J. Theoretical Investigations on the Electronic and Optical Characteristics of Fused-Ring Homopolymers: Comparison of Oligomer Method and PBC−DFT Method. *Chem. Phys. Lett.* **2013**, *570*, 153−158.

(35) Pandey, L.; Risko, C.; Norton, J. E.; Brédas, J.-L. Donor−Acceptor Copolymers of Relevance for Organic Photovoltaics: A Theoretical Investigation of the Impact of Chemical Structure Modifications on the Electronic and Optical Properties. *Macromolecules* **2012**, *45*, 6405−6414.

(36) Ko, S.; Mondal, R.; Risko, C.; Lee, J. K.; Hong, S.; McGehee, M. D.; Brédas, J.-L.; Bao, Z. Tuning the Optoelectronic Properties of Vinylene-Linked Donor−Acceptor Copolymers for Organic Photovoltaics. *Macromolecules* **2010**, *43*, 6685−6698.

(37) Salvatori, P.; Mosconi, E.; Wang, E.; Andersson, M.; Muccini, M.; De Angelis, F. Computational Modeling of Isoindigo-Based Polymers Used in Organic Solar Cells. *J. Phys. Chem. C* **2013**, *117*, 17940−17954.

(38) Gibson, G. L.; McCormick, T. M.; Seferos, D. S. Atomistic Band Gap Engineering in Donor−Acceptor Polymers. *J. Am. Chem. Soc.* **2012**, *134*, 539−547.

(39) Zhang, L.; Zhang, Q.; Ren, H.; Yan, H.; Zhang, J.; Zhang, H.; Gu, J. Calculation of Band Gap in Long Alkyl-Substituted Heterocyclic-Thiophene-Conjugated Polymers with Electron Donor−Acceptor Fragment. *Sol. Energy Mater. Sol. Cells* **2008**, *92*, 581−587.

(40) Manninen, V.; Niskanen, M.; Hukka, T. I.; Pasker, F.; Claus, S.; Höger, S.; Baek, J.; Umeyama, T.; Imahori, H.; Lemmetyinen, H. Conjugated Donor-Acceptor (D-A) Copolymers in Inverted Organic Solar Cells—A Combined Experimental and Modelling Study. *J. Mater. Chem. A* **2013**, *1*, 7451−7462.

(41) Niskanen, M.; Hukka, T. I. Modeling of Photoactive Conjugated Donor-Acceptor Copolymers: The Effect of the Exact HF Exchange in DFT Functionals on Geometries and Gap Energies of Oligomer and Periodic Models. *Phys. Chem. Chem. Phys.* **2014**, *16*, 13294−13305.

(42) Suramitr, S.; Meeto, W.; Wolschann, P.; Hannongbua, S. Understanding on Absorption and Fluorescence Electronic Transitions of Carbazole-Based Conducting Polymers: TD-DFT Approaches. *Theor. Chem. Acc.* **2010**, *125*, 35−44.

(43) Brédas, J. L. Relationship between Band Gap and Bond Length Alternation in Organic Conjugated Polymers. *J. Chem. Phys.* **1985**, *82*, 3808−3811.

(44) Kirtman, B.; Champagne, B.; Bishop, D. M. Electric Field Simulation of Substituents in Donor−Acceptor Polyenes: A Comparison with Ab Initio Predictions for Dipole Moments, Polarizabilities, and Hyperpolarizabilities. *J. Am. Chem. Soc.* **2000**, *122*, 8007−8012.

(45) Jacquemin, D.; Femenias, A.; Chermette, H.; Ciofini, I.; Adamo, C.; André, J.-M.; Perpète, E. A. Assessment of Several Hybrid DFT Functionals for the Evaluation of Bond Length Alternation of Increasingly Long Oligomers. *J. Phys. Chem. A* **2006**, *110*, 5952−5959.

(46) Körzdörfer, T.; Parrish, R. M.; Sears, J. S.; Sherrill, C. D.; Brédas, J.-L. On the Relationship between Bond-Length Alternation and Many-Electron Self-Interaction Error. *J. Chem. Phys.* **2012**, *137*, 124305.

(47) Jacquemin, D.; Adamo, C. Bond Length Alternation of Conjugated Oligomers: Wave Function and DFT Benchmarks. *J. Chem. Theory Comput.* **2011**, *7*, 369−376.

(48) Gierschner, J.; Cornil, J.; Egelhaaf, H.-J. Optical Bandgaps of π-Conjugated Organic Materials at the Polymer Limit: Experiment and Theory. *Adv. Mater.* **2007**, *19*, 173−191.

(49) Wykes, M.; Milián-Medina, B.; Gierschner, J. Computational Engineering of Low Bandgap Copolymers. *Front. Chem.* **2013**, *1*, DOI: 10.3389/fchem.2013.00035

(50) Zade, S. S.; Bendikov, M. From Oligomers to Polymer: Convergence in the HOMO-LUMO Gaps of Conjugated Oligomers. *Org. Lett.* **2006**, *8*, 5243−5246.

(51) Zade, S. S.; Zamoshchik, N.; Bendikov, M. From Short Conjugated Oligomers to Conjugated Polymers. Lessons from Studies on Long Conjugated Oligomers. *Acc. Chem. Res.* **2011**, *44*, 14−24.

(52) Kudin, K. N.; Scuseria, G. E. A Fast Multipole Algorithm for the Efficient Treatment of the Coulomb Problem in Electronic Structure Calculations of Periodic Systems with Gaussian Orbitals. *Chem. Phys. Lett.* **1998**, *289*, 611−616.

(53) Kudin, K. N.; Scuseria, G. E. Linear-Scaling Density-Functional Theory with Gaussian Orbitals and Periodic Boundary Conditions: Efficient Evaluation of Energy and Forces via the Fast Multipole Method. *Phys. Rev. B: Condens. Matter Mater. Phys.* **2000**, *61*, 16440−16453.

(54) Cao, H.; Ma, J.; Zhang, G.; Jiang, Y. Borole/Thiophene Cooligomers and Copolymers with Quinoid Structures and Biradical Characters. *Macromolecules* **2005**, *38*, 1123−1130.

(55) Walker, W.; Veldman, B.; Chiechi, R.; Patil, S.; Bendikov, M.; Wudl, F. Visible and Near-Infrared Absorbing, Low Band Gap Conjugated Oligomers Based on Cyclopentadieneones. *Macromolecules* **2008**, *41*, 7278−7280.

(56) Patra, A.; Wijsboom, Y. H.; Zade, S. S.; Li, M.; Sheynin, Y.; Leitus, G.; Bendikov, M. Poly(3,4-Ethylenedioxyselenophene). *J. Am. Chem. Soc.* **2008**, *130*, 6734−6736.

(57) Tian, Y.-H.; Kertesz, M. Ladder-Type Polyenazine Based on Intramolecular S⋯N Interactions: A Theoretical Study of a Small-Bandgap Polymer. *Macromolecules* **2009**, *42*, 6123−6127.

(58) Chou, Y.-M.; Chen, W.-H.; Liang, C.-C. Substituent Effects and Photo-Physical Properties in Polythiophene and Its Derivatives: A PBC-DFT Study. *J. Mol. Struct.: THEOCHEM* **2009**, *894*, 117−120.

(59) Tian, Y.-H.; Kertesz, M. Low-Bandgap Pyrazine Polymers: Ladder-Type Connectivity by Intramolecular S⋯N(sp2) Interactions and Hydrogen Bonds. *Macromolecules* **2009**, *42*, 2309−2312.

(60) Kumar, A.; Bokria, J. G.; Buyukmumcu, Z.; Dey, T.; Sotzing, G. A. Poly(thieno[3,4-b]furan), a New Low Band Gap Polymer: Experiment and Theory. *Macromolecules* **2008**, *41*, 7098−7108.

(61) Pappenfus, T. M.; Schmidt, J. A.; Koehn, R. E.; Alia, J. D. PBC-DFT Applied to Donor−Acceptor Copolymers in Organic Solar Cells: Comparisons between Theoretical Methods and Experimental Data. *Macromolecules* **2011**, *44*, 2354−2357.

(62) Niedzialek, D.; Lemaur, V.; Dudenko, D.; Shu, J.; Hansen, M. R.; Andreasen, J. W.; Pisula, W.; Müllen, K.; Cornil, J.; Beljonne, D. Probing the Relation between Charge Transport and Supramolecular Organization down to ångström Resolution in a Benzothiadiazole-Cyclopentadithiophene Copolymer. *Adv. Mater.* **2013**, *25*, 1939−1947.

(63) McNaught, A. D.; Wilkinson, A. *IUPAC. Compendium of Chemical Terminology (the "Gold Book")*, 2nd ed.; Blackwell Scientific Publications: Oxford, 1997.

(64) Frisch, M. J.; Trucks, G. W.; Schlegel, H. B.; Scuseria, G. E.; Robb, M. A.; Cheeseman, J. R.; Scalmani, G.; Barone, V.; Mennucci,

B.; Petersson, G. A.; et al. *Gaussian 09*, Revision C.01; Gaussian, Inc.: Wallingford, CT, 2009.

(65) Becke, A. D. Density-Functional Thermochemistry. III. The Role of Exact Exchange. *J. Chem. Phys.* **1993**, *98*, 5648–5652.

(66) Lee, C.; Yang, W.; Parr, R. G. Development of the Colle-Salvetti Correlation-Energy Formula into a Functional of the Electron Density. *Phys. Rev. B: Condens. Matter Mater. Phys.* **1988**, *37*, 785–789.

(67) Yanai, T.; Tew, D. P.; Handy, N. C. A New Hybrid Exchange–Correlation Functional Using the Coulomb-Attenuating Method (CAM-B3LYP). *Chem. Phys. Lett.* **2004**, *393*, 51–57.

(68) Chai, J.-D.; Head-Gordon, M. Long-Range Corrected Hybrid Density Functionals with Damped Atom-Atom Dispersion Corrections. *Phys. Chem. Chem. Phys.* **2008**, *10*, 6615–6620.

(69) Zhurko, G. A.; Zhurko, D. A. ChemCraft version 1.70. http://www.chemcraftprog.com.

(70) Ros, P.; Schuit, G. C. A. Molecular Orbital Calculations on Copper Chloride Complexes. *Theor. Chim. Acta* **1966**, *4*, 1–12.

(71) Multiwfn 3.3.6. http://multiwfn.codeplex.com/.

(72) Lu, T.; Chen, F. Multiwfn: A Multifunctional Wavefunction Analyzer. *J. Comput. Chem.* **2012**, *33*, 580–592.

(73) Lu, T.; Chen, F. Calculation of Molecular Orbital Composition. *Acta Chim. Sin.* **2011**, *69*, 2393–2406.

(74) Martin, R. L. Natural Transition Orbitals. *J. Chem. Phys.* **2003**, *118*, 4775.

(75) Cancès, E.; Mennucci, B.; Tomasi, J. A New Integral Equation Formalism for the Polarizable Continuum Model: Theoretical Background and Applications to Isotropic and Anisotropic Dielectrics. *J. Chem. Phys.* **1997**, *107*, 3032.

(76) Mennucci, B.; Cancès, E.; Tomasi, J. Evaluation of Solvent Effects in Isotropic and Anisotropic Dielectrics and in Ionic Solutions with a Unified Integral Equation Method: Theoretical Bases, Computational Implementation, and Numerical Applications. *J. Phys. Chem. B* **1997**, *101*, 10506–10517.

(77) Milián-Medina, B.; Gierschner, J. π-Conjugation. *Wiley Interdiscip. Rev. Comput. Mol. Sci.* **2012**, *2*, 513–524.

(78) Kuhn, W. Über Das Absorptionsspektrum Der Polyene. *Helv. Chim. Acta* **1948**, *31*, 1780–1799.

(79) Lewis, G. N.; Calvin, M. The Color of Organic Substances. *Chem. Rev.* **1939**, *25*, 273–328.

(80) Meier, H.; Stalmach, U.; Kolshorn, H. Effective Conjugation Length and UV/vis Spectra of Oligomers. *Acta Polym.* **1997**, *48*, 379–384.

(81) Rieger, R.; Beckmann, D.; Mavrinskiy, A.; Kastler, M.; Müllen, K. Backbone Curvature in Polythiophenes. *Chem. Mater.* **2010**, *22*, 5314–5318.

(82) Osaka, I.; Abe, T.; Shinamura, S.; Takimiya, K. Impact of Isomeric Structures on Transistor Performances in Naphthodithiophene Semiconducting Polymers. *J. Am. Chem. Soc.* **2011**, *133*, 6852–6860.

(83) Deng, Y.; Chen, Y.; Zhang, X.; Tian, H.; Bao, C.; Yan, D.; Geng, Y.; Wang, F. Donor–Acceptor Conjugated Polymers with Dithienocarbazoles as Donor Units: Effect of Structure on Semiconducting Properties. *Macromolecules* **2012**, *45*, 8621–8627.

(84) Bartelt, J. A.; Beiley, Z. M.; Hoke, E. T.; Mateker, W. R.; Douglas, J. D.; Collins, B. A.; Tumbleston, J. R.; Graham, K. R.; Amassian, A.; Ade, H.; et al. The Importance of Fullerene Percolation in the Mixed Regions of Polymer-Fullerene Bulk Heterojunction Solar Cells. *Adv. Energy Mater.* **2013**, *3*, 364–374.

(85) Körzdörfer, T.; Sears, J. S.; Sutton, C.; Brédas, J.-L. Long-Range Corrected Hybrid Functionals for π-Conjugated Systems: Dependence of the Range-Separation Parameter on Conjugation Length. *J. Chem. Phys.* **2011**, *135*, 204107.

(86) Banerji, N.; Gagnon, E.; Morgantini, P.-Y.; Valouch, S.; Mohebbi, A. R.; Seo, J.-H.; Leclerc, M.; Heeger, A. J. Breaking Down the Problem: Optical Transitions, Electronic Structure, and Photoconductivity in Conjugated Polymer PCDTBT and in Its Separate Building Blocks. *J. Phys. Chem. C* **2012**, *116*, 11456–11469.

(87) Bredas, J.-L. Mind the Gap! *Mater. Horiz.* **2014**, *1*, 17–19.

(88) Köhler, A.; Beljonne, D. The Singlet–Triplet Exchange Energy in Conjugated Polymers. *Adv. Funct. Mater.* **2004**, *14*, 11–18.

(89) Beaujuge, P. M.; Amb, C. M.; Reynolds, J. R. Spectral Engineering in π-Conjugated Polymers with Intramolecular Donor-Acceptor Interactions. *Acc. Chem. Res.* **2010**, *43*, 1396–1407.

(90) Jenekhe, S. A.; Lu, L.; Alam, M. M. New Conjugated Polymers with Donor–Acceptor Architectures: Synthesis and Photophysics of Carbazole–Quinoline and Phenothiazine–Quinoline Copolymers and Oligomers Exhibiting Large Intramolecular Charge Transfer. *Macromolecules* **2001**, *34*, 7315–7324.

(91) Kulkarni, A. P.; Zhu, Y.; Babel, A.; Wu, P.-T.; Jenekhe, S. A. New Ambipolar Organic Semiconductors. 2. Effects of Electron Acceptor Strength on Intramolecular Charge Transfer Photophysics, Highly Efficient Electroluminescence, and Field-Effect Charge Transport of Phenoxazine-Based Donor–Acceptor Materials. *Chem. Mater.* **2008**, *20*, 4212–4223.

PUBLICATION

II

PAPER

On describing the optoelectronic characteristics of poly(benzodithiophene-*co*-quinoxaline)– fullerene complexes: the influence of optimally tuned density functionals†

T. Kastinen,*[a] M. Niskanen,[ab] C. Risko,[c] O. Cramariuc*[d] and T. I. Hukka*[a]

Here, we investigate the effects of both tuning the range-separation parameter of long-range corrected (LRC) density functionals and including dispersion corrections on describing the local optoelectronic properties of polymer–fullerene interfaces that are critical to the performance of polymer solar cells (PSCs). Focusing on recently studied (Chen, *et al.*, *Chem. Mater.*, 2012, **24**, 4766–4772) PSC active layers derived from poly(benzodithiophene-*co*-quinoxaline) and substituted fullerene PC$_{71}$BM, we compare the performance of global hybrid functionals (B3LYP and B3LYP-D) alongside two LRC functionals (ωB97X and ωB97X-D) and their optimally tuned (OT) analogs (OT-ωB97X and OT-ωB97X-D). Our results confirm that OT-LRC functionals generally improve the description of the optical properties of the individual materials with respect to experiment. For electron-donor (eD)–electron-acceptor (eA) complexes used to describe the local optoelectronic properties of the material interface, PC$_{71}$BM is found to preferentially settle near the quinoxaline acceptor units on the copolymer backbone, regardless of the functional, though dispersion corrections have a strong influence on the intermolecular distances and, in turn, the nature of the excited states. All functionals yield very similar descriptions of the transition maxima for the complexes, *i.e.* predominant local excitations on the copolymer. Importantly, tuning the range-separation parameter of the LRC functional is shown to have a profound effect, as the OT functionals allow for the description of the charge transfer states of the eD–eA complexes, while the non-tuned LRC functionals predict only local intramolecular excitations. These results hold considerable importance for deriving the appropriate physical understanding of the interfacial structure–property–function relationships of PSCs.

[a] *Department of Chemistry and Bioengineering, Tampere University of Technology, P.O. Box 541, FI-33101 Tampere, Finland. E-mail: tuuva.kastinen@tut.fi, terttu.hukka@tut.fi*

[b] *Department of Physics, Imperial College London, South Kensington Campus, London SW7 2AZ, UK*

[c] *Department of Chemistry and Center for Applied Energy Research, University of Kentucky, Lexington, Kentucky 40506-0055, USA*

[d] *Department of Physics, Tampere University of Technology, P.O. Box 692, FI-33101 Tampere, Finland. E-mail: oana.cramariuc@tut.fi*

† Electronic supplementary information (ESI) available: Details concerning the optoelectronic properties of D–A copolymer models and fullerene derivatives: PES scan of the monomer, total and relative energies of the copolymer models, bond numbers and bond length differences of copolymer models, DFT and TDDFT results of O3-*anti* and fullerene derivatives at their B3LYP-optimized geometries, and the UV-vis spectra of O3-*anti* in solution. Additionally, more details concerning the structures of the O3p–PC$_{71}$BM models and their results, *i.e.* potential energy scans, interaction energies, excited state properties, UV-vis spectra, and NTOs, are provided. See DOI: 10.1039/c6cp04567g

Introduction

Polymer solar cells (PSCs), where π-conjugated polymers acting as electron-donor (eD) materials are paired with molecular electron-acceptor (eA) materials, typically fullerene derivatives, to comprise the photoactive layer, have shown considerable photovoltaic performance gains over the past few years.[1–7] In particular, the design of copolymers[8,9] incorporating electron-rich donor (D) moieties and electron-deficient acceptor (A) moieties in the constitutional repeating unit (CRU) has been a key driver in the improved performance of PSCs. Fine tuning of the structural and electronic properties of the D–A copolymer, *e.g.* ionization energies (IEs), electron affinities (EAs), and optical characteristics, through an appropriate choice of donor and acceptor moieties allows synthetic chemists to aim for "ideal" optoelectronic properties,[1,10,11] and improve device performance through materials design.

Thin-film PSCs take advantage of the bulk heterojunction (BHJ) architecture,[12] obtained by blending eD and eA materials. The BHJ interpenetrating network maximizes the interfacial contact surface area, leading to high efficiencies of exciton

27654 | *Phys. Chem. Chem. Phys.*, 2016, **18**, 27654–27670

This journal is © the Owner Societies 2016

dissociation, occurring through interfacial charge-transfer (CT) excited states, in the solar cell. The relative orientations of eD and eA molecules at these eD–eA interfaces have a great impact on the exciton dissociation and charge generation and recombination processes that are critical for the performance of a PSC.[13–15]

Theoretical modeling can offer considerable insight into the structure–property–function relationships of the eD–eA interface. However, the accuracy of the theoretical description of these phenomena depends greatly on the level of the theory employed, and thus it is important to validate the methods being applied in these studies.[16,17] Density functional theory (DFT) and its time-dependent (TDDFT) analog are widely used methods to explore the optoelectronic properties of organic electronic materials due to their balance of accuracy and computational efficiency.[13–15,18–28] The choice of approximate exchange–correlation (xc) functional sets limits to both the accuracy and the efficiency of the DFT methods. Global hybrid functionals that include a fixed, global fraction of explicit Hartree–Fock (HF) exchange, *e.g.* B3LYP (20% HF exchange), have become especially popular in studying organic electronic materials due to an improved description of various molecular properties (*e.g.* geometries, interaction energies, vibrational energies, *etc.*). However, it is well known that B3LYP and other global hybrid functionals have shortcomings in describing several properties of interest in these materials, including the underestimation of the bond-length alternation (BLA) pattern within the π-conjugated framework,[29] IEs,[30] fundamental gaps,[30,31] and excited-state energies,[22] and the overestimation of the wave function delocalization,[29] torsional barriers,[32,33] and intermolecular electronic couplings.[34] Many of these issues originate from the many-electron self-interaction error (MSIE)[35] and an incorrect description of the asymptotic region of the xc potential. While the inclusion of full (100%) HF exchange would correct these differences, short-range (SR) electron correlation effects, which are best described by semilocal exchange, should also be taken into account for the correct description of chemical bonding, *etc.*[34]

In range-separated hybrid (RSH) functionals,[36–38] the combination of both types of exchanges is achieved by separating the electron–electron interaction into long-range (LR) and SR parts using some separation operator, *e.g.* the standard error function (erf):

$$\frac{1}{r_{12}} = \underbrace{\frac{\text{erf}(\omega r_{12})}{r_{12}}}_{\text{LR}} + \underbrace{\frac{1 - \text{erf}(\omega r_{12})}{r_{12}}}_{\text{SR}}, \qquad (1)$$

where ω is the range-separation parameter. The inverse of ω, *i.e.* $1/\omega$, is then a characteristic length scale for the transition between the LR and SR descriptions. The LR and SR parts of the Coulomb operator are treated differently depending on the approach: in so-called screened-exchange hybrid functionals,[39–42] a finite amount of HF exchange is used at SR and none at LR; this implementation, for instance, has a reduced computational cost for extended, *i.e.*, solid state systems.[40] In the class of RSH functionals referred to as long range-corrected (LRC) hybrid functionals,[30,34,38,43–46] the full HF exchange and semilocal correlation are employed to treat the LR part of eqn (1), while a semilocal or standard hybrid DFT functional is employed to treat the SR part of eqn (1). Previous studies[30,47–49] have shown ω to be sensitive

to the system of interest, and thus using default values of ω found in many computational chemistry software suites can lead to incorrect results for a particular system. Determining the optimal ω, generally using the tuning procedure introduced by Stein, Kronik, and Baer (see the Computational details section for more information on the procedure),[49,50] has been proven to be an efficient method for achieving an optimal ω for organic electronic materials. These so-called optimally tuned (OT) LRC functionals have been applied previously in the studies of homopolymers,[51,52] D–A copolymers,[20,22,23,52] and fullerene derivatives[53,54] employed in PSCs. In the case of D–A copolymers, the tuning of ω improves[20,22,23] the description of the singlet vertical transition energies, leading to better correspondence between theoretical UV-vis absorption spectra and those obtained experimentally. In addition, OT-LRC functionals have been employed to study the nature of low-lying singlet and triplet excited states in model pentacene–C_{60} complexes[24,25,27,28] and those of benzothiadiazole-based (D–A–A)-type donor molecules, DTDCTB and C_{60}.[55]

Moreover, weak dispersion interactions are known to play an important role in describing eD–eA interface configurations. Functionals incorporating empirical dispersion corrections have been employed in some studies of eD–eA interfaces, including model complexes of pentacene–C_{60}[25] and DTDCTB–C_{60}.[56] Of relevance to this work, investigations of eD–eA interface configurations with D–A copolymers and fullerene derivatives have been carried out with the global hybrid B3LYP[57] and the non-tuned LRC CAM-B3LYP.[58–61] However, systematic computational studies to determine the effect of both the tuning of a LRC functional and the inclusion of dispersion corrections on the description of this type of interface remain limited.[62,63]

In this study, we investigate the optoelectronic properties of the eD–eA interface formed between a benzodithiophene-quinoxaline-based D–A copolymer, *i.e.* poly{4,8-bis(2′-ethylhexyloxy)-benzo[1,2-*b*:4,5-*b*′]-dithiophene-*alt*-[5,8-bis(5′-thiophen-2′-yl)-6,7-difluoro-2,3-bis(3″-hexyloxyphenyl)quinoxaline]},[7] as the eD (Fig. 1a) and PC$_{71}$BM (Fig. 1b) as the eA; the properties of PC$_{61}$BM (Fig. 1b) are also characterized. Heterocyclic quinoxalines have been used as acceptor units in several D–A copolymer-based BHJ PSCs[64–67] due to the high EAs induced by two nitrogen atoms in the second benzene ring of quinoxaline. The benzo[1,2-*b*:4,5-*b*′]-dithiophene (BDT) unit, where one benzene and two thiophene rings are fused together, has been successfully used as a donor in D–A copolymers of high-performing BHJ PSCs.[2–6] Additionally, a BDT-based copolymer using thieno[3,4-*b*]thiophene as an acceptor unit has shown promising properties as a hole transport material in a perovskite solar cell.[68] A comparison of the results obtained from conventional hybrid functionals and non-tuned and OT-LRC functionals sheds new light on the ability of DFT to describe characteristics of these optically and electronically active systems.

Computational details

Models

The D–A copolymer CRU consists of the BDT donor unit, the quinoxaline acceptor unit, and one thiophene on each side of
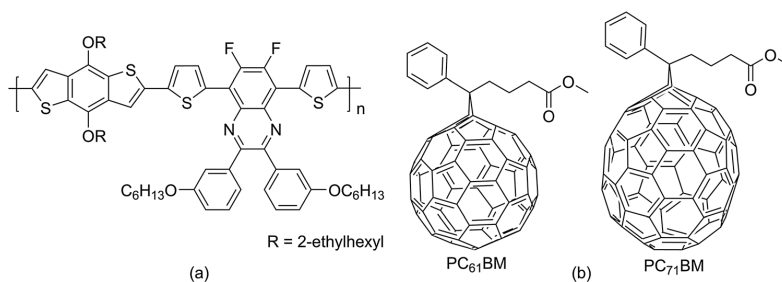
Fig. 1 Structures of the (a) D–A copolymer and (b) fullerene derivatives.

the acceptor as a spacer, see Fig. 1a. The dihedral angles within one CRU were determined using relaxed potential energy surface (PES) scans (see Methods and Fig. S1, ESI†). The oligomeric (O3, $n = 3$) and periodic (P, $n = \infty$) models of an alternating copolymer backbone were constructed in two different conformations (Fig. 2), *i.e.* the CRUs were placed either *syn* or *anti* to each other: in O3-*syn*/P-*syn*, the quinoxaline units are on the same side of the backbone and in O3-*anti*/P-*anti*, every other quinoxaline unit is on the opposite side of the backbone. We note that these conformations studied in vacuum present only two examples of a large number of conformers that can exist in real, disordered solution or solid thin film environments. In the oligomeric models, the optimized monomer was used as the CRU, whereas in the periodic calculations, the optimized O3-*syn* and O3-*anti* were used as the repeating units of P-*syn* and P-*anti*, respectively, to ensure the creation of repeatable structures. The 2-ethylhexyl and hexyl chains of the copolymer were replaced by methyl groups to reduce the computational cost. We note, however, that long alkyl

side chains would impact the solid-state packing and resulting solid-state optoelectronic characteristics.[69] While it is beyond the scope of this study, these effects should be considered when modeling the packing of the molecules in the active layer.

In addition to the fully optimized copolymer models, we constructed a planarized trimer model O3-*anti*, *i.e.* O3p hereafter, in which the dihedral angles of the backbone defined in Fig. 2 were constrained to 180°, while optimizing the geometry otherwise fully. Additionally, the substituents, *i.e.* the hexyloxyphenyl side groups of the quinoxaline acceptor unit, were replaced by hydrogens to reduce the computational cost, see ESI† Table S1 for the effect of these modifications on the electronic properties of the trimer. The planarized trimer was employed in the studies of six different eD–eA models consisting of O3p as the eD and PC$_{71}$BM (the α isomer)[70] as the eA, as the combination of these materials has been examined experimentally.[7] The O3p trimer was oriented on the *xy* plane along the *x* axis, see Fig. S2 (ESI†). In the first three eD–eA models, *i.e.* **1a–3a**, (Fig. 3), PC$_{71}$BM was
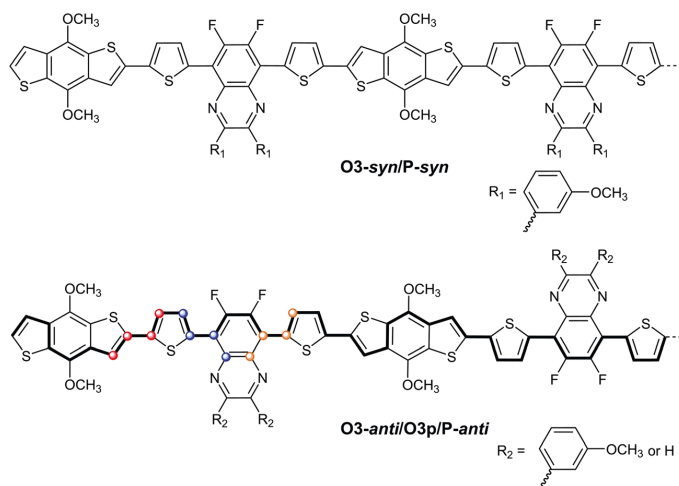

Fig. 2 Patterns of the backbones of the oligomeric and periodic copolymer models. The substituents (R$_1$, R$_2$) of the quinoxaline acceptor units are 3-methoxyphenyls in the fully optimized structures and hydrogens in the planarized O3-*anti* structure, *i.e.* O3p. The colored circles in the first CRU of O3-*anti*/P-*anti* represent the atoms defining the dihedral angles constrained to 180° throughout the entire trimer backbone O3p. The conjugation path used for calculating the BLAs is in bold in the figure of O3-*anti*/P-*anti*.
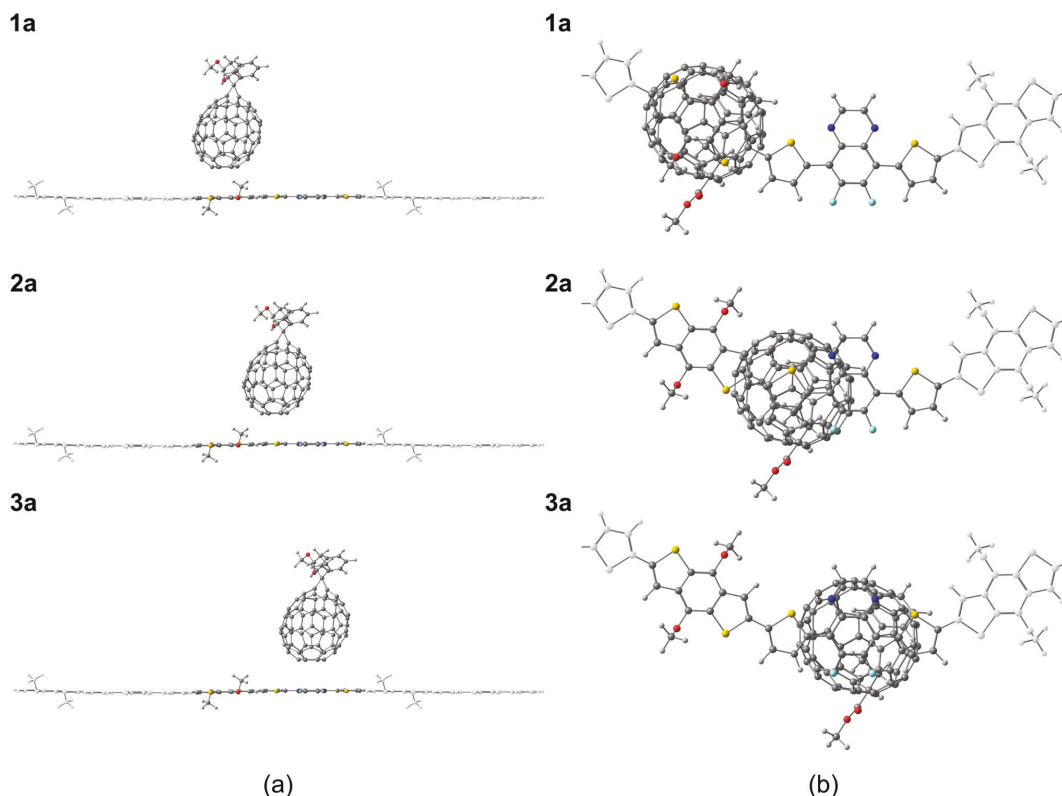
Fig. 3 Vertical eD–eA models represented from (a) the side and (b) the bottom of the models. In the models, PC$_{71}$BM (eA) is positioned vertically on the donor (**1a**), thiophene spacer (**2a**), or acceptor (**3a**) unit of the planarized O3p trimer model (eD) of the D–A copolymer.

positioned vertically (*i.e.* along the *z* axis) on the top of the trimer as follows: in **1a** above the donor unit, in **2a** above the thiophene spacer, and in **3a** above the acceptor unit. In **1b**–**3b** (Fig. S3, ESI†), PC$_{71}$BM was positioned horizontally (*i.e.* along the *x* axis) on the same units of the trimer as in **1a**–**3a**, respectively. After this, the intermolecular distance between O3p and PC$_{71}$BM was increased stepwise as described under Methods. See Fig. S4 (ESI†) for the positions of the superposed rings and centroids in O3p and PC$_{71}$BM.

Methods

All DFT, periodic boundary condition (PBC)[71,72] DFT, and TDDFT calculations were carried out in vacuum, unless specified otherwise, using the Gaussian 09 suite of programs (Revisions C.01[73] and D.01[74]). The ground-state geometry of the monomer was optimized at the B3LYP/6-31G** level of theory. The ground-state geometries of the copolymer models (Fig. 1a and 2) and fullerene derivatives (Fig. 1b) were optimized using the B3LYP,[75,76] B3LYP-D (B3LYP together with the D3 version of Grimme's dispersion,[77] GD3), ωB97X,[45] and ωB97X-D[46] functionals, as well as the corresponding optimally tuned ωB97X and ωB97X-D functionals, which are labelled with an OT-prefix hereafter (*i.e.* OT-ωB97X and

OT-ωB97X-D, respectively), with the 6-31G** basis set. Moreover, single-point (SP) calculations of the eD–eA, *i.e.* O3p–PC$_{71}$BM models, were carried out at the same levels of theory. Pictorial presentations of the geometries and natural transition orbitals (NTOs) were generated using ChemCraft 1.8.[78] The contributions of the electron densities to the NTOs were determined using the C-squared Population Analysis (C-SPA)[79] as implemented in Multiwfn 3.3.6.[80–82]

The IE tuning procedure developed by Stein, Kronik, and Baer[49,50] was employed to determine the optimal range-separation parameters for individual molecules and the O3p–PC$_{71}$BM models. The idea of the approach is to enforce the known relation[83–86] between the highest occupied Kohn–Sham eigenvalue and the IE that exist for the perfect xc functional by seeking a value of ω such that the HOMO energy ($\varepsilon_{HOMO}(N)$) for an *N*-electron (neutral) system equals $-IE(N)$. This can be carried out by minimizing the following equation:

$$J_{IE}(\omega) = |\varepsilon^{\omega}_{HOMO}(N) + E^{\omega}(N-1) - E^{\omega}(N)|, \qquad (2)$$

where $E^{\omega}(N)$ and $E^{\omega}(N-1)$ are the ground state energies of the *N* and *N* − 1 (cation) electron systems, respectively. As there is

This journal is © the Owner Societies 2016

Phys. Chem. Chem. Phys., 2016, **18**, 27654–27670 | **27657**

no analogous theorem to relate the LUMO energy to the EA, the IE of the $N + 1$ (anion) electron system is usually considered, as it is the same as the EA of the N electron system if relaxation effects are not taken into account.[50] Then, the following expression can be used for the EA:

$$J_{EA}(\omega) = |\varepsilon_{HOMO}^{\omega}(N + 1) + E^{\omega}(N) - E^{\omega}(N + 1)|, \qquad (3)$$

where $\varepsilon_{HOMO}(N + 1)$ and $E^{\omega}(N + 1)$ are the HOMO energy and the ground state energy of the $N + 1$ electron system, respectively. ω is the same in both eqn (2) and (3). To tune the fundamental gap of the system,[31,87] such a ω value is searched for that minimizes both eqn (2) and (3):

$$J_{gap}(\omega) = J_{IE}(\omega) + J_{EA}(\omega). \qquad (4)$$

The range-separation parameters of the ωB97X and ωB97X-D functionals, originally 0.3 and 0.2 bohr^{-1}, respectively, were optimized for the oligomeric trimer models of the D–A copolymer, fullerene derivatives (PC$_{61}$BM and PC$_{71}$BM), and the O3p–PC$_{71}$BM models with an accuracy of 0.01 bohr^{-1}. The optimized B3LYP/6-31G** geometries were used as the starting structures. The 6-31G* basis set was used in all ω tuning calculations. The OT ω values obtained for the trimers were used for the corresponding periodic models of the D–A copolymer. For the individual molecules, we used the gap tuning procedure (eqn (4)), whereas for the O3p–PC$_{71}$BM model systems, we determined the optimal ω values by minimizing the modified version[24,25,49] of eqn (4), which takes both the IE of the eD (O3p) and the EA of the eA (PC$_{71}$BM) into account:

$$J(\omega) = |\varepsilon_{HOMO}^{\omega}(N) + E_D^{\omega}(N - 1) - E_D^{\omega}(N)| + |\varepsilon_{HOMO}^{\omega}(M + 1)$$
$$+ E_A^{\omega}(M) - E_A^{\omega}(M + 1)|, \qquad (5)$$

where $\varepsilon_{HOMO}(N)$ and $\varepsilon_{HOMO}(M + 1)$ are the HOMO energies of the neutral O3p and the anion of PC$_{71}$BM, respectively, $E_D^{\omega}(N)$ and $E_A^{\omega}(M)$ are the total energies of the neutral O3p and PC$_{71}$BM, respectively, and $E_D^{\omega}(N - 1)$ and $E_A^{\omega}(M + 1)$ are the total energies of the cation of O3p and the anion of PC$_{71}$BM, respectively. Here we make the assumption that the eD and eA molecules dominate the IE and EA, respectively. For each ω in the studied range, the (vertical) IE was always calculated as the energy difference between the cation and the neutral, which were both at the optimized neutral geometry (see eqn (2)). Similarly, the (vertical) EA was calculated as the energy difference between the neutral and the anion, both at the optimized anion geometry (see eqn (3)).

Dihedral angles α, β_1, and β_2 of the monomer (see Fig. S1) were determined using the relaxed PES scans, where the geometry of the monomer was optimized at constrained $\alpha/\beta_1/\beta_2$ intervals of 5° between 0° and 360°. The structure of the monomer was confirmed as a minimum by the absence of the imaginary frequencies in a frequency calculation following the optimization at the same B3LYP/6-31G** level of theory.

The periodic models of the D–A copolymer were optimized using the default density of the k-points. The length of the translation vector Tv determines the number of k-points, $i.e.$ the longer the vector the less the k-points in the reciprocal space. The initial lengths of Tv were $ca.$ 47 Å and 58 Å, resulting in 8 and 6 k-points in P-syn and P-$anti$, respectively.

BLAs were calculated for the optimized ground-state geometries of the oligomeric trimer and periodic models of the D–A copolymer. Each BLA value was determined as the average difference in length between the adjacent C–C single and C=C double bonds within the conjugation path in a molecule (see Fig. 2), $i.e.$ within the shortest path between the terminal carbon atoms.[88] The total BLA values for the trimers were compared to the BLA$_{middle}$ values taken from the innermost CRU of the trimers and the BLA$_\infty$ values calculated for the periodic models.

The eD–eA models, $i.e.$ the O3p–PC$_{71}$BM models (see Fig. 3 and Fig. S3, ESI†), were built from the B3LYP-optimized geometries using Materials Studio 8.0.[89] The one-dimensional (rigid) potential energy scans of the models were carried out using Gaussian 09 via SP energy calculations, while increasing the vertical distance between O3p and PC$_{71}$BM from 3.0 Å to 5.0 Å (to 6.0 Å in the case of OT-ωB97X) by steps of 0.1 Å. The distance was measured between the centroid of a benzene ring of PC$_{71}$BM shown in Fig. S4 (ESI†), and that of the benzene/thiophene ring of the central CRU of the O3p trimer. Additionally, the center-to-center distances, $i.e.$ the distance between the centroid of PC$_{71}$BM and that of the benzene/thiophene ring of the O3p trimer, were monitored. The interaction energies (E_{int}) for the models were calculated as

$$E_{int} = E_{O3p-PC_{71}BM} - (E_{O3p} + E_{PC_{71}BM}), \qquad (6)$$

where the SP energies of the isolated O3p trimer (E_{O3p}) and PC$_{71}$BM ($E_{PC_{71}BM}$) were subtracted from the SP energy of the combined O3p–PC$_{71}$BM model ($E_{O3p-PC_{71}BM}$).

The vertical transition energies were calculated using TDDFT for the first 20 singlet excited states of the O3-$anti$, the first 50 singlet excited states of PC$_{61}$BM and PC$_{71}$BM, and the first 10 singlet excited states of the O3p–PC$_{71}$BM models. The geometries of the O3-$anti$ and fullerene derivatives were optimized using the same functional as those employed in the TDDFT calculation; as a check, the B3LYP optimized geometries were also employed. To compare with the experimental UV-vis absorption spectra measured in solution, the TDDFT calculations were also carried out in 1,2-dichlorobenzene for O3-$anti$ and in toluene for PC$_{61}$BM and PC$_{71}$BM. Solvation effects were included by means of the integral equation formalism of the polarizable continuum model (IEFPCM)[90,91] using the dielectric constants of 9.99 and 2.37 for 1,2-dichlorobenzene and toluene, respectively. The graphical presentations of the UV-vis absorption spectra were created via convolution of the singlet vertical transition energies and oscillator strengths (f) using a Gaussian-shape broadening with a full width at half maximum (fwhm) of 0.30 eV. The nature of the electronic transitions was described using NTOs[92] as a representation for the transition density matrix. The Revision D.01 of Gaussian 09 was used to calculate NTOs.

Results and discussion

Optimally tuned range-separation parameters

The OT ω values of the individual trimers, fullerene derivatives, and the combined O3p–PC$_{71}$BM models are shown in Table 1.

27658 | $Phys. Chem. Chem. Phys.$, 2016, **18**, 27654–27670

This journal is © the Owner Societies 2016

Table 1 Optimally tuned range-separation parameters ω (in bohr^{-1}) of the LRC-functionals determined using the gap tuning procedures[a] with the 6-31G* basis set

Model	OT-ωB97X	OT-ωB97X-D
O3-*syn*	0.10	—
O3-*anti*	0.10	0.09
O3p (O3p-*anti*)[b]	0.11	0.10
PC$_{61}$BM	0.16	0.15
PC$_{71}$BM	0.14	0.13
O3p–PC$_{71}$BM[c]	0.13	0.12

[a] The OT ω values of the individual molecules were determined using eqn (4). In the case of the O3p–PC$_{71}$BM models, eqn (5) was used. [b] Planarized O3 with the *anti*-conformation. [c] The same ω was applied to all six models, **1a**–**3a** and **1b**–**3b**.

In general, all optimal ω values are smaller than the default ω used in the original LRC-functionals ωB97X (0.3 bohr^{-1}) and ωB97X-D (0.2 bohr^{-1}), as expected due to the extended π-conjugation in these systems.[20,22,23,30] The optimal ω values show the same mutual ordering as the default values, but the difference between them is significantly smaller; for the same compound, ω of OT-ωB97X is only 0.01 bohr^{-1} larger than that of OT-ωB97X-D. The optimal ω values of the trimer models are between 0.09 and 0.11 bohr^{-1} corresponding to the characteristic length scale (1/ω) of *ca.* 9–11 bohr, *e.g.* 5–6 Å. These values are consistent with those (0.10–0.17 bohr^{-1}) obtained with different LRC functionals for other D–A copolymers in previous studies.[20,22,23] Furthermore, our calculations show that the conformation does not have any

influence on the optimal ω value of the ωB97X functional. However, we did not tune ω of ωB97X-D for O3-*syn*, as these calculations would have been too time-consuming.

The OT ω values (0.13–0.16 bohr^{-1}) obtained for PC$_{61}$BM and PC$_{71}$BM are somewhat larger than those obtained for the trimers, but smaller than those obtained previously for the same fullerene derivatives[53] and C$_{60}$[28,87] with other LRC-functionals. The optimal ω values of the ωB97X-D functional are very close to those obtained[54] previously with the same functional. The characteristic length scales (1/ω) of PC$_{61}$BM and PC$_{71}$BM are *ca.* 6–8 bohr, *e.g.* 3–4 Å. The OT ω values for the O3p–PC$_{71}$BM models are between those obtained for the individual O3p and PC$_{71}$BM, but somewhat closer to those obtained for PC$_{71}$BM. Altogether, these results indicate that the default ω values of ωB97X and ωB97X-D are too large for the studied systems, as have been reported also in the previous studies of the organic optoelectronic materials using different OT-LRC functionals.[20,22,23,53]

Ground state structural properties of the copolymer models

The results for the monomeric PES calculations are presented in Fig. S1 (ESI†). The PES curves indicate that the backbone of the monomer is nonplanar, namely the optimal dihedral angle between the BDT donor and thiophene is *ca.* 160° and that between thiophenes and the quinoxaline acceptor is *ca.* 15°. These deviations from the planarity are also observed for the B3LYP-optimized ground-state geometries of the trimers (O3-*syn* and O3-*anti*) of the studied D–A copolymer (Fig. 4). The backbones
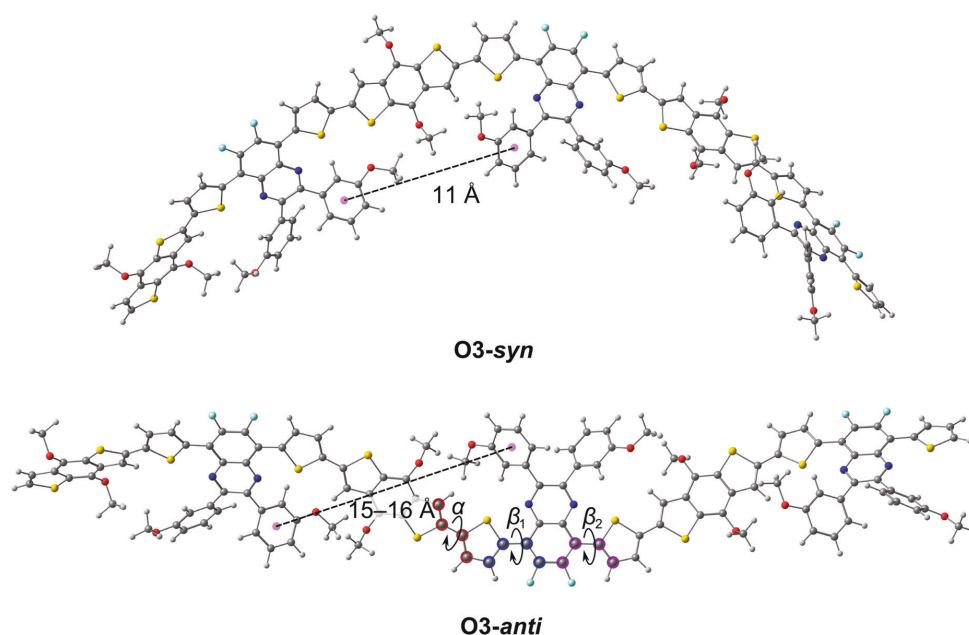
Fig. 4 Ground-state geometries of the trimer models O3-*syn* and O3-*anti* fully optimized at the B3LYP/6-31G** level of theory. The dashed lines indicate the distances between the centroids (pink dummy atoms) of the methoxyphenyl groups of two neighboring CRUs. The studied dihedral angles of O3-*anti*/P-*anti* are marked with the circles and arrows.

of both conformers are helical, with O3-*syn* having a more pronounced helix structure, an effect due to the orientation of the methoxyphenyl groups. In O3-*syn*, all methoxyphenyl groups are on the same side of the backbone, which results in smaller distances (*ca.* 11 Å) between the phenyl groups of the neighboring CRUs compared to those of O3-*anti* (15–16 Å), where the methoxyphenyl groups are on the opposite sides of the backbone. A similar helical geometry was also observed for an alternating thiophene–quinoxaline (TQ) D–A copolymer by Hedström and Persson,[93] who concluded that the suitable positions of the neighboring alkoxyphenyl groups enable nonbonded stacking interactions between them leading to the helical geometry of TQ, because in TQ the distance between the alkoxyphenyl groups corresponds to the reported π–π interaction distances (3.4–4.1 Å).[94] However, in the case of the D–A copolymer studied here, the thiophene spacers and BDT units together increase the distances between the quinoxaline units significantly, and therefore, it can be concluded that the π–π interactions between the alkoxyphenyl groups do not drive towards the helix formation.

The other functionals used in this study yield similar optimized geometries for O3-*anti* as those obtained with B3LYP. The dispersion corrected functionals (B3LYP-D and ωB97X-D) yield slightly (0.4–0.8 Å) shorter distances between the methoxyphenyl groups than other functionals. Additionally, the OT-LRC functionals yield only marginally (0.2–0.4 Å) longer distances than the non-tuned LRC functionals. In the case of O3-*syn*, ωB97X predicts the same distances between the methoxyphenyl groups as B3LYP, whereas OT-ωB97X increases the distances by 2.6 Å.

All functionals yield the optimized geometry of the periodic model P-*anti* corresponding to that of O3-*anti*. However, the helix structures of the optimized geometries of P-*syn* are less pronounced than those of O3-*syn* and the distances between the methoxyphenyl groups increase by 1.0–5.0 Å being now closer to those of the *anti*-conformations. The *anti*-conformations of both the trimer and periodic models are predicted (Table S2, ESI†) to be energetically more favorable than the *syn*-conformations. As the conformation can be assumed to affect the optoelectronic properties of the theoretical models[26] only slightly, the *syn*-conformations have been omitted from the further studies.

The dihedral angles of the oligomeric O3-*anti* and periodic P-*anti* models optimized with different functionals are listed in Table 2. The functional choice has some effect on the dihedral angles, although the values predicted with both the hybrid and LRC functionals are in the same range. For O3-*anti*, the deviations from the planarity are 7–17° predicted by B3LYP. The inclusion of dispersion corrections (in B3LYP-D) increases the nonplanarity slightly, *i.e.* up to 10–20°. Both the original, non-tuned LRC functionals (ωB97X and ωB97X-D) and the OT-LRC functionals predict more planar structures, which is consistent with the larger amounts of HF exchange when compared to the hybrid functionals, as has been previously observed.[20]

Table 2 Dihedral angles α, β₁, and β₂ (in degrees)[a] of the ground-state geometries of the oligomeric O3-*anti* (*n* = 3) and periodic P-*anti* (*n* = ∞) models optimized with different functionals and the 6-31** basis set

| Functional | ω (bohr^{-1}) | O3-*anti*[b] | | | P-*anti*[c] | | |
		α	β₁	β₂	α	β₁	β₂
B3LYP	—	163	−10[e]	−7	158	−15	−10
B3LYP-D[d]	—	160	−12	−10	—	—	—
ωB97X	0.30	157	−16	−20	155	−18	−19
ωB97X-D[d]	0.20	156	−15	−17	—	—	—
OT-ωB97X	0.10	161	−21	−21	160	−21	−19
OT-ωB97X-D[d]	0.09	159	−18	−13	—	—	—

[a] See Fig. 4 for the studied dihedrals. [b] The dihedral angles are from the innermost CRU of the trimer. [c] The dihedrals are from the innermost monomer unit of the periodic repeating unit. [d] Not implemented in the PBC code. Negative dihedral angles indicate an anticlockwise rotation relative to the bond connected to the dihedral angle atom. [e] Negative dihedral angles indicate.

The BLA and BLA$_{middle}$ values of O3-*anti* and the corresponding BLA$_\infty$ values of P-*anti* of the ground-state geometries optimized with different functionals are presented in Table 3. The BLA values are in the same range and have the same trends between the functionals as observed in the previous studies[20,26] for D–A copolymers. That is, the LRC functionals yield somewhat larger BLA values, *i.e.* larger differences between the single and double bond lengths than the hybrid functionals due to the larger amounts of exact HF exchange in the functional,[20] and suggest a more aromatic nature for both O3-*anti* and P-*anti* than the hybrid functionals. The same applies to the calculated differences in bond lengths between B3LYP and other functionals (see Fig. S5 and S6, ESI†). The dispersion corrections in B3LYP-D do not have significant effects on the bond lengths relative to B3LYP, and the BLA values obtained with and without dispersion corrections are almost identical. The BLA values and bond lengths obtained with the OT-LRC functionals are between those obtained with the hybrid functionals and the non-tuned LRC functionals, but somewhat closer to the B3LYP and B3LYP-D values. The non-tuned LRC functionals and OT-ωB97X-D lengthen the single bonds and shorten the double bonds whereas OT-ωB97X lengthens both the single and double bonds with respect to B3LYP. The ωB97X-D functional yields somewhat smaller BLA values and shorter bonds than ωB97X. The OT-ωB97X-D and OT-ωB97X functionals yield almost identical BLAs, however, OT-ωB97X-D predicts somewhat shorter bonds. In all cases, the BLA$_{middle}$ values calculated from the middle CRU of the trimer are slightly

Table 3 BLA and BLA$_{middle}$ values for O3-*anti* (*n* = 3) and BLA$_\infty$ for P-*anti* (*n* = ∞) calculated with different functionals and the 6-31G** basis set

Functional	ω (bohr^{-1})	BLA (Å)	BLA$_{middle}$[a] (Å)	BLA$_\infty$[b] (Å)
B3LYP	—	0.040	0.036	0.039
B3LYP-D[c]	—	0.040	0.037	—
ωB97X	0.30	0.061	0.059	0.060
ωB97X-D[c]	0.20	0.055	0.052	—
OT-ωB97X	0.10	0.046	0.043	0.044
OT-ωB97X-D[c]	0.09	0.046	0.042	—

[a] BLAs calculated for the innermost CRU of O3-*anti*. [b] BLAs calculated for the periodic P-*anti*. [c] Not implemented in the PBC code.

smaller than the total BLA values due to the chain end effects present in the full oligomeric model. The BLA_∞ values of P-*anti* are very close to the BLA_{middle} values of O3-*anti*.

Electronic and optical properties of the copolymer models

The electronic and optical properties of the copolymer models (O3-*anti* and P-*anti*, see Table 4) were investigated with different functionals at the geometries optimized with the corresponding functionals. For the sake of comparison, the oligomeric results obtained at the B3LYP-optimized O3-*anti* geometry are presented in Table S3 (ESI†). In general, relative to the hybrid B3LYP and B3LYP-D functionals both the non-tuned and OT-LRC functionals yield stabilized (smaller) HOMO energies and destabilized (larger) LUMO energies resulting in larger HOMO–LUMO gaps. The OT-ωB97X and OT-ωB97X-D functionals yield *ca.* 2.1 eV and 1.4 eV smaller gap values, respectively, than the corresponding non-tuned LRC functionals. Moreover, both OT-LRC functionals predict identical gap values due to their very similar ω values. Except for the LUMO calculated with B3LYP, the periodic HOMO and LUMO energies are stabilized resulting in the slightly larger gap values than the corresponding oligomeric values. This is opposite to previous studies,[20,26] where the gap values of the periodic D–A copolymer models have been smaller than those of the oligomeric models due to the extended conjugation in the periodic backbones. Here, slightly larger deviations from the planarity in the periodic models (Table 2) could explain the larger gap values.

Calculated UV-vis absorption spectra of O3-*anti* are illustrated in Fig. 5. The spectra are characterized by two bands: one dominating at lower energy, which corresponds to the $S_0 \rightarrow S_1$ transition, and another at higher energy. The vertical transition energies of the $S_0 \rightarrow S_1$ transition are reported in Table 4. These results show good agreement with the shape of the experimental spectrum[7] presented also in Fig. 5. However, the calculated

vertical transition energies (Table 4) and consequently the spectra are shifted depending on the functional used. When compared with the experimental spectrum, B3LYP underestimates the energies of the absorption bands leading to a red-shifted spectrum. In contrast, the non-tuned LRC functionals overestimate the energies and yield blue-shifted spectra with respect to the experimental spectrum. The OT-LRC functionals correct the vertical transition energies back towards lower energies and are in best agreement with the experimental spectrum. The oscillator strengths increase on going from hybrid < OT-LRC < non-tuned LRC functionals. The $S_0 \rightarrow S_1$ vertical transition energies (Table 4) and spectra (Fig. S7, ESI†) calculated in solvent are almost identical to those calculated in vacuum, except for some marginal blue-/red-shifts in energies and somewhat larger oscillator strengths in solvent. Overall, these findings are in line with the previous studies[20,22,23] reporting the improved description of the excitation energies of the D–A copolymers when using the OT-LRC functionals.

The computed NTOs of the copolymer model O3-*anti* (Fig. 6) provide insight into the nature of the lowest intramolecular electronic transition. The eigenvalues λ, which are also presented in Fig. 6, are the fractions of the particular hole–electron pair contribution for the studied transition. Only the NTOs calculated with OT-ωB97X, the functional that provides the best agreement with the experimental spectrum (see Table 4 and Fig. 5), are illustrated together with those calculated with B3LYP. In the case of B3LYP, one electron–hole pair dominates ($\lambda = 0.91$), as the $S_0 \rightarrow S_1$ transition is mainly HOMO $\rightarrow$ LUMO (*ca.* 90%, Table 4) in nature. However, the LRC functionals predict additional electronic configurations and thus, in the case of OT-ωB97X, two electron–hole pairs are required to describe the $S_0 \rightarrow S_1$ excitation. This is in line with previous results of Pandey *et al.*,[22] where a OT-ωB97 functional provided more localized description of the $S_0 \rightarrow S_1$ excitations of several D–A copolymers with a

Table 4 HOMO, LUMO, and HOMO–LUMO gap ($E_{HOMO–LUMO}$) energies calculated using DFT[a] for O3-*anti* ($n = 3$) and using PBC-DFT for P-*anti* ($n = \infty$, in parentheses) together with the vertical transition energies (E_{vert,S_1}), oscillator strengths (f), and electronic configurations of the $S_0 \rightarrow S_1$ transition calculated using TDDFT[a] for O3-*anti* with the different functionals and the 6-31G** basis set

Functional	ω (bohr^{-1})	HOMO (eV)	LUMO (eV)	$E_{HOMO–LUMO}$ (eV)	E_{vert,S_1} (eV)	f	Electronic configuration[c]
B3LYP	—	−4.84 (−4.90)	−2.69 (−2.68)	2.15 (2.22)	1.82 [1.83]	2.95 [3.30]	H → L, 90% [88%] H−1 → L+1, 7% [7%]
B3LYP-D[b]	—	−4.85 (—)	−2.70 (—)	2.15 (—)	—[d]	—[d]	—[d]
ωB97X	0.30	−7.07 (−7.13)	−0.81 (−0.84)	6.26 (6.29)	3.09 [3.08]	4.37 [4.61]	H → L, 38% [39%] H−1 → L+1, 13% [15%]
ωB97X-D[b]	0.20	−6.69 (—)	−1.09 (—)	5.60 (—)	2.82 [2.81]	3.93 [4.24]	H → L, 42% [43%] H−1 → L+1, 14% [15%]
OT-ωB97X	0.10	−5.65 (−5.68)	−1.45 (−1.47)	4.20 (4.21)	2.27 [2.28]	3.70 [4.08]	H → L, 59% [59%] H−1 → L+1, 15% [16%]
OT-ωB97X-D[b]	0.09	−5.79 (—)	−1.59 (—)	4.20 (—)	2.28 [2.28]	3.60 [3.94]	H → L, 61% [60%] H−1 → L+1, 17% [17%]

[a] Corresponding DFT and TDDFT calculations were carried out at the same levels of theory using the geometries optimized with the corresponding functionals. The TDDFT values calculated in 1,2-dichlorobenzene are presented in square brackets. [b] Not implemented in the PBC code. [c] Only the two most contributing electronic configurations are included. [d] Computationally too demanding. The experimental cyclic voltammetry values[7] are −5.52 eV (HOMO) and −3.30 eV (LUMO), respectively, giving an electrochemical gap of 2.22 eV. The absorption maximum[7] (in 1,2-dichlorobenzene) is at 2.24 eV (553 nm).
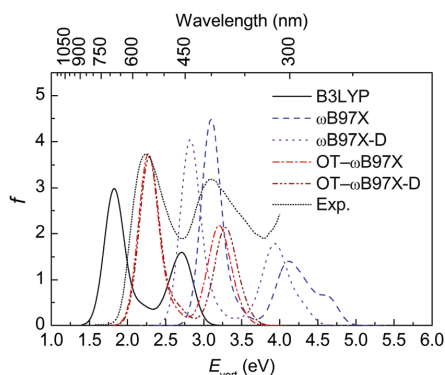
This journal is © the Owner Societies 2016

Phys. Chem. Chem. Phys., 2016, **18**, 27654–27670 | **27661**

Fig. 5 UV-vis absorption spectra of O3-*anti* (*n* = 3) calculated in vacuum using TDDFT with different functionals and the 6-31G** basis set. The geometries were optimized using DFT at the corresponding level of theory. The digitized experimental UV-vis absorption spectrum of the studied D–A copolymer[7] is also presented for comparison (the vertical axis is relative here and has been scaled to match the maximum *f* of the OT-ωB97X spectrum).

greater number of electron–hole pairs when compared to B3LYP. Both functionals predict partial CT character for the given excitation, *i.e.* charge density is transferred from the BDT donor unit and the thiophene spacers to the quinoxaline acceptor unit, with the hole delocalized over several neighboring units and the electron mainly on the quinoxaline acceptor units. However, the contributions calculated with B3LYP, see Fig. 6, predict that more charge density would be localized on the BDT donor units than on the thiophenes. In the second electron–hole pair predicted by OT-ωB97X (2 in Fig. 6), the contributions of the backbone units are close to those of the first pair but both the hole and the electron

are localized mainly on the specific segment of the backbone. The OT-ωB97X-D functional predicts very similar contributions as OT-ωB97X (see Table S4, ESI†). In the hole NTOs calculated with the non-tuned LRC functionals, the contribution of the BDT donor units is smaller and that of the thiophene and quinoxaline acceptor units is somewhat larger than that predicted by the OT-LRC functionals. In the electron NTOs calculated with the non-tuned LRC functionals, the opposite trend is observed: the contribution of the donor and thiophene units is somewhat larger and that of the acceptor units is smaller than that predicted by the OT-LRC functionals.

Electronic and optical properties of the fullerene derivatives

The electronic and optical properties of $PC_{61}BM$ and $PC_{71}BM$, presented in Tables 5 and 6, respectively, were calculated with different functionals at the geometries optimized with the corresponding functionals. For comparison, the results calculated at the B3LYP-optimized geometry are presented in Tables S5 and S6 (ESI†), respectively. As in the case of O3-*anti*, all the LRC functionals predict stabilized HOMO energies and destabilized LUMO energies, and thus larger HOMO–LUMO gaps with respect to the results of the hybrid functionals. The OT-LRC functionals predict somewhat smaller (*ca.* 0.5–1.1 eV) gap values than the non-tuned LRC functionals. In addition, the gap values predicted here by both OT-ωB97X and OT-ωB97XD are almost identical to each other as well as the gap values obtained for $PC_{61}BM$ (5.3 eV) and $PC_{71}BM$ (4.9 eV) with the OT LC-BLYP functional in the previous study.[53] In the case of $PC_{61}BM$, OT-ωB97X-D yields the HOMO energy (−7.05 eV) closest to the experimental IE (7.17 ± 0.04[95]) measured in the gas phase.

The calculated UV-vis spectra of $PC_{61}BM$ and $PC_{71}BM$ are presented in Fig. 7a and b, respectively. As B3LYP-D yields identical spectra to B3LYP, they are not illustrated in the figure for B3LYP-D. In the case of $PC_{61}BM$, the hybrid functionals
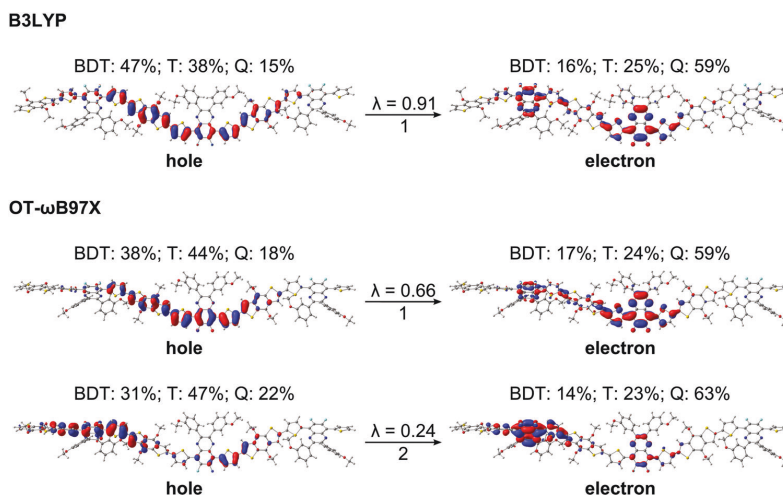

Fig. 6 NTOs and the contributions[79] of the donor (BDT), thiophene spacer (T), and quinoxaline acceptor (Q) units to the NTOs for the $S_0 \rightarrow S_1$ transition of O3-*anti* (*n* = 3) calculated with different functionals and the 6-31G** basis set (isodensity contour = 0.025).

27662 | *Phys. Chem. Chem. Phys.*, 2016, **18**, 27654–27670

This journal is © the Owner Societies 2016

Table 5 HOMO, LUMO, and HOMO−LUMO gap ($E_{\text{HOMO−LUMO}}$) energies of $PC_{61}BM$ calculated using DFT[a] and the vertical transition energies ($E_{\text{vert,max}}$), oscillator strengths (f), and electronic configurations of the excitation corresponding to the absorption maximum in the UV-vis spectrum calculated using TDDFT[a] employing different functionals and the 6-31G** basis set

Functional	ω (bohr^{-1})	HOMO (eV)	LUMO (eV)	$E_{\text{HOMO−LUMO}}$ (eV)	$E_{\text{vert,max}}$ (eV)	f	Electronic configuration[b]
B3LYP	—	−5.56	−3.00	2.56	3.50 (3.50)	0.01 (0.02)	H−1 → L+4, 31% (31%) H−11 → L, 27% (25%)
B3LYP-D	—	−5.55	−2.99	2.56	3.50 (3.50)	0.01 (0.02)	H−1 → L+4, 27% (29%) H−11 → L, 22% (21%)
ωB97X	0.30	−7.62	−1.34	6.28	4.82 (4.75)	0.64 (1.12)	H−2 → L+3, 25% (24%) H−1 → L+4, 13% (H−7 → L, 14%)
ωB97X-D	0.20	−7.34	−1.56	5.78	4.51 (4.46)	0.28 (0.78)	H−2 → L+3, 12% (24%) H → L+6, 12% (H → L+5, 13%)
OT-ωB97X	0.16	−6.95	−1.65	5.30	4.18 (4.13)	0.15 (0.41)	H−9 → L, 15% H−1 → L+4, 10% (H−2 → L+3, 30%) (H−8 → L, 16%)
OT-ωB97X-D	0.15	−7.05	−1.72	5.33	4.26 (4.21)	0.15 (0.42)	H−9 → L, 14% H → L+3, 9% (H−2 → L+3, 25%) (H−8 → L, 16%)

[a] Corresponding DFT and TDDFT calculations were carried out at the same levels of theory using the geometries optimized with the corresponding functionals. The TDDFT values calculated in toluene are presented in parentheses. [b] Only the two most contributing electronic configurations are included. Experimental values of IE and EA of $PC_{61}BM$ (in the gas phase) are 7.17 ± 0.04[95] eV and 2.63 eV,[96] respectively. The experimental absorption maximum[70] (in toluene) is at *ca.* 3.75 eV (331 nm).

Table 6 HOMO, LUMO, and HOMO−LUMO gap ($E_{\text{HOMO−LUMO}}$) energies of $PC_{71}BM$ calculated using DFT[a] and the vertical transition energies ($E_{\text{vert,max}}$), oscillator strengths (f), and electronic configurations of the excitation corresponding to the first absorption maximum in the UV-vis spectrum calculated using TDDFT[a] employing different functionals and the 6-31G** basis set

Functional	ω (bohr^{-1})	HOMO (eV)	LUMO (eV)	$E_{\text{HOMO−LUMO}}$ (eV)	$E_{\text{vert,max}}$ (eV)	f	Electronic configuration[b]
B3LYP	—	−5.52	−2.98	2.54	2.37 (2.34)	0.04 (0.06)	H−1 → L+1, 37% H−2 → L+2, 18% (H−2 → L+1, 71%) (H−5 → L, 6%)
B3LYP-D	—	−5.51	−2.97	2.54	2.37 (2.36)	0.04 (0.06)	H−1 → L+1, 37% (35%) H−2 → L+2, 17% (27%)
ωB97X	0.30	−7.38	−1.38	6.00	2.97 (2.96)	0.05 (0.09)	H → L+2, 55% (58%) H−3 → L+1, 15% (12%)
ωB97X-D	0.20	−7.16	−1.60	5.56	2.77 (2.76)	0.04 (0.08)	H → L+2, 69% (71%) H−3 → L+1, 9% (8%)
OT-ωB97X	0.14	−6.67	−1.76	4.91	2.59 (2.58)	0.04 (0.07)	H−1 → L+1, 64% (67%) H−2 → L+2, 5% (6%)
OT-ωB97X-D	0.13	−6.79	−1.83	4.96	2.64 (2.63)	0.04 (0.07)	H−1 → L+1, 63% (67%) H−5 → L, 6% (H−2 → L+2, 6%)

[a] Corresponding DFT and TDDFT calculations were carried out at the same levels of theory. The TDDFT values calculated in toluene are presented in parentheses. [b] Only the two most contributing electronic configurations are included. Experimental values[97,98] of IE, EA, and fundamental gap of $PC_{71}BM$ (measured from films) are 5.9 eV, 3.8 eV, and 2.1 eV, respectively. The experimental absorption maxima[70] (in toluene) are at *ca.* 2.68 eV (462 nm) and *ca.* 3.33 eV (372 nm).

describe the experimental spectrum[70] (Fig. 7a) the best. All LRC functionals overestimate the vertical transition energies (see Table 5) of $PC_{61}BM$ and thus blue-shift the spectra. In the case of $PC_{71}BM$, the hybrid functionals underestimate the vertical

energies (see Table 6) and red-shift the spectra with respect to the experimental one[70] (Fig. 7b), whereas the non-tuned LRC functionals overestimate the vertical energies and blue-shift the spectra. The OT-LRC functionals describe the experimental
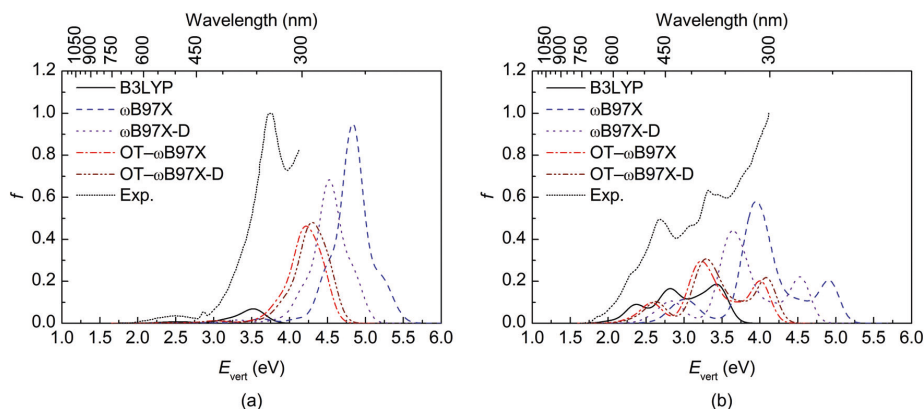
Fig. 7 UV-vis absorption spectra of (a) $PC_{61}BM$ and (b) $PC_{71}BM$ calculated in vacuum using TDDFT with different functionals and the 6-31G** basis set. The geometries were optimized using DFT with the corresponding functional and the 6-31G** basis set. The (normalized) digitized experimental UV-vis absorption spectra of fullerene derivatives[70] are also presented for comparison (the scales of the vertical axes are relative here).

spectrum of $PC_{71}BM$ better and the one predicted by OT-ωB97X-D has the best overall agreement with the experiment. The oscillator strengths predicted by different functionals have the same trend as in the case of O3-*anti*, *i.e.* hybrid < OT-LRC < non-tuned LRC functionals.

Minimized intermolecular distances in the O3p–$PC_{71}BM$ models

The intermolecular separation between $PC_{71}BM$ and the D–A copolymer, modelled with the planarized trimer, O3p, was determined with several functionals for two different orientations of $PC_{71}BM$, *i.e.* the vertical (**a**) and horizontal (**b**) models presented in Fig. 3 and Fig. S3 (ESI†), respectively. The potential energy curves

as a function of the intermolecular separation are presented in Fig. S8 (ESI†) and the optimal (*i.e.* minimized) intermolecular and center-to-center distances together with the interaction energies are presented in Table 7. The orientation does not affect the optimal distances significantly. However, the (absolute) interaction energies are somewhat larger (0.0–10.5 kJ mol^{-1}) when the fullerene derivative is positioned horizontally above the D–A copolymer model. Overall, the B3LYP and OT-ωB97X functionals predict the largest intermolecular distances (B3LYP: 4.0–4.4 Å; OT-ωB97X: 4.7–5.3 Å), whereas the other functionals predict congruent distances (3.3–3.7 Å). Consequently, the smallest absolute interaction energies are predicted by the same functionals for both orientations (B3LYP: 0.4–1.3 kJ mol^{-1}; OT-ωB97X: 0.2–0.9 kJ mol^{-1}).

Table 7 Optimal intermolecular distances (d_{opt}, Å), center-to-center distances ($d_{c\text{-to-}c}$, Å), and the corresponding interaction energies (E_{int}, kJ mol^{-1})[a] between the planarized O3p trimer and $PC_{71}BM$ in the O3p–$PC_{71}BM$ models calculated with various functionals and the 6-31G** basis set

| | | Model | | | | | | | | |
| | | **1a** | | | **2a** | | | **3a** | | |
Functional	ω (bohr^{-1})	d_{opt}	$d_{c\text{-to-}c}$	E_{int}	d_{opt}	$d_{c\text{-to-}c}$	E_{int}	d_{opt}	$d_{c\text{-to-}c}$	E_{int}
B3LYP	—	4.4	9.5	−0.8	4.2	9.3	−0.4	4.0	9.1	−1.0
B3LYP-D	—	3.6	8.7	−51.1	3.4	8.5	−47.6	3.3	8.4	−55.5
ωB97X	0.30	3.7	8.8	−19.6	3.6	8.7	−15.5	3.4	8.5	−19.5
ωB97X-D	0.20	3.6	8.7	−52.8	3.4	8.5	−47.5	3.3	8.4	−58.0
OT-ωB97X	0.13	5.3	10.4	−0.2	4.8	9.9	−0.3	4.7	9.8	−0.5
OT-ωB97X-D	0.12	3.7	8.8	−35.5	3.5	8.6	−34.5	3.4	8.5	−42.0

| | | Model | | | | | | | | |
| | | **1b** | | | **2b** | | | **3b** | | |
Functional	ω (bohr^{-1})	d_{opt}	$d_{c\text{-to-}c}$	E_{int}	d_{opt}	$d_{c\text{-to-}c}$	E_{int}	d_{opt}	$d_{c\text{-to-}c}$	E_{int}
B3LYP	—	4.4	8.1	−0.7	4.1	7.8	−0.9	4.0	7.7	−1.3
B3LYP-D	—	3.6	7.3	−58.0	3.4	7.1	−58.1	3.3	7.0	−63.7
ωB97X	0.30	3.7	7.4	−21.5	3.5	7.2	−19.7	3.4	7.1	−22.7
ωB97X-D	0.20	3.6	7.3	−59.5	3.4	7.1	−57.7	3.3	7.0	−66.1
OT-ωB97X	0.13	5.3	9.0	−0.2	4.8	8.5	−0.6	4.7	8.4	−0.9
OT-ωB97X-D	0.12	3.7	7.4	−40.8	3.5	7.2	−41.5	3.3	7.0	−47.0

[a] Calculated using eqn (6).

27664 | *Phys. Chem. Chem. Phys.*, 2016, **18**, 27654–27670

This journal is © the Owner Societies 2016

The non-tuned ωB97X functional and OT-ωB97X-D predict clearly larger interaction energies (ωB97X: 15.5–22.7 kJ mol^{-1}; OT-ωB97X-D: 34.5–47.0 kJ mol^{-1}) and B3LYP-D and the non-tuned ωB97X-D predict the largest interaction energies (B3LYP-D: 47.6–63.7 kJ mol^{-1}; ωB97X-D: 47.5–66.1 kJ mol^{-1}). The reason for the larger intermolecular distances (and smaller interaction energies) with OT-ωB97X compared to ωB97X might be due to a too small ω for describing these kinds of systems and therefore the OT-ωB97X functional is behaving closer to a pure density functional (B97, in the limiting case with $\omega = 0$) than to an LRC functional. The dispersion corrections in OT-ωB97X-D cancel this effect that the ω tuning has on the intermolecular distances. The interaction energies calculated at the constant intermolecular distance of 3.5 Å have the same trend (Table S7, ESI†).

Nevertheless, all functionals predict that PC$_{71}$BM is closest to the acceptor unit for this D–A copolymer (models **3a** and **3b**) and furthest from the copolymer donor unit (models **1a** and **1b**). Moreover, the interaction between the acceptor unit of the copolymer and PC$_{71}$BM (**3a** and **3b**) is predicted to be the strongest (except with ωB97X for **3a**). The interaction energies predicted for the other models do not follow the same trend as the calculated intermolecular distances, and in the **a**-models the interaction between the donor unit and PC$_{71}$BM is stronger than that between thiophene and PC$_{71}$BM, whereas the opposite holds for the most part in the **b**-models. The stronger driving force for the interaction between the acceptor unit of the copolymer and PC$_{71}$BM predicted here may play a role in certain polymers and the preferred binding sites. These results are in some agreement with previous experimental findings[99] regarding the more favorable interaction between the acceptor unit of the D–A copolymer and PC$_{61}$BM than that between the donor unit and PC$_{61}$BM. This has been explained with the accessibility of the particular units directed by the degree of branching in the alkyl substituents. Although we do not take the alkyl chains into account here, they can be expected to impact the nature of the polymer–fullerene interactions in this particular system. However, not all D–A copolymers follow this trend and the opposite results have been observed both experimentally[99] and theoretically,[62] as well.

Excited singlet state properties of the O3p–PC$_{71}$BM models

We carried out TDDFT calculations with our chosen set of functionals (B3LYP-D was omitted due to the convergence problems) to see the effect on the description of the singlet excited states of the O3p–PC$_{71}$BM models. First, we used a constant intermolecular distance of 3.5 Å between O3p and PC$_{71}$BM to exclude the possible influence of a varying intermolecular distance on the excited state properties.[25] The corresponding oscillator strengths, vertical transition energies, and nature of the electronic transitions are presented in Tables S8–S10 (ESI†), respectively. Then, we carried out the TDDFT calculations at the optimized intermolecular distances for comparison. These results are presented in Tables S11–S13 (ESI†).

At a constant intermolecular distance of 3.5 Å, the orientation of PC$_{71}$BM (models **1a–3a** and **1b–3b**) has either a negligible or at most a moderate effect (*ca.* 0.0–1.1) on the oscillator strengths (Table S8, ESI†) and a negligible effect on the vertical transition

energies (Table S9, ESI†), the latter being almost identical for these two orientations with the same states when calculated with the same functional. At the transition with the largest oscillator strength (1.7–5.2, Table S8, ESI†), *i.e.* the transition maximum, the f is the largest when PC$_{71}$BM is on the top of the BDT donor unit of O3p and the smallest when PC$_{71}$BM is on the top of the quinoxaline acceptor unit (with the exception of **2a** with B3LYP where two transitions have high f, see Table S8, ESI†). B3LYP yields crucially smaller oscillator strengths and smaller transition energies than the LRC functionals. Moreover, B3LYP predicts mainly intermolecular CT between O3p and PC$_{71}$BM (Table S10, ESI†) for the lowest 10 singlet vertical transitions in all models. Many of these CT states are 'pure' (PCT) meaning that over 90 percentage points (pps) of the charge density transfer from O3p to PC$_{71}$BM. The non-tuned LRC functionals predict, in contrast, local intramolecular excitations either in O3p (LT) or PC$_{71}$BM (LF) instead of the CT states, whereas the OT-LRC functionals predict both local intramolecular excitations and intermolecular CT states (overlapping within one transition, see below the state S4 for the model **3b**). At the transition maximum, B3LYP predicts a partial intermolecular CT from O3p to PC$_{71}$BM (overlapping with an intramolecular excitation within O3), whereas all the other functionals predict local intramolecular excitation in the O3p trimer (LT, see Table S10, ESI†). The transitions corresponding to the intermolecular CT from O3p to PC$_{71}$BM, which we will discuss more below, or the local intramolecular excitations within O3p and PC$_{71}$BM have moderate oscillator strengths (0.1–0.6). Additionally, there also exist negligible, *i.e.* $f < 0.1$, local excitations within PC$_{71}$BM and some intermolecular CTs.

At the minimized intermolecular distances (Table 7) most of the trends observed above with the constant distance of 3.5 Å remain the same (Tables S11–S13, ESI†). Differences in the oscillator strengths (Δf mainly 0.0–0.6; 1.0–2.8 only for a few states) and vertical transition energies (ΔE_{vert} *ca.* 0.0 eV) are minor or negligible. At the transition maxima, the oscillator strengths become smaller if the intermolecular distance decreases from 3.5 Å, and *vice versa*. Simultaneously, when the distance changes, the nature of the transition maximum changes in a few cases, especially in the model **3b** where an intermolecular CT state (from O3p to PC$_{71}$BM) appears when the distance decreases and overlaps with the local excitation in O3p (Table S13, ESI†) predicted by OT-ωB97X-D. With the other functionals, the number of CT states generally either decreases or remains the same, but decreases when the distance increases clearly from the constant distance of 3.5 Å (Table S10, ESI†), as in the case of OT-ωB97X, which does not predict any CT states at the optimal distances of 4.7–5.3 Å.

The vertical transition energies and the corresponding spectra calculated with OT-ωB97X-D for the O3p–PC$_{71}$BM models **3a** and **3b** and the O3 and PC$_{71}$BM are illustrated in Fig. S9 (ESI†) to provide more insight into the relative positions of the vertical transitions of the combined systems and the single molecules. The transition maximum of O3p (2.21 eV, with $\omega = 0.12$ bohr^{-1}) is slightly higher in energy than that of the O3p–PC$_{71}$BM models (2.19 eV). Interestingly, the transition maxima of the O3p–PC$_{71}$BM models predicted by both OT-ωB97X and OT-ωB97X-D (2.19–2.21 eV) match surprisingly well with the experimental

absorption maxima[7] (*ca.* 2.18–2.21 eV) of the copolymer–PC71BM (1 : 1) blend film, although our calculations of single eD–eA pairs do not fully describe the real, solid-state environment.

As mentioned above, the transition maxima (Tables S8 and S11, ESI†) originate mainly from the intramolecular excitation of the O3p trimer. The same result has been previously predicted for other copolymer–PC61BM complexes.[58,59] The corresponding NTOs calculated with B3LYP and OT-ωB97X-D for the vertical **3a** and horizontal **3b** models at the optimal intermolecular distances are presented in Fig. 8a and 9a, respectively (for the
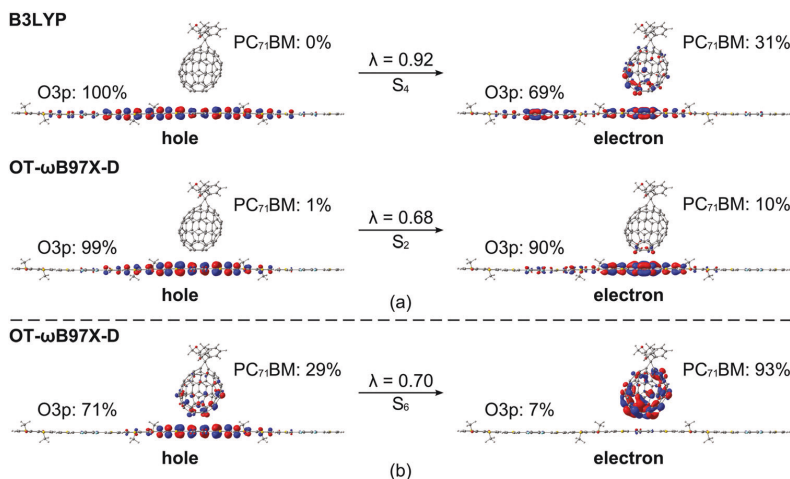
Fig. 8 NTOs for the (a) transition maxima and (b) CT transition of **3a** at the minimized distances calculated with different functionals and the 6-31G** basis set (isodensity contour = 0.025). In addition, the contributions (%) of O3p and PC71BM to the NTOs and contributions (λ) of the NTO pair to particular excitation are presented.
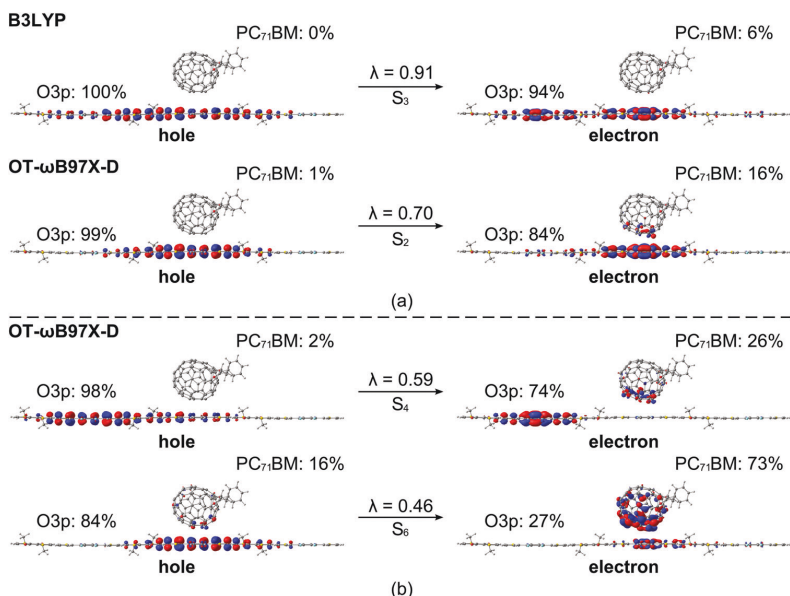
Fig. 9 NTOs for the (a) transition maxima and (b) CT transitions of **3b** at the minimized distances calculated with different functionals and the 6-31G** basis set (isodensity contour = 0.025). In addition, the contributions (%) of O3p and PC71BM to the NTOs and contributions (λ) of the NTO pair to particular excitation are presented.

constant distance of 3.5 Å see Fig. S10 and S12, ESI†). Both functionals predict the hole to be localized on the trimer. However, B3LYP delocalizes the hole NTO almost along the entire O3p backbone, whereas OT-ωB97X-D localizes the hole mainly on the middle CRU of the trimer, below PC$_{71}$BM. In the vertical **3a** model, B3LYP predicts a partial intermolecular CT (31 pp) from O3p to PC$_{71}$BM, *i.e.* the electron is localized on both molecules, but mainly on O3p. In the horizontal **3b** model, the extent of the CT predicted by B3LYP (6 pp) is rather negligible. With OT-ωB97X-D, a small CT (**3a**: 9 pp, **3b**: 15 pp) is observed and part of the electron is localized also on PC$_{71}$BM. Other LRC functionals, *i.e.* ωB97X, ωB97X-D, and OT-ωB97X, yield almost identical charge distributions, *i.e.* local excitations within O3p, for example see Fig. S10 and S12 (ESI†) for the constant intermolecular distance of 3.5 Å. Thus, apart from the small CT nature predicted by B3LYP and OT-ωB97X-D, all functionals yield quite similar descriptions of the transition maxima.

Additional vertical transitions that exhibit CT nature with moderate oscillator strengths (*ca.* 0.2–0.5, Tables S11 and S13, ESI†) are predicted by OT-ωB97X-D at the optimal intermolecular distance. Partial CTs from O3p to PC$_{71}$BM are predicted for the S$_0$ → S$_4$ transition of **3b** (24 pp) and for the S$_0$ → S$_6$ transition of both **3a** (64 pp) and **3b** (57 pp); for the NTOs see Fig. 8b and 9b. Also compare Fig. S11 (ESI†) for the NTOs of the S$_0$ → S$_6$ transitions of **3a** (Tables S8 and S10, ESI†) and Fig. S13 (ESI†) for the NTOs of the S$_0$ → S$_4$ and S$_0$ → S$_6$ transitions of **3b** (Tables S8 and S10, ESI†) calculated with different functionals at the constant intermolecular distance of 3.5 Å. Based on these results, it is found that OT-ωB97X-D is the only LRC functional among those studied that predicts a clear CT nature at the optimal intermolecular distances for **3a** and **3b**, *i.e.* when PC$_{71}$BM is on the top of the acceptor unit of the D–A copolymer. Although the OT-ωB97X-D functional predicts CT states for also other models, their oscillator strengths are smaller (see Tables S11 and S13, ESI†).

Conclusions

In this study, we have compared conventional hybrid functionals with the non-tuned and optimally tuned LRC functionals (with and without dispersion corrections) in the characterization of the local interfacial structure and optoelectronic properties of the eD–eA complexes of poly(benzodithiophene-*co*-quinoxaline) and PC$_{71}$BM. In addition, we have studied the isolated molecules, *i.e.* the fullerene derivatives (PC$_{61}$BM and PC$_{71}$BM), which are widely used as eAs, and the D–A trimer.

Our calculations of the trimer–PC$_{71}$BM complexes predict that the fullerene derivative has a stronger interaction with the quinoxaline acceptor in the D–A copolymer, regardless of the functional, a trend similar to that suggested experimentally for some D–A copolymers.[99] The orientation of PC$_{71}$BM has a minimal effect on the excited state properties of the complexes, although the interactions between the trimer and PC$_{71}$BM are somewhat more efficient when PC$_{71}$BM lies horizontally with respect to the trimer. The choice of the functional has a clear influence on the results of the trimer–PC$_{71}$BM complexes affecting not only

the optimal distances between the trimer and PC$_{71}$BM but also the excitation energies and the nature of the excited states. While all functionals yield very similar descriptions of the transition maxima of the complexes, *i.e.* predominant local excitation within the trimer, they show clear differences, as well. At the optimal intermolecular distances, the hybrid B3LYP tends to predict pure intermolecular CT nature (from the trimer to PC$_{71}$BM) for several of the lowest singlet excited states, while the non-tuned LRC functionals and OT-ωB97X yield only localized excited states. The OT-ωB97X-D functional is the only LRC functional among the studied ones to predict CT states for the trimer–PC$_{71}$BM complexes, but only for a few states compared to B3LYP.

To conclude, OT-LRC functionals can improve the description of the properties of the organic solar cell materials, especially in the case of their optical properties. The inclusion of dispersion corrections in these particular systems does not appear to have a significant effect on the results of the isolated molecules. However, in the combined eD–eA models, the inclusion of dispersion corrections is highly recommended for capturing weak dispersion interactions in the complexes. Moreover, the tuning of the range-separation parameter should be taken into account when modeling local eD–eA configurations of polymer–fullerene interfaces as it may affect the descriptions of the excited singlet states of the complexes. The analyses and results presented here serve as important guidelines for the selection of appropriate density functionals for future theoretical studies of eD–eA interfaces. Such computational investigations will be important as the field moves forward, as they can provide essential molecular-scale details of the CT states, the energies, distributions, and relaxation processes of which can be probed experimentally,[100–102] that are critical to the exciton dissociation and charge recombination processes in functioning solar cells. The capability to understand and control the correlations among CT processes and the quantum efficiencies of PSCs offer a distinctive knob to turn to further improve material design for organic photovoltaics.[63,103]

Acknowledgements

Notes and references

1 H. Zhou, L. Yang and W. You, *Macromolecules*, 2012, **45**, 607–632.
2 Y. Liang, Z. Xu, J. Xia, S.-T. Tsai, Y. Wu, G. Li, C. Ray and L. Yu, *Adv. Mater.*, 2010, **22**, E135–E138.
3 Z. He, C. Zhong, S. Su, M. Xu, H. Wu and Y. Cao, *Nat. Photonics*, 2012, **6**, 591–595.

4 S. C. Price, A. C. Stuart, L. Yang, H. Zhou and W. You, *J. Am. Chem. Soc.*, 2011, **133**, 4625–4631.

5 H. Zhou, L. Yang, A. C. Stuart, S. C. Price, S. Liu and W. You, *Angew. Chem., Int. Ed.*, 2011, **50**, 2995–2998.

6 C. Cabanetos, A. El Labban, J. A. Bartelt, J. D. Douglas, W. R. Mateker, J. M. J. Fréchet, M. D. McGehee and P. M. Beaujuge, *J. Am. Chem. Soc.*, 2013, **135**, 4656–4659.

7 H.-C. Chen, Y.-H. Chen, C.-C. Liu, Y.-C. Chien, S.-W. Chou and P.-T. Chou, *Chem. Mater.*, 2012, **24**, 4766–4772.

8 Z.-H. Zhou, T. Maruyama, T. Kanbara, T. Ikeda, K. Ichimura, T. Yamamoto and K. Tokuda, *J. Chem. Soc., Chem. Commun.*, 1991, 1210–1212.

9 E. E. Havinga, W. ten Hoeve and H. Wynberg, *Polym. Bull.*, 1992, **29**, 119–126.

10 M. C. Scharber, D. Mühlbacher, M. Koppe, P. Denk, C. Waldauf, A. J. Heeger and C. J. Brabec, *Adv. Mater.*, 2006, **18**, 789–794.

11 C. Soci, I.-W. Hwang, D. Moses, Z. Zhu, D. Waller, R. Gaudiana, C. J. Brabec and A. J. Heeger, *Adv. Funct. Mater.*, 2007, **17**, 632–636.

12 G. Yu, J. Gao, J. C. Hummelen, F. Wudl and A. J. Heeger, *Science*, 1995, **270**, 1789–1791.

13 Y. Yi, V. Coropceanu and J.-L. Brédas, *J. Am. Chem. Soc.*, 2009, **131**, 15777–15783.

14 A. Ojala, A. Petersen, A. Fuchs, R. Lovrincic, C. Pölking, J. Trollmann, J. Hwang, C. Lennartz, H. Reichelt, H. W. Höffken, A. Pucci, P. Erk, T. Kirchartz and F. Würthner, *Adv. Funct. Mater.*, 2012, **22**, 86–96.

15 Y. Yi, V. Coropceanu and J.-L. Brédas, *J. Mater. Chem.*, 2011, **21**, 1479–1486.

16 D. Beljonne, J. Cornil, L. Muccioli, C. Zannoni, J.-L. Brédas and F. Castet, *Chem. Mater.*, 2011, **23**, 591–609.

17 K. M. Pelzer and S. B. Darling, *Mol. Syst. Des. Eng.*, 2016, **1**, 10–24.

18 C. Risko, M. D. McGehee and J.-L. Bredas, *Chem. Sci.*, 2011, **2**, 1200–1218.

19 V. Manninen, M. Niskanen, T. I. Hukka, F. Pasker, S. Claus, S. Höger, J. Baek, T. Umeyama, H. Imahori and H. Lemmetyinen, *J. Mater. Chem. A*, 2013, **1**, 7451–7462.

20 M. Niskanen and T. I. Hukka, *Phys. Chem. Chem. Phys.*, 2014, **16**, 13294–13305.

21 L. Pandey, C. Risko, J. E. Norton and J.-L. Brédas, *Macromolecules*, 2012, **45**, 6405–6414.

22 L. Pandey, C. Doiron, J. S. Sears and J.-L. Brédas, *Phys. Chem. Chem. Phys.*, 2012, **14**, 14243–14248.

23 I. T. Lima, C. Risko, S. G. Aziz, D. A. da Silva Filho and J.-L. Brédas, *J. Mater. Chem. C*, 2014, **2**, 8873–8879.

24 B. Yang, Y. Yi, C.-R. Zhang, S. G. Aziz, V. Coropceanu and J.-L. Brédas, *J. Phys. Chem. C*, 2014, **118**, 27648–27656.

25 C.-R. Zhang, J. S. Sears, B. Yang, S. G. Aziz, V. Coropceanu and J.-L. Brédas, *J. Chem. Theory Comput.*, 2014, **10**, 2379–2388.

26 T. Kastinen, M. Niskanen, C. Risko, O. Cramariuc and T. I. Hukka, *J. Phys. Chem. A*, 2016, **120**, 1051–1064.

27 T. Minami, M. Nakano and F. Castet, *J. Phys. Chem. Lett.*, 2011, **2**, 1725–1730.

28 T. Minami, S. Ito and M. Nakano, *Int. J. Quantum Chem.*, 2013, **113**, 252–256.

29 T. Körzdörfer, R. M. Parrish, J. S. Sears, C. D. Sherrill and J.-L. Brédas, *J. Chem. Phys.*, 2012, **137**, 124305.

30 T. Körzdörfer, J. S. Sears, C. Sutton and J.-L. Brédas, *J. Chem. Phys.*, 2011, **135**, 204107.

31 T. Stein, H. Eisenberg, L. Kronik and R. Baer, *Phys. Rev. Lett.*, 2010, **105**, 266802.

32 J. S. Sears, R. R. Chance and J.-L. Brédas, *J. Am. Chem. Soc.*, 2010, **132**, 13313–13319.

33 C. Sutton, T. Körzdörfer, M. T. Gray, M. Brunsfeld, R. M. Parrish, C. D. Sherrill, J. S. Sears and J.-L. Brédas, *J. Chem. Phys.*, 2014, **140**, 054310.

34 T. Körzdörfer and J.-L. Brédas, *Acc. Chem. Res.*, 2014, **47**, 3284–3291.

35 P. Mori-Sánchez, A. J. Cohen and W. Yang, *J. Chem. Phys.*, 2006, **125**, 201102.

36 A. Savin and H.-J. Flad, *Int. J. Quantum Chem.*, 1995, **56**, 327–332.

37 T. Leininger, H. Stoll, H.-J. Werner and A. Savin, *Chem. Phys. Lett.*, 1997, **275**, 151–160.

38 H. Iikura, T. Tsuneda, T. Yanai and K. Hirao, *J. Chem. Phys.*, 2001, **115**, 3540.

39 J. Heyd, G. E. Scuseria and M. Ernzerhof, *J. Chem. Phys.*, 2003, **118**, 8207.

40 A. V Krukau, O. A. Vydrov, A. F. Izmaylov and G. E. Scuseria, *J. Chem. Phys.*, 2006, **125**, 224106.

41 A. V Krukau, G. E. Scuseria, J. P. Perdew and A. Savin, *J. Chem. Phys.*, 2008, **129**, 124103.

42 J. Heyd, G. E. Scuseria and M. Ernzerhof, *J. Chem. Phys.*, 2006, **124**, 219906.

43 O. A. Vydrov and G. E. Scuseria, *J. Chem. Phys.*, 2006, **125**, 234109.

44 T. Yanai, D. P. Tew and N. C. Handy, *Chem. Phys. Lett.*, 2004, **393**, 51–57.

45 J.-D. Chai and M. Head-Gordon, *J. Chem. Phys.*, 2008, **128**, 084106.

46 J.-D. Chai and M. Head-Gordon, *Phys. Chem. Chem. Phys.*, 2008, **10**, 6615–6620.

47 R. Baer and D. Neuhauser, *Phys. Rev. Lett.*, 2005, **94**, 043002.

48 E. Livshits and R. Baer, *Phys. Chem. Chem. Phys.*, 2007, **9**, 2932–2941.

49 T. Stein, L. Kronik and R. Baer, *J. Am. Chem. Soc.*, 2009, **131**, 2818–2820.

50 T. Stein, L. Kronik and R. Baer, *J. Chem. Phys.*, 2009, **131**, 244119.

51 H. Sun and J. Autschbach, *J. Chem. Theory Comput.*, 2014, **10**, 1035–1047.

52 M. Wykes, B. Milián-Medina and J. Gierschner, *Front. Chem.*, 2013, **1**, 1–12.

53 M. E. Foster, J. D. Azoulay, B. M. Wong and M. D. Allendorf, *Chem. Sci.*, 2014, **5**, 2081–2090.

54 N. R. Tummala, Z. Zheng, S. G. Aziz, V. Coropceanu and J.-L. Brédas, *J. Phys. Chem. Lett.*, 2015, **6**, 3657–3662.

55 X. Shen, G. Han and Y. Yi, *Phys. Chem. Chem. Phys.*, 2016, **18**, 15955–15963.

56 X. Shen, G. Han, D. Fan, Y. Xie and Y. Yi, *J. Phys. Chem. C*, 2015, **119**, 11320–11326.

57 S. Few, J. M. Frost, J. Kirkpatrick and J. Nelson, *J. Phys. Chem. C*, 2014, **118**, 8253–8261.

58 Y. Li, T. Pullerits, M. Zhao and M. Sun, *J. Phys. Chem. C*, 2011, **115**, 21865–21873.

59 C. Leng, H. Qin, Y. Si and Y. Zhao, *J. Phys. Chem. C*, 2014, **118**, 1843–1855.

60 Y. Li, D. Qi, P. Song and F. Ma, *Materials*, 2015, **8**, 42–56.

61 Y. Li, Y. Feng and M. Sun, *Sci. Rep.*, 2015, **5**, 13970.

62 L. Pandey, PhD thesis, Georgia Institute of Technology, 2013.

63 D. Niedzialek, I. Duchemin, T. B. de Queiroz, S. Osella, A. Rao, R. Friend, X. Blase, S. Kümmel and D. Beljonne, *Adv. Funct. Mater.*, 2015, **25**, 1972–1984.

64 W. Mammo, S. Admassie, A. Gadisa, F. Zhang, O. Inganäs and M. R. Andersson, *Sol. Energy Mater. Sol. Cells*, 2007, **91**, 1010–1018.

65 A. Gadisa, W. Mammo, L. M. Andersson, S. Admassie, F. Zhang, M. R. Andersson and O. Inganäs, *Adv. Funct. Mater.*, 2007, **17**, 3836–3842.

66 L. Huo, Z. Tan, X. Wang, Y. Zhou, M. Han and Y. Li, *J. Polym. Sci., Part A: Polym. Chem.*, 2008, **46**, 4038–4049.

67 J.-Y. Lee, W.-S. Shin, J.-R. Haw and D.-K. Moon, *J. Mater. Chem.*, 2009, **19**, 4938–4945.

68 W. Chen, X. Bao, Q. Zhu, D. Zhu, M. Qiu, M. Sun and R. Yang, *J. Mater. Chem. C*, 2015, **3**, 10070–10073.

69 D. Niedzialek, V. Lemaur, D. Dudenko, J. Shu, M. R. Hansen, J. W. Andreasen, W. Pisula, K. Müllen, J. Cornil and D. Beljonne, *Adv. Mater.*, 2013, **25**, 1939–1947.

70 M. M. Wienk, J. M. Kroon, W. J. H. Verhees, J. Knol, J. C. Hummelen, P. A. van Hal and R. A. J. Janssen, *Angew. Chem., Int. Ed.*, 2003, **42**, 3371–3375.

71 K. N. Kudin and G. E. Scuseria, *Chem. Phys. Lett.*, 1998, **289**, 611–616.

72 K. N. Kudin and G. E. Scuseria, *Phys. Rev. B: Condens. Matter Mater. Phys.*, 2000, **61**, 16440–16453.

73 M. J. Frisch, G. W. Trucks, H. B. Schlegel, G. E. Scuseria, M. A. Robb, J. R. Cheeseman, G. Scalmani, V. Barone, B. Mennucci, G. A. Petersson, H. Nakatsuji, M. Caricato, X. Li, H. P. Hratchian, A. F. Izmaylov, J. Bloino, G. Zheng, J. L. Sonnenberg, M. Hada, M. Ehara, K. Toyota, R. Fukuda, J. Hasegawa, M. Ishida, T. Nakajima, Y. Honda, O. Kitao, H. Nakai, T. Vreven, J. A. J. Montgomery, J. E. Peralta, F. Ogliaro, M. Bearpark, J. J. Heyd, E. Brothers, K. N. Kudin, V. N. Staroverov, R. Kobayashi, J. Normand, K. Raghavachari, A. Rendell, J. C. Burant, S. S. Iyengar, J. Tomasi, M. Cossi, N. Rega, J. M. Millam, M. Klene, J. E. Knox, J. B. Cross, V. Bakken, C. Adamo, J. Jaramillo, R. Gomperts, R. E. Stratmann, O. Yazyev, A. J. Austin, R. Cammi, C. Pomelli, J. W. Ochterski, R. L. Martin, K. Morokuma, V. G. Zakrzewski, G. A. Voth, P. Salvador, J. J. Dannenberg, S. Dapprich, A. D. Daniels, Ö. Farkas, J. B. Foresman, J. V. Ortiz, J. Cioslowski and D. J. Fox,

Gaussian 09, Revision C.01, Gaussian, Inc., Wallingford, CT, 2009.

74 M. J. Frisch, G. W. Trucks, H. B. Schlegel, G. E. Scuseria, M. A. Robb, J. R. Cheeseman, G. Scalmani, V. Barone, B. Mennucci, G. A. Petersson, H. Nakatsuji, M. Caricato, X. Li, H. P. Hratchian, A. F. Izmaylov, J. Bloino, G. Zheng, J. L. Sonnenberg, M. Hada, M. Ehara, K. Toyota, R. Fukuda, J. Hasegawa, M. Ishida, T. Nakajima, Y. Honda, O. Kitao, H. Nakai, T. Vreven, J. A. J. Montgomery, J. E. Peralta, F. Ogliaro, M. Bearpark, J. J. Heyd, E. Brothers, K. N. Kudin, V. N. Staroverov, R. Kobayashi, J. Normand, K. Raghavachari, A. Rendell, J. C. Burant, S. S. Iyengar, J. Tomasi, M. Cossi, N. Rega, J. M. Millam, M. Klene, J. E. Knox, J. B. Cross, V. Bakken, C. Adamo, J. Jaramillo, R. Gomperts, R. E. Stratmann, O. Yazyev, A. J. Austin, R. Cammi, C. Pomelli, J. W. Ochterski, R. L. Martin, K. Morokuma, V. G. Zakrzewski, G. A. Voth, P. Salvador, J. J. Dannenberg, S. Dapprich, A. D. Daniels, Ö. Farkas, J. B. Foresman, J. V. Ortiz, J. Cioslowski and D. J. Fox, *Gaussian 09, Revision D.01*, Gaussian, Inc., Wallingford, CT, 2009.

75 A. D. Becke, *J. Chem. Phys.*, 1993, **98**, 5648–5652.

76 C. Lee, W. Yang and R. G. Parr, *Phys. Rev. B: Condens. Matter Mater. Phys.*, 1988, **37**, 785–789.

77 S. Grimme, J. Antony, S. Ehrlich and H. Krieg, *J. Chem. Phys.*, 2010, **132**, 154104.

78 G. A. Andrienko, *ChemCraft Version 1.8.*, available at http://www.chemcraftprog.com.

79 P. Ros and G. C. A. Schuit, *Theor. Chim. Acta*, 1966, **4**, 1–12.

80 *Multiwfn 3.3.6.*, http://multiwfn.codeplex.com/, accessed June 2016.

81 T. Lu and F. Chen, *J. Comput. Chem.*, 2012, **33**, 580–592.

82 T. Lu and F. Chen, *Acta Chim. Sin.*, 2011, **69**, 2393–2406.

83 J. P. Perdew, M. Levy and J. L. Balduz, *Phys. Rev. Lett.*, 1982, **49**, 1691–1694.

84 M. Levy, J. P. Perdew and V. Sahni, *Phys. Rev. A: At., Mol., Opt. Phys.*, 1984, **30**, 2745–2748.

85 C.-O. Almbladh and U. von Barth, *Phys. Rev. B: Condens. Matter Mater. Phys.*, 1985, **31**, 3231–3244.

86 J. P. Perdew and M. Levy, *Phys. Rev. B: Condens. Matter Mater. Phys.*, 1997, **56**, 16021–16028.

87 S. Refaely-Abramson, R. Baer and L. Kronik, *Phys. Rev. B: Condens. Matter Mater. Phys.*, 2011, **84**, 075144.

88 F. Meyers, S. R. Marder, B. M. Pierce and J. L. Bredas, *J. Am. Chem. Soc.*, 1994, **116**, 10703–10714.

89 *Materials Studio Modeling Environment, V8.0.0.843*, Dassault Systèmes BIOVIA, San Diego, 2014.

90 E. Cancès, B. Mennucci and J. Tomasi, *J. Chem. Phys.*, 1997, **107**, 3032.

91 B. Mennucci, E. Cancès and J. Tomasi, *J. Phys. Chem. B*, 1997, **101**, 10506–10517.

92 R. L. Martin, *J. Chem. Phys.*, 2003, **118**, 4775.

93 S. Hedström and P. Persson, *J. Phys. Chem. C*, 2012, **116**, 26700–26706.

94 M. O. Sinnokrot, E. F. Valeev and C. D. Sherrill, *J. Am. Chem. Soc.*, 2002, **124**, 10887–10893.

This journal is © the Owner Societies 2016

Phys. Chem. Chem. Phys., 2016, **18**, 27654–27670 | **27669**

95 K. Akaike, K. Kanai, H. Yoshida, J. Tsutsumi, T. Nishi, N. Sato, Y. Ouchi and K. Seki, *J. Appl. Phys.*, 2008, **104**, 023710.

96 B. W. Larson, J. B. Whitaker, X.-B. Wang, A. A. Popov, G. Rumbles, N. Kopidakis, S. H. Strauss and O. V. Boltalina, *J. Phys. Chem. C*, 2013, **117**, 14958–14964.

97 Q. Bao, O. Sandberg, D. Dagnelund, S. Sandén, S. Braun, H. Aarnio, X. Liu, W. M. Chen, R. Österbacka and M. Fahlman, *Adv. Funct. Mater.*, 2014, **24**, 6309–6316.

98 H. Yoshida, *J. Phys. Chem. C*, 2014, **118**, 24377–24382.

99 K. R. Graham, C. Cabanetos, J. P. Jahnke, M. N. Idso, A. El Labban, G. O. Ngongang Ndjawa, T. Heumueller, K. Vandewal, A. Salleo, B. F. Chmelka, A. Amassian, P. M. Beaujuge and M. D. McGehee, *J. Am. Chem. Soc.*, 2014, **136**, 9608–9618.

100 K. Vandewal, S. Albrecht, E. T. Hoke, K. R. Graham, J. Widmer, J. D. Douglas, M. Schubert, W. R. Mateker, J. T. Bloking, G. F. Burkhard, A. Sellinger, J. M. Frechet, A. Amassian, M. K. Riede, M. D. McGehee, D. Neher and A. Salleo, *Nat. Mater.*, 2014, **13**, 63–68.

101 D. Veldman, O. Ipek, S. C. J. Meskers, J. Sweelssen, M. M. Koetse, S. C. Veenstra, J. M. Kroon, S. S. van Bavel, J. Loos and R. A. J. Janssen, *J. Am. Chem. Soc.*, 2008, **130**, 7721–7735.

102 K. Tvingstedt, K. Vandewal, A. Gadisa, F. Zhang, J. Manca and O. Inganäs, *J. Am. Chem. Soc.*, 2009, **131**, 11819–11824.

103 M. A. Faist, T. Kirchartz, W. Gong, R. S. Ashraf, I. McCulloch, J. C. de Mello, N. J. Ekins-Daukes, D. D. C. Bradley and J. Nelson, *J. Am. Chem. Soc.*, 2012, **134**, 685–692.

PUBLICATION

III

"Electronic couplings and rates of excited state charge transfer processes at poly(thiophene-*co*-quinoxaline)–PC$_{71}$BM interfaces: two- versus multi-state treatments"

T. Kastinen, D. A. da Silva Filho, L. Paunonen, M. Linares, L. A. Ribeiro Junior, O. Cramariuc, and T. I. Hukka

Check for updates

Electronic couplings and rates of excited state charge transfer processes at poly(thiophene-*co*-quinoxaline)–PC₇₁BM interfaces: two- *versus* multi-state treatments†

Tuuva Kastinen, [ID] *[a] Demetrio Antonio da Silva Filho, [ID] [b] Lassi Paunonen, [ID] [c]
Mathieu Linares, [ID] [def] Luiz Antonio Ribeiro Junior, [ID] [b] Oana Cramariuc [ID] [gh] and
Terttu I. Hukka [ID] *[a]

Electronic coupling between adjacent molecules is one of the key parameters determining the charge transfer (CT) rates in bulk heterojunction (BHJ) polymer solar cells (PSCs). We calculate theoretically electronic couplings for exciton dissociation (ED) and charge recombination (CR) processes at local poly(thiophene-*co*-quinoxaline) (TQ)–PC₇₁BM interfaces. We use eigenstate-based coupling schemes, *i.e.* the generalized Mulliken–Hush (GMH) and fragment charge difference (FCD) schemes, including 2 to multiple (3–11) states. Moreover, we study the effects of functionals, excited state methods, basis sets, surrounding media, and relative placements of TQ and PC₇₁BM on the coupling values. Generally, both schemes provide consistent couplings with the global hybrid functionals, which yield more charge-localized diabatic states and constant coupling values regardless of the number of states, and so the 2-state schemes may be sufficient. The (non-tuned and optimally tuned) long-range corrected (LRC) functionals result in more notable mixing of the local components with the CT states. Employing multiple states reduces the mixing and thus improves the LRC results, although the method still affects the GMH CR couplings. As the FCD scheme is less sensitive, we recommend combining it with the multi-state treatment for polymer–fullerene systems when using the LRC functionals. Finally, we employ the 11-state FCD couplings to calculate the ED and CR rates, which are consistent with the experimental rates of the polymer–fullerene systems. Our results provide more insight into choosing a suitable eigenstate-based coupling scheme for predicting the electronic couplings and CT rates in photoactive systems.

[a] *Chemistry and Advanced Materials, Faculty of Engineering and Natural Sciences, Tampere University, FI-33014 Tampere University, P. O. Box 541, Finland. E-mail: tuuva.kastinen@tuni.fi, terttu.hukka@tuni.fi*

[b] *Institute of Physics, University of Brasília, Brasília, DF, Brazil*

[c] *Mathematics, Faculty of Information Technology and Communication Sciences, Tampere University, FI-33014 Tampere University, P. O. Box 692, Finland*

[d] *Laboratory of Organic Electronics, ITN, Campus Norrköping, Linköping University, SE-581 83 Linköping, Sweden*

[e] *Scientific Visualization Group, ITN, Campus Norrköping, Linköping University, SE-581 83 Linköping, Sweden*

[f] *Swedish e-Science Research Centre (SeRC), Linköping University, SE-581 83 Linköping, Sweden*

[g] *Physics, Faculty of Engineering and Natural Sciences, Tampere University, FI-33014 Tampere University, P. O. Box 692, Finland*

[h] *Centrul IT pentru Stiinta si Tehnologie, Av. Radu Beller 25, Bucharest, Romania*

† Electronic supplementary information (ESI) available: Additional information regarding the TQ–PC₇₁BM models and the methods; the excited state properties of the isolated TQ and PC₇₁BM models and the corresponding complexes investigated with B3LYP and CAM-B3LYP; the OT *ω* for the isolated TQ and PC₇₁BM models and the 3T4Q–PC₇₁BM/3Q4T–PC₇₁BM complexes; vertical excitation energies, and adiabatic and diabatic Δ*μ* and Δ*q* values for the CT₁ and LE states; NTOs of 3T4Q–PC₇₁BM, and electronic couplings of 3T4Q–PC₇₁BM and 3Q4T–PC₇₁BM; and bond length alternations of 3T4Q and 3Q4T. See DOI: 10.1039/c9cp04837e

Introduction

Polymer solar cells (PSCs), which consist of conjugated donor–acceptor (D–A) copolymers as electron donor (eD) materials, have recently reached power conversion efficiencies (PCEs) up to 12%[1,2] when using a fullerene derivative, *e.g.* PC₇₁BM (phenyl-C₇₁-butyric acid methyl ester), as an electron acceptor (eA) material. In recent years, PCEs up to 13–14%[3,4] have been achieved with non-fullerene materials as the eAs. These best performing PSCs make use of a bulk heterojunction (BHJ) architecture[5] in the photoactive layer, where the eD is mixed with the eA, ensuring the closest contact and an efficient charge transfer (CT) between the eD and eA materials.

Charge generation at the eD–eA interface is based on photo-induced electron transfer (PET), whose efficiency is determined by the following CT processes[6,7] (Fig. 1a): (i) absorption of light by the eD (or the eA in some cases) leading to the formation of a locally excited state (LE, *i.e.* eD*–eA) and excitons (*i.e.* coulombically bound electron–hole pairs); (ii) diffusion of excitons to the eD–eA interface; (iii) exciton dissociation (ED) *via* an

25606 | *Phys. Chem. Chem. Phys.*, 2019, **21**, 25606–25625

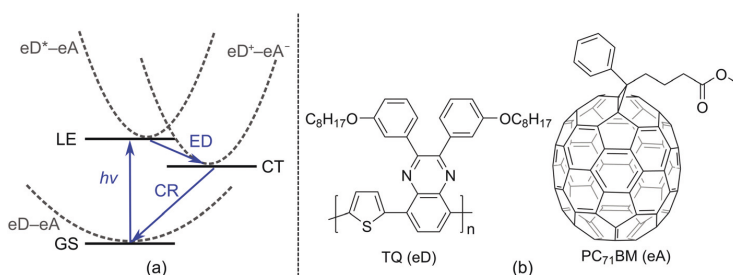This journal is © the Owner Societies 2019

Fig. 1 (a) Schematic energy diagram illustrating the main steps of the photophysical processes occurring in the photoactive layer of a BHJ PSC. (b) Structures of an eD (TQ) and an eA (PC$_{71}$BM).

electron transfer from the eD* to eA and the formation of a CT state (eD$^+$–eA$^-$); (iv) if the charge carriers overcome the Coulomb binding energy, their separation into free carriers; and (v) migration of charges towards the electrodes. Alternatively, the CT state can decay *via* radiative emission or irradiative charge recombination (CR) to the ground state (GS, *i.e.* eD–eA), which hinders the charge generation and thus reduces the performance of the device. Thus, maximizing the ED (and charge separation) rate and minimizing the CR rate are crucial for the efficiency of a PSC.

Predicting the rates of the ED and CR processes gives more insight into the efficiency of the charge generation at the eD–eA interface. In the high-temperature (weak-coupling), $k_BT \gg \hbar\omega$, regime, the semi-classical Marcus theory[8–10] can be used to calculate the ED and CR rates:

$$k_{ED/CR} = \frac{|H_{if}|^2}{\hbar} \sqrt{\frac{\pi}{\lambda k_B T}} \exp\left[-\frac{(\Delta G^\circ + \lambda)^2}{4\lambda k_B T}\right], \qquad (1)$$

where H_{if} is the electronic coupling (also referred to as a transfer integral) between the initial (i) and final (f) states of the CT process considered;[11] k_B and $\hbar$ are the Boltzmann and reduced Planck constants, respectively; T is the temperature; λ is the reorganization energy (consisting of the inner, λ_i, and outer, λ_s, contributions, see the ESI†); and ΔG° is the Gibbs free energy. As the ED and CR rates are directly proportional to H_{if}, it is one of the key parameters determining them.[7]

The electronic coupling H_{if} describes the strength of the interaction between the initial and final charge-localized (diabatic) states. It is defined as the off-diagonal matrix element of the electronic Hamiltonian (*H*): $H_{if} = \langle \psi_i | H | \psi_f \rangle$, where ψ_i and ψ_f are the wave functions of the initial and final diabatic states of interest.[11] Thus, the value of H_{if} depends on the overlap of ψ_i and ψ_f and is very sensitive to the relative intermolecular position and distance of the eD and eA molecules.[12,13] For this reason, an accurate estimation and prediction of the H_{if} values between the interacting species is a challenging subject of research in biology, chemistry, and physics.[11,14]

Experimentally, H_{if} has been evaluated from spectroscopic data by fitting them into theoretical expressions.[15] Theoretically, a number of computational methods based on *ab initio* quantum mechanics (QM) have been proposed and applied to

estimate the CT couplings.[11,16,17] For calculating H_{if} of the CT processes involving excited states, *e.g.* ED and CR, different diabatization schemes have been developed. In these schemes, adiabatic states retrieved from QM calculations are transformed to diabatic states by using either the wave-function, as in the Boys localization,[18] the Edmiston–Ruedenberg localization,[19] and block diagonalization,[20,21] or an additional operator, *e.g.* dipole moment (μ) in the generalized Mulliken–Hush (GMH)[22,23] scheme or charge difference (Δq) in the fragment charge difference (FCD)[24] scheme. In addition, more simple approaches have been developed recently, where electronic couplings are obtained either directly[25] from excitation energies and oscillator strengths or by defining the quasi-diabatic states,[26] which are derived from the excited electronic states of the reference structures. In this paper, we will focus on the GMH and FCD schemes that are available in the Q-Chem software,[27] as they have proven to be useful and flexible for calculating electronic couplings for the excited state processes[22,24,28] and they can be employed for large molecules, as well.[16]

Previously, a number of theoretical investigations have been reported using the two-state GMH and FCD schemes for determining H_{if} at local photoactive eD–eA interfaces, such as phthalocyanine–C$_{60}$,[29] pentacene–C$_{60}$,[30–32] and D–A copolymer–fullerene systems.[33–39] In particular, the two-state GMH scheme has been used in several studies of D–A copolymers and fullerene derivatives.[33–38] However, in these studies, mainly the electronic couplings between the GS and excited states, *i.e.* the CR couplings, have been taken into account,[33–36] while there are fewer studies[37,38] which consider the couplings between the excited states, *e.g.* the LE and CT states, in the case of the ED process. In the PET, all these states are relevant for describing the ED and CR processes at the copolymer–fullerene interfaces. Moreover, to the best of our knowledge the effectiveness of the FCD scheme for predicting H_{if} in these systems in comparison with the GMH scheme has not yet been studied, and thus further information about this is required.

Typically, two eigenstates are included in the GMH and FCD calculations to form charge-localized diabatic states. However, previous studies of the complexes consisting of small or medium sized organic molecules,[28,40,41] DNA π stacks,[24,42–44] donor–bridge–acceptor systems,[28,45] and TiO$_2$–dye systems[46] have shown that sometimes several adiabatic states are necessary

to describe the diabatic states accurately. In such instances, the corresponding multi-state GMH and FCD approaches are required.[28,40] This is commonly the case, for example, when the component of the local excitation of the eD or eA is mixed with the CT state, and the two-state GMH scheme may lead to overestimated electronic coupling values.[47] However, to our knowledge, there are not yet studies which take account of the multi-state effects when predicting the coupling values with either the GMH or FCD scheme for the photoactive components of the active layers in PSCs containing D–A copolymers.

Previous studies have shown[48,49] that electronic couplings are sensitive to the choice of density functional theory (DFT). Global hybrid functionals with a fixed, global fraction of explicit Hartree–Fock (HF) exchange, including especially B3LYP,[50,51] have been generally a popular choice in the theoretical studies of photovoltaic compounds, but they are known to tend to overdelocalize the electron density due to the many-electron self-interaction error (MSIE).[52,53] However, among the global hybrids, PBE0,[54–56] which is mainly based on fundamental constants rather than on fitting to empirical parameters, has been demonstrated to produce relatively accurate electron densities for a set of atomic species[57] and also for larger organic molecules with two to ten heavy atoms (e.g. carbon, oxygen, nitrogen, and sulfur).[58] Long-range corrected (LRC) functionals, where the exchange term in the Kohn–Sham energy functional is partitioned into short-range (SR) and long-range (LR) components by employing a splitting function (e.g. the standard error function or its extended versions[59]), have resulted in improved excitation energies of copolymers and copolymer–fullerene systems with respect to B3LYP.[53] In LRC functionals, DFT exchange is used for the SR part to treat the SR static correlation effects, while semilocal correlation is used for the LR part together with the full (100%) HF exchange, which will ensure the correct description of the asymptotic potential.[53] In particular, the LRC functional CAM-B3LYP[60] has been employed to reveal the excited state properties in the previous GMH coupling and CT rate calculations of copolymer–fullerene systems.[33–36] However, here we note that not all functionals based on the range separation formalism actually include the full HF exchange, CAM-B3LYP with the 65% HF exchange in the LR component being one example, which may have consequences on the predicted values.[61] In LRC functionals, the amount of (de)localization error is dependent on the range-separation parameter (ω), which defines the switching between the SR and LR. As ω is system-dependent,[62] using the default ω values can lead to inaccurate results, and thus to address the problem of the MSIE, optimally tuned (OT) LRC functionals have been introduced.[53] Tuning of ω in the LRC functionals is known to improve the calculated excitation energies of D–A copolymers with respect to the experimental ones.[63–66] Moreover, the FCD scheme has been reported to yield electronic couplings of stacked small molecules (i.e. ethylene, pyrrole, and naphthalene) closer to the experimental Mulliken–Hush values, when the OT version of the LRC Baer–Neuhauser–Livshits (BNL)[67,68] functional

(incorporating the full 100% HF exchange into the LR component) has been used.[49]

In the present work, we calculate the electronic couplings of the ED and CR processes at local polymer–fullerene interfaces with two- and multi-state GMH and FCD schemes. For our model systems of the eD–eA interfacial complexes, we have chosen to use a D–A copolymer, poly[thiophene-2,5-diyl-alt-2,3-bis-(3-octyloxyphenyl)quinoxaline-5,8-diyl][69,70] (TQ, Fig. 1b), as the eD and a fullerene derivative, $PC_{71}BM$,[71] as the eA. These photoactive components have been widely used in BHJ PSCs, demonstrating promising efficiencies and high open-circuit voltages,[72] making them a representative model system for this study. In particular, TQ has several interesting characteristics such as being an easily synthesized copolymer with a low bandgap, whose solubility and twisting can be effectively controlled with different side chains.[70,73] Recently, TQ and its fluorinated counterparts have been employed successfully as the eDs also in all-polymer solar cells.[74] Furthermore, from a theoretical point of view, a small size of TQ allows using suitably long oligomers in the complex systems, while maintaining small enough states in the computationally heavy time-dependent (TD) DFT calculations.

Our purpose is to determine how the inclusion of multiple states affects the GMH and FCD couplings of relatively large photovoltaic complexes. Additionally, we consider the performance of the aforementioned coupling schemes relative to the choice of functional, excited state method, basis set, and surrounding medium. We have selected a small series of representative functionals, namely two global hybrid functionals, B3LYP and PBE0, and two LRC functionals, (non-tuned) CAM-B3LYP and OT-BNL, which we have chosen based on the reasons presented above. As the tuning of ω in the LRC functionals is known to improve results for the polymer–fullerene systems with respect to the global hybrid and non-tuned LRC functionals (see above), we pay close attention to the performance of the tuned LRC functional with respect to the other selected functionals. Finally, we calculate the rates for the ED and CR processes at two TQ–$PC_{71}BM$ interface configurations, where $PC_{71}BM$ locates on either the D or A unit of TQ. Our findings provide insight into choosing the electronic coupling schemes for these types of eD–eA systems used in PSCs.

Computational details

Models

Two different series of TQ–$PC_{71}BM$ complexes were constructed using the separately-optimized B3LYP GS geometries of the (neutral) TQ oligomers and $PC_{71}BM$ (the α isomer[71]): one, where $PC_{71}BM$ was on top of the middle thiophene (the D unit) of TQ, and another, where $PC_{71}BM$ was on top of the middle quinoxaline (the A unit) of TQ (see the ESI† for more detailed information about the models). The alkoxyphenyl side groups of the TQ oligomers (Fig. 1b) were replaced with hydrogens to reduce the computational cost and to ensure planar backbones. Because the DFT-based methods, e.g. TDDFT, set restrictions to

Paper

the sizes of the eD–eA complexes, we modeled the TQ oligomers with several lengths to choose the TQ models that would best represent the polymeric limit in the electronic coupling calculations. We note that the studied complexes present only two options for the possible placements of $PC_{71}BM$ on TQ that can exist in real solution or thin film environments. Although the face-on configurations (*i.e.* $PC_{71}BM$ on top of TQ) can be expected to yield larger electronic couplings than the edge-on configurations (*i.e.* $PC_{71}BM$ on the side of TQ),[39,75,76] there might be a relative positioning of the compounds different from the ones used here that yields the maximum electronic coupling between them. The intermolecular distance between TQ and $PC_{71}BM$ (*d*, Fig. 2a) was set at 3.5 Å, which is an average we predicted in our previous study for poly(benzodithiophene-*co*-quinoxaline)–$PC_{71}BM$ complexes with functionals including long-range and dispersion corrections.[66] The same intermolecular distance has also been employed in other theoretical polymer–fullerene interface studies.[34,77] The distances between the centers of mass (R_{eD-eA}, Fig. 2a) of TQ and $PC_{71}BM$ are *ca.* 8.6 Å.

Methods

We carried out the DFT and TDDFT calculations using the Q-Chem 4.2 software.[27] The medium was taken into account, as specified later. The GS geometries of the isolated models of the neutral TQ oligomers and $PC_{71}BM$ and their radical states (cations for TQ and anions for $PC_{71}BM$; only for the longest TQ oligomers, see the ESI†) were fully optimized in vacuum using DFT with the global hybrid functional B3LYP and the 6-31G** basis set. Moreover, the geometries of the lowest singlet excited (S_1) of the longest TQ oligomers were optimized with TDDFT at the same level of theory. In all the geometry

optimizations, the fine grid EML(75,302) with 75 Euler–Maclaurin radial grid points[78] and 302 Lebedev angular grid points,[79] an SCF convergence criterion of 10^{-9}, and a cutoff for neglect of two electron integrals of 10^{-14} were employed. In the single point (SP) calculations of the isolated compounds related to the excited state, reorganization energy, and Gibbs free energy calculations and those of the selected complexes (Fig. 2b) related to the excited state and electronic coupling calculations, the 6-31G* basis set, the standard SG-1 grid, and the default values for the SCF convergence (10^{-5}) and cutoff of two electron integrals (10^{-8}) were used, unless stated otherwise. The excited state SP energy calculations of both the isolated models and the complexes were carried out for the lowest 10 singlet excited states with both the full TDDFT and TDA-DFT schemes, incorporating the Tamm–Dancoff approximation (TDA)[80] in the latter. We note that sometimes ED and CR processes may involve triplet states,[81] but here we have concentrated on those including only singlet states. B3LYP and the LRC functional CAM-B3LYP (with the default range-separation parameter, ω, of 0.33 Bohr^{-1}) were used in all SP calculations. Additionally, the global hybrid functional, PBE0, and the OT version of the BNL LRC functional (OT-BNL) were used in the SP calculations of the selected TQ–$PC_{71}BM$ complexes (see 'Models' and 'Length of the TQ oligomer and the polymeric limit'). The OT ω values (originally 0.5 Bohr^{-1}) for the selected TQ–$PC_{71}BM$ complexes were determined using eqn (S1) and the tuning procedure is presented in the ESI.† We note that, in addition to the tuning of ω, incorporation of some amount of HF exchange in the SR component has been observed to improve the prediction of the optoelectronic properties of several aromatic heterocycles,[82] DNA nucleobase compounds and their complexes,[61] and compounds employed in organic
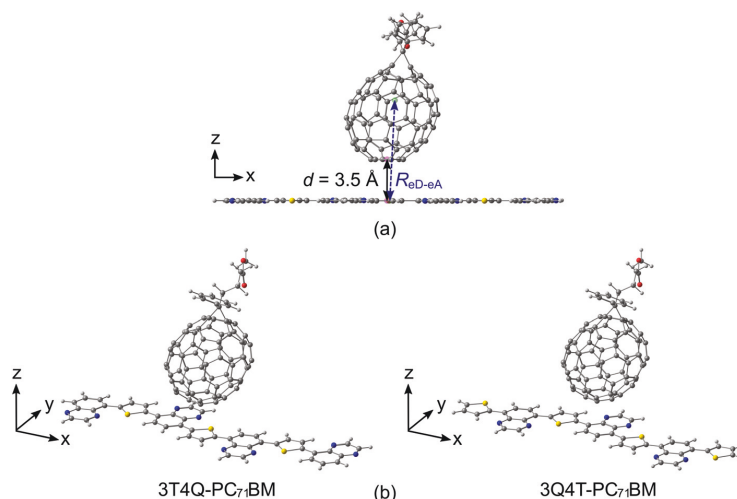

Fig. 2 Illustration of (a) intermolecular distance, *d*, and effective separation, R_{eD-eA}, between TQ and $PC_{71}BM$ in the studied TQ–$PC_{71}BM$ complexes. These distances were determined between the specified centroids, pink spheres for *d*, and the centers of mass, green spheres for R_{eD-eA}. (b) TQ–$PC_{71}BM$ complexes with the longest TQ oligomer models, where $PC_{71}BM$ is either above thiophene (3T4Q) or quinoxaline (3Q4T).

light emitting diodes.[59] The BNL functional we employ here does include only the LR HF exchange, but due to the extent of the various theoretical aspects studied here, we have chosen to concentrate only on the effect of the ω tuning in this study. Pictorial representations of the geometries and natural transition orbitals (NTOs)[83] were generated using ChemCraft 1.8.[84] The contributions of the electron densities of TQ and $PC_{71}BM$ to the NTOs were determined with the C-squared Population Analysis (C-SPA).[85]

Furthermore, we checked the role of the basis set and surrounding medium in the electronic couplings. We employed, besides 6-31G*, also 6-31G** and 6-31+G* with TDDFT and the B3LYP functional, and 6-31G** with the PBE0, CAM-B3LYP, and OT-BNL functionals. As these calculations were too heavy for the studied complexes, we were unable to verify the effect of 6-31+G* with the LRC functionals and the effect of any larger basis sets. Nor did we consider the other types of basis sets (e.g. Dunning's) here. The influence of the medium was taken into account in the coupling and CT rate calculations by means of the conductor-like polarizable continuum model (CPCM)[86,87] with a Switching/Gaussian (SWIG) implementation[88] without geometry optimizations. Two different polarized media were considered: (i) a solvent with the static (ε_s) and dynamic (optical, ε_{op}) dielectric constants of 10.1210 and 2.4072 for 1,2-dichlorobenzene (1,2-DCB, at 293.15 K),[89] respectively, and (ii) a blend, i.e. a film with ε_s and ε_{op} of 3.6000[90] and 3.2761, respectively. The ε_{op} of the blend was calculated[77] by $\varepsilon_{op} = n^2$ from the experimental refractive index (n) of the TQ–$PC_{71}BM$ blend (ca. 1.81 at 532 nm).[91]

For determining the electronic couplings, we used both the GMH[22,23] and FCD[24] schemes as implemented in Q-Chem 4.2[27] to calculate the adiabatic electronic (μ_{ii}^{ad}) and transition dipole moments (μ_{ij}^{ad}) (within the GMH scheme) and the charge differences (Δq_{ii}^{ad} and Δq_{ij}^{ad}, within the FCD scheme) for the GS and ten lowest singlet excited states. Among these 11 adiabatic states, the relevant states for the ED and CR processes, i.e. the GS [eD–eA], the LE state of TQ [eD*–eA], and the lowest CT state [CT$_1$, eD$^+$–eA$^-$] (Fig. 1), were assigned on the basis of the μ_{ii} and Δq_{ii} values and the NTOs (for more details see 'Assignment of the states' in the ESI†). The electronic couplings (eqn (S2)–(S11), ESI†), reorganization energies (eqn (S12)–(S18), ESI†), and Gibbs free energies (eqn (S19)–(S22), ESI†) for the ED and CR processes were calculated using the equations presented in the ESI.† The CT rates for the ED and CR processes were calculated with the Marcus theory (eqn (1)) at a temperature of 293.15 K. The 11-state FCD H_{if} values (eqn (S2)–(S4) in the ESI†) were used in the CT rate calculations.

Results and discussion

Length of the TQ oligomer and the polymeric limit

To select the TQ model that best represents the polymeric limit in the electronic coupling and CT rate calculations, we have studied the effect of the TQ length on the excited state properties of the isolated TQ models and the TQ–$PC_{71}BM$ complexes (Fig. S1, ESI†). The results apply to both the B3LYP and

CAM-B3LYP functionals used in these calculations unless stated otherwise (see the ESI† for more detailed information). In general, both the T- and Q-series follow similar trends (Tables S1–S3, ESI†). The S_1 energies of the isolated TQ oligomers with the corresponding lengths are almost equal (Table S1, ESI†): the singlet energies decrease only slightly, when the chain length increases, as expected.[28,40,45] The placement of $PC_{71}BM$, i.e. above either the central T or Q unit of the TQ oligomer, has a negligible or a very small effect on the excited state energies and oscillator strengths in the complexes of the T- and Q-series with the corresponding lengths (Tables S2 and S3, ESI†). In contrast, the energies of the main vertical excitation ($E_{vert,main}$, i.e. the excitation having the largest oscillator strength) and the CT$_1$ state decrease (the peaks red-shift), and the oscillator strengths of the peaks increase (except for the CT$_1$ state with CAM-B3LYP), when the length, and, therefore, the contribution of the TQ oligomer, increases in the complex. In the complexes with the shortest TQs, only local excitations of $PC_{71}BM$ (LF) are observed and no LE or CT states are predicted (Tables S2 and S3, ESI†) within the ten lowest singlet excited states. The oligomers consisting of five units, i.e. 3T2Q and 3Q2T, are long enough for the LE and CT states to appear in the complexes, with LE being the main excitation. However, we have selected the complexes with the longest oligomers consisting of seven units, i.e. 3T4Q–$PC_{71}BM$ and 3Q4T–$PC_{71}BM$, for the further calculations, as they have even more distinguishable LE and CT$_1$ states with both B3LYP and CAM-B3LYP. Foremost, the B3LYP energies of the CT$_1$ (ca. 1.6 eV) and LE states (ca. 1.9 eV) of 3T4Q–$PC_{71}BM$ and 3Q4T–$PC_{71}BM$ are closest to the experimental excited state energies ($E_{CT} = 1.4$–1.5 eV[92,93] and $E_{LE} = 1.97$ eV taken from the absorption maximum in the experimental UV-Vis absorption spectrum of a TQ–$PC_{71}BM$ (3:1) film[93]). For the aforementioned reasons, 3T4Q–$PC_{71}BM$ and 3Q4T–$PC_{71}BM$ are expected to be our best candidates for further modeling of the properties of the TQ–$PC_{71}BM$ complexes.

Effect of the functional on the excited state characteristics and electronic couplings

The functional has a clear effect on the excited state characteristics (i.e. excitation energies and nature of the state) of the studied complexes, 3T4Q–$PC_{71}BM$ and 3Q4T–$PC_{71}BM$ (Fig. 2b). Generally, when considering the 10 lowest adiabatic states of the complexes obtained with TDDFT (in vacuum), the excitation energies for the S_1–S_{10} states increase in the order B3LYP (20% HF) < PBE0 (25% HF) < OT-BNL (with an OT ω of 0.17 Bohr^{-1}, see Table S4, ESI†) < CAM-B3LYP (Table S5, ESI†). The global hybrids B3LYP and PBE0 predict the three lowest excited states as the CT states, whereas the fourth state is the intramolecular excitation of TQ, i.e. the LE state. This ordering of the CT$_1$ and LE states, i.e. the CT$_1$ state is lower in energy than the LE state, is consistent with the experimental results[92,93] (see above). Above the CT$_1$ and LE states in energy, the global hybrids predict local excitations of $PC_{71}BM$, i.e. the LF states, and higher-energy CT states, whose nature ('pure' vs. partial CT) and number (between one and three) vary somewhat regarding

the functional and position of $PC_{71}BM$ on TQ. With the LRC functionals, CAM-B3LYP and OT-BNL, the order of the CT_1 and LE states is reverse, i.e. the CT_1 state is higher in energy (the fifth or sixth state) than the LE state (the second excited state in the most cases), which is in contrast to the results given by the global hybrids and experiments.[92,93] Additionally, the LRC functionals predict fewer CT states among the calculated 10 lowest adiabatic excited states than the global hybrids.

These differences in the tendencies between the global hybrid and LRC functionals to predict the ordering of the states of polymer–fullerene complexes have been previously observed also for other systems by us[66] and others.[81] Moreover, Zheng et al. observed the same ordering of the CT_1 and LE states also for pentacene–C_{60} complexes[94] when using the OT LRC ωB97X-D and BNL functionals. Zheng et al. noticed that the OT values of ω are smaller when using PCM compared to those obtained in vacuum. Moreover, the energy of the CT_1 state is affected by ω and decreases with decreasing ω, eventually locating at an energy lower than that of the LE state. However, in their recent paper, Kronik and Kümmel pointed out[95] that including the PCM in the tuning of ω may lead to inconsistent results, as the PCM affects the total energies but not the DFT eigenvalues, resulting in the OT ω values that are notably smaller than those in vacuum. Thus, we have used the OT ω of OT-BNL obtained under vacuum also in the 1,2-DCB and blend environments explained later.

The functional has a notable effect on the nature of the adiabatic CT_1 state of the studied complexes, whereas the nature of the LE state is very similar regardless of the functional. The global hybrid functionals predict almost negligible mixing of the local states with the adiabatic CT_1 state, which is observed from the adiabatic Δq_{ii} values of the CT_1 state (i.e. Δq_{CT1}^{ad} of 1.9–2.0 in Tables 1 and 2) as they are already close to the ideal value of 2.[28]

Table 1 Adiabatic and diabatic electric dipole moments ($\Delta\mu_{ii}^{ad}$ and $\Delta\mu^{diab}$)[a] and charge differences (Δq_{ii}^{ad} and Δq^{diab}) for the CT_1 and LE states of 3T4Q–$PC_{71}BM$ calculated with the 2–11-state GMH and FCD schemes[b] using TDDFT and the 6-31G* basis set

Scheme		GMH				FCD			
Functional	N^c	$\Delta\mu_{CT1}^{ad}$	$\Delta\mu_{CT1}^{diab}$	$\Delta\mu_{LE}^{ad}$	$\Delta\mu_{LE}^{diab}$	Δq_{CT1}^{ad}	Δq_{CT1}^{diab}	Δq_{LE}^{ad}	Δq_{LE}^{diab}
B3LYP	2	31.0	31.0	1.1	0.6	1.9	1.9	0.1	0.1
	3		31.6		0.5		2.0		0.1
	4		31.4		0.5		2.0		0.1
	11		31.2		0.3		2.0		0.0
PBE0	2	29.9	30.0	1.4	0.7	1.9	1.9	0.1	0.1
	3		30.6		0.7		2.0		0.1
	4		30.5		0.7		2.0		0.1
	11		30.2		0.2		2.0		0.0
CAM-B3LYP	2	12.5	12.5	1.3	1.1	0.7	0.7	0.1	0.0
	3		13.6		0.2		0.8		0.0
	4		19.4		0.1		1.5		0.0
	11		26.6		0.6		1.9		0.0
OT-BNL	2	11.3	11.4	1.7	2.1	0.7	0.7	0.2	0.0
	3		13.5		0.4		0.8		0.0
	4		20.1		0.5		1.6		0.0
	11		24.5		0.3		1.8		0.0

[a] Relative to the GS. [b] Values calculated in vacuum. [c] Number of states.

Table 2 Adiabatic and diabatic electric dipole moments ($\Delta\mu_{ii}^{ad}$ and $\Delta\mu^{diab}$)[a] and charge differences (Δq_{ii}^{ad} and Δq^{diab}) for the CT_1 and LE states of 3Q4T–$PC_{71}BM$ calculated with the 2–11-state GMH and FCD schemes[b] using TDDFT and the 6-31G* basis set

Scheme		GMH				FCD			
Functional	N^c	$\Delta\mu_{CT1}^{ad}$	$\Delta\mu_{CT1}^{diab}$	$\Delta\mu_{LE}^{ad}$	$\Delta\mu_{LE}^{diab}$	Δq_{CT1}^{ad}	Δq_{CT1}^{diab}	Δq_{LE}^{ad}	Δq_{LE}^{diab}
B3LYP	2	31.4	31.4	0.2	0.0	2.0	2.0	0.0	0.0
	3		31.6		0.0		2.0		0.0
	4		31.6		0.0		2.0		0.0
	11		31.4		0.1		2.0		0.0
PBE0	2	30.5	30.5	0.1	0.2	2.0	2.0	0.0	0.0
	3		30.7		0.1		2.0		0.0
	4		30.8		0.1		2.0		0.0
	11		30.7		0.3		2.0		0.0
CAM-B3LYP	2	16.6	16.6	0.8	0.8	1.1	1.1	0.1	0.0
	3		17.4		0.0		1.2		0.0
	4		21.8		0.0		1.6		0.0
	11		27.9		0.3		1.9		0.0
OT-BNL	2	15.9	15.9	0.6	1.3	1.1	1.1	0.1	0.0
	3		17.3		0.7		1.2		0.0
	4		21.6		0.7		1.7		0.0
	11		26.3		0.5		1.9		0.0

[a] Relative to the GS. [b] Values calculated in vacuum. [c] Number of states.

This can be observed also from the NTOs of the two complexes (Fig. 3 and Fig. S2, ESI†), for which B3LYP and PBE0 predict a complete CT from TQ to $PC_{71}BM$, as the hole NTO localizes totally on TQ and the electron NTO on $PC_{71}BM$. Similarly, the adiabatic $\Delta\mu_{ii}$ values of the CT_1 state (i.e. $\Delta\mu_{CT1}^{ad}$ in Table 1) are rather large (29.9–31.4 D), although not close to the ideal dipole moments (41.1 D for 3T4Q–$PC_{71}BM$ and 41.3 D for 3Q4T–$PC_{71}BM$, see the ESI†). The LRC functionals predict a partial CT character for the CT_1 state ($\Delta\mu_{CT1}^{ad}$ of 11.3–16.6 D and Δq_{CT1}^{ad} of 0.7–1.1, Tables 1 and 2), i.e. mixing of the local LF states with the CT state. When considering the corresponding NTOs, it can be seen that the hole NTO of the CT_1 state localizes on both TQ and $PC_{71}BM$ and the electron NTO on $PC_{71}BM$. In this case, 3T4Q–$PC_{71}BM$ has somewhat larger mixing of a LF component with the CT state and thus a smaller amount of CT compared to 3Q4T–$PC_{71}BM$. For the LE state, the global hybrid and LRC functionals predict small adiabatic Δq_{ii} (i.e. Δq_{LE}^{ad} of 0.0–0.1 in Tables 1 and 2) and $\Delta\mu_{ii}$ values (i.e. $\Delta\mu_{LE}^{ad}$ of 0.1–1.7 D in Tables 1 and 2). The NTOs of the LE state of both complexes have the same shapes with all four functionals, i.e. both the hole and electron NTOs are delocalized along the TQ backbone, although the global hybrids yield slightly more delocalized descriptions compared to the LRC functionals. Additionally, OT-BNL predicts a small amount of CT mixed with the LE state. These differences between the global hybrid and (non-tuned and OT) LRC functionals in predicting the nature of the adiabatic states of polymer–fullerene complexes have been previously observed also by us[66] and others.[81]

The nature of the diabatic states of the complexes obtained with the 2–11-state GMH and FCD schemes is very similar to that of the adiabatic ones when employing the global hybrid functionals, whereas with the LRC functionals the diabatic states are more localized than the adiabatic states. With B3LYP and PBE0, the $\Delta\mu^{diab}$ (GMH) and Δq^{diab} (FCD) values of the LE and CT_1 states do not differ much from the adiabatic values (Tables 1 and 2).

This journal is © the Owner Societies 2019

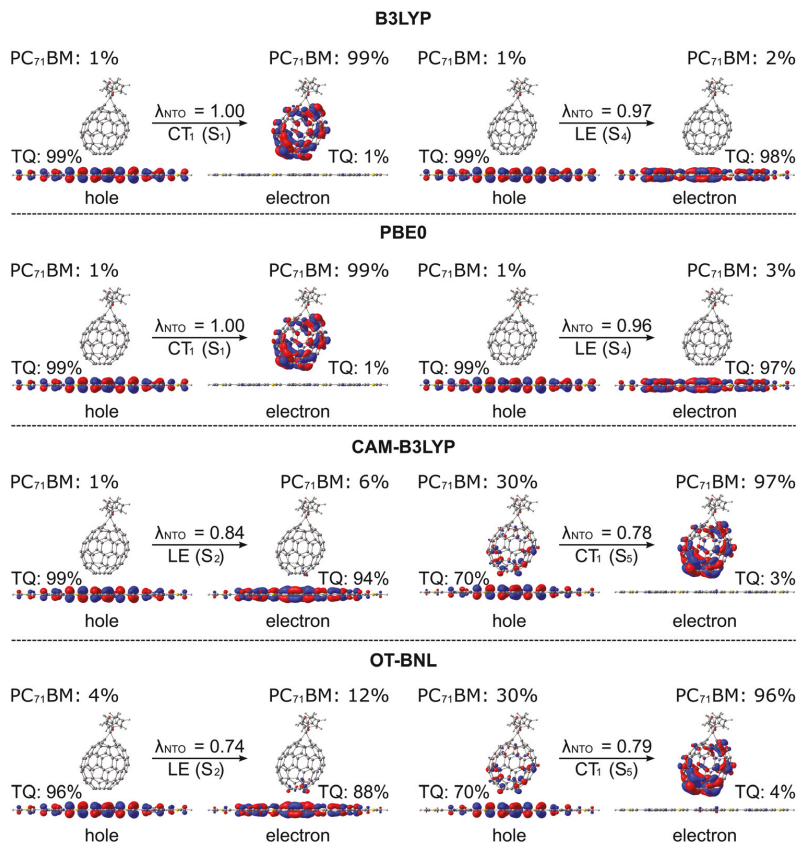Phys. Chem. Chem. Phys., 2019, **21**, 25606–25625 | **25611**

Fig. 3 NTOs (the main pair) corresponding to the CT_1 and LE states of the 3Q4T–PC_{71}BM complex calculated with TDDFT using different functionals and the 6-31G* basis set (isodensity contour = 0.025). Additionally, the contributions (%) of TQ and PC_{71}BM to the NTOs and contributions (λ_{NTO}) of the NTO pair to the particular state are presented.

This is most probably because the mixing of the states is small already for the adiabatic states, as mentioned above. The Δq_{CT1}^{diab} values predicted by the 2–11-state FCD schemes with the global hybrids mainly reach the ideal value of 2, indicating a complete CT from TQ to PC_{71}BM. However, the $\Delta\mu_{CT1}^{diab}$ values calculated with the 2–11-state GMH schemes and the global hybrids are still smaller than the ideal dipole moments (41.1 D for 3T4Q–PC_{71}BM and 41.3 D for 3Q4T–PC_{71}BM). This might indicate that the number of states used here is not enough for generating more localized diabatic states in the GMH schemes and thus for reaching the ideal dipole moments. When employing the LRC functionals in the 2–11-state FCD schemes, the diabatization effectively removes the local components that are present in the CT_1 state, yielding Δq_{CT1}^{diab} values of 1.8–1.9, which are quite close to the ideal one. Similarly, the $\Delta\mu_{CT1}^{diab}$ values, predicted with the 3–11-state GMH schemes and the LRC functionals, are now clearly larger than the adiabatic ones (Tables 1 and 2), although still not reaching the ideal dipole moments either. Thus, diabatization has a larger effect on the localization of the

CT_1 state with the (non-tuned and OT) LRC functionals compared to the global hybrids.

In most cases, all functionals predict that the 2–11-state CR electronic couplings calculated in vacuum are larger than the corresponding ED couplings (Tables S14 and S15, ESI†). However, when PC_{71}BM is above quinoxaline (the A unit) of TQ (3Q4T–PC_{71}BM), the LRC functionals predict mainly the opposite, i.e. larger ED couplings than the CR couplings with both the GMH and FCD schemes (except for the 11-state GMH scheme). The global hybrid functionals yield quite similar couplings (Fig. 4 and Fig. S3, ESI†), whereas the LRC functionals predict somewhat larger values (Fig. 5 and Fig. S4, ESI†). Overall, the ED couplings predicted with B3LYP and PBE0 for 3T4Q–PC_{71}BM and 3Q4T–PC_{71}BM are ca. 36–47 meV and 21–31 meV, respectively, whereas the CR couplings are ca. 43–56 meV and 25–34 meV, respectively. The ED couplings calculated with CAM-B3LYP and OT-BNL for 3T4Q–PC_{71}BM and 3Q4T–PC_{71}BM are ca. 49–83 meV and 33–56 meV, respectively, and the CR couplings are ca. 74–142 meV and 3–92 meV, respectively.
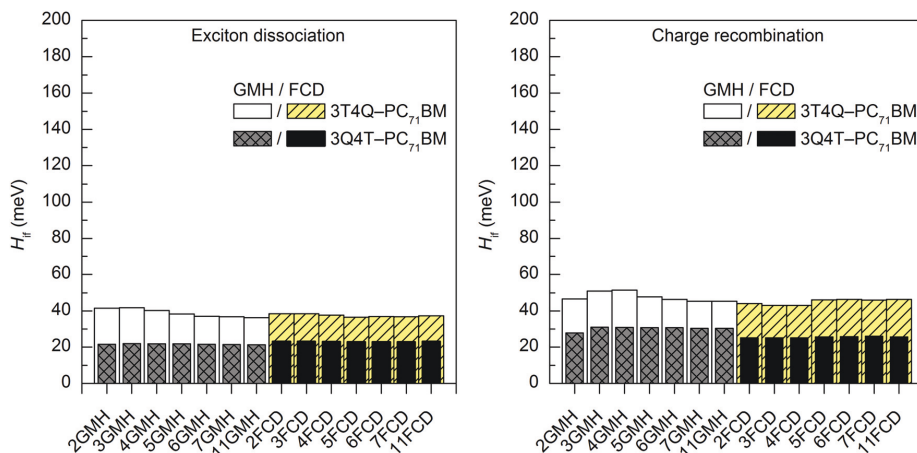
Fig. 4 Electronic coupling values of the studied TQ–PC$_{71}$BM complexes calculated with TDDFT at the B3LYP/6-31G* level of theory using the GMH and FCD schemes with different numbers of states (2–11).
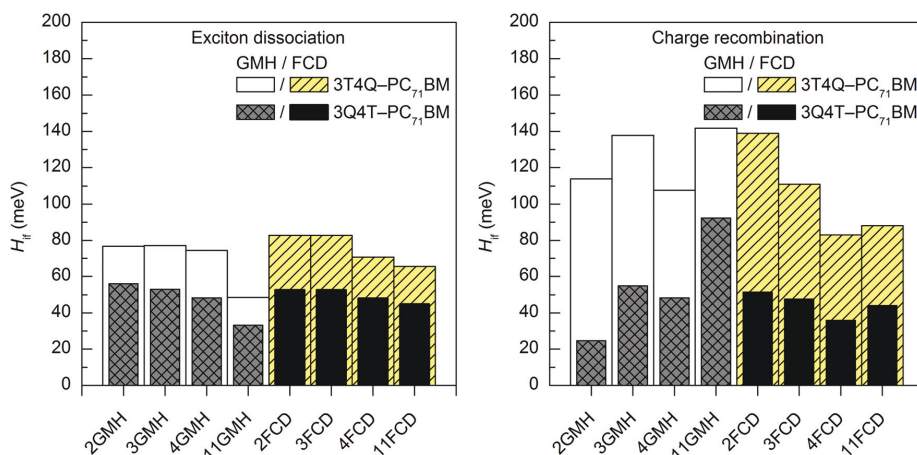

Fig. 5 Electronic coupling values of the studied TQ–PC$_{71}$BM complexes calculated with TDDFT at the OT-BNL/6-31G* level of theory using the GMH and FCD schemes with different numbers of states (2–11).

In general, the couplings increase in the order of B3LYP (20% HF) < PBE0 (25% HF) < CAM-B3LYP ≤ OT-BNL. Sini *et al.* also noticed that the coupling values increase with the increasing amount of HF exchange[48] in their study of a tetra-thiafulvalene–tetracyanoquinodimethane complex with the direct coupling method.[13] Even though we have not calculated the amounts of effective HF exchange[48] in CAM-B3LYP and OT-BNL for our complexes, as this would require a larger set of functionals with the known amounts of HF exchange, we expect that the electronic coupling value increases with the increasing amount of effective HF exchange in the functional.

To summarize, the functional has a notable effect on the excited state characteristics, *i.e.* the vertical excitation energies

and nature of the adiabatic and diabatic states, and therefore the electronic couplings. With the global hybrid functionals, both the adiabatic and diabatic CT$_1$ states have a similar, localized nature, *i.e.* a complete CT from TQ to PC$_{71}$BM. With the LRC functionals, local components mixed with the adiabatic CT$_1$ state are effectively removed by diabatization, especially with the FCD scheme. The couplings are larger with the LRC functionals than with the global hybrids.

Effect of the number of states on the electronic coupling values

The evolutions of the ED and CR electronic couplings of the selected complexes (in vacuum) with different numbers of states indicate that the functional has a clear effect on the

relationship between the coupling and the number of states (Fig. 4 and Fig. S3, ESI,† for the global hybrids, and Fig. 5 and Fig. S4, ESI,† for the LRC functionals). The corresponding numerical values are given in Tables S14 and S15, ESI.† With the global hybrid functionals, the number of states does not seem to have a very strong effect on the coupling values, as increasing the number of states decreases both the ED and CR couplings only slightly (by 0–5 meV) and they are rather constant with both the GMH and FCD schemes. This is most probably because the global hybrids predict small or negligible mixing of the adiabatic states for the studied TQ–PC$_{71}$BM complexes (see 'Effect of the functional on the excited state characteristics and electronic couplings' above), and the diabatization does not change the nature of the states much even with the increased number of states. This can be observed from the $\Delta\mu_{CT1}^{diab}$ and Δq_{CT1}^{diab} values (Tables 1 and 2), as they remain rather unchanged with an increasing number of states and are already close or equal to the ideal ones of 41.1 D and 41.3 D (for 3T4Q–PC$_{71}$BM and 3Q4T–PC$_{71}$BM, respectively) and of 2, respectively. Additionally, the GMH and FCD schemes yield quite similar coupling values when using the global hybrids, indicating that both schemes yield similar diabatic states.[28] Thus, with the global hybrids, the 2-state schemes seem to be sufficient for calculating the electronic couplings.

With the LRC-functionals (Fig. 5 and Fig. S4, ESI†), the electronic couplings of the studied complexes change more significantly with the number of states compared to the global hybrids. The GMH and FCD ED couplings predicted with the LRC functionals decrease with the increasing number of states, although in some cases the 3-state results are slightly higher than the 2-state results (Tables S14 and S15, ESI†). The 2–4-state GMH ED couplings are rather similar, whereas the 11-state values are notably smaller. With the FCD scheme, the ED couplings decrease in a more constant way. The GMH and FCD CR couplings oscillate somewhat with the increasing number of states. The GMH scheme predicts larger CR couplings with 11 states than with 2–4 states, whereas the FCD CR couplings mainly decrease when the number of states increases. Here, the tuning of ω does not seem to have a strong effect on the overall trends in the couplings, as both CAM-B3LYP and OT-BNL predict similar changes.

The number of states used here is restricted by the size of the systems and the computational time limit and therefore we are not able to judge whether the electronic couplings obtained with the LRC functionals have converged to certain values[28] already with 11 states or whether more states would improve the results. However, both the $\Delta\mu_{CT1}^{diab}$ and Δq_{CT1}^{diab} values increase with the increasing number of states (Tables 1 and 2). Moreover, even though the 11-state $\Delta\mu_{CT1}^{diab}$ values do not reach the ideal dipole moments of 41.1 D and 41.3 D (for 3T4Q–PC$_{71}$BM and 3Q4T–PC$_{71}$BM, respectively), they have improved compared to the 2–4-state values. Furthermore, the Δq_{CT1}^{diab} values are almost equal to the ideal value of 2. Thus, the 11-state GMH and FCD schemes can be expected to yield better descriptions of the diabatic states and the couplings than the 2–4 states, and for that reason, we have employed the 11-state GMH and FCD schemes in the further electronic coupling calculations.

Effect of the TD method on the excited state characteristics and the electronic couplings

Generally, the TD method does not seem to have any effect on the vertical excitation energies of the studied TQ–PC$_{71}$BM complexes, as both TDDFT and TDA yield almost identical values (in vacuum, Tables S5 and S6, ESI†). Next to equal excitation energies with both TD methods have also been observed for both small molecules[80] and large interfacial complexes (pentacene–C$_{60}$[94] and copolymer–fullerene[96]) in previous studies. However, here we observe that the number of CT states and the ordering of the states are in some cases slightly different with TDDFT and TDA, especially with the LRC functionals, which seem to have an effect on the GMH electronic couplings (see below).

The nature of the adiabatic LE and CT$_1$ states does not change significantly with the TD method when employed together with the global hybrid functionals, as TDDFT and TDA yield similar $\Delta\mu_{ii}^{ad}$ and Δq_{ii}^{ad} values in most cases (Tables 1 and 2 and Table S13, ESI†). With the LRC functionals, TDA yields slightly larger (0.2–0.5) Δq_{CT1}^{ad} values and somewhat larger (2.8–4.5) $\Delta\mu_{CT1}^{ad}$ values than TDDFT; that is, the mixing of the LF component with the adiabatic CT$_1$ state is not as strong with TDA as with TDDFT. However, diabatization of the adiabatic states with the 11-state GMH and FCD schemes results mostly in similar $\Delta\mu^{diab}$ and Δq^{diab} values with both TDDFT and TDA for diabatic LE and CT$_1$ states.

Both TD methods yield very similar 11-state electronic couplings with the global hybrid functionals, with the difference between them being only 0–4 meV (Fig. 6 and 7 and Tables S14–S16, ESI†). In addition, the 11-state FCD couplings calculated with the LRC functionals are only moderately different (by 0–12 meV) when using either TDDFT or TDA. However, the 11-state GMH couplings obtained with TDDFT and TDA and the LRC functionals differ more, namely by 2–49 meV, with TDA predicting larger couplings in most cases. The largest differences between the two TD methods are in the GMH CR couplings, which is most probably due to the differences in the $\Delta\mu^{ad}$ values other than those of the CT$_1$ and LE states. The tuning of ω does not seem to have a clear effect, as overall both the non-tuned CAM-B3LYP and OT-BNL functionals predict the same trends. Overall, TDA predicts the same trends as TDDFT: mostly larger CR couplings than the ED couplings (and *vice versa* for some 11-state FCD results for 3Q4T–PC$_{71}$BM with the LRC functionals), larger ED and CR couplings for 3T4Q–PC$_{71}$BM than for 3Q4T–PC$_{71}$BM, and larger ED and CR couplings with the LRC functionals than with the global hybrids.

To conclude, for the studied TQ–PC$_{71}$BM complexes, TDA yields consistent results with TDDFT when using the global hybrids. Thus, as TDA is computationally less costly,[97] it is a good alternative to TDDFT when combined with the global hybrids. However, when using the LRC functionals, these two TD methods might end up with rather different GMH electronic couplings. Thus, when using TDA together with the LRC functionals, the FCD scheme seems to be a more reliable choice, as the Δq values are generally not affected as much by the choice of TD method as the $\Delta\mu$ values.
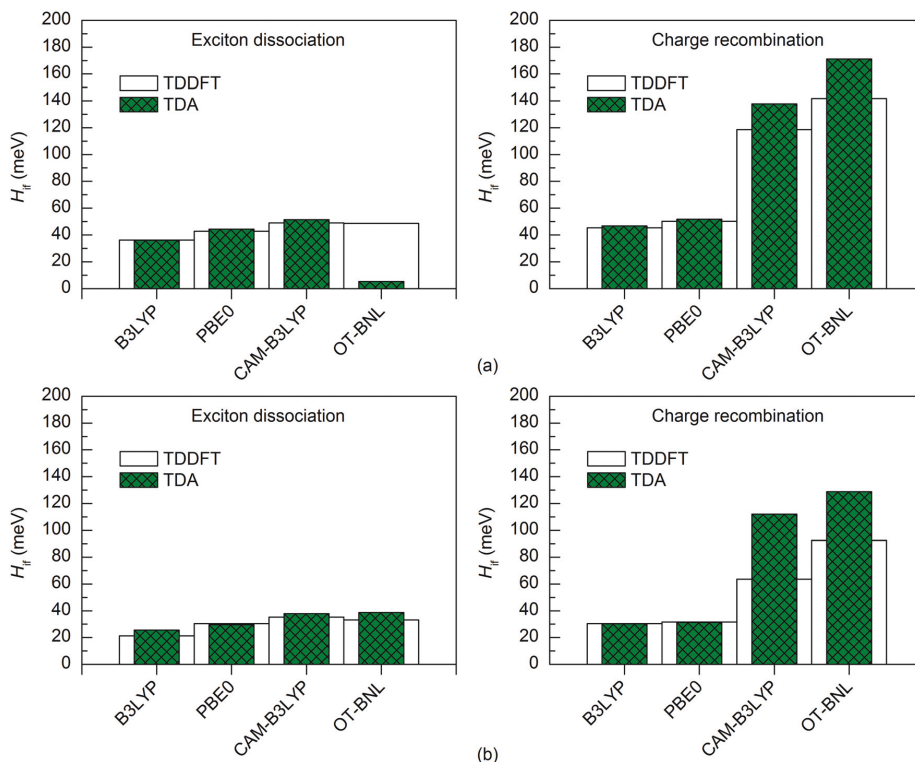
25614 | *Phys. Chem. Chem. Phys.*, 2019, **21**, 25606–25625

This journal is © the Owner Societies 2019

Fig. 6 Electronic couplings of (a) 3T4Q–PC$_{71}$BM and (b) 3Q4T–PC$_{71}$BM calculated with the 11-state GMH scheme using TDDFT and TDA with different functionals and the 6-31G* basis set.

Effect of the basis set

The basis set has a minimal effect on the exited state energies of the studied complexes: the vertical excitation energies are almost the same with both the 6-31G* (Table S5, ESI†) and 6-31G** (Table S7, ESI†) basis sets. With B3LYP, the 6-31+G* basis set yields only slightly (0.0–0.2 eV, Table S8, ESI†) smaller excitation energies for 3T4Q–PC$_{71}$BM than the two smaller basis sets. As this calculation was computationally already very demanding, we did not carry out the calculation for 3Q4T–PC$_{71}$BM at the same level of theory.

The basis set does not affect the nature of the adiabatic CT$_1$ and LE states much and their $\Delta\mu_{ii}^{ad}$ and Δq_{ii}^{ad} values calculated with the 11-state GMH and FCD schemes are mostly the same with 6-31G* (Tables 1 and 2) and 6-31G** (Table S12, ESI†). The only exception is $\Delta\mu_{CT1}^{ad}$ of 3Q4T–PC$_{71}$BM calculated with CAM-B3LYP, which is 0.7 D smaller with 6-31G** (15.9 D) than with 6-31G* (16.6 D), indicating a larger amount of the local component in the CT$_1$ state. The 6-31+G* basis set yields smaller Δq_{CT1}^{ad} of 1.6 with B3LYP than 6-31G* or 6-31G** (1.9 for both basis sets, see Tables 1 and 2 and Table S12, ESI†). The diabatic CT$_1$ and LE states determined with the 11-state GMH and FCD schemes have almost the same $\Delta\mu^{diab}$ and Δq^{diab} values with both 6-31G* (Tables 1 and 2) and

6-31G** (Table S12, ESI†), which indicates that both basis sets yield similar descriptions of these states. Interestingly, the Δq_{CT1}^{diab} value predicted with 6-31+G* and B3LYP does not change from the adiabatic value of 1.6 (Table S12, ESI†), indicating that in this case the diabatization does not remove the mixing of the local states with the CT$_1$ state.

The basis set has only a small effect on the 11-state electronic couplings when using the global hybrid functionals: the couplings calculated with the 6-31G* and 6-31G** basis sets (Fig. 8 and 9 and Tables S14, S15, S17, and S18, ESI†) differ by 0–5 meV. This is consistent with the study of Voityuk and Rösch,[24] in which they have presented their FCD scheme and observed that inclusion of polarization functions on hydrogen does not influence the 2-state GMH and FCD couplings of the small DNA fragments, when using HF. Here, moreover, the couplings predicted with the 6-31+G* basis set and B3LYP for 3T4Q–PC$_{71}$BM are only 1–2 meV larger than with 6-31G* and 6-31G** (Fig. 9 and Table S17, ESI†). This is also in line with the study of Voityuk and Rösch,[24] where the polarization functions on hydrogen and diffusion functions (on all atoms) (6-31G* vs. 6-31+G*) have been reported to have only a small (5%) effect on the couplings. Here, the smaller Δq_{CT1}^{diab} value obtained with 6-31+G* (see above) does not affect the couplings, which may be due to the compensation of other states included in
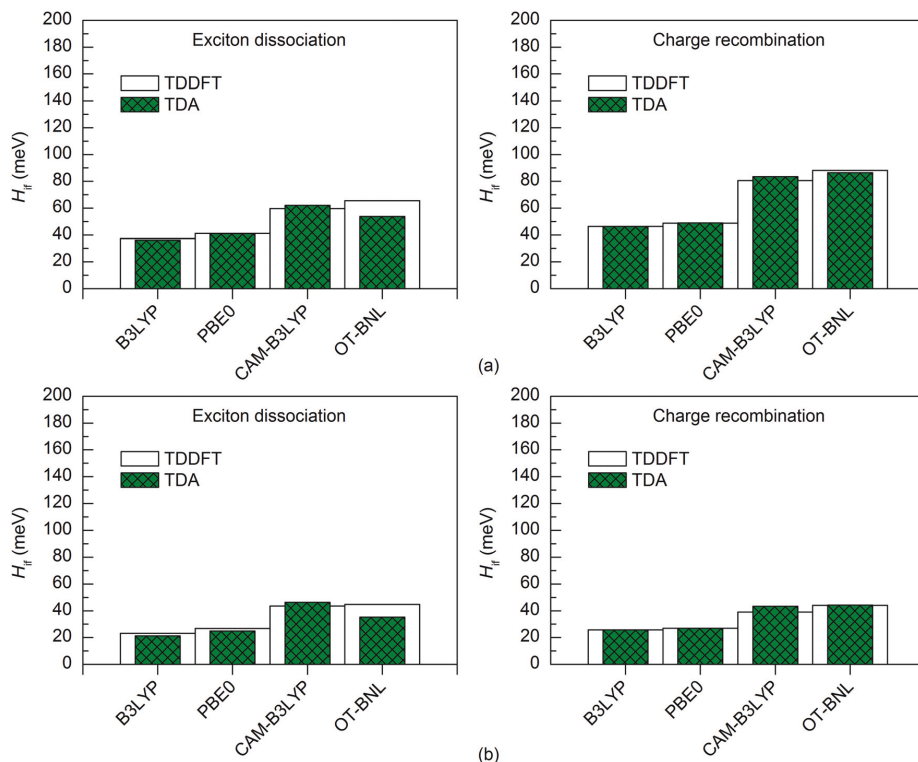
Fig. 7 Electronic couplings of (a) 3T4Q–PC$_{71}$BM and (b) 3Q4T–PC$_{71}$BM calculated with the 11-state FCD scheme using TDDFT and TDA with different functionals and the 6-31G* basis set.

the calculations. With the LRC functionals, the differences in the 11-state ED couplings predicted with two basis sets together with both the GMH and FCD schemes are also rather small, i.e. 0–9 meV. However, the 11-state GMH CR couplings predicted by the LRC functionals differ more, as the 6-31G** basis set yields somewhat larger (19–47 meV) couplings than 6-31G*. Generally, the 6-31G** basis set yields larger couplings in all cases, except for some PBE0 and OT-BNL values of 3Q4T–PC$_{71}$BM. Thus, the size of the basis set can have an effect on the dipole moments and the GMH couplings when using the LRC functionals as opposite to the global hybrids. Similar to the results obtained with different numbers of states and different TD methods, the tuning of ω does not have a notable effect on the results and both CAM-B3LYP and OT-BNL predict the same trends.

Effect of the surrounding medium

The excitation energies of the selected complexes are practically the same in different environments differing only by 0.0–0.1 eV (Tables S5, S9, and S10, ESI†). Thus, the polarity of the medium does not affect the adiabatic energies of the LE and CT$_1$ states in most cases. However, with the LRC functionals, the order of the excited states is somewhat different in 1,2-DCB and the blend from that under vacuum and the CT$_1$ state is at a higher

energy (the sixth or seventh state). Zheng et al. also observed higher CT$_1$ state energies for the pentacene–C$_{60}$ complex with the OT ωB97X-D functional when using PCM compared to vacuum.[94]

The nature of the adiabatic CT$_1$ and LE states are generally quite similar in different media (Table S11, ESI†). However, in some cases the portion of the LF component in the CT$_1$ state increases slightly in 1,2-DCB and the blend than under vacuum; namely, all functionals predict somewhat smaller $\Delta\mu_{\text{CT1}}^{\text{ad}}$ and the LRC functionals yield smaller $\Delta q_{\text{CT1}}^{\text{ad}}$. For the LE state, the $\Delta\mu_{\text{LE}}^{\text{ad}}$ and $\Delta q_{\text{LE}}^{\text{ad}}$ values are mainly the same or smaller in 1,2-DCB and the blend than under vacuum, but for 3T4Q–PC$_{71}$BM the global hybrids predict larger values in 1,2-DCB and the blend. When comparing the diabatic states of the studied complexes obtained with the 11-state electronic coupling schemes in different media, the nature of LE states remains unchanged, and the $\Delta\mu_{\text{LE}}^{\text{diab}}$ and $\Delta q_{\text{LE}}^{\text{diab}}$ values are close to zero in all the media. Moreover, the nature of the CT$_1$ state remains mainly unaffected by the medium polarity, although the $\Delta\mu_{\text{CT1}}^{\text{diab}}$ values of both complexes and the $\Delta q_{\text{CT1}}^{\text{diab}}$ values of 3T4Q–PC$_{71}$BM are slightly smaller in 1,2-DCB and the blend than under vacuum. This indicates that, while the diabatic states are quite similar in the different media, the diabatization does not completely
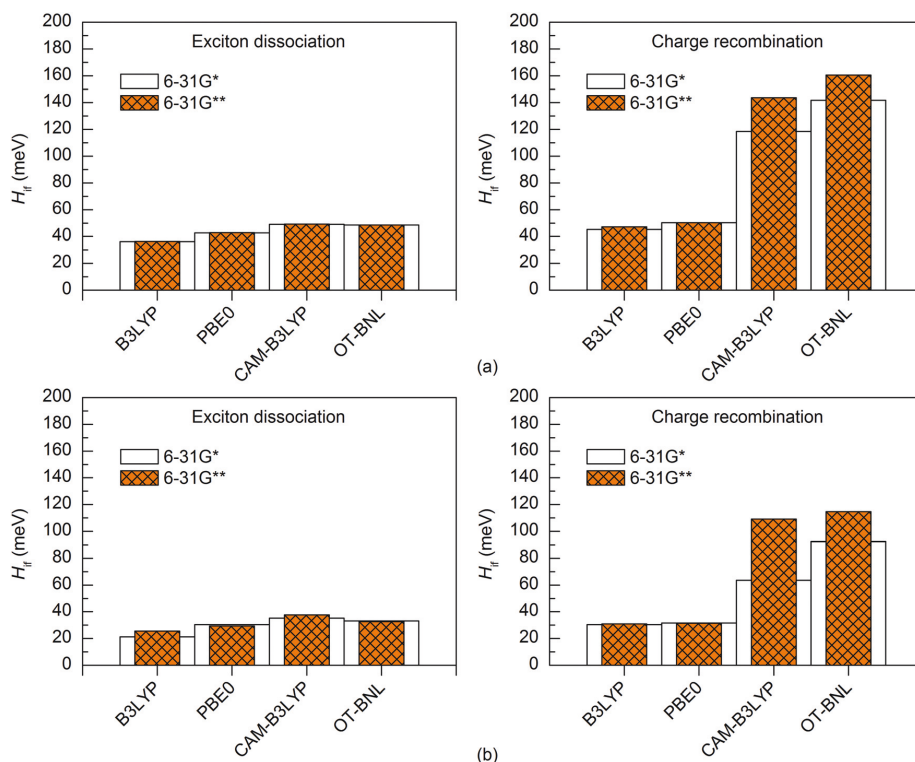
Fig. 8 Electronic couplings of (a) 3T4Q–PC$_{71}$BM and (b) 3Q4T–PC$_{71}$BM calculated with the 11-state GMH scheme using TDDFT with different functionals and basis sets.

remove the local component present in the adiabatic CT$_1$ state in 1,2-DCB and the blend and thus the amount of CT is slightly reduced compared to that under vacuum.

The surrounding medium has only a small effect on the 11-state electronic couplings (Fig. 10 and 11 and Tables S14, S15, S19, and S20, ESI†) of the complexes when using the global hybrid functionals. Moreover, the GMH and FCD results are very similar. The couplings increase only slightly (by *ca.* 0–11 meV) in the order of vacuum < blend < 1,2-DCB, *i.e.* with the increasing polarity of the medium (ε_s of 3.6 for the TQ–PC$_{71}$BM blend and 10.1210 for 1,2-DCB) in most cases. A similar trend has been observed by Lemaur *et al.* with the GMH couplings of a phthalocyanine–perylene bisimide (Pc–PTCDI) complex.[6] With the LRC functionals, the effect of the environment on the 11-state couplings is generally also moderate (0–22 meV), but the GMH CR couplings differ more significantly, especially for 3T4Q–PC$_{71}$BM (by *ca.* 11–110 meV). In this case, the GMH CR couplings predicted with OT-BNL seem to be most affected by the choice of medium. Overall, the electronic couplings calculated in the different media with the LRC functionals do not follow any clear trend, although the couplings are in most cases smaller under vacuum than in 1,2-DCB or the blend. In addition, similar to that under vacuum, the 11-state FCD

couplings differ somewhat from the GMH couplings in 1,2-DCB or the blend.

Effect of the placement of PC$_{71}$BM on TQ

The placement of PC$_{71}$BM on TQ (Fig. 2b) has no effect on the vertical excitation energies and they are practically the same for both 3T4Q–PC$_{71}$BM and 3Q4T–PC$_{71}$BM (Tables S5–S7, S9, and S10, ESI†) regardless of the calculation method or surrounding medium. We have also observed negligible changes in the excitation energies for poly(benzodithiophene-*co*-quinoxaline)–fullerene complexes, when the orientation of PC$_{71}$BM is altered.[66] As the adiabatic and diabatic $\Delta\mu_{CT1}$ and Δq_{CT1} values are somewhat larger for 3Q4T–PC$_{71}$BM (Tables 1 and 2 and Tables S11–S13, ESI†), it has smaller mixing of the local LF component to the CT$_1$ state compared to 3T4Q–PC$_{71}$BM, indicating more efficient CT from TQ to PC$_{71}$BM.

In contrast to the vertical excitation energies, the electronic couplings are clearly affected by the placement of PC$_{71}$BM, as can be expected based on the previous studies of the local eD–eA interfaces of photoactive materials.[30,31,75,76,98] The ED couplings of 3T4Q–PC$_{71}$BM and 3Q4T–PC$_{71}$BM are 36–83 meV and 21–52 meV, respectively, whereas the CR couplings are 45–252 meV and 25–150 meV, respectively (Tables S14–S20, ESI†).
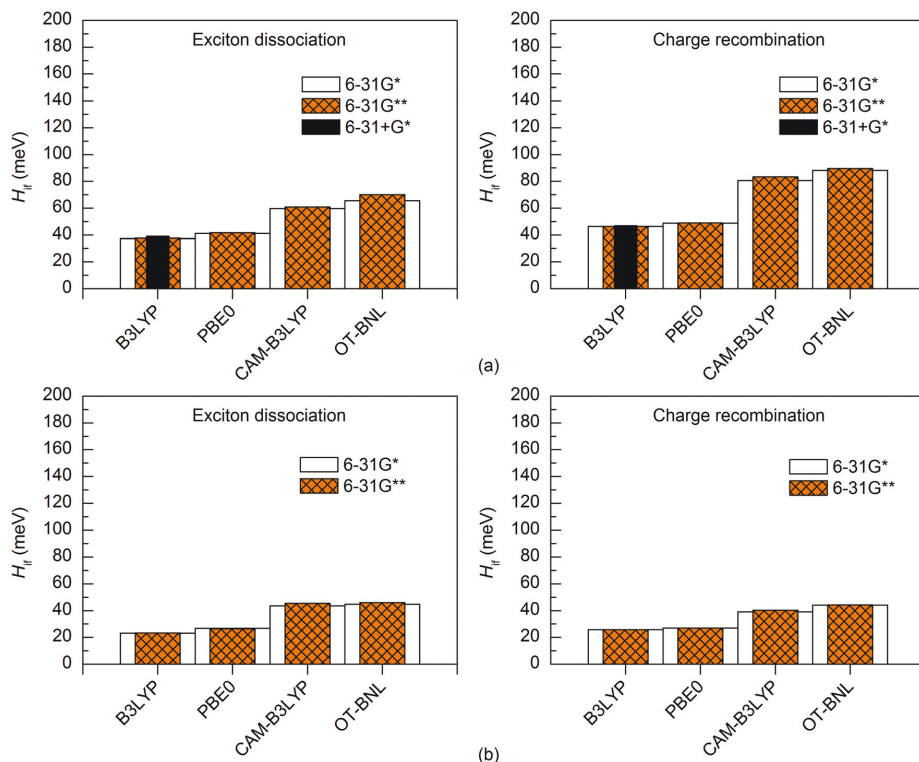
This journal is © the Owner Societies 2019

Phys. Chem. Chem. Phys., 2019, **21**, 25606–25625 | **25617**

Fig. 9 Electronic couplings of (a) 3T4Q–PC$_{71}$BM and (b) 3Q4T–PC$_{71}$BM calculated with the 11-state FCD scheme using TDDFT with different functionals and basis sets.

Thus, the ED and CR couplings are *ca.* 4–30 meV and 12–132 meV stronger, respectively, when PC$_{71}$BM is located on the thiophene donor unit of TQ (3T4Q–PC$_{71}$BM) than when PC$_{71}$BM is on the quinoxaline acceptor unit of TQ (3Q4T–PC$_{71}$BM). Based on the coupling values, we anticipate faster ED and CR rates for 3T4Q–PC$_{71}$BM than for 3Q4T–PC$_{71}$BM, which is also observed from the calculated CT rates of the complexes in 1,2-DCB (see 'Calculating charge transfer rates in 1,2-DCB and the blend' below). For 3T4Q–PC$_{71}$BM, the CR couplings are larger than the ED couplings, in all cases. For 3Q4T–PC$_{71}$BM, the opposite, *i.e.* larger ED couplings than the CR couplings, is predicted when using the 11-state FCD scheme (and 2–4-state GMH and FCD schemes in some cases) in conjunction with the LRC functionals.

A similar effect of the relative placement on the ED and CR electronic couplings was observed by Wang *et al.* when examining 1473 complexes of polybenzo[1,2-*b*:4,5-*b'*]dithiophene–thieno[3,4-*c*]pyrrole-4,6-dione and PC$_{61}$BM extracted from the molecular dynamics simulations.[99] They predicted larger ED and CR coupling values when PC$_{61}$BM was closer to the D unit than the A unit of the copolymer, although they employed a different coupling scheme (fragment orbital approach) and functional (ωB97X-D). In their later study of a benzothiadiazole-quaterthiophene-based copolymer with PC$_{71}$BM, Wang *et al.* also

observed[39] larger CR couplings with the 2-state FCD and the OT ωB97X-D functional when PC$_{71}$BM was on top of the D unit than on top of the A unit of the copolymer. Furthermore, Wang *et al.* also predicted larger couplings for the CR process than for the ED process.[99] Likewise, similar results have been obtained for the PTB7-Th–PC$_{71}$BM complex with the 2-state GMH[37] and for the α-sexithienyl–C$_{60}$ complex[98] with a diabatic-state approach.[75,100] However, no clear conclusion can be drawn merely from the above findings, as opposite results have been observed, as well.[76,98]

The differences between the electronic couplings of the two complexes are quite similar despite the calculation method (*i.e.* coupling scheme, functional, number of states, basis set, and surrounding medium), especially with the global hybrid functionals (*ca.* 4–28 meV). However, the LRC functionals predict more notable differences (7–132 meV) between the electronic couplings of 3T4Q–PC$_{71}$BM and 3Q4T–PC$_{71}$BM, especially for the CR couplings (33–132 meV).

Effect of the coupling scheme on the electronic couplings

The choice of coupling scheme has either a small or a significant effect on the coupling values of the two complexes depending on the calculation method (*i.e.* functional, basis set, and surrounding medium) used. With the global hybrids,
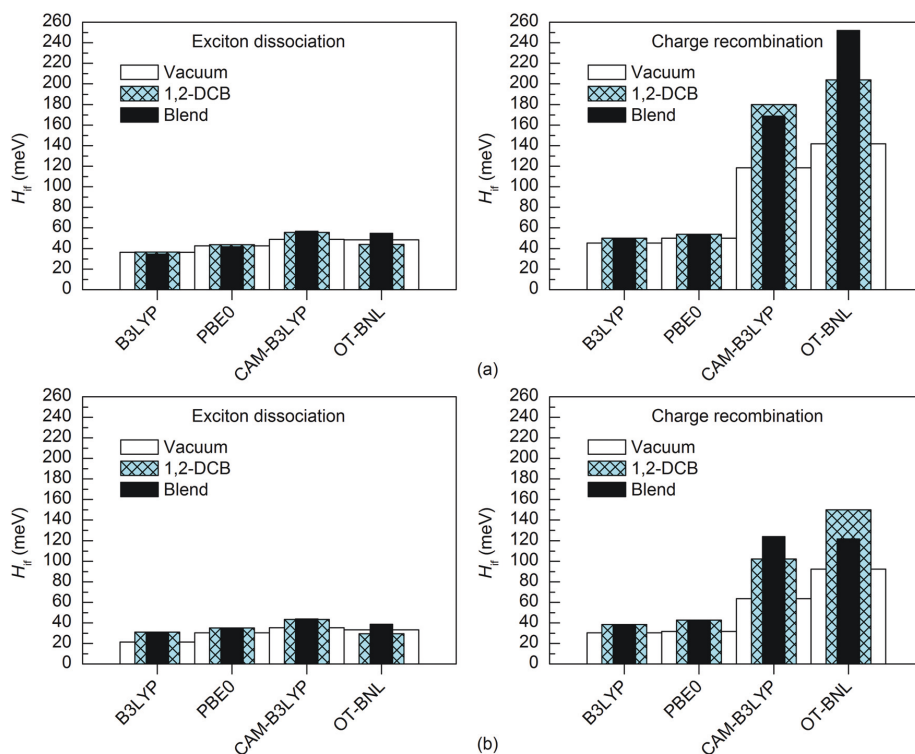
Fig. 10 Electronic couplings of (a) 3T4Q–PC$_{71}$BM and (b) 3Q4T–PC$_{71}$BM in vacuum, 1,2-DCB, and the blend calculated with the 11-state GMH scheme using TDDFT with different functionals and the 6-31G* basis set.

the 2–11-state GMH and FCD electronic couplings are quite similar despite the basis set or surrounding medium and the GMH values are only slightly (0–17 meV) larger in most cases. Moreover, both schemes predict mainly larger CR couplings compared to the ED couplings when using the global hybrids (Tables S14 and S15, ESI†), except for some FCD values of 3Q4T–PC$_{71}$BM calculated with PBE0 (Table S15, ESI†). With the LRC functionals, the differences (0–157 meV) between the GMH and FCD couplings are more significant compared to the global hybrids, especially in the case of the CR values. Moreover, large differences between the GMH and FCD couplings are predicted with the 6-31G** basis set (60–71 meV, in vacuum) and with the 6-31G* basis set in the 1,2-DCB or blend media (61–156 meV). Both schemes predict larger CR couplings than ED couplings for 3T4Q–PC$_{71}$BM in all cases and for 3Q4T–PC$_{71}$BM in some cases (Tables S14 and S15, ESI†). For 3Q4T–PC$_{71}$BM, the 2–11-state FCD and 2–4-state GMH schemes in conjunction with the LRC functionals predict mainly larger ED couplings than the CR couplings.

Thus, the GMH scheme and more precisely the $\Delta\mu$ values employed in the GMH scheme seem to be more sensitive to the choice of functional, basis set, and surrounding medium than the FCD scheme. These findings complement the earlier studies, which have pointed out that the Δq values in the FCD scheme are less sensitive to the mixing of the local excited and CT states, while the $\Delta\mu$ values in the GMH scheme are more affected by the mixing of the states.[16,45] The GMH electronic couplings have been observed to improve when employing a solvent model (e.g. the image charge approximation, ICA), as it can lower the energy of the CT$_1$ state and thus decouple it from the undesired high-lying local excitations.[16,47] However, this is not always the case, as can be seen from our results above, where the CT$_1$ state energies and the couplings increase somewhat in 1,2-DCB compared to vacuum. Lee et al. also observed relatively larger GMH couplings for a series of heptacyclo-[6.6.0.0.^{2,6}0.^{3,13}01.^{4,11}0^{5,9}.0^{10,14}]-tetradecane-linked D–A molecules than the FCD values with and without the ICA solvent model, when the couplings should be small due to symmetry.[45] Increasing the number of states has also resulted in improved GMH and FCD couplings.[28] As stated above, in this study, both coupling schemes yield very similar values despite the number of states when using the global hybrid functionals (Fig. 4 and 5 and Fig. S3 and S4, ESI†). However, with the LRC functionals, the number of states affects the couplings more, especially the CR values. With the GMH scheme, the CR values oscillate with the increasing number of states, whereas with the FCD scheme,
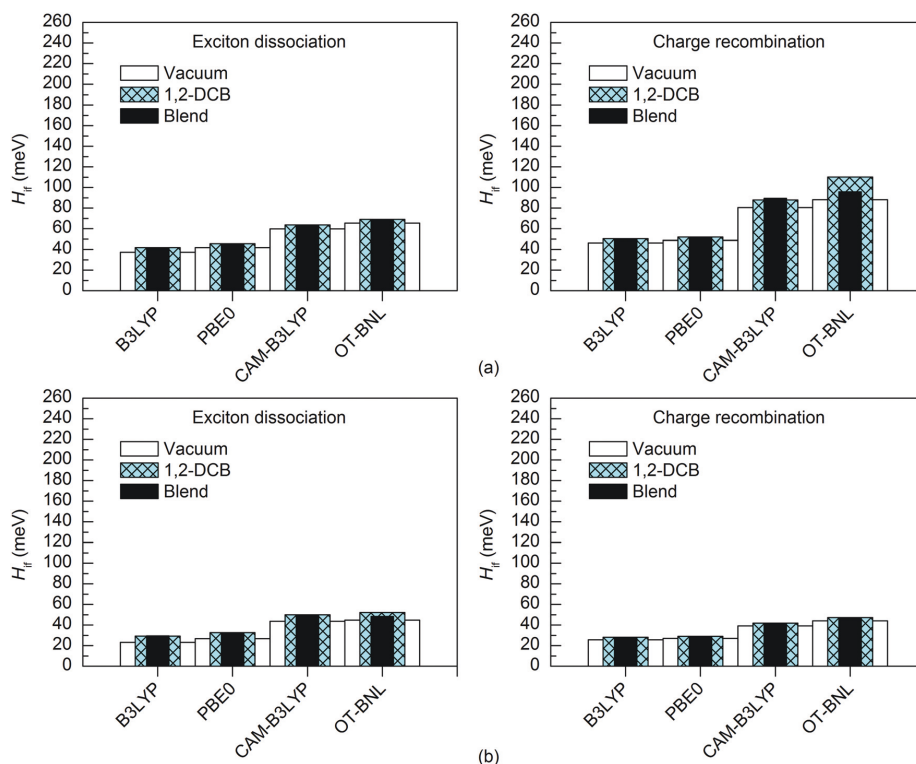
This journal is © the Owner Societies 2019

Phys. Chem. Chem. Phys., 2019, **21**, 25606–25625 | **25619**

Fig. 11 Electronic couplings of (a) 3T4Q–PC$_{71}$BM and (b) 3Q4T–PC$_{71}$BM in vacuum, 1,2-DCB, and the blend calculated with the 11-state FCD scheme using TDDFT with different functionals and the 6-31G* basis set.

they decrease. Overall, the FCD scheme seems to produce couplings that are more constant and, when combined with the multi-state treatment, may be more suitable than GMH for calculating the couplings for the polymer–fullerene systems. Thus, we will employ the 11-state FCD couplings for calculating the ED and CR rates.

Calculating charge transfer rates in 1,2-DCB and the blend

Finally, we have estimated the CT rates for the ED and CR processes at the two TQ–PC$_{71}$BM interfaces modelled by complexes

using the 11-state FCD electronic couplings. The couplings and other parameters required for calculating the rates in both 1,2-DCB and the blend are listed in Tables 3 and 4, respectively. Generally, the inner reorganization energies (λ_i) of both complexes are smaller for the ED process than for the CR process. This can be attributed to the larger geometric changes (Fig. S5, ESI†) taking place in TQ during CR, i.e. when going from the cation geometry to that of the neutral GS (eD$^+$ → eD), than during ED, i.e. when going from the S$_1$ geometry to that of the cation (eD* → eD$^+$). In other words, the geometries of the cation and the S$_1$ states of TQ are closer to

Table 3 Electronic couplings (H_{if})[a], internal reorganization energies (λ_i), Gibbs free energies (ΔG°), and Coulomb energies (ΔE_{Coul}) for the ED and CR processes of the TQ–PC$_{71}$BM complexes in 1,2-DCB with different functionals and the 6-31G* basis set

Functional	Complex	$H_{if,ED}$ (meV)	$H_{if,CR}$ (meV)	$\lambda_{i,ED}$ (eV)	$\lambda_{i,CR}$ (eV)	ΔG_{ED} (eV)	ΔG_{CR} (eV)	$\Delta E_{Coul,ED}$ (eV)	$\Delta E_{Coul,CR}$ (eV)
B3LYP	3T4Q–PC$_{71}$BM	41.9	50.3	0.1298	0.2039	−0.1373	−1.6166	−0.1373	0.1376
	3Q4T–PC$_{71}$BM	29.2	28.0	0.1308	0.2058	−0.1501	−1.5981	−0.1374	0.1372
PBE0	3T4Q–PC$_{71}$BM	48.8	52.0	0.1377	0.2180	−0.2673	−1.5951	−0.1370	0.1372
	3Q4T–PC$_{71}$BM	32.5	29.0	0.1386	0.2198	−0.2788	−1.5773	−0.1371	0.1368
CAM-B3LYP	3T4Q–PC$_{71}$BM	63.5	87.9	0.1882	0.3014	−0.3179	−1.9903	−0.1421	0.1422
	3Q4T–PC$_{71}$BM	49.9	41.7	0.1890	0.3035	−0.3139	−1.9927	−0.1421	0.1419
OT-BNL	3T4Q–PC$_{71}$BM	68.9	110.2	0.1728	0.2643	−0.2438	−1.7420	−0.1413	0.1415
	3Q4T–PC$_{71}$BM	52.2	47.1	0.1737	0.2660	−0.2479	−1.7322	−0.1419	0.1416

[a] Electronic couplings obtained with the 11-state FCD scheme.

Table 4 Electronic couplings (H_{if})[a], internal reorganization energies (λ_i), Gibbs free energies (ΔG°), and Coulomb energies (ΔE_{Coul}) for the ED and CR processes of the TQ–PC$_{71}$BM complexes in the blend with different functionals and the 6-31G* basis set

Functional	Complex	$H_{if,ED}$ (meV)	$H_{if,CR}$ (meV)	$\lambda_{i,ED}$ (eV)	$\lambda_{i,CR}$ (eV)	ΔG°_{ED} (eV)	ΔG°_{CR} (eV)	$\Delta E_{Coul,ED}$ (eV)	$\Delta E_{Coul,CR}$ (eV)
B3LYP	3T4Q–PC$_{71}$BM	41.8	50.2	0.1423	0.2160	0.0274	−1.7451	−0.3778	0.3786
	3Q4T–PC$_{71}$BM	29.4	27.7	0.1434	0.2181	−0.0813	−1.6443	−0.4755	0.4618
PBE0	3T4Q–PC$_{71}$BM	45.5	51.9	0.1509	0.2309	−0.1006	−1.7250	−0.3770	0.3776
	3Q4T–PC$_{71}$BM	32.6	28.9	0.1519	0.2329	−0.2202	−1.6540	−0.4871	0.4322
CAM-B3LYP	3T4Q–PC$_{71}$BM	63.1	89.5	0.2067	0.3215	−0.1539	−2.1203	−0.3903	0.3907
	3Q4T–PC$_{71}$BM	49.4	41.6	0.2077	0.3232	−0.2423	−2.0818	−0.4856	0.4333
OT-BNL	3T4Q–PC$_{71}$BM	69.1	95.8	0.1871	0.2798	−0.0803	−1.8723	−0.3884	0.3889
	3Q4T–PC$_{71}$BM	48.3	47.3	0.1881	0.2814	−0.2109	−1.8090	−0.5179	0.4447

[a] Electronic couplings obtained with the 11-state FCD scheme.

each other than those of the cation and GS. The contributions of the geometric changes of PC$_{71}$BM to λ_i are the same during the ED and CR, *i.e.* when going from the GS to the radical anion and *vice versa*, respectively. The polarity of the medium has only a minimal effect on the λ_i values, which are basically the same in 1,2-DCB and the blend. The global hybrids yield somewhat smaller λ_i values than the LRC functionals in the increasing order of B3LYP < PBE0 < OT-BNL < CAM-B3LYP. The position of PC$_{71}$BM on TQ does not affect λ_i much and the values are almost the same for the two complexes, λ_i of 3Q4T–PC$_{71}$BM being slightly larger than that of 3T4Q–PC$_{71}$BM, indicating slightly larger geometric changes for 3Q4T. As the accurate prediction of the outer reorganization energy (λ_s) is a rather challenging task and it is highly affected by the uncertainty of the calculated parameters,[7,77] we have chosen to keep it as an adjusted parameter in the range of 0.10–0.75 eV. The selection of this range is based on the values of λ_s (0.11–0.50 eV) used in the previous theoretical studies of other copolymer–fullerene systems.[33,38,77,81] We have also considered the λ_s values of 0.5–0.75 eV, because in some cases the CR rates start to compete with the ED rates in this region (see below). This region is also in line with the experimental λ of 0.22–0.8 eV[101–103] obtained for the blends of different copolymers and fullerene derivatives.

All the functionals predict spontaneous ED and CR processes ($\Delta G^\circ < 0$) for the studied complexes, in other words, favorable processes in both media (Tables 3 and 4). Only the ED process of 3T4Q–PC$_{71}$BM predicted by B3LYP in the blend is not spontaneous. The experimental estimation for $-\Delta G^\circ_{ED}$ of the TQ–PC$_{71}$BM blend is 0.1–0.3 eV, which is obtained[104] as the difference between the optical bandgap of TQ (1.6–1.7 eV[70,93]) and the CT state energy (1.4–1.5 eV[92,93]). Thus, the calculated ΔG°_{ED} values are consistent with the experimental ones. For the selected range of λ_s (0.10–0.75 eV), all the functionals predict that ED occurs in the Marcus normal region ($|\Delta G^\circ_{ED}| < \lambda_{ED}$) in the blend. In 1,2-DCB, B3LYP and OT-BNL predict that ED takes place in the normal region for the selected range of λ_s, whereas PBE0 and CAM-B3LYP predict that ED occurs in the normal region when $\lambda_s \geq 0.14$. The CR process occurs in the inverted region of Marcus ($|\Delta G^\circ_{CR}| \gg \lambda_{CR}$) in all cases, which leads to slower CR rates than ED rates (see below).[9] The ED and CR processes of another photovoltaic system, Pc–PTCDI,[6] have also been observed to occur in the Marcus normal and inverted regions, respectively.

The sum of ΔG_{ED} and ΔG_{CR} is almost constant, regardless of the medium, and increases in the order of B3LYP (*ca.* 1.7–1.8 eV) < PBE0 (1.8–1.9 eV) < OT-BNL (2.0 eV) < CAM-B3LYP (2.3 eV). The constant sum indicates that the polarity of the medium does not have a significant effect on the separation between the GS and LE states.[6] As the other energies, except that of eD* (the optimized S_1 geometry of TQ), are canceled out from the sums of ΔG_{ED} and ΔG_{CR}, the energies of eD* are consistent with the energies of the LE state (Tables S9 and S10, ESI,† S_4 for the global hybrids and S_2 for the LRC functionals). When the polarity, ε_s, increases (from 3.6 of the TQ–PC$_{71}$BM blend to 10.1210 of 1,2-DCB), ΔG°_{ED} and $\Delta E_{Coul,CR}$ decrease, *i.e.* become more negative, whereas ΔG°_{CR} and $\Delta E_{Coul,ED}$ increase. Lemaur *et al.* observed[6] the same dependence of ΔG° and ΔE_{Coul} on the polarity of the medium for the modeled Pc–PTCDI complex.

The evolutions of the ED and CR rates of the studied complexes as functions of λ_s are illustrated in Fig. 12 and 13 for the 1,2-DCB and blend environments, respectively. Generally, the ED process occurs more rapidly than CR, although B3LYP, PBE0, and OT-BNL predict competing CR rates with larger λ_s (>*ca.* 0.66 eV). The ED rates are slightly faster in 1,2-DCB (10^{10}–10^{13} s^{-1}) than in the blend (10^9–10^{13} s^{-1}), decreasing with increasing λ_s. Similarly, the CR rates are faster in 1,2-DCB (10^{-14}–10^{12} s^{-1}) than in the blend (10^{-16}–10^{11} s^{-1}), increasing with increasing λ_s. The LRC functionals predict higher ED rates compared to the global hybrids in the increasing order of B3LYP < PBE0 < OT-BNL < CAM-B3LYP. The magnitude of the ED rate predicted with B3LYP differs from those predicted with the other functionals. In the case of the CR rates, there is no clear trend between the global hybrid and LRC functionals, as the CR rates increase mainly in the order of CAM-B3LYP < B3LYP < OT-BNL < PBE0. Here, the magnitude of the CAM-B3LYP CR rate is different from that given by the other functionals. The ED and CR rates in the blend are mainly larger, when PC$_{71}$BM is on top of the A unit of TQ (3Q4T–PC$_{71}$BM) than when it is on top of the D unit (3T4Q–PC$_{71}$BM) (except for some CR rates predicted by PBE0 with $\lambda_s > 0.65$ eV and CAM-B3LYP with $\lambda_s > 0.4$ eV). In 1,2-DCB, 3T4Q–PC$_{71}$BM has larger ED and CR rates than 3Q4T–PC$_{71}$BM. In 1,2-DCB, both complexes have relatively similar λ_i and ΔG° values (Table 3), in which case the electronic coupling determines the rate differences between the two complexes. However, in
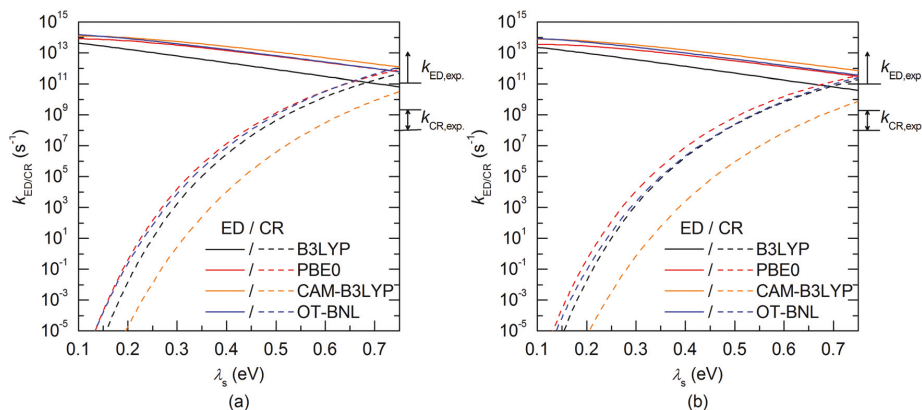
This journal is © the Owner Societies 2019

Phys. Chem. Chem. Phys., 2019, **21**, 25606–25625 | **25621**

Fig. 12 Evolutions of the ED and CR rates (k_{ED} and k_{CR}) as functions of λ_s for (a) 3T4Q–PC$_{71}$BM and (b) 3Q4T–PC$_{71}$BM calculated in 1,2-DCB with different functionals and the 6-31G* basis set. The ranges for the experimental k_{ED} and k_{CR} are also shown in the figures.

Fig. 13 Evolutions of the ED and CR rates (k_{ED} and k_{CR}) as functions of λ_s for (a) 3T4Q–PC$_{71}$BM and (b) 3Q4T–PC$_{71}$BM calculated in the blend with different functionals and the 6-31G* basis set. The ranges for the experimental k_{ED} and k_{CR} are also shown in the figures.
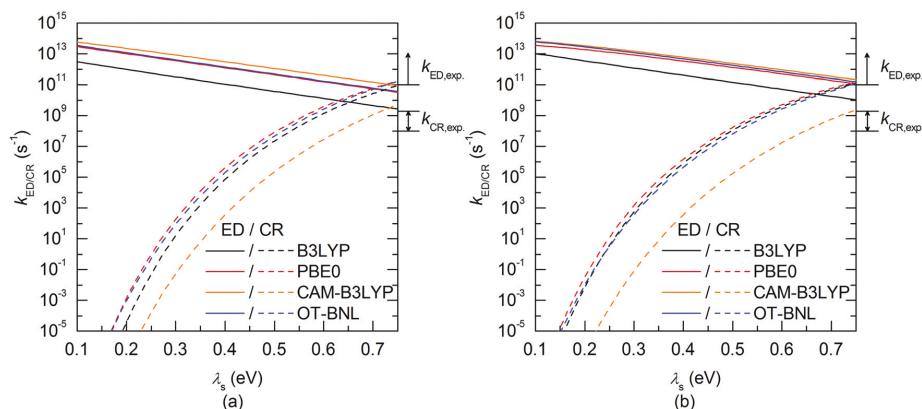
the blend (Table 4), the ΔG° values of the two complexes differ to such an extent that ΔG° becomes the determining factor for the rates.

The value of λ_s determines, especially in the case of the CR rates, whether the ED and CR rates are in the ranges of the experimental ED ($>10^{11}$)[105] for TQ–PC$_{61}$BM and CR rates (*ca.* 10^8–10^9) for different copolymer–fullerene blends. The numerical values of the CT rates at λ_s of 0.56 eV (Table 5), *i.e.* at the average of λ_s (*ca.* 0.42–0.63 eV in 1,2-DCB and 0.49–0.69 eV in the blend), for which the ED and CR rates are calculated with different functionals and in different environments are within the experimental rates. Moreover, our choices regarding the calculation methods, *e.g.* using the vacuum OT ω value in the 1,2-DCB and blend calculations or using the B3LYP geometries in all calculations, can induce some uncertainties in the calculated rates and rate parameters. However, as we have kept these computational settings consistent in all

the calculations, we expect their relative effect to be the same. To conclude, all the functionals yield mostly ED and CR rates that are consistent with the experimental ones with larger λ_s values (see above), while smaller λ_s values lead to vanishingly small CR rates.

Conclusions

We have determined the electronic couplings of the ED and CR processes at the local interfaces of solar cell materials TQ and PC$_{71}$BM theoretically using the two- and multi-state GMH and FCD coupling schemes. The results show that the choice of functional has the most significant effect on the excited state characteristics and the coupling values, especially with the GMH scheme. Mainly, the global hybrid functionals predict a more localized adiabatic CT$_1$ state, *i.e.* almost a complete CT

25622 | *Phys. Chem. Chem. Phys.,* 2019, **21**, 25606–25625

This journal is © the Owner Societies 2019

Table 5 Total reorganization energies (λ_{ED} and λ_{CR})[a] and the rates (k_{ED} and k_{CR}) for the ED and CR processes of the TQ–PC$_{71}$BM complexes calculated in 1,2-DCB and the blend (in parentheses) with different functionals and the 6-31G* basis set using λ_s of 0.56 eV[b]

Functional	Complex	λ_{ED} (eV)	k_{ED} (s^{-1})	λ_{CR} (eV)	k_{CR} (s^{-1})
B3LYP	3T4Q–PC$_{71}$BM	0.6898 (0.7023)	4.5×10^{11} (1.9×10^{10})	0.7639 (0.7760)	4.0×10^{9} (3.0×10^{8})
	3Q4T–PC$_{71}$BM	0.6908 (0.7034)	2.6×10^{11} (7.5×10^{10})	0.7658 (0.7781)	2.0×10^{9} (1.1×10^{9})
PBE0	3T4Q–PC$_{71}$BM	0.6977 (0.7109)	3.5×10^{12} (2.3×10^{11})	0.7780 (0.7909)	1.1×10^{10} (9.3×10^{8})
	3Q4T–PC$_{71}$BM	0.6986 (0.7119)	1.8×10^{12} (7.4×10^{11})	0.7798 (0.7929)	5.0×10^{9} (1.5×10^{9})
CAM-B3LYP	3T4Q–PC$_{71}$BM	0.7482 (0.7667)	6.8×10^{12} (6.0×10^{11})	0.8614 (0.8815)	6.2×10^{7} (4.8×10^{6})
	3Q4T–PC$_{71}$BM	0.7490 (0.7677)	4.0×10^{12} (1.3×10^{12})	0.8635 (0.8832)	1.4×10^{7} (3.2×10^{6})
OT-BNL	3T4Q–PC$_{71}$BM	0.7328 (0.7471)	3.7×10^{12} (2.6×10^{11})	0.8243 (0.8398)	9.2×10^{9} (5.9×10^{8})
	3Q4T–PC$_{71}$BM	0.7337 (0.7481)	2.2×10^{12} (1.0×10^{12})	0.8260 (0.8414)	2.2×10^{9} (6.8×10^{8})

[a] Sum of λ_i (values in Table 2) and λ_s of 0.53 eV. [b] Taken as the average of the λ_s values for which the calculated ED and CR rates are within the experimental ones (see text).

from TQ to PC$_{71}$BM, whereas the LRC functionals predict a small component of the intramolecular excitation of PC$_{71}$BM mixed with the CT$_1$ state. When comparing the two- and multi-state couplings, the number of states does not have a very strong effect on the coupling values with the global hybrid functionals, and the GMH and FCD couplings are quite similar. Thus, with the global hybrid functionals, the 2-state schemes seem to be sufficient for calculating the couplings of the studied system. However, with the non-tuned and OT LRC functionals, the multi-state coupling schemes yield a more localized description of the CT$_1$ state and thus improve couplings with respect to the two-state values. Furthermore, with the LRC functionals, the FCD scheme yields a more localized CT$_1$ state and constant couplings while being less sensitive to the choice of calculation method compared to the GMH scheme. Thus, the FCD scheme combined with the multi-state treatment is recommended for calculating the couplings when using the LRC functionals.

The electronic couplings are clearly affected by the position of PC$_{71}$BM and stronger couplings are observed when PC$_{71}$BM is on the donor unit of TQ than when PC$_{71}$BM is on the acceptor unit of TQ. In most cases, the CR couplings of the studied TQ–PC$_{71}$BM complexes are larger than the corresponding ED couplings. However, for the complex, where PC$_{71}$BM is on top of the acceptor unit of TQ, the LRC functionals predict mainly larger ED couplings. Overall, the calculated ED rates are in the range of the experimental values. However, the calculated CR values are consistent with the experimental rates only with certain values of the external reorganization energy. Nevertheless, the ED process is generally predicted to occur more rapidly than the CR process in the TQ–PC$_{71}$BM complexes, which is in agreement with the previous experimental results that the particular system functions efficiently in the PSCs. The slower CR rates are the consequence of the increasingly negative values of the Gibbs free energy relative to reorganization energies due to which the CR process occurs in the Marcus inverted region. We note that our study did not consider dispersion corrections, which are important for describing weak dispersion interaction in the eD–eA interface configurations, especially when determining the inter-molecular distances.[66] The effect of the dispersion on the multi-state electronic couplings will be the subject of future work by our group.

Conflicts of interest

There are no conflicts to declare.

Acknowledgements

References

1 J. Zhao, Y. Li, G. Yang, K. Jiang, H. Lin, H. Ade, W. Ma and H. Yan, *Nat. Energy*, 2016, **1**, 15027.

2 Y. Jin, Z. Chen, M. Xiao, J. Peng, B. Fan, L. Ying, G. Zhang, X.-F. Jiang, Q. Yin, Z. Liang, F. Huang and Y. Cao, *Adv. Energy Mater.*, 2017, **7**, 1700944.

3 W. Zhao, S. Li, H. Yao, S. Zhang, Y. Zhang, B. Yang and J. Hou, *J. Am. Chem. Soc.*, 2017, **139**, 7148–7151.

4 S. Li, L. Ye, W. Zhao, H. Yan, B. Yang, D. Liu, W. Li, H. Ade and J. Hou, *J. Am. Chem. Soc.*, 2018, **140**, 7159–7167.

5 G. Yu, J. Gao, J. C. Hummelen, F. Wudl and A. J. Heeger, *Science*, 1995, **270**, 1789–1791.

6 V. Lemaur, M. Steel, D. Beljonne, J.-L. Brédas and J. Cornil, *J. Am. Chem. Soc.*, 2005, **127**, 6077–6086.

7 P. Song, Y. Li, F. Ma, T. Pullerits and M. Sun, *Chem. Rec.*, 2016, **16**, 734–753.

8 R. A. Marcus, *J. Chem. Phys.*, 1956, **24**, 966–978.

9 R. A. Marcus and N. Sutin, *Biochim. Biophys. Acta, Rev. Bioenerg.*, 1985, **811**, 265–322.

10 R. A. Marcus, *Rev. Mod. Phys.*, 1993, **65**, 599–610.

11 M. D. Newton, *Chem. Rev.*, 1991, **91**, 767–792.

12 J. L. Brédas, J. P. Calbert, D. A. da Silva Filho and J. Cornil, *Proc. Natl. Acad. Sci. U. S. A.*, 2002, **99**, 5804–5809.

13 E. F. Valeev, V. Coropceanu, D. A. da Silva Filho, S. Salman and J.-L. Brédas, *J. Am. Chem. Soc.*, 2006, **128**, 9882–9886.

14 V. Coropceanu, J. Cornil, D. A. da Silva Filho, Y. Olivier, R. Silbey and J.-L. Brédas, *Chem. Rev.*, 2007, **107**, 926–952.

15 M. Bixon, J. Jortner and J. W. Verhoeven, *J. Am. Chem. Soc.*, 1994, **116**, 7349–7355.

16 C.-P. Hsu, *Acc. Chem. Res.*, 2009, **42**, 509–518.

17 Y. Zhao and W. Liang, *Chem. Soc. Rev.*, 2012, **41**, 1075–1087.

18 J. M. Foster and S. F. Boys, *Rev. Mod. Phys.*, 1960, **32**, 300–302.

19 C. Edmiston and K. Ruedenberg, *Rev. Mod. Phys.*, 1963, **35**, 457–465.

20 T. Pacher, L. S. Cederbaum and H. Köppel, *J. Chem. Phys.*, 1988, **89**, 7367–7381.

21 Y. Mo, J. Gao and S. D. Peyerimhoff, *J. Chem. Phys.*, 2000, **112**, 5530–5538.

22 R. J. Cave and M. D. Newton, *Chem. Phys. Lett.*, 1996, **249**, 15–19.

23 R. J. Cave and M. D. Newton, *J. Chem. Phys.*, 1997, **106**, 9213–9226.

24 A. A. Voityuk and N. Rösch, *J. Chem. Phys.*, 2002, **117**, 5607–5616.

25 L. Blancafort and A. A. Voityuk, *Phys. Chem. Chem. Phys.*, 2017, **19**, 31007–31010.

26 A. A. Voityuk, *J. Phys. Chem. A*, 2017, **121**, 5414–5419.

27 Y. Shao, Z. Gan, E. Epifanovsky, A. T. B. Gilbert, M. Wormit, J. Kussmann, A. W. Lange, A. Behn, J. Deng, X. Feng, D. Ghosh, M. Goldey, P. R. Horn, L. D. Jacobson, I. Kaliman, R. Z. Khaliullin, T. Kuś, A. Landau, J. Liu, E. I. Proynov, Y. M. Rhee, R. M. Richard, M. A. Rohrdanz, R. P. Steele, E. J. Sundstrom, H. L. Woodcock III, P. M. Zimmerman, D. Zuev, B. Albrecht, E. Alguire, B. Austin, G. J. O. Beran, Y. A. Bernard, E. Berquist, K. Brandhorst, K. B. Bravaya, S. T. Brown, D. Casanova, C.-M. Chang, Y. Chen, S. H. Chien, K. D. Closser, D. L. Crittenden, M. Diedenhofen, R. A. DiStasio, H. Do, A. Dutoi, R. G. Edgar, S. Fatehi, L. Fusti-Molnar, A. Ghysels, A. Golubeva-Zadorozhnaya, J. Gomes, M. W. D. Hanson-Heine, P. H. P. Harbach, A. W. Hauser, E. G. Hohenstein, Z. C. Holden, T.-C. Jagau, H. Ji, B. Kaduk, K. Khistyaev, J. Kim, J. Kim, R. A. King, P. Klunzinger, D. Kosenkov, T. Kowalczyk, C. M. Krauter, K. U. Lao, A. D. Laurent, K. V. Lawler, S. V. Levchenko, C. Y. Lin, F. Liu, E. Livshits, R. C. Lochan, A. Luenser, P. Manohar, S. F. Manzer, S.-P. Mao, N. Mardirossian, A. V. Marenich, S. A. Maurer, N. J. Mayhall, E. Neuscamman, C. M. Oana, R. Olivares-Amaya, D. P. O'Neill, J. A. Parkhill, T. M. Perrine, R. Peverati, A. Prociuk, D. R. Rehn, E. Rosta, N. J. Russ, S. M. Sharada, S. Sharma, D. W. Small, A. Sodt, T. Stein, D. Stück, Y.-C. Su, A. J. W. Thom, T. Tsuchimochi, V. Vanovschi, L. Vogt, O. Vydrov, T. Wang, M. A. Watson, J. Wenzel, A. White, C. F. Williams, J. Yang, S. Yeganeh, S. R. Yost, Z.-Q. You, I. Y. Zhang, X. Zhang, Y. Zhao, B. R. Brooks, G. K. L. Chan, D. M. Chipman, C. J. Cramer, W. A. Goddard, M. S. Gordon, W. J. Hehre, A. Klamt, H. F. Schaefer, M. W. Schmidt, C. D. Sherrill, D. G. Truhlar, A. Warshel, X. Xu, A. Aspuru-Guzik, R. Baer, A. T. Bell, N. A. Besley, J.-D. Chai, A. Dreuw, B. D. Dunietz, T. R. Furlani, S. R. Gwaltney, C.-P. Hsu, Y. Jung, J. Kong, D. S. Lambrecht, W. Liang, C. Ochsenfeld, V. A. Rassolov, L. V. Slipchenko, J. E. Subotnik, T. Van Voorhis, J. M. Herbert, A. I. Krylov, P. M. W. Gill and M. Head-Gordon, *Mol. Phys.*, 2015, **113**, 184–215.

28 C.-H. Yang and C.-P. Hsu, *J. Chem. Phys.*, 2013, **139**, 154104.

29 M. H. Lee, B. D. Dunietz and E. Geva, *J. Phys. Chem. Lett.*, 2014, **5**, 3810–3816.

30 B.-C. Lin, B. T. Koo, P. Clancy and C.-P. Hsu, *J. Phys. Chem. C*, 2014, **118**, 23605–23613.

31 X.-K. Chen, M. K. Ravva, H. Li, S. M. Ryno and J.-L. Brédas, *Adv. Energy Mater.*, 2016, **6**, 1601325.

32 Z. Zheng, N. R. Tummala, Y.-T. Fu, V. Coropceanu and J.-L. Brédas, *ACS Appl. Mater. Interfaces*, 2017, **9**, 18095–18102.

33 Y. Li, T. Pullerits, M. Zhao and M. Sun, *J. Phys. Chem. C*, 2011, **115**, 21865–21873.

34 S.-B. Li, Y.-A. Duan, Y. Geng, H.-B. Li, J.-Z. Zhang, H.-L. Xu, M. Zhang and Z.-M. Su, *Phys. Chem. Chem. Phys.*, 2014, **16**, 25799–25808.

35 Y. Li, D. Qi, P. Song and F. Ma, *Materials*, 2015, **8**, 42–56.

36 Y. Li, Y. Feng and M. Sun, *Sci. Rep.*, 2015, **5**, 13970.

37 D. Qian, Z. Zheng, H. Yao, W. Tress, T. R. Hopper, S. Chen, S. Li, J. Liu, S. Chen, J. Zhang, X.-K. Liu, B. Gao, L. Ouyang, Y. Jin, G. Pozina, I. A. Buyanova, W. M. Chen, O. Inganäs, V. Coropceanu, J.-L. Bredas, H. Yan, J. Hou, F. Zhang, A. A. Bakulin and F. Gao, *Nat. Mater.*, 2018, **17**, 703–709.

38 P. Song, Q. Zhou, Y. Li, F. Ma and M. Sun, *Phys. Chem. Chem. Phys.*, 2017, **19**, 16105–16112.

39 T. Wang, X.-K. Chen, A. Ashokan, Z. Zheng, M. K. Ravva and J.-L. Brédas, *Adv. Funct. Mater.*, 2018, **28**, 1705868.

40 M. Rust, J. Lappe and R. J. Cave, *J. Phys. Chem. A*, 2002, **106**, 3930–3940.

41 C. Lambert, S. Amthor and J. Schelter, *J. Phys. Chem. A*, 2004, **108**, 6474–6486.

42 A. A. Voityuk, *J. Chem. Phys.*, 2006, **124**, 064505.

43 C. Butchosa, S. Simon, L. Blancafort and A. Voityuk, *J. Phys. Chem. B*, 2012, **116**, 7815–7820.

44 A. A. Voityuk, *J. Phys. Chem. C*, 2013, **117**, 2670–2675.

45 S.-J. Lee, H.-C. Chen, Z.-Q. You, K.-L. Liu, T. J. Chow, I.-C. Chen and C.-P. Hsu, *Mol. Phys.*, 2010, **108**, 2775–2789.

46 H.-H. Chou, C.-H. Yang, J. T. Lin and C.-P. Hsu, *J. Phys. Chem. C*, 2017, **121**, 983–992.

47 H.-C. Chen and C.-P. Hsu, *J. Phys. Chem. A*, 2005, **109**, 11989–11995.

48 G. Sini, J. S. Sears and J.-L. Bredas, *J. Chem. Theory Comput.*, 2011, **7**, 602–609.

49 Z.-Q. You, Y.-C. Hung and C.-P. Hsu, *J. Phys. Chem. B*, 2015, **119**, 7480–7490.

50 A. D. Becke, *J. Chem. Phys.*, 1993, **98**, 5648–5652.

51 C. Lee, W. Yang and R. G. Parr, *Phys. Rev. B: Condens. Matter Mater. Phys.*, 1988, **37**, 785–789.

52 P. Mori-Sánchez, A. J. Cohen and W. Yang, *J. Chem. Phys.*, 2006, **125**, 201102.

53 T. Körzdörfer and J.-L. Brédas, *Acc. Chem. Res.*, 2014, **47**, 3284–3291.

54 J. P. Perdew, K. Burke and M. Ernzerhof, *Phys. Rev. Lett.*, 1996, **77**, 3865–3868.

55 J. P. Perdew, K. Burke and M. Ernzerhof, *Phys. Rev. Lett.*, 1997, **78**, 1396.

56 C. Adamo and V. Barone, *J. Chem. Phys.*, 1999, **110**, 6158–6170.

57 M. G. Medvedev, I. S. Bushmarinov, J. Sun, J. P. Perdew and K. A. Lyssenko, *Science*, 2017, **355**, 49–52.

58 P. Bleiziffer, K. Schaller and S. Riniker, *J. Chem. Inf. Model.*, 2018, **58**, 579–590.

59 M. Alipour and Z. Safari, *J. Phys. Chem. C*, 2019, **123**, 746–761.

60 T. Yanai, D. P. Tew and N. C. Handy, *Chem. Phys. Lett.*, 2004, **393**, 51–57.

61 A. E. Raeber and B. M. Wong, *J. Chem. Theory Comput.*, 2015, **11**, 2199–2209.

62 T. Körzdörfer, J. S. Sears, C. Sutton and J.-L. Brédas, *J. Chem. Phys.*, 2011, **135**, 204107.

63 L. Pandey, C. Doiron, J. S. Sears and J.-L. Brédas, *Phys. Chem. Chem. Phys.*, 2012, **14**, 14243–14248.

64 I. T. Lima, C. Risko, S. G. Aziz, D. A. da Silva Filho and J.-L. Brédas, *J. Mater. Chem. C*, 2014, **2**, 8873–8879.

65 M. Niskanen and T. I. Hukka, *Phys. Chem. Chem. Phys.*, 2014, **16**, 13294–13305.

66 T. Kastinen, M. Niskanen, C. Risko, O. Cramariuc and T. I. Hukka, *Phys. Chem. Chem. Phys.*, 2016, **18**, 27654–27670.

67 R. Baer and D. Neuhauser, *Phys. Rev. Lett.*, 2005, **94**, 043002.

68 E. Livshits and R. Baer, *Phys. Chem. Chem. Phys.*, 2007, **9**, 2932–2941.

69 T. Yamamoto, Z. Zhou, T. Kanbara, M. Shimura, K. Kizu, T. Maruyama, Y. Nakamura, T. Fukuda, B.-L. Lee, N. Ooba, S. Tomaru, T. Kurihara, T. Kaino, K. Kubota and S. Sasaki, *J. Am. Chem. Soc.*, 1996, **118**, 10389–10399.

70 E. Wang, L. Hou, Z. Wang, S. Hellström, F. Zhang, O. Inganäs and M. R. Andersson, *Adv. Mater.*, 2010, **22**, 5240–5244.

71 M. M. Wienk, J. M. Kroon, W. J. H. Verhees, J. Knol, J. C. Hummelen, P. A. van Hal and R. A. J. Janssen, *Angew. Chem., Int. Ed.*, 2003, **42**, 3371–3375.

72 Y. Kim, H. R. Yeom, J. Y. Kim and C. Yang, *Energy Environ. Sci.*, 2013, **6**, 1909.

73 E. Wang, J. Bergqvist, K. Vandewal, Z. Ma, L. Hou, A. Lundin, S. Himmelberger, A. Salleo, C. Müller, O. Inganäs, F. Zhang and M. R. Andersson, *Adv. Energy Mater.*, 2013, **3**, 806–814.

74 S. Chen, Y. An, G. K. Dutta, Y. Kim, Z.-G. Zhang, Y. Li and C. Yang, *Adv. Funct. Mater.*, 2017, **27**, 1603564.

75 Y. Yi, V. Coropceanu and J.-L. Brédas, *J. Am. Chem. Soc.*, 2009, **131**, 15777–15783.

76 L. Pandey, PhD thesis, Georgia Institute of Technology, 2013.

77 T. Liu and A. Troisi, *J. Phys. Chem. C*, 2011, **115**, 2406–2415.

78 C. W. Murray, N. C. Handy and G. J. Laming, *Mol. Phys.*, 1993, **78**, 997–1014.

79 V. I. Lebedev and D. N. Laikov, *Dokl. Math.*, 1999, **59**, 477–481.

80 S. Hirata and M. Head-Gordon, *Chem. Phys. Lett.*, 1999, **314**, 291–299.

81 C. Leng, H. Qin, Y. Si and Y. Zhao, *J. Phys. Chem. C*, 2014, **118**, 1843–1855.

82 D. A. Egger, S. Weissman, S. Refaely-Abramson, S. Sharifzadeh, M. Dauth, R. Baer, S. Kümmel, J. B. Neaton, E. Zojer and L. Kronik, *J. Chem. Theory Comput.*, 2014, **10**, 1934–1952.

83 R. L. Martin, *J. Chem. Phys.*, 2003, **118**, 4775–4777.

84 G. A. Zhurko, *Chemcraft – graphical program for visualization of quantum chemistry computations*, Ivanovo, Russia, 2005, https://chemcraftprog.com.

85 P. Ros and G. C. A. Schuit, *Theor. Chim. Acta*, 1966, **4**, 1–12.

86 V. Barone and M. Cossi, *J. Phys. Chem. A*, 1998, **102**, 1995–2001.

87 M. Cossi, N. Rega, G. Scalmani and V. Barone, *J. Comput. Chem.*, 2003, **24**, 669–681.

88 A. W. Lange and J. M. Herbert, *J. Chem. Phys.*, 2010, **133**, 244111.

89 Physical Constants of Organic Compounds, in *CRC Handbook of Chemistry and Physics*, ed. J. R. Rumble, CRC Press/Taylor & Francis, Boca Raton, FL, 99th edn, 2018.

90 A. Melianas, F. Etzold, T. J. Savenije, F. Laquai, O. Inganäs and M. Kemerink, *Nat. Commun.*, 2015, **6**, 8778.

91 M. Campoy-Quiles, C. Müller, M. Garriga, E. Wang, O. Inganäs and M. I. Alonso, *Thin Solid Films*, 2014, **571**, 371–376.

92 D. H. K. Murthy, A. Melianas, Z. Tang, G. Juška, K. Arlauskas, F. Zhang, L. D. A. Siebbeles, O. Inganäs and T. J. Savenije, *Adv. Funct. Mater.*, 2013, **23**, 4262–4268.

93 A. A. Bakulin, Y. Xia, H. J. Bakker, O. Inganäs and F. Gao, *J. Phys. Chem. C*, 2016, **120**, 4219–4226.

94 Z. Zheng, J.-L. Brédas and V. Coropceanu, *J. Phys. Chem. Lett.*, 2016, **7**, 2616–2621.

95 L. Kronik and S. Kümmel, *Adv. Mater.*, 2018, **30**, 1706560.

96 G. Boschetto, M. Krompiec and C. K. Skylaris, *J. Phys. Chem. C*, 2018, **122**, 17024–17034.

97 A. Dreuw and M. Head-Gordon, *Chem. Rev.*, 2005, **105**, 4009–4037.

98 Y. Yi, V. Coropceanu and J.-L. Brédas, *J. Mater. Chem.*, 2011, **21**, 1479–1486.

99 T. Wang, M. K. Ravva and J.-L. Brédas, *Adv. Funct. Mater.*, 2016, **26**, 5913–5921.

100 T. Kawatsu, V. Coropceanu, A. Ye and J.-L. Brédas, *J. Phys. Chem. C*, 2008, **112**, 3429–3433.

101 S. Albrecht, K. Vandewal, J. R. Tumbleston, F. S. U. Fischer, J. D. Douglas, J. M. J. Fréchet, S. Ludwigs, H. Ade, A. Salleo and D. Neher, *Adv. Mater.*, 2014, **26**, 2533–2539.

102 D. C. Coffey, B. W. Larson, A. W. Hains, J. B. Whitaker, N. Kopidakis, O. V. Boltalina, S. H. Strauss and G. Rumbles, *J. Phys. Chem. C*, 2012, **116**, 8916–8923.

103 A. J. Ward, A. Ruseckas, M. M. Kareem, B. Ebenhoch, L. A. Serrano, M. Al-Eid, B. Fitzpatrick, V. M. Rotello, G. Cooke and I. D. W. Samuel, *Adv. Mater.*, 2015, **27**, 2496–2500.

104 J. Bergqvist, C. Lindqvist, O. Bäcke, Z. Ma, Z. Tang, W. Tress, S. Gustafsson, E. Wang, E. Olsson, M. R. Andersson, O. Inganäs and C. Müller, *J. Mater. Chem. A*, 2014, **2**, 6146–6152.

105 D. A. Vithanage, E. Wang, Z. Wang, F. Ma, O. Inganäs, M. R. Andersson, A. Yartsev, V. Sundström and T. Pascher, *Adv. Energy Mater.*, 2014, **4**, 1301706.

PUBLICATION

IV

"Charge transfer characteristics of fullerene-free polymer solar cells via multi-state electronic coupling treatment"

T. Kastinen and T. I. Hukka

ROYAL SOCIETY
OF CHEMISTRY

Check for updates

Charge transfer characteristics of fullerene-free polymer solar cells *via* multi-state electronic coupling treatment†

Tuuva Kastinen [ID] * and Terttu I. Hukka [ID] *

Recently, non-fullerene (NF) polymer solar cells (PSCs), where new electron acceptor (eA) materials are blended with a donor–acceptor (D–A) copolymer as an electron donor (eD), have shown promising power conversion efficiencies up to 18%. Some of the best-performing NF PSCs use the eD copolymers **PBDT-TzBI**, **PDTB-EF-T**, and **PBDB-T-2F**, and either a D–A copolymer **P(NDI2OD-T2)** or small molecule acceptors (SMAs) **ITIC-4F** and **ITIC-2Cl** as the NF eA compounds. Here we investigate these systems with density functional theory methods and extend our previous study of the multi-state fragment charge difference (FCD) electronic coupling scheme by applying it to the calculations of charge transfer (CT) rates for exciton dissociation and charge recombination (CR) processes at local eD–eA interfaces. Despite similar backbone structures and optical properties, the studied eD copolymers have different conformational, ionization, excitation, and CT characteristics. The electronic couplings and CT rates depend strongly on the relative positioning of the eD and eA compounds in the eD–eA complexes. While the main CT path is from eD to the eA compound, CT from eA to the eD compound is also predicted in the polymer–polymer **PBDT-TzBI–P(NDI2OD-T2)** system. The multi-state FCD electronic couplings are independent of the number of the excited states included in the calculations when using a dispersion-corrected optimally tuned long-range corrected functional. The calculated CR rates are slower in the polymer–SMA systems than in the polymer–polymer system, which could partly account for their higher experimentally observed efficiencies in devices.

Introduction

Polymer solar cells (PSCs) have a great potential as a low-cost, lightweight, flexible, and scalable technology for light conversion.[1,2] So far, the most studied systems have included fullerene derivatives as the electron acceptor (eA) materials with conjugated donor–acceptor (D–A) copolymers as the electron donor (eD) materials. Although these fullerene-based PSCs have achieved promising power conversion efficiencies (PCEs) of *ca.*

Chemistry and Advanced Materials, Faculty of Engineering and Natural Sciences, Tampere University, P.O. Box 541, FI-33014 Tampere, Finland. E-mail: tuuva. kastinen@tuni.fi; terttu.hukka@tuni.fi; Tel: +358 40 198 1133

† Electronic supplementary information (ESI) available: More details on the construction of the eD–eA complexes. Additional information regarding the methods. The following details on the results: the OT ω for the individual eD and eA compounds and the eD–eA complexes. Relaxed PES scans of the selected dihedrals in the monomer models of the eD and eA copolymers and **ITIC**. The BLA$_{total}$ values of the eD and eA compounds and bond length differences between the geometries of the charged (radical and S$_1$) and neutral (GS) eD and eA compounds in vacuum and CHCl$_3$. Additional optoelectronic properties (HOMO, LUMO, and HOMO–LUMO gap energies, IEs, EAs, vertical excitation energies, oscillator strengths, and UV-vis absorption spectra) of the eD and eA compounds. The optimized geometries and relative energies of the eD–eA complexes. The multi-state FCD electronic couplings, additional CT parameters, and rates of the eD–eA complexes. See DOI: 10.1039/d0se00306a

12%,[3,4] they possess several hindrances, such as limited possibilities to tune the chemical structures and energy levels of fullerene derivatives, high synthesis cost, poor light absorption in the visible and infrared spectral regions, and morphological instabilities.[5,6] To overcome these limitations, the researchers have developed alternative eA materials with tunable structural and optoelectronic features, which can be matched with a wider range of eD copolymers. As a consequence, a rapid and encouraging progress has been made in designing fullerene-free, *i.e.* non-fullerene (NF) PSCs during the past few years.[5,7]

In all-polymer solar cells (APSCs), D–A copolymers composed of electron-rich donor and electron-deficient acceptor units in the constitutional repeating unit (CRU) are employed as both the eD and eA materials. This type of a design strategy[8,9] has enabled fine-tuning of the structural and optoelectronic properties, *e.g.* ionization energies (IE), electron affinities (EA), and optical gaps, of the D–A copolymers by selecting the backbone donor and acceptor units with the desirable characteristics.[10] Controlling these features for the eA compounds can yield APSC devices with improved light absorption, higher open-circuit voltage, and enhanced long-term stability compared to the conventional, fullerene-based PSCs.[5] Especially, naphthalene diimide (NDI) based copolymers have been popular eA materials in APSCs due to their large EAs, high electron mobilities,

Electron acceptors

P(NDI2OD-T2)

R = 2-octyldodecyl

ITIC, R₁ = 4-hexylphenyl; R₂, R₃ = H
IT-2Cl, R₁ = 4-hexylphenyl; R₂ = Cl, R₃ = H
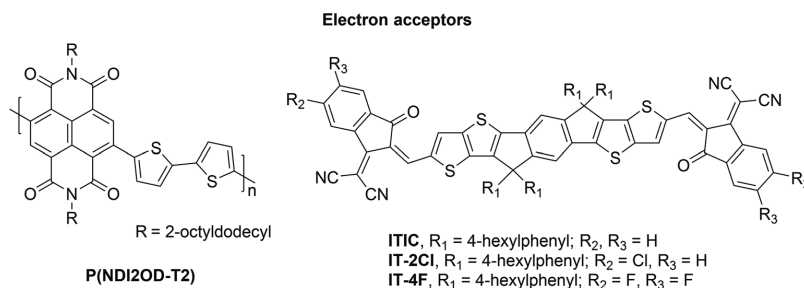**IT-4F**, R₁ = 4-hexylphenyl; R₂ = F, R₃ = F

Fig. 1 Molecular structures of the studied eA compounds.

and good thermal and oxidative stabilities.[11,12] The highest PCEs have been *ca.* 12%[13,14] for APSCs using poly[[*N,N'*-bis(2-octyldodecyl)naphthalene-1,4,5,8-bis(dicarboximide)-2,6-diyl)-*alt*-5,5′-(2,2′-bithiophene)] (**P(NDI2OD-T2)**), also referred to as N2200) as the eA material[15] (Fig. 1). These efficiencies have been surpassed recently with a new eA copolymer (PJ1), which is based on a small molecule acceptor (SMA) building block leading to the PCE of 14.4%.[16]

Another emerging type of the efficient NF PSCs makes use of π-conjugated SMAs as the eA materials, whose acceptor–donor–acceptor (A–D–A) structure leads to strong intramolecular electron push–pull effects similar to the ones in D–A copolymers. For example, in a successful **ITIC**,[17] an electron-donating, bulky seven-ring indacenodithieno[3,2-*b*]thiophene (IT) core is end-capped with electron-withdrawing 2-(3-oxo-2,3-dihydroinden-1-

ylidene)malononitrile (INCN) groups. This type of a rigid A–D–A structured backbone results in the extended conjugation and reduces reorganization energy, which is beneficial for charge transport.[17,18] However, on the downside, planar backbones with the extended conjugation may lead to the undesired aggregation behavior for **ITIC** (and other SMAs) and consequently decreased efficiencies of PSCs. Thus, four 4-hexylphenyl have been substituted to the IT core to restrict the planarity and consequently aggregation of **ITIC** in blend films. The advantages of **ITIC** derivatives are strong light absorption and good electron mobility. Furthermore, their properties can be easily tuned *via* molecular modifications, while simultaneously maintaining their key aspects of efficient eAs.[19,20] For example, NF-SMA PSCs based on **ITIC** derivatives with halogenated (*e.g.* fluorinated or chlorinated) end groups have some of the highest
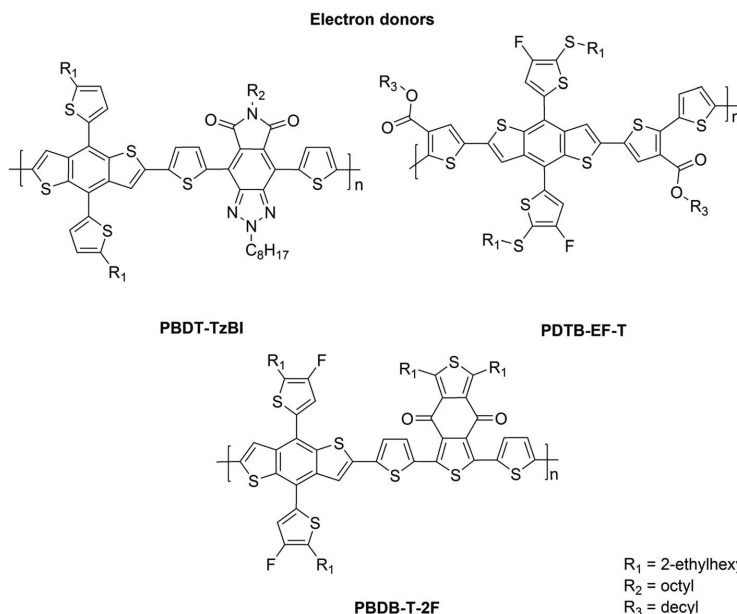
Electron donors

PBDT-TzBI

PDTB-EF-T

PBDB-T-2F

R₁ = 2-ethylhexyl
R₂ = octyl
R₃ = decyl

Fig. 2 CRUs of the studied eD copolymers.

PCEs (*ca.* 15%) for PSCs.[21–23] The record PCEs (*ca.* 18%[24]) for the NF PSCs have been achieved recently with a SMA[25] (Y6) consisting of dithienothiophen[3.2-*b*]-pyrrolobenzothiadiazole core and 2-(5,6-difluoro-3-oxo-2,3-dihydro-1*H*-inden-1-ylidene) malononitrile side groups.

The NF eA materials discussed above have either small (*i.e.* below 1.50 eV; *ca.* 1.48 eV for **P(NDI2OD-T2)**) or medium (*i.e.* 1.50–1.90 eV; *ca.* 1.60 eV for **ITIC**) bandgaps.[26] Thus, to achieve a wide absorption of the solar spectrum and efficient NF PSCs, they are typically combined with medium- or wide-bandgap (>1.9 eV) copolymers as the eD compounds. These kinds of copolymers (Fig. 2) include poly[4,8-bis(5-(2-ethylhexyl)thiophen-2-yl)benzo[1,2-*b*:4,5-*b'*]dithiophene-*co*-4,8-di(thien-2-yl)-6-octyl-2-octyl-5*H*-pyrrolo[3,4-*f*]benzotriazole-5,7(6*H*)-dione] (referred to as **PBDT-TzBI** in this work; known also as PTzBI[27] or PTZBIBDT[28]), **PDTB-EF-T**,[29] and poly[[2,6-(4,8-bis(5-(2-ethylhexyl)-4-fluorothiophen-2-yl)benzo[1,2-*b*:4,5-*b'*]dithiophene))-*alt*-(5,5-(1',3'-bis(thiophen-2-yl)-5',7'-bis(2-ethylhexyl)benzo[1',2'-*c*:4',5'-*c'*]dithiophene-4,8-dione)],[30,31] see the ref. 32 for the alternative naming (referred to as **PBDT-2F**[33] in this work; known also as **PBDB-TF**[21] or PM6[31]). Among these eDs, **PBDB-TzBI**[28] and **PBDB-T-2F**[31] have been originally developed for fullerene-based PSCs.

All of the aforementioned copolymers have the same weak, electron-rich donor unit, benzo[1,2-*b*:4,5-*b'*]dithiophene (BDT), but different electron-deficient acceptor units, TzBI in **PBDT-TzBI**[28] and 1,3-bis(thiophen-2-yl)-5,7-bis(2-ethylhexyl)benzo[1,2-*c*:4,5-*c'*]dithiophene-4,8-dione (BDD)[34,35] in **PBDB-T-2F**. In addition, there are thiophene spacers between the donor and acceptor units, which have a role in controlling planarity, and accordingly, aggregation.[36] The introduction of thiophenes in the copolymer backbone also weakens the intramolecular charge transfer (CT) character between the donor and acceptor units, which leads to the medium or wide band gaps in these copolymers.[37] In **PDTB-EF-T**, the thiophenes with the electron-withdrawing ester groups have been used instead of a strong electron-deficient unit.[29] Additionally, the desired IEs, EAs and structural characteristics of these copolymers have been achieved by attaching different functional groups, such as aromatic rings (*e.g.* thiophene) and electronegative atoms, *e.g.* fluorine,[29,31,33,38] to their backbones.

Theoretical quantum chemical calculations provide means for determining intrinsic structure–property relationships of π-conjugated PSC materials. Moreover, they can provide insight into the CT processes taking place at local interfaces of the eD and eA compounds. So far, there have been a number of studies on structural and optoelectronic properties of individual NF PSC compounds with density functional theory (DFT) methods.[25,39–42] For example, Wang *et al.* have investigated both the electronic and optical properties of two NF SMAs (IDIC and IDTBR) and five D–A copolymers and their interfacial characteristics.[41] The effect of fluorination on the characteristics of the eD copolymers and **ITIC** has been examined by Benatto *et al.*[43] Local interfaces in the NF devices have been exploited, as well.[23,41,44–49] Han *et al.* have studied the impact of different eD molecular architectures on the interfacial arrangements and electronic properties of the NF organic solar cells based on

small-molecule eDs and the SMA **ITIC-4F** with the multiscale simulations combining molecular dynamics (MD) and DFT calculations.[45] Moreover, they have compared the interfacial complexes consisting of **PBDB-T-2F** as the eD copolymer and either PC$_{71}$BM or **ITIC** as the eA compound with both MD and DFT.[44] The NF PSC systems of **PBDB-T-2F** and different **ITIC** derivatives have been the subject of other MD simulations, as well.[46–49] Han *et al.* have also compared the packing of the **ITIC** and PC$_{71}$BM acceptor thin films with MD simulations.[50] While these studies have included electronic structure calculations of some of the aforementioned efficient NF PSC compounds, they have mostly concentrated on the MD simulations of the blend morphologies, and thus a deeper understanding of the electronic structure–function relations and CT characteristics of these compounds is still required.

For the efficient charge generation in PSCs, the rates of exciton dissociation (ED) should be maximized, whereas the rates of charge recombination (CR) should be minimized.[51] In the previous theoretical studies of the NF PSCs systems, the ED and CR rates have also been evaluated to gain deeper understanding of these CT pathways.[47–49] The electronic coupling (H_{if}) between the initial (i) and final (f) charge-localized, *i.e.* diabatic states is one of the key parameters defining the CT rates.[52] Number of different theoretical approaches have been developed for calculating the couplings.[53–55] In the studies of polymer–fullerene-based PSC systems, the two-state fragment charge difference (FCD)[56] and generalized Mulliken–Hush (GMH)[57,58] schemes have been popular choices.[59–62] However, if a component of the local excitation is mixing with the CT state of interest, multiple adiabatic states should be included to obtain a more accurate description of the diabatic states.[63,64] In our previous studies,[65,66] we have observed the tendency of the long-range-corrected (LRC) functionals to predict mixed CT states for the polymer–fullerene systems. Our latest study[66] showed that use of the multi-state FCD and GMH schemes[64] with both the non-tuned and optimally-tuned (OT) LRC functionals reduces this mixing. In the previous studies of the NF PSC systems, the GMH scheme has been applied in conjunction with the (non-tuned) LRC functional CAM-B3LYP for **PBDB-T**–**ITIC**[47,48] and with the OT-ωB97X-D functional for **PBDB-T**–IT-OM.[49] However, the FCD scheme, which we observed[66] to be less sensitive to the number of states and the choice of the calculation method compared to GMH, does not seem to have been applied for the NF PSC systems yet. Furthermore, it is beneficial to investigate, whether the inclusion of multiple states effects the electronic couplings of the NF PSC systems. Information regarding the effect of the dispersion corrections included in the DFT functional on the multi-state coupling calculations is still missing, as well.

In this work, we will investigate *via* DFT and time-dependent DFT (TDDFT) methods a selected set of eD (Fig. 2) and eA (Fig. 1) compounds, which have been recently employed in some of the most efficient NF PSCs.[6,27,29,33,67] The selected eD compounds include D–A copolymers **PBDT-TzBI**, **PDTB-EF-T**, and **PBDB-T-2F**, whereas for the eA compounds, the D–A copolymer **P(NDI2OD-T2)**, the SMA **ITIC**, and its fluorinated and chlorinated counterparts, **ITIC-4F** and **ITIC-2Cl**, respectively,

have been chosen. We use theory to shed light on those characteristics that make the selected compounds successful and on the CT processes that take place at their local eD–eA interfaces. The first part of the work will explore the structural, ionization, excitation, and optoelectronic properties of the individual eD and eA compounds. In the second part, we will examine the local interfacial configurations, CT characteristics, and CT rates for the ED (eD*–eA $\rightarrow$ eD$^+$–eA$^-$) and CR (eD$^+$–eA$^-$ $\rightarrow$ eD–eA) processes of the corresponding eD–eA complexes. For obtaining the CT rates, we utilize the multi-state FCD scheme to calculate the electronic couplings. This work extends our previous study[66] of the effects of the two- *versus* multi-state treatments on electronic couplings in fullerene-based PSC systems by exploring the influence of multiple states and dispersion corrections on coupling values of the studied NF PSCs. Based on our[65] and other's findings[68,69] on organic solar cell systems, dispersion corrections are important for describing weak dispersion interactions at their local eD–eA interfaces. Furthermore, tuned LRC functionals have performed well in calculations of both the individual PSC compounds[70,71] and local interfaces.[65,66] Thus, the OT version of the dispersion corrected LRC functional ωB97X-D[72] was selected to investigate the effects of both the tuning of a LRC functional and dispersion corrections on the electronic coupling values. In some of the TDDFT calculations, we employ also the global hybrid PBE0 [73–75] functional for comparison.

Computational details

Models

The eD and eA compounds studied here (see Fig. 1 and 2) comprise both of the D–A copolymers (**PBDT-TzBI**, **PDTB-EF-T**, **PBDB-T-2F**, and **P(NDI2OD-T2)**) and the A–D–A-type SMAs (**ITIC**, **ITIC-2Cl**, and **ITIC-4F**). In most calculations, the full-length side chains of the compounds were replaced by methyl groups to reduce the computational cost, except for some of the relaxed potential energy surface (PES) scans of the side groups to check the dihedral angles within the side groups and between the side groups and the backbone donor or acceptor units. We note, however, that long alkyl side chains affect the solid-state packing and resulting optoelectronic characteristics,[76] and they should be included, *e.g.* when the atomistic simulations of blends are carried out.

The eD and eA copolymer models are defined by their CRUs (*i.e.* the repeating units, n). A CRU consists of donor and acceptor units and additional thiophene spacers. The monomer and oligomer models of the copolymers consist of 1–4 CRUs and will be referred to as **BDT-TzBI**, **DTB-EF-T**, **BDB-T-2F**, and **NDI2OD-T2** (without P in front). The relative orientations of their backbone units were selected based on the relaxed PES scans (see Methods below and Fig. S1–S3† for the studied dihedrals). Within the CRU of a D–A copolymer, neighboring donor and acceptor units can be either *anti* to each other, *i.e.* the neighboring heteroatoms of the units are on the opposite sides, or *syn* to each other, *i.e.* the neighboring heteroatoms are on the same side. Similarly, the neighboring CRUs can be either *anti* or *syn* with respect to each other. In the text, the

conformations are referred to as: *anti/anti* or *anti–anti/anti*, where the first word (or words) refers to the conformation(s) within one CRU and the second word to the conformation between two CRUs. Here, we have considered only the energetically most stable conformations for each copolymer.

Monomer models (*i.e.* hydrogen-terminated CRUs, $n = 1$) of the D–A copolymers were used in the PES calculations to determine the optimal dihedral angles within the backbone. Furthermore, the monomers were employed in the eD–eA complexes (see below). In the studies of the structural, ionization, and excitation characteristics of the individual eD and eA compounds, trimers ($n = 3$) were used as the oligomeric models of the D–A copolymers. As an exception, **P(NDI2OD-T2)** was modeled using a tetramer ($n = 4$) to keep the relative conjugation lengths (*i.e.* the number of the double bonds, N, within the shortest path between the terminal carbon atoms of the backbone) in the copolymer models consistent with each other.

The eD–eA complexes were constructed using the optimized GS geometries of the monomer models of the eD and eA copolymers and the **ITIC**-based eA compounds. In addition, dimer models of both the eD copolymer **PBDT-TzBI** and eA copolymer **P(NDI2OD-T2)** were used in one complex configuration to study the effect of a longer oligomer on the local structure and CT characteristics at the eD–eA interface. In all complexes, the eD models were oriented in the *xy* plane along the *x* axis. Three configurations of each complex were studied: the eA model was positioned above the donor, thiophene, and acceptor unit of the eD model along the *x* axis by superposing the centroids of the specific heterocyclic aromatic rings with the initial intermolecular distance of 4 Å (see the ESI† for further information of construction of different configurations). After this, the complexes were fully optimized without any constraints (see Methods).

Methods

All the calculations were carried out with the Gaussian 16 Rev.B01 suite of programs,[77] except for the electronic coupling calculations of the complexes, which were carried out with the Q-Chem 4.2 software.[78] The LRC ωB97X-D functional[72] was selected, as it includes the dispersion corrections and is recommended for studying systems with extended π-conjugated structures.[68]

To determine the relative orientations of the backbone units in the eD and eA compounds for the further calculations, the torsional potentials between the adjacent units within the monomer models of the eD and eA copolymers and the eA compound **ITIC** in their neutral GS geometries were determined with the relaxed PES scans at the ωB97X-D/6-31G** level of theory in vacuum (with the default range-separation parameter, ω, of 0.2 bohr^{-1}). The PES scans were carried out also for the dihedral angles between the BDT donor unit and the full-length alkyl thiophene side groups of the eD models (**BDT-TzBI**, **DTB-EF-T**, and **BDB-T-2F**) in addition to those between the BDD acceptor unit and alkyl side chains of **BDB-T-2F** to check their relative orientations (Fig. S3†). The constrained geometry optimizations were carried out at 5° intervals, *i.e.* the studied

dihedral angle was kept fixed while fully optimizing the geometry of the rest of the compound.

For all the other DFT and TDDFT calculations, the optimally tuned dispersion corrected functional, OT-ωB97X-D, was used with the 6-31G** basis set, unless stated otherwise (see the next paragraph). For this purpose, the ω value in ωB97X-D was optimally tuned in vacuum with the gap tuning procedures for the individual eD and eA compounds[79,80] (eqn (S1) in ESI†) and the eD–eA complexes[65,66,80,81] (eqn (S2) in ESI†). The OT ω values were determined with an accuracy of 0.01 bohr^{-1} using the 6-31G** basis set. The GS geometries of the neutral eD and eA compounds and their radicals, *i.e.* cations and anions, were fully optimized with DFT. In the characterization of the individual compounds, calculations were carried out in vacuum, solvent, and blend environments, unless stated otherwise. Solvation effects were included by means of the conductor-like polarizable continuum model (CPCM)[82,83] using the static (ε_s) and dynamic (*i.e.* optical, ε_{op}) dielectric constants of 4.7113 and 2.090627, respectively, for CHCl$_3$. For the blend environment, the ε_s and ε_{op} of 4.00 and 2.25 were used, respectively, which are approximate values employed in previous studies for different organic semiconductors.[84,85] For studying ionization of the eD and eA compounds, their vertical and adiabatic ionization energies (IEs, VIE and AIE) and electron affinities (EAs, VEA and AEA) were calculated with eqn (S3)–(S6) (ESI†). The intramolecular reorganization energies for the hole (λ_h) and electron (λ_e) transfer of the eD and eA compounds were calculated with eqn (S7) and (S8).†

For examining the intramolecular CT character of the NF PSC compounds and determining their UV-vis absorption spectra, the vertical excitation energies for the 10 lowest excited singlet states of the isolated eD and eA compounds were carried out with TDDFT. For the **ITIC** derivatives, the vertical excitations for the 20 lowest excited singlet states were required to yield the best description of the UV-vis spectra. Additionally, the TDDFT calculations of the individual eD and eA compounds were carried out in CHCl$_3$ at the PBE0/6-31G** level of theory using the OT-ωB97X-D-optimized geometries for comparing with the OT-ωB97X-D calculated spectra. The graphical illustrations of the UV-vis absorption spectra were created *via* convolution of the calculated singlet vertical transition energies and oscillator strengths using a Gaussian-shape broadening with a full width at half-maximum (FWHM) of 0.30 eV.

The nature of the excited states for both the individual NF PSC compounds and their complexes was described using natural transition orbitals (NTOs)[86] as a representation for the transition density matrix. The NTOs for the complexes were obtained from the TDDFT calculations carried out with Q-Chem, whereas the NTOs of the individual compounds were generated from the TDDFT calculations using Gaussian. Only the dominant pairs of the NTOs, *i.e.* those with the largest eigenvalues (λ_{NTO}) indicating the fraction of a particular hole–electron excitation to the overall transition,[86,87] were considered. In the case of the individual compounds, the contributions of the backbone units to the NTOs were determined using the C-Squared Population Analysis (C-SPA)[88] as implemented in Multiwfn 3.6.[89–91] For the eD–eA complexes, the nature of the

states was determined from the pictorial presentations of the NTOs and calculating the contributions of the eD and eA compounds to the NTOs by using the C-SPA within a self-made code. Pictorial presentations of the geometries and NTOs were generated using ChemCraft 1.8.[92]

The CT rates for the ED and CR processes taking place at the local interfacial complexes were calculated with the semi-classical Marcus theory:[93–95]

$$k_{ED/CR} = \frac{|H_{if}|^2}{\hbar} \sqrt{\frac{\pi}{\lambda k_B T}} \exp\left[-\frac{(\Delta G^\circ + \lambda)^2}{4\lambda k_B T} \right], \qquad (1)$$

where H_{if} is the electronic coupling between the initial and final states of the CT process considered;[96] k_B and $\hbar$ are the Boltzmann and reduced Planck constants, respectively; T is temperature (293.15 K here); λ the (intermolecular) reorganization energy (with the inner, λ_i, and outer, λ_i contributions, see eqn (S9) in ESI†); and ΔG° the Gibbs free energy. For calculating the inner reorganization energy, λ_i (eqn (S10)–(S15) in ESI†), and ΔG° (eqn (S16)–(S19) in ESI†), the geometries of the lowest excited singlet states (S$_1$) of the isolated eD monomers were optimized with TDDFT and those of the radicals (cations of these eD monomers and the anions of the eA compounds) were optimized with DFT. For defining the electronic couplings, vertical excitation energies, and adiabatic charge differences for the 10 lowest excited singlet states of the eD–eA complexes were calculated using TDDFT in the FCD scheme,[56] which is incorporated in the Q-Chem 4.2 software.[78] For the complexes of the polymer–polymer system of **PBDT-TzBI** and **P(NDI2OD-T2)**, the 25 lowest excited singlet states were considered. The two-state FCD coupling values (see eqn (S20) and (S21)†) obtained from the Q-Chem calculations were taken directly, whereas the electronic couplings with multiple states (>2) were determined with the multi-state version of FCD[64] in accordance with our previous work[66] (for further details, see eqn (S22)–(S25) in ESI†).

Results and discussion

Ground-state structural properties of the eD and eA compounds

To better understand the characteristics of the studied NF PSC compounds, we begin by exploring the geometrical structures of the individual eD oligomers and eA compounds. The shapes and sizes of the π-conjugated donor and acceptor units and the inclusions of the additional spacer units between them are among the factors defining the shapes of the backbones of both the D–A copolymers[97] and SMAs.[98] In addition, conformational preferences and resulting torsions induced by weak non-bonding interactions[99] between heteroatoms and between heteroatoms and hydrogens in the adjacent electron-rich and electron-deficient units affect the shape of the backbone.[44,100]

First, we will consider the eD copolymers. Based on their OT-ωB97X-D-optimized (see Tables S1 and S2† for the OT ω values) GS trimer geometries, **BDT-TzBI**, **DTB-EF-T**, and **BDB-T-2F** have twisted backbones with different curvatures (Table 1 and Fig. 3). The backbones of **BDT-TzBI** and **BDB-T-2F** have sine wave patterns, whereas that of **DTB-EF-T** has a zigzag pattern.[101]

Table 1 Energetically the most stable conformations, backbone types, and planarity of the backbones of the studied eD and eA compounds[a] calculated at the OT-ωB97X-D/6-31G** level of theory in different environments. The dihedral angles[b] for the eD and eA compounds calculated in blend

Type	Compound	n^c	N^d	Conformation	Backbone type	Planarity	Dihedral angle[b] (°)			
							α_1	α_2	α_3	$\theta_{\mathrm{CRU-CRU}}{}^e$
eD	**BDT-TzBI**	3	30	*Anti–syn/anti*	Sine wave	Twisted	157–159	41–42	43–44	159–162
	DTB-EF-T	3	30	*Anti/syn*	Zigzag	Twisted	159–162	159–160	131–152	45
	BDB-T-2F	3	30	*Anti–syn/anti*	Sine wave	Twisted	156–162	39–44	43–44	175–178
eA	**NDI2OD-T2**	4	28	*Syn–anti/syn*	Helical	Twisted	56–57	152–153	—	60–61
	ITIC	—	—	*Anti*	Linear	Planar	180	—	—	—
	ITIC-4F	—	—	*Anti*	Linear	Planar	180	—	—	—
	ITIC-2Cl	—	—	*Anti*	Linear	Planar	180	—	—	—

[a] The neutral GS geometries. [b] See Fig. S1 and S2 for the definition of the dihedral angles. The dihedral angles of the eD and eA compounds determined in vacuum and CHCl$_3$ are presented in Table S3. [c] Number of the CRUs in the studied oligomer. [d] Number of the double bonds in the studied oligomer. [e] Between the CRUs in the oligomers.

Furthermore, the curvature of the backbone increases in the order of **DTB-EF-T** < **BDT-TzBI** < **BDB-T-2F**, which can impact the degrees of ordering and folding of the copolymer chains and the mixing of the eD and eA compounds in the blends.[97] The backbones of the eD trimers are predicted to have similar torsional twists of 2–49° from planarity regardless of the surrounding medium (Table 1 and Fig. 3; see also Table S3 and Fig. S1† for the PES curves). In all cases, each BDT donor unit and its neighboring thiophene spacers are *anti* to each other in the eD trimer models due to the repulsive S···S interactions.[99] The thiophenes and acceptor units are *syn* to each other in **BDT-TzBI** and **BDB-T-2F** because of the possible nontraditional hydrogen bonding[99] between the carbonyl oxygen of the acceptor unit and the C–H hydrogen of the neighboring thiophene. In **DTB-EF-T**, the thiophenes are *anti* to each other,

except for those between the adjacent CRUs that are *syn* to each other due to a possible hydrogen bonding between the hydrogen of the unsubstituted thiophene and the carbonyl oxygen of the ester group in the thiophene of the next CRU. The same conformation has been also predicted for the dimer model of **PDTB-EF-T** in the original study of Li *et al.*[29]

Next, we will turn our attention to the eA compounds. The OT-ωB97X-D functional predicts that the eA tetramer **NDI2OD-T2** has a slightly helical backbone with a small curvature most probably due to the *syn–anti/syn* conformation (see below). The thiophene donors are predicted to be *anti* to each other with the torsion from planarity of *ca.* 27–28° between them (see Tables 1 and S3†), which is in line with, although somewhat smaller than the previous findings (the torsion of 32° from planarity by B3LYP/6-311G**[102]). The thiophene donor and NDI acceptor
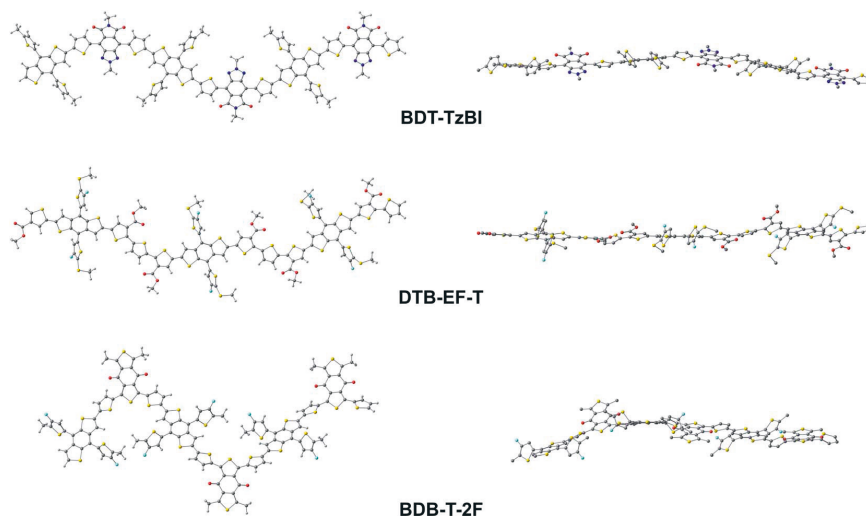
Fig. 3 Optimized GS geometries of the trimers of the studied eD copolymers calculated at the OT-ωB97X-D/6-31G** level of theory (in blend). In the side-view figures (on the right), the hydrogens are not shown for the clarity.

units of **NDI2OD-T2** are not in the same plane due to the relatively large dihedral angles (*ca.* 60°) between them (Tables 1, S3, Fig. 4 and S2†). Similar, although somewhat smaller dihedrals have been predicted previously theoretically (*syn*-conformation: 42° and *anti*-conformation: 138°) using the global hybrid functional B3LYP (with the 6-311G** basis set) and experimentally (*syn*: 37° and *anti*: 142°) with the IR and reflection–absorption IR spectroscopy measurements.[102] Here, the use of a LRC functional and truncated side groups could explain, respectively, the differences compared to the previous theoretical and experimental results.[102] Larger (*ca.* 65°) than the experimental dihedrals have been obtained previously also with a (non-tuned) LRC CAM-B3LYP functional.[103] Here, the adjacent NDI acceptor and thiophene donor units in **NDI2OD-T2** are predicted to be *syn* to each other, *i.e.* the sulfur atoms of the thiophene donors and the closest carbonyl oxygens of the neighboring acceptor units are on the same side. Previous theoretical studies have predicted varying results for the preferred orientation between the NDI and thiophenes depending on the copolymer model and functional: (i) equally stable *anti* and *syn* conformations (for the dimer model, B3LYP/6-31G*),[104] (ii) more favorable *anti* (for the monomer and pentamer models, B3LYP/6-311G**),[102] or (iii) more favorable *syn* conformation (for the dimer model, CAM-B3LYP/6-31G*).[103] Furthermore, the inclusion of full-length side chains and presence of the other **NDI2OD-T2** chains play a role in defining the more favorable conformation in the real blend environment.[105]

The OT-LRC functional OT-ωB97X-D predicts that the backbones of the SMA compounds **ITIC**, **ITIC-4F**, and **ITIC-2Cl** are completely planar (Table 1, Fig. 4 and S2†). In the experimental X-ray diffraction analysis of **ITIC** and fluorinated **ITIC** derivatives,

somewhat larger torsions (4–16°) between the IT core and the INCN end-groups have been observed for their single-crystal structures.[106] Based on our calculations, **ITIC** prefers the *syn*-conformation, where the sulfurs of the IT donor core and the carbonyl oxygens of electron-deficient INCN end-groups are on the same side. This finding is consistent with both the previous theoretical calculations carried out at the B3LYP/6-31G** level of theory[107] and experimental X-ray diffraction analysis.[106] Based on these modeling results on **ITIC** compounds, both the extended π-conjugation and planarity have been gained *via* fused sp2-hybridized rings, which agree with the experimental goals for SMAs to pursue strong light absorption and good charge mobility, respectively.[17,18]

The degree of the aromaticity and delocalization of the π-electrons in the polymers, *i.e.* π-conjugation, is described by the bond length alternation (BLA) parameter, which is defined here as the average value of the differences between adjacent single and double C–C bonds. Greater delocalization leads to equalized bond lengths and thus to the lower BLA values.[108,109] The BLA values calculated for the centermost CRUs (BLA_{middle}) of the (neutral) GS geometries of the eD trimers **BDT-TzBI**, **DTB-EF-T**, and **BDB-T-2F** are very similar (Table 2, see Table S4† for the total BLA values) indicating similar delocalization along their conjugation paths (see Fig. 5). Moreover, the BLA_{middle} of the eA tetramer **NDI2OD-2T**, which has been calculated for the innermost donor and acceptor units, is only slightly larger than those of the eD trimers. If two innermost CRUs of **NDI2OD-2T** are considered instead, the BLA_{middle} values increase somewhat. Based on the positive BLA_{middle}, these eD and eA copolymers have highly alternated single and double C–C bond patterns in their backbones (also referred to as an "aromatic" character in literature sometimes[109,110]). The environment does not seem to have
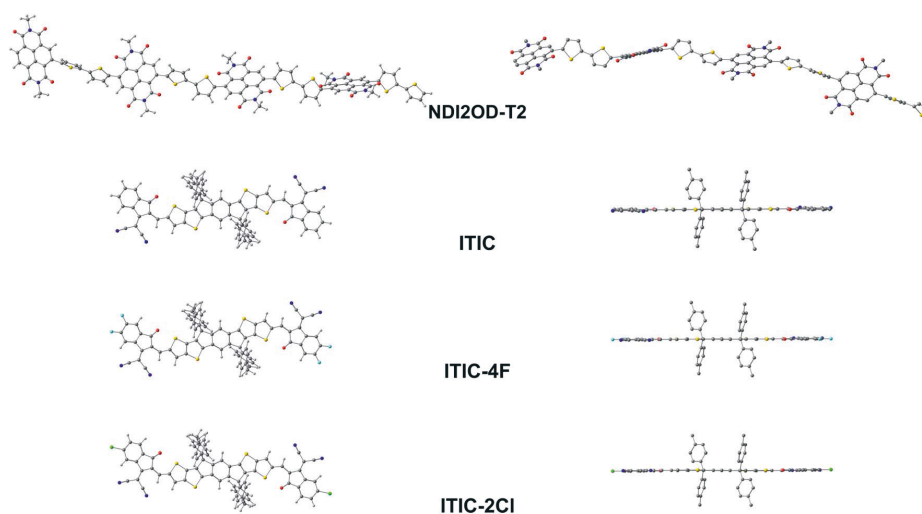

Fig. 4 Optimized GS geometries of the tetramer of the studied eA copolymer (**NDI2OD-T2**) and the SMA eA compounds (**ITIC**, **ITIC-4F**, and **ITIC-2Cl**) calculated at the OT-ωB97X-D/6-31G** level of theory (in blend). In the side-view figures (on the right), the hydrogens are not shown for the clarity.

Table 2 BLA_{middle} values[a] and intramolecular reorganization energies[b] of the studied eD and eA compounds[c] calculated at the OT-ωB97X-D/6-31G** level of theory in vacuum, CHCl$_3$ (in parentheses), and blend (in brackets)

Compound	BLA$_{middle}$				Intramolecular reorganization energies	
	S$_0$ (GS)	S$_1$	Cation	Anion	λ_h (eV)	λ_e (eV)
BDT-TzBI	0.046	0.006	0.016	0.017	0.30	0.42
	(0.047)	(0.000)	(0.025)	(0.021)	(0.30)	(0.44)
	[0.047]	[0.001]	[0.025]	[0.022]	[0.31]	[0.46]
DTB-EF-T	0.044	0.012^d	0.010	0.019	0.30	0.50
	(0.045)		(0.022)	(0.023)	(0.38)	(0.60)
	[0.045]		[0.021]	[0.023]	[0.38]	[0.60]
BDB-T-2F	0.046	0.005	0.018	0.039	0.27	0.18
	(0.047)	(0.000)	(0.023)	(0.030)	(0.38)	(0.43)
	[0.047]	[0.000]	[0.041]	[0.030]	[0.42]	[0.46]
NDI2OD-T2	0.048^e/0.051^f	—	0.039^e/0.029^f	0.031^e/0.038^f	0.75	0.43
	(0.049^e/0.052^f)		(0.011^e/0.033^f)	(0.037^e/0.046^f)	(0.64)	(0.42)
	[0.049^e/0.052^f]		[0.010^e/0.032^f]	[0.049^e/0.052^f]	[0.65]	[0.34]
ITIC	—	—	—	—	0.24	0.26
					(0.22)	(0.24)
					[0.22]	[0.25]
ITIC-4F	—	—	—	—	0.25	0.27
					(0.22)	(0.25)
					[0.22]	[0.25]
ITIC-2Cl	—	—	—	—	0.24	0.26
					(0.22)	(0.24)
					[0.22]	[0.24]

[a] Calculated for the conjugation paths presented in Fig. 5. [b] For the hole (λ_h) and electron transfer (λ_e). Calculated with eqn (S7) and (S8). [c] In the case of the copolymers, $n = 3$ for **BDT-TzBI**, **DTB-EF-T**, and **BDB-T-2F** and $n = 4$ for **NDI2OD-2T**. [d] The S$_1$ geometries of **DTB-EF-T** did not converge in either CHCl$_3$ or blend. [e] For the (three) innermost donor and acceptor units. [f] For the two innermost CRUs.

strong effect on the BLA_{middle} values, as they are very similar in blend, CHCl$_3$, and vacuum. Here we note that for molecules with a large degree of conjugation (i.e. long polyene and cyanine chains), the tuning of ω may lead to incorrect BLA values, which may originate from the lack of size-consistency and an unbalanced description of σ and π orbitals in the tuned LRC functionals.[111] However, as we are merely interested in the relative results between different compounds and not the absolute values, we expect the OT-LRC functional to be suitable for this case.

In conclusion, while some similar features are observed for the studied eD and eA compounds, they have distinguished features in the shapes of their backbones, degrees of the planarity, and conformational preferences, which may have impact on their packing and mixing behavior in the photoactive blends. However, we note that in the case of the copolymers, more than one backbone conformation can coexist in real solvent and solid-state environments.[105,112] Moreover, the polymer chains may adopt conformations in blends other than those predicted for single chains due to the stabilizing effects of the bulk interchain interactions.[113] The inclusion of the full-length side chains can also lead to somewhat different results compared to our models with truncated CH$_3$ side groups. For example, DFT PES scans of several D–A copolymers have been noted to yield more planar structures for the monomer models of CRUs than in aggregates given by MD simulations.[114] Nevertheless, these results shed more light on the intrinsic properties that may impact the interactions between the studied eD and eA compounds at their eD–eA interfaces.

Ionization of the eD and eA compounds

In the next paragraphs, we compare the ionization (both the oxidation and reduction) characteristics of the studied eD and eA compounds. In general, oxidation and reduction cause notable changes in the geometries of the eD and eA oligomers, as is observed from the bond length differences (Fig. 5 for blend and Fig. S4† for vacuum and CHCl$_3$) and the BLA values (Tables 2 and S4†) of the radicals (cation and anion) with respect to the corresponding neutral compounds. The largest changes in the eD and eA oligomers caused by oxidation and reduction occur mainly in their middle regions, i.e. the centermost CRUs, although there are some variations depending on the surrounding medium. Moreover, larger intramolecular reorganization energies for the hole (λ_h) and electron (λ_e) transfer, which correspond to the relaxation energies of the compounds upon oxidation and reduction, respectively, are predicted in blend and CHCl$_3$ indicating somewhat larger geometrical changes in these environments compared to vacuum (Table 2). Ionization of the neutral oligomers mainly shortens the single bonds and lengthens the double bonds resulting in an inverse single–double C–C bond pattern compared to the neutral GS geometries. Decreased bond length alternation between single and double bonds and thus increased delocalization can be observed also from smaller BLA_{middle} values of the most radicals compared to the neutral compounds (Table 2).

Oxidation induces rather similar geometrical changes to all three eD trimer models, as can be observed from their bond length difference patterns (Fig. 5 and S4†). However, the
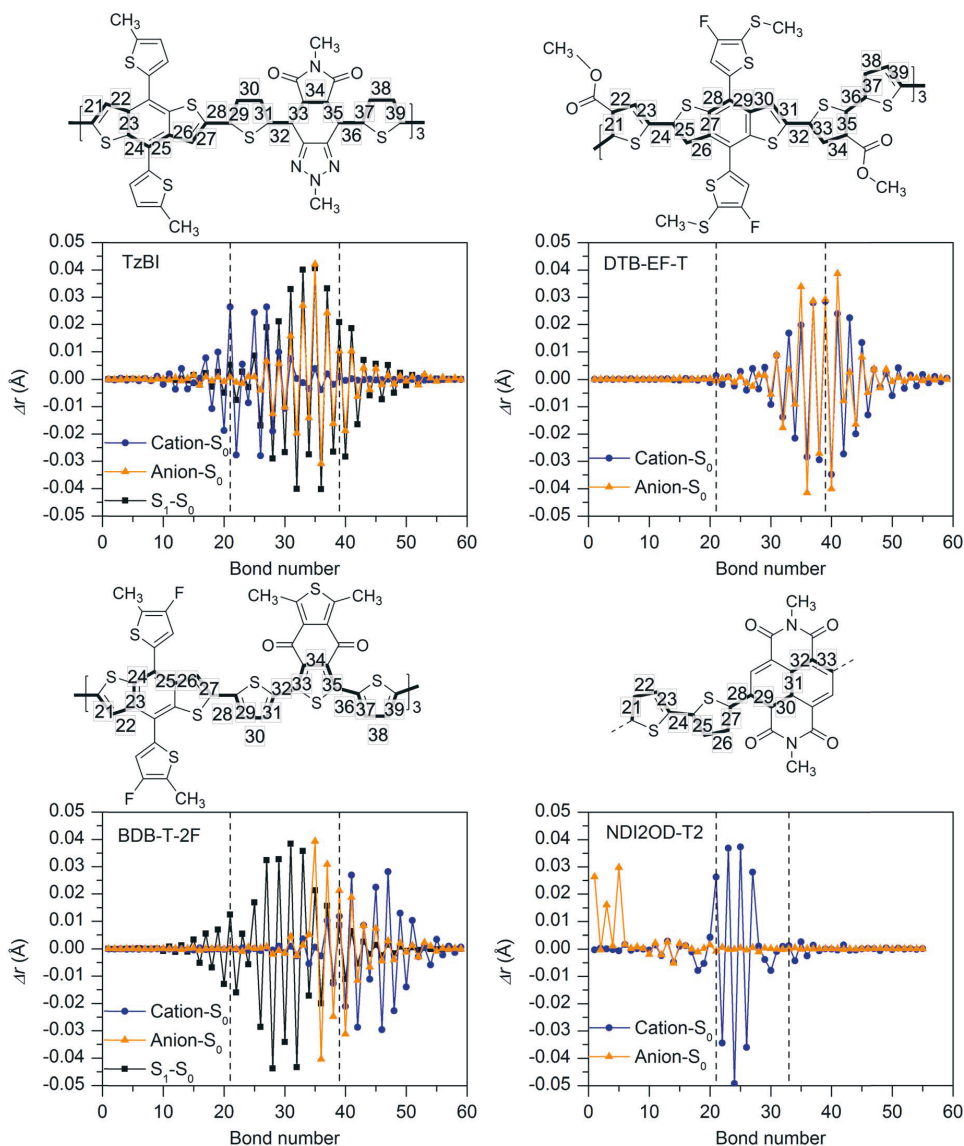
Fig. 5 Differences in the bond lengths (Δr) between the OT-ωB97X-D/6-31**-optimized (in blend) geometries of charged (radical cation, radical anion, or S_1) and neutral (GS) compounds with respect to the bond numbers of the eD and eA compounds along the conjugation paths presented above the graphs. The numbering in the chemical structures corresponds to the middle CRUs, which are represented with the dashed lines in the graphs. As **NDI2OD-T2** is the tetramer, three centermost units are considered for it instead of the middle CRUs.

backbone regions, which are affected the most by oxidation, are somewhat different for them. In **BDT-TzBI** and **BDB-T-2F**, the largest changes are observed in both the BDT donor and thiophene spacer units, whereas in **DTB-EF-T**, the largest changes caused by oxidation take place in both the unsubstituted electron-rich and ester-substituted electron-deficient thiophenes (see 'Excited-state characteristics of the isolated eD and

eA compounds' below), while the BDT donor units are mainly unaffected. The λ_h values (Table 2) and IEs (both VIEs and AIEs, Fig. S5 and Table S5 in ESI†) of the eD trimers increase slightly in the order of **BDT-TzBI** < **DTB-EF-T** ≤ **BDB-T-2F** in both blend and CHCl₃, which indicates the smallest changes for **BDT-TzBI** making it the easiest to oxidize among the studied eD trimers (in vacuum, the trends in the λ_h and IE values vary more). The

calculated λ_h values suggest that the hole mobilities of the eD compounds increase in the order of **BDB-T-2F** < **DTB-EF-T** < **BDT-TzBI**, which is in line with the experimental hole mobilities predicted for the corresponding copolymers.[28,29,115]

Reduction of the eD trimers takes mainly place in different backbone regions than oxidation, namely in the acceptor units and neighboring thiophenes for **BDT-TzBI** and **BDB-T-2F**. The surrounding medium has some effect on these regions, as reduction of **BDB-T-2F** affects mostly its thiophene spacers in vacuum instead of the BDD acceptor unit. In **DTB-EF-T**, reduction takes place in the same units as oxidation, *i.e.* the unsubstituted electron-rich and substituted electron-deficient thiophenes. The λ_e values of the eD trimers increase in the order of **BDB-T-2F** < **BDT-TzBI** < **DTB-EF-T** (in all media) following the same trend as their λ_h values in vacuum (Table 2). Overall, the λ_h values are predicted to be smaller than the λ_e values for the eD compounds indicating faster hole mobilities,[43] as can be expected from their nature as the hole-transporting materials.[103]

Similar trends in ionization are observed for the eA tetramer **NDI2OD-T2** as for the eD trimers **BDT-TzBI** and **BDB-T-2F** in all media, namely the oxidation of **NDI2OD-T2** takes place in the electron-rich thiophene donor units, whereas the reduction affects mostly the NDI acceptor unit and some of the

thiophenes. However, larger geometrical changes take place in **NDI2OD-2T** upon oxidation compared to the other eD and eA compounds, as can be concluded from the bond length difference patterns (Fig. 5 and S4†) and the larger λ_h values of **NDI2OD-2T** (Table 2). This is most probably due to the two neighboring, unsubstituted thiophene donor units within the CRU of **NDI2OD-2T**, which introduce more flexibility and degrees of freedom to the backbone compared to the more conjugated donor units in the other eD and eA compounds. On the contrary, reduction induces only small changes to the more rigid NDI acceptor unit of **NDI2OD-T2**, as can be observed from the bond length differences (predicted in all media) and the λ_e value (predicted in blend). Overall, the calculated reorganization energies are consistent with the previously predicted λ_h (0.38–0.56 eV [103,116]) and λ_e (0.30 eV [103]) values for the oligomers ($n = 1$–5) of **P(NDI2OD-2T)** with the (non-tuned) LRC CAM-B3LYP functional. The smaller λ_e values of **NDI2OD-2T** compared to its λ_h values indicate faster electron mobility than the hole mobility, as expected from its electron-transporting nature.

Based on their somewhat smaller λ_h and λ_e values, the geometrical changes upon oxidation and reduction in the eA **ITIC** derivatives are not as large as in the eD and eA copolymer

Fig. 6 NTOs (the dominant pairs) for the main excitations (*i.e.* $S_0 \rightarrow S_1$ transitions) of the studied eD compounds calculated with TDDFT at the OT-ωB97X-D/6-31G** level of theory in blend (isodensity contour = 0.025). Additionally, the contributions (%) of the electron densities of donor (D), acceptor (A), and thiophene (T) units of the oligomers to the NTOs and the fraction of each NTO pair (λ_{NTO}) related to the $S_0 \rightarrow S_1$ transition are presented.

models. In addition, the λ_h and λ_e values of **ITIC** derivatives are almost identical with each other despite the different substituents in their electron-withdrawing INCN end-groups. The smaller λ_h and λ_e values are not surprising,[43,117] as one aim of the rigid A–D–A type backbones of the **ITIC**-based compounds has been to reduce their reorganization energies for improved charge transport. In comparison, the studied eD and eA oligomers have more flexibility and degrees of freedom between their backbone units, which lead to the larger reorganization energies for the hole and electron transfer.

Excited-state characteristics of the isolated eD and eA compounds

Next, we turn our attention to the excitation characteristics of the studied NF PSC compounds. First, the intramolecular CT characters of the eD and eA compounds will be compared by examing the NTOs of their main transitions, *i.e.* those with the largest oscillator strengths corresponding to the absorption maxima in their calculated UV-vis spectra (Fig. S6 and Table S6†). In the eD and eA oligomers (*i.e.* trimers for eDs and tetramer for the eA copolymer), both the hole and electron NTO determined in blend are mainly localized in the middle CRU (or CRUs, see Fig. 6 and 7). The surrounding medium does not have much effect on the charge distribution, and the NTOs predicted

in vacuum and $CHCl_3$ are almost the same (see Table S7†) and thus are not presented here.

In all compounds, a partial intramolecular CT is observed from the electron-rich donor units to the electron-deficient acceptor units, as expected.[17,18,65,100,118] In the eD trimers, charge transfers also from the thiophene spacers to the acceptor units, namely the hole NTOs are more localized on the donor and thiophene units, whereas the electron NTOs are more localized on the acceptor units. This contribution of the thiophenes to the CT is in line with their known, weakening effect on the push–pull interaction between the donor and acceptor units.[37] The nature of CT is rather similar in **BDT-TzBI** and **BDB-T-2F**, which have the same electron-rich units, *i.e.* the BDT donor and thiophene spacer units, but different acceptor units. However, a somewhat larger amount of charge density moves from the electron-rich units to the acceptor unit in the case of **BDT-TzBI** compared to **BDB-T-2F** (TzBI: 31 percentage points, *i.e.* pp, *vs.* **BDB-T-2F**: 16 pp, see Table S7†). We predicted also in our previous study[65] a similar kind of CT character for a copolymer with a similar backbone structure, where the BDT donor unit and the quinoxaline acceptor unit were separated by the thiophene spacers. As the corresponding eD copolymers have been incorporated in the efficient fullerene-based and NF PSCs, this kind of a backbone structure and resulting CT character can be concluded to be beneficial for the performance of the

D/T1: 39%; D/T2: 39%; A: 22%   **NDI2OD-T2**   D/T1: 7%; D/T2: 6%; A: 87%

$$\frac{\lambda_{NTO} = 0.59}{NTO\ pair\ 1}$$

hole   **electron**

D (core): 79%; A (end-groups): 21%   **ITIC**   D (core): 54%; A (end-groups): 46%

$$\frac{\lambda_{NTO} = 0.87}{NTO\ pair\ 1}$$

hole   **electron**

D (core): 78%; A (end-groups): 22%   **ITIC-2Cl**   D (core): 53%; A (end-groups): 47%

$$\frac{\lambda_{NTO} = 0.87}{NTO\ pair\ 1}$$

hole   **electron**

D (core): 78%; A (end-groups): 22%   **ITIC-4F**   D (core): 53%; A (end-groups): 47%

$$\frac{\lambda_{NTO} = 0.87}{NTO\ pair\ 1}$$

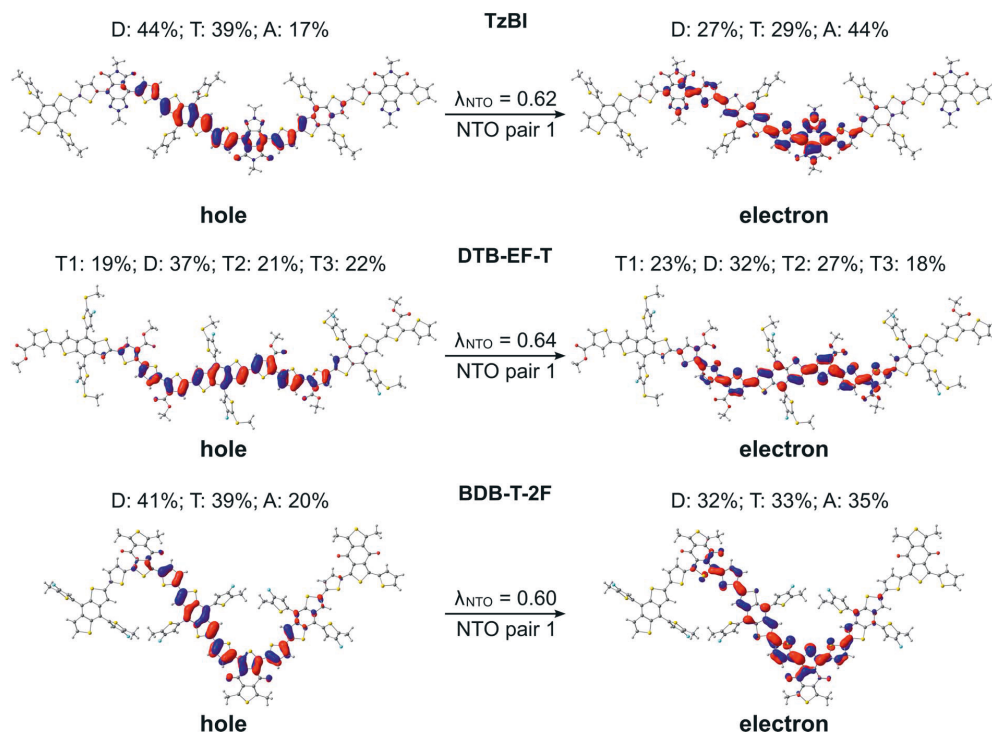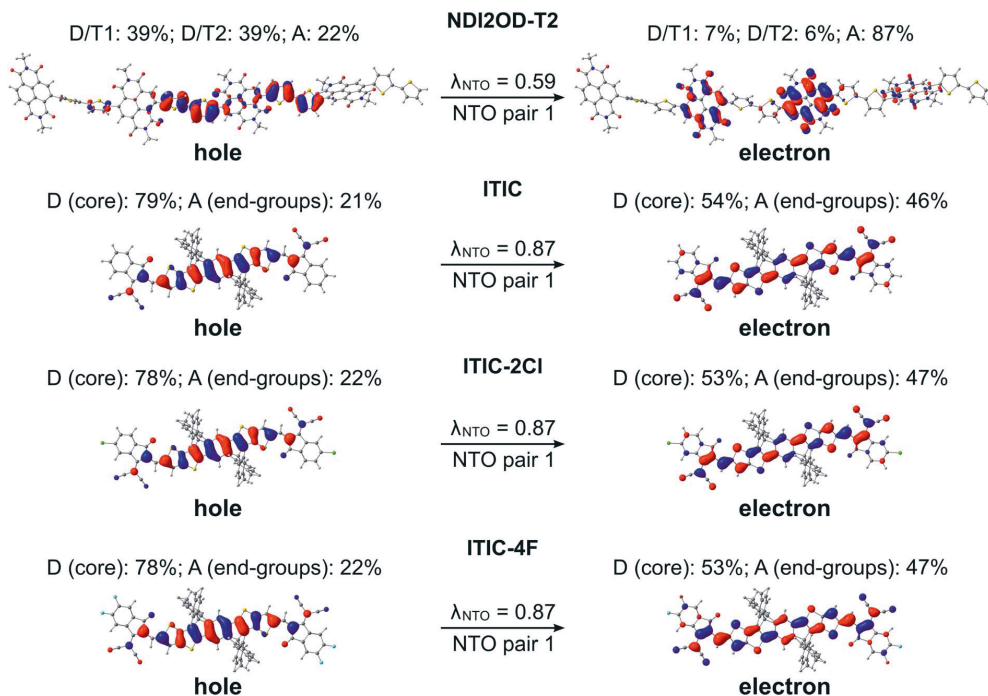**hole**   **electron**

Fig. 7 NTOs (the dominant pair) for the main excitations (*i.e.* $S_0 \rightarrow S_1$ transitions) of the studied eA compounds calculated with TDDFT at the OT-ωB97X–D/6–31G** level of theory in blend (isodensity contour = 0.025). Additionally, the contributions (%) of the electron densities of the donor (D) and acceptor (A) units of the compounds to the NTOs and the λ_{NTO} values are also presented.

PSCs. However, no exact conclusion on the efficiencies can be drawn merely based on these factors. Namely, **DTB-EF-T**, whose corresponding copolymer has been employed in the highly efficient NF PSC, has somewhat different backbone structure and intramolecular CT characteristics. In **DTB-EF-T**, both the hole and electron NTOs are quite evenly distributed along the BDT donor and thiophene units and only a small amount of charge (*ca.* 9 pp) is transferred from the BDT donor units and unsubstituted thiophenes to the electron-deficient thiophenes with the ester side groups.

In the eA tetramer **NDI2OD-T2** (Fig. 7), the hole NTOs are more clearly localized on the thiophene donor units and the electron NTOs on the NDI acceptor units compared to the NTOs in the eD trimers, which are more delocalized along several donor and acceptor units (see Fig. 6). This is most probably due to the larger twists between the donor and acceptor units in **NDI2OD-T2** compared to the eD trimers (see Table 1) hindering the delocalization along the backbone.

For all three **ITIC**-based SMAs, the hole NTO is more localized on the electron-donating IT core group, whereas the electron NTO is quite evenly distributed on both the core and electron-withdrawing INCN end-groups (Fig. 7). Fluorination and chlorination of the INCN end-groups have been stated to enhance the intramolecular CT nature of **ITIC**, as based on the larger dipole moments predicted for the halogenated regional parts.[33] However, the introduction of either F or Cl atoms did not affect the electron density distributions of the highest occupied molecular orbital (HOMO) and lowest unoccupied molecular orbital (LUMO). The same is observed here with the NTOs, which are also very similar to each other indicating that the fluorination and chlorination does not affect the electron density distribution much in these models. However, slightly smaller vertical excitation energies of the main, $S_0 \rightarrow S_1$ transition (Table S6†) and consequently red-shifted UV-vis spectra of **ITIC-4F** and **ITIC-2Cl** (Fig. S6†) indicate some enhancement in their intramolecular CT character with respect to **ITIC**, which is in line with the experimentally predicted UV-vis absorption spectra.[33]

Next, we compare the GS and S_1 state geometries of the eD trimers to display the structural changes taking place upon the excitation and resulting vibrational relaxation. The S_1 relaxation energies increase from those calculated for **BDT-TzBI** (210 kJ mol^{-1} in vacuum; 204 kJ mol^{-1} in CHCl$_3$; 205 kJ mol^{-1} in blend) and **DTB-EF-T** (217 kJ mol^{-1} in vacuum) to those for **BDB-T-2F** (221 kJ mol^{-1} in vacuum; 213 kJ mol^{-1} in CHCl$_3$; 214 kJ mol^{-1} in blend). Smaller relaxation energies indicate smaller geometrical changes in **BDT-TzBI** than in the other two eD trimers upon excitation. These trends are similar as those of the λ_h values calculated in CHCl$_3$ and blend (see above, Table 2). The BLA$_{middle}$ values for the optimized S_1 geometries of the eD **BDT-TzBI** and **BDB-T-2F** trimers are practically zero in all media indicating highly delocalized structures (Table 2). The BLA$_{middle}$ value of **DTB-EF-T** (in vacuum) is also notable smaller due to more delocalized backbone compared to the neutral GS geometry. The largest differences in the bond lengths between the GS and S_1 state geometries of the eD trimers are mainly in the acceptor and neighboring thiophene units of the middle CRU,

i.e. in the same regions as for reduction (Fig. 5 and S4†). However, small structural changes occur in the BDT donor of BTB-T-2F, as well, which might explain its larger S_1 relaxation energies.

Local interfacial eD–eA configurations

After establishing the structural and optoelectronic features of the individual eD and eA compounds, we will focus next on the eD–eA complexes and their structural and CT characteristics to better understand the interactions at their local eD–eA interfaces. In the case of the polymer–polymer system **BDT-TzBI–NDI2OD-T2**, the most stable configuration is predicted to form when the NDI acceptor units of **NDI2OD-T2** ($n = 1$) and **BDT-TzBI** ($n = 1$) are face-to-face, while their donor units are also face-to-face (the AA(1) configuration, see Tables S8–S10† and Fig. 8 and S7†). In another possible configuration (*i.e.* the DA(2) configuration with the energy difference of 0.9 kJ mol^{-1} compared to the most stable one), the acceptor unit of **NDI2OD-T2** and the donor units of **BDT-TzBI** are face-to-face, while the donor units of **NDI2OD-T2** and the acceptor unit of **BDT-TzBI** are face-to-face. This agrees with the experimental evidence[119] for the face-to-face stacking between the similar PTzBI-Si copolymer and P(NDI2OD-T2). These kinds of face-to-face orientations are essential for forming strong π-orbital overlap at the polymer–polymer interfaces, reducing the binding energy of the excitons, and promoting the formation of free charge carriers.[37] The calculated distances between the backbones of **BDT-TzBI** and **NDI2OD-T2** are *ca.* 3.4–4.0 Å with the average of 3.7 Å, which is consistent with the experimental π–π distance (3.7 Å).[120] Based on the electrostatic potential energy surface maps (Table S11†) calculated for the different configurations of **BDT-TzBI–NDI2OD-T2**, there are subtle differences in the electronegative and electropositive regions, which could have roles in defining the energetically favorable positioning of **BDT-TzBI** and **NDI2OD-T2** observed in the studied set of configurations.

In the case of the polymer–SMA systems, energetically favored placement of the eA SMA compound above the eD copolymer compounds depends on the system. Namely, for **DTB-EF-T–ITIC-4F**, the most stable configuration is predicted to be the one where the electron-withdrawing end-group of **ITIC-4F** is on the top of the BDT donor unit of **DTB-EF-T** (the DA configuration, see Table S9†). Even in the model, where the end-group of **ITIC-4F** has been initially positioned on the top of the acceptor (the AA configuration) **ITIC-4F** has shifted so that the end-group is located above the bond connecting the acceptor and donor units of **DTB-EF-T**. However, in **BDB-T-2F–ITIC-2Cl**, energetically the most favorable configuration is the one where the end-group of **ITIC-2Cl** is on the top of the BDD acceptor unit of **BDB-T-2F** (the AA configuration, see Table S10†). This is consistent with the previous atomistic simulations of the **BDB-T-2F–ITIC** systems,[49,121] where the end-groups of **ITIC** are observed to locate more probably on the top of the acceptor unit than the donor unit of **BDB-T-2F**.

We note that our models of the monomers with the truncated side groups cannot entirely describe the best possible arrangements of the studied compounds, as the full side chains
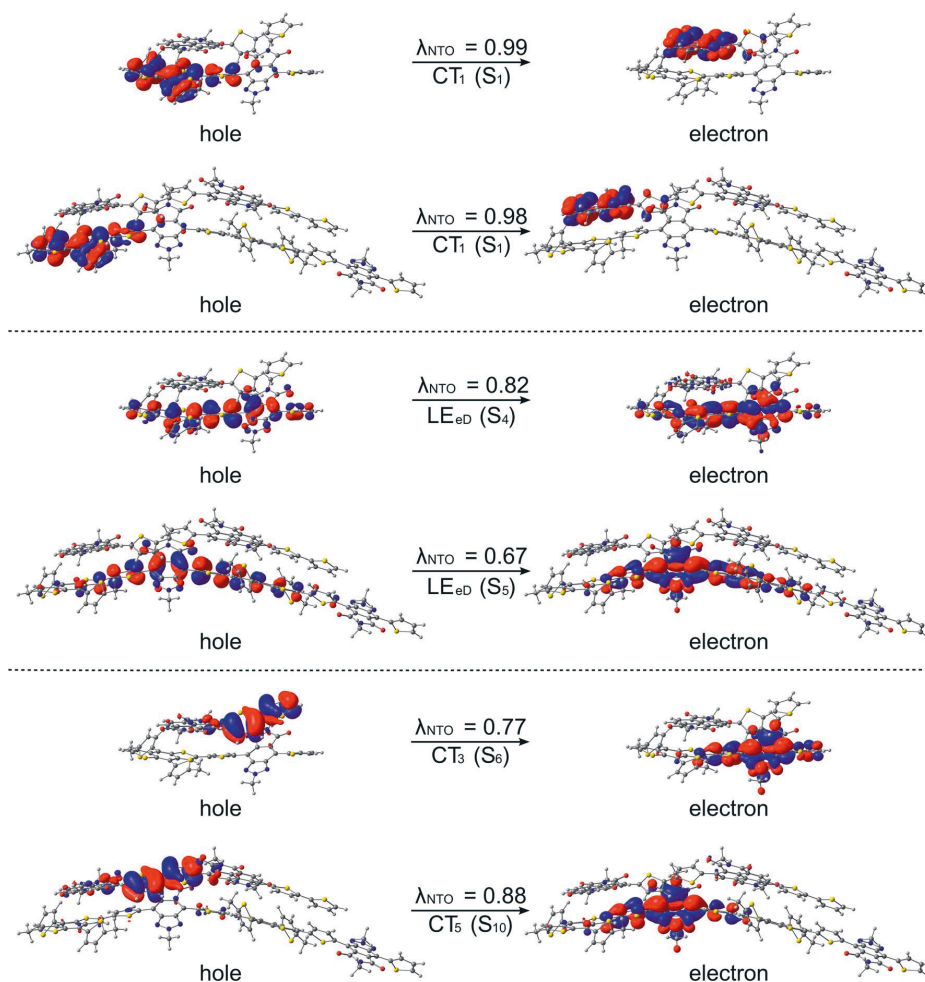
Fig. 8 NTOs (the dominant pairs) for the CT and LE states of the **BDT-TzBI–NDI2OD-T2** complexes (the DA(2) configurations) calculated with TDDFT at the OT-ωB97X-D/6-31G** level of theory in blend. The complexes have been constructed using either the monomer or dimer models of both **PBDT-TzBI** and **P(NDI2OD-T2)**. Additionally, the λ_{NTO} values are also presented.

will most likely set steric hindrances in some configurations and prevent the compounds getting as close as in the monomer-based complexes studied here. Additionally, the single CRU models (monomers) do not take the effects that the additional CRUs might have on the preferred relative positioning in the copolymer backbone into account. Thus, we optimized the geometry of **BDT-TzBI–NDI2OD-T2** also by using the dimers of **PBDT-TzBI** and **P(NDI2OD-T2)** for the DA(2) configuration, for comparison (see Table S8† and Fig. 8). The relative positions of **BDT-TzBI** and **NDI2OD-T2** in the dimer configuration are rather similar as in the monomer configuration, indicating that the sizes of the D–A oligomers do not seem to have a significant effect at least not for this system. More importantly, the predicted CT characteristics in complexes are very similar for both

the monomer and dimer models (see 'Charge transfer characteristics in the local interfacial eD–eA complexes' below). Unfortunately, the geometry optimization of the DA(2) dimer configuration was computationally so demanding that we were unable to verify the effect of size for the other systems. Thus, even though our truncated models may introduce some inaccuracies to the results, our models can give some insight into the relative placements of the studied eD and eA compounds and the CT characteristics at their local interfaces.

Charge transfer characteristics in the local interfacial eD–eA complexes

Next, the nature of the excited states relevant to the ED and CR processes of the eD–eA complexes will be examined. The most

stable configurations of the interfacial eD–eA complexes will be investigated in the case of the polymer–SMA systems. For the polymer–polymer **BDT-TzBI–NDI2OD-T2** system, the DA(2) configuration will be discussed instead due to its larger electronic couplings and CT rates compared to the most stable AA(1) configuration (see "Calculating the CT rates for the local interfacial eD–eA complexes" below). In the DA(2) configuration of **BDT-TzBI–NDI2OD-T2**, the S_1 state is the CT_1 state, where the hole NTO is delocalized on the BDT donor and thiophene units of **BDT-TzBI** and the electron NTO is localized on the NDI acceptor unit of **NDI2OD-T2** (Fig. 8). In other words, the charge transfers from the electron-rich units of **BDT-TzBI** to the electron-deficient unit of **NDI2OD-T2**. The LE state, which is the local excitation of the eD compound, **BDT-TzBI**, is predicted to be higher in energy (*i.e.* the S_4 state here) than the CT_1 state. An opposite ordering of the LE and CT_1 states is sometimes detected for the copolymer–PC$_{71}$BM complexes with both the non-tuned LRC and OT LRC functionals.[65,66] Interestingly, in the third lowest CT state, *i.e.* CT_3, CT is observed from the eA compound **NDI2OD-T2** to the eD compound **BDT-TzBI**. Namely, the charge transfers from the thiophene donor units of **NDI2OD-T2** to several units of **BDT-TzBI**, the largest amount of the electron NTO being on the TzBI acceptor unit. This kind of a CT could originate from the hole transfer from the eA compound to eD, also referred to as the "Channel II" CT process, which may participate in the regular electron transfer process from the eD compound to eA in charge generation of APSCs.[37,122]

As mentioned above (see "Local interfacial eD–eA configurations"), the use of longer oligomers for constructing the complexes would have been more ideal instead of the truncated monomer models. However, when comparing the NTOs of the monomer and dimer models of the DA(2) configuration of **BDT-TzBI–NDI2OD-T2**, it can be observed that the nature of the CT processes is rather similar in both models (Fig. 8). Moreover, the ordering of the states is the same, namely the CT_1 state is below both the LE state and the CT state (CT_5 for the dimer model, CT_3 for the monomer model), where the CT occurs from the eA compound to the eD compound. For both the monomer and dimer configurations, the hole and electron NTOs of the CT states are localized in the equally large regions regardless the

sizes of the eD and eA models. The LE state, while having the same shape in both the monomer and dimer configurations, is not distributed only on a single CRU but on the both CRUs in the dimer configuration. To conclude, as both the monomer and dimer models have very similar charge distributions, the smaller monomer models can be expected to provide sufficiently good description of the nature of the states for this NF PSC system.

The relative positioning of **BDT-TzBI** and **NDI2OD-T2** has some effect on the nature of the states, although the overall shapes of the NTOs are rather similar. Namely, in the AA(1) configuration (Fig. S7†), the hole NTO of CT_1 and the electron NTO of CT_3 are more delocalized along the whole backbone of **BDT-TzBI** compared to the DA(2) configuration (Fig. 8). Moreover, a small amount of a local excitation of the eA compound **NDI2OD-T2** is mixed with the CT_1 state in the AA(1) configuration. We have observed the similar mixing of the local and CT states also for different copolymer–PC$_{71}$BM complexes in our previous theoretical studies.[65,66] This is due to the tendency of the LRC functionals to predict the mixed states for these kinds of photoactive systems. The absence of the local excitations in the CT state of the DA(2) configuration might explain its faster ED and CR rates compared to the AA(1) configuration (see Table 3 and Fig. 11). However, previous experimental[123] and theoretical[51,123] studies have also speculated that the delocalized CT states at the eD–eA interfaces of organic solar cells could be beneficial for decreasing the Coulomb binding energy as a result of reduced electrostatic attraction between the hole and electron.

The studied polymer–SMA systems exhibit the same ordering of the states as the polymer–polymer system **BDT-TzBI–NDI2OD-T2**, *i.e.* the CT_1 (S_2) is at a lower energy than the LE state (S_7 for **DTB-EF-T–ITIC-4F** and S_4 for **BDB-T-2F–ITIC-2Cl**, Fig. 9 and 10). In both **DTB-EF-T–ITIC-4F** and **BDB-T-2F–ITIC-2Cl**, the natures of the CT_1 states are quite similar and CT occurs from the eD compound, *i.e.* **DTB-EF-T** and **BDB-T-2F**, to the end-group of the ITIC-based eA compound, *i.e.* **ITIC-4F** and **ITIC-2Cl**, respectively. In the both polymer–SMA systems, the hole NTO of the CT_1 state is distributed over several backbone units of the eD compounds, although in **DTB-EF-T**, the charge density is more localized on the donor unit, whereas in **BDB-T-**

Table 3 Charge transfer rate parameters^a for the ED and CR processes for the selected configurations of the eD–eA complexes^b calculated at the OT-ωB97X-D/6-31G** level of theory in blend

Complex	Configuration	$H_{\mathrm{if,ED}}$ (meV)	$H_{\mathrm{if,CR}}$ (meV)	$\lambda_{\mathrm{i,ED}}$ (eV)	$\lambda_{\mathrm{i,CR}}$ (eV)	$\Delta G^{\circ}_{\mathrm{ED}}$ (eV)	$\Delta G^{\circ}_{\mathrm{CR}}$ (eV)	k_{ED}^c (s^{-1})	k_{CR}^c (s^{-1})
BDT-TzBI–NDI2OD-T2	DA(2)	37.54	72.74	0.43	0.30	−0.81	−1.70	1.92×10^{13}	9.78×10^9
	AA(1)	16.55	47.76	0.43	0.32	−0.68	−1.81	2.12×10^{12}	1.13×10^9
DTB-EF-T–ITIC-4F	DA	110.91	99.80	0.22	0.30	−0.56	−2.03	1.52×10^{14}	5.83×10^6
	AA	0.35	24.38	0.23	0.32	−0.59	−2.01	1.65×10^9	1.70×10^6
BDB-T-2F–ITIC-2Cl	DA	6.87	70.37	0.28	0.24	−0.36	−2.00	1.77×10^{12}	3.18×10^5
	AA	33.82	131.83	0.32	0.30	−0.50	−1.83	5.05×10^{12}	1.72×10^9

^{a} Electronic couplings (H_{if}) calculated with the multi-state (11 states) FCD scheme (eqn (S22)–(S24)), inner (intermolecular) reorganization energies (λ_{i}, eqn (S10)–(S15)), Gibbs free energies (ΔG°, eqn (S16)–(S19)), and CT rates (k, eqn (1)). The Coulomb energies (eqn (S17) and (S19)) are presented in Table S15. ^{b} See Table S16 for the parameters and rates for the other configurations of **BDT-TzBI–NDI2OD-T2**. ^{c} The rates presented in this table were calculated using the external reorganization energy of 0.53 eV, chosen from the range of the possible values shown in Fig. 11.
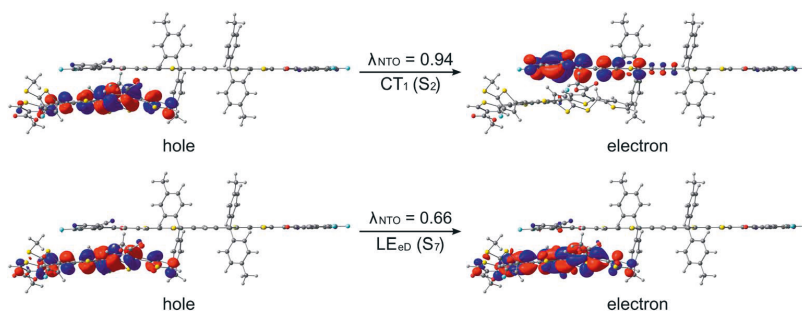
Fig. 9 NTOs (the dominant pairs) for the CT_1 and LE states of the **DTB-EF-T–ITIC-4F** complex (the DA configuration) calculated with TDDFT at the OT-ωB97X-D/6-31G** level of theory in blend. Additionally, the λ_{NTO} values are also presented.

Fig. 10 NTOs (the dominant pairs) for the CT_1 and LE states of the **BDB-T-2F–ITIC-2Cl** complex (the AA configuration) calculated with TDDFT at the OT-ωB97X-D/6-31G** level of theory in blend. Additionally, the λ_{NTO} values are also presented.
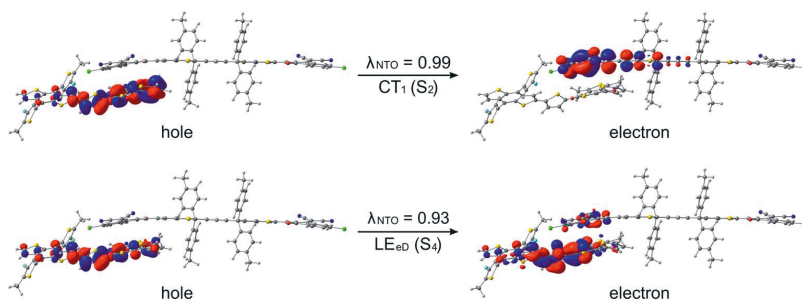
2F, it mainly localizes on the acceptor unit. Here, no CT from the eA **ITIC** compounds to the eD monomers were observed for the polymer–SMA systems, although there have been experimental evidence for the "Channel II" process also in several polymer–SMA systems.[124] However, only the 10 lowest excited singlet states have been considered here, so it is possible that this type of a "Channel II" CT could be observed at higher-energy states.

Calculating the CT rates for the local interfacial eD–eA complexes

Finally, we have calculated the CT rate parameters and rates for the ED and CR processes (Tables 3 and S12–S16). First, we will consider the electronic couplings, which, as expected, are highly sensitive to the relative positions of the eD and eA compounds.[66,125–128] Overall, the largest couplings are predicted mainly for the most stable polymer–SMA systems, *i.e.* the DA and AA configurations of **DTB-EF-T–ITIC-4F** and **BDB-T-2F–ITIC-2Cl**, respectively (see Tables 3, S12, and S13†). In the **BDT-TzBI–NDI2OD-T2** polymer–polymer system, the second most stable DA(2) configuration has somewhat stronger couplings than the most stable AA(1) configuration; the energy difference between the configurations is 0.9 kJ mol^{-1}. The CR couplings are predicted to be larger than the ED couplings in all the other

systems, except in the DA configuration of **DTB-EF-T–ITIC-4F**. We observed larger CR couplings compared to ED couplings also previously in our study of the copolymer–fullerene system.[66]

Next, we will discuss the effect of the dispersion corrected OT-LRC functional on calculating the electronic couplings for different NF PSC systems with the two- and multi-state FCD schemes in complement to our previous study[66] of the multi-state electronic couplings of polymer–fullerene PSC system. In that case, both the non-tuned CAM-B3LYP and OT-BNL LRC functionals predicted oscillating coupling values especially for the CR couplings of the TQ–PC$_{71}$BM complexes with the increasing number of the states.[66] On the contrary, both the ED and CR couplings predicted here for the polymer–polymer **BDT-TzBI–NDI2OD-T2** are relatively constant with different number of states (2–26, Table S12†). Similar trends, *i.e.* consistent two- and multi (11)-state electronic couplings, are also predicted for the polymer–SMA systems (Table S13†), although in their case the effect of the larger number of states could not be confirmed due to the convergence problems in computations. Here, we have only carried out the calculations with the dispersion corrections and with tuning the default value of ω (*i.e.* using the optimally tuned OT-ωB97X-D functional) so we cannot determine, whether the constant couplings result from the

dispersion corrections or from the tuning of the ω. Moreover, the studied system may affect the couplings, as well. However, as the dispersion corrections are important for the correct description of the local interfacial eD–eA complexes,[65,68,69] their inclusion can be expected to be beneficial also for calculating electronic couplings in these PSC systems. Thus, while final conclusions cannot be drawn merely from these results, they are still encouraging in a sense that dispersion corrections seem to stabilize the coupling values when employed with the OT-LRC functionals.

The second important CT rate parameter is the inner (intermolecular) reorganization energy, λ_i, which describes the structural changes in the geometries of the eD and eA compounds upon CT.[126] For the efficient ED process and fast ED rates, the reorganization energy of the system should be minimized. In most cases, the λ_i (and consequently the total λ, $i.e.$ $\lambda_i + \lambda_s$) values are larger for the ED process than for the CR process (Table 3) indicating that the faster ED rates with respect to the CR rates are due to the other CT parameters (see below). The λ_i values predicted for **BDB-T-2F–ITIC-2Cl** agree with those ($\lambda_{i,ED}$ of $ca.$ 0.20 eV and $\lambda_{i,CR}$ of $ca.$ 0.25–0.29 eV) calculated previously for the similar system of **BDB-T-2F** and methoxy-substituted **ITIC** (**ITIC-OM**) by Wang and Brédas.[49] A closer look at the contributions of the eD and eA compounds to the inner reorganization energies reveals the differences in their geometrical changes during the ED and CR processes (Table S14†). The eD trimers **BDT-TzBI** and **BDB-T-2F** are predicted to undergo larger geometric changes upon ED ($i.e.$ eD* → eD$^+$) than CR ($i.e.$ eD$^+$ → eD), whereas the geometrical changes in **DTB-EF-T** are larger during CR than ED. In other words, for **BDT-TzBI** and **BDB-T-2F**, the geometries of the S_1 state and cation differ more than those of the cation and neutral species. The contribution of the eA compound is the same for both ED and CR, $i.e.$ when going from the GS geometry to that of the radical anion (eA → eA$^-$) and $vice$ $versa$ (eA$^-$ → eA). Overall, the $\lambda_{i,CR}$ values for the studied NF PSC systems are close to each other, whereas the $\lambda_{i,ED}$ values increase somewhat in the order of **DTB-EF-T–ITIC-4F** < **BDB-T-2F–ITIC-2Cl** < **BDT-TzBI–NDI2OD-T2**. This ordering indicates smaller geometrical relaxation upon ED for the polymer–SMA systems compared to the polymer–polymer system, which may be one factor explaining the higher efficiencies predicted for these SMA containing NF PSCs.[27,29,129]

Next, we will consider the third CT parameter, $i.e.$ the Gibbs free energy for the CT reaction that is the energy difference ($i.e.$ driving force) between the LE and CT$_1$ states for the ED process and between the CT$_1$ state and GS for the CR process. For the efficient ED process, the ΔG°_{ED} value should be maximized. Based on the negative values of ΔG°, both the ED and CR processes are predicted to be spontaneous in all the complexes (Table 3). The $|\Delta G^\circ_{ED}|$ values of **BDB-T-2F–ITIC-2Cl** are consistent with those (0.11–0.45 eV) predicted previously for the similar **BDB-T-2F–ITIC-OM** systems at the OT-ωB97XD/6-31G* level of theory.[49] The value of the external reorganization energy defines (the range of 0.10–0.75 eV has been considered here for λ_s, see ESI† for the justification), whether the ED processes of the studied systems take place in the Marcus normal region ($|\Delta G^\circ_{ED}| < \lambda_{ED}$, where $\lambda_{ED} = \lambda_{i,ED} + \lambda_s$). The CR processes of all

the systems are predicted to occur deep in the Marcus inverted region ($|\Delta G^\circ_{CR}| \gg \lambda_{CR}$, where $\lambda_{CR} = \lambda_{i,CR} + \lambda_s$), which will have consequences on the predicted CR rates (see below). The $|\Delta G^\circ_{ED}|$ values of the polymer–SMA systems are smaller than those of the polymer–polymer system **BDT-TzBI–NDI2OD-T2**, but because their $\lambda_{i,ED}$ values are also smaller and the electronic couplings larger (for the most stable configurations) their ED rates are relatively similar with the polymer–polymer **BDT-TzBI–NDI2OD-T2** system (see above). The larger $|\Delta G^\circ_{CR}|$ of the polymer–SMA systems, in turn, will lead to the slower CR rates with respect to **BDT-TzBI–NDI2OD-T2** (see below).

After examining the individual CT parameters, the rates for the ED and CR processes of the studied NF PSC systems are presented as a function of λ_s (0.10–0.75 eV) in Fig. 11 and S8.† For all the systems, the ED rates are larger than the CR rates (10^{12} to 10^{14} s^{-1} and below 10^{12} s^{-1}, respectively). Even though no irrevocable conclusions regarding the relative efficiencies of the studied NF PSC systems can be drawn based on their ED rates, which depend highly on the relative orientations of the eD and eA compounds (see below), we can conclude the following. The CR rates of the polymer–SMA systems are predicted to be slower compared to those of the polymer–polymer system, which could be one factor defining the higher efficiencies of the polymer–SMA systems **PDTB-EF-T–ITIC-4F** and **PBDB-T-2F–ITIC-2Cl** compared to those of the polymer–polymer system **PBDT-TzBI–P(NDI2OD-T2)**. The calculated ED rates are consistent with those ($\sim 10^8$ to 10^{12} s^{-1}) predicted for the systems consisting of **BDB-T-2F** and different derivatives of **ITIC** by using the Marcus theory.[47–49] Similarly, the CR rates calculated here are mostly in line with those (10^2–10^{10} s^{-1}) predicted for the complexes of **BDB-T-2F** and **ITIC** derivatives.[47–49] However, vanishingly small CR rates are observed here with the smaller values of λ_s, which could be due to that the CR processes of all the systems occur deep into the Marcus inverted region ($|\Delta G^\circ_{CR}| \gg \lambda_{CR}$).[130] As the Marcus theory may predict underestimated rates in such a case,[49,131] another, $e.g.$ the Marcus–Levich–Jortner rate model[132] could be more suitable for calculating the CR rates in these PSC systems.

The relative orientations of the eD and eA compounds (see Tables S8–S10† for the optimized configurations) have a significant influence on the calculated rates, and the different configurations of the same system can have completely different rates. As an example, the DA configuration of the copolymer–SMA system **DTB-EF-T–ITIC-4F**, where the electron-withdrawing end-group of **ITIC-4F** is on the top of the BDT donor unit of **DTB-EF-T**, is predicted to have the fastest ED rate among the studied PSC systems. However, **DTB-EF-T–ITIC-4F** has the slowest ED rate among the studied systems, when the end-group of **ITIC-4F** is on the top of the acceptor unit of **DTB-EF-T** ($i.e.$ ester-substituted thiophene; the AA configuration). As other CT parameters of these two configurations are relatively similar (Table 3), the smaller ED rates of the AA configuration can be attributed to its significantly smaller electronic couplings compared to those of the DA configuration.

For the polymer–SMA systems, the energetically more stable configurations have faster ED and CR rates following the same trends as their electronic couplings. However, for the polymer–
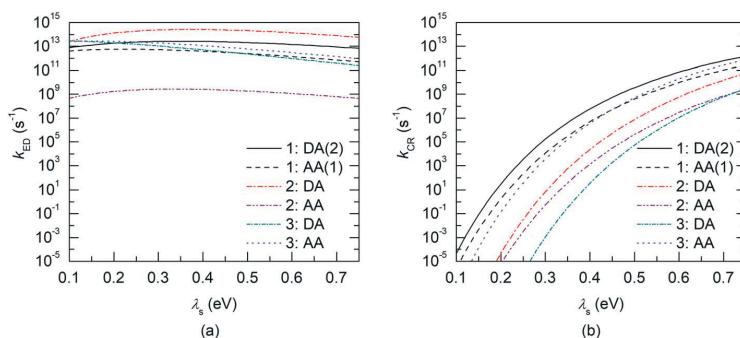
Fig. 11 Evolutions of the charge transfer rates (k_{ED} and k_{CR}) as functions of λ_s (0.1–0.75 eV) for the (a) ED and (b) CR processes of the **BDT–TzBI–NDI2OD-T2** (1), **DTB-EF-T–ITIC-4F** (2), and **BDB-T-2F–ITIC-2Cl** (3) complexes calculated at the OT-ωB97X–D/6-31G** level of theory in blend.

polymer **BDT-TzBI–NDI2OD-T2** system, the most stable configuration, *i.e.* the AA(1) configuration, has generally the slowest ED and CR rates among the studied complex configurations of **BDT-TzBI–NDI2OD-T2** (Fig. S8†) due to its smaller $|\Delta G_{ED}^{\circ}|$ value and moderate ED electronic couplings. Moreover, based on the larger $|\Delta G_{CR}^{\circ}|$ value of the AA(1) configuration with respect to the other configurations of **BDT-TzBI–NDI2OD-T2**, the CR process leading to AA(1) takes place deeper in the Marcus inverted region leading to the slower CR rates. While we have not included the full-length side groups, which also impact the interfacial orientations and stacking distances of the compounds, our findings complement the experimental findings for the importance of the optimal molecular orientation at the eD–eA interfaces.[37]

Conclusions

In this work, the structural, optoelectronic, and CT characteristics of several eD and eA compounds and their local interfacial eD–eA complexes have been examined with the DFT and TDDFT methods. The chosen compounds are based on some of the most efficient NF PSC systems to date, including both the APSC system and those containing eD copolymers and NF SMAs. We have extended our previous study of multi-state electronic couplings by comparing the two- and multi-state couplings for the ED and CR processes of these systems and exploring the effects of both the tuning of a LRC functional and the inclusion of the dispersion corrections on the electronic coupling values. Finally, the CT rates for the ED and CR processes in the studied NF PSC systems have been calculated using the semi-classical Marcus theory.

The results indicate that the studied eD copolymers **PBDT-TzBI**, **PDTB-EF-T**, and **PBDB-T-2F** have some similar features, such as similar torsions in their backbones and UV-vis absorption profiles. However, the conformational preferences and varying backbone curvatures of these eD copolymers may lead to significant differences in their packing behavior in the blend environment. Moreover, a closer look at the structural deformations caused by ionization and excitation reveal subtle differences in the regions of their backbones, which are affected

most by these processes. While all the studied eD copolymer models show a partial intramolecular CT character, the amount of transferred charge density is smaller in **DTB-EF-T** than in **BDT-TzBI** and **BDB-T-2F**. In general, both the twisted backbone structures, which originate from the additional degrees of freedom caused by the thiophene spacers between the donor and acceptor units of the modelled eD copolymers, and the predicted intramolecular CT characteristics are concluded to be beneficial for the performance of the PSCs.

Based on our computational studies of the CT characteristics in various possible face-to-face orientations between the eD and eA compounds in the eD–eA complexes of the NF PSC systems, the following conclusions were reached. In addition to the conventional CT from the eD compound to the eA compound, which is prominent in all NF PSC systems, the CT process is also observed from the eA compound **NDI2OD-T2** to the eD compound, which indicates that **NDI2OD-T2** could contribute to the charge generation in the studied polymer–polymer system. In the polymer–SMA systems, the energetically most favorable configurations have the strongest electronic couplings and the fastest CT rates. However, the positioning of the eA with respect to the eD is predicted to be different in **DTB-EF-T–ITIC-4F** and **BDB-T-2F–ITIC-2Cl**. In the case of the polymer–polymer system, the most stable configuration leads to smaller electronic couplings and slower CT rates compared to the second most stable configuration. Our results agree with the reports in the literature that the electronic couplings are highly dependent on the relative positioning of the eD and eA compounds which should be carefully controlled to ensure the fast ED rates, but slow CR rates.

The present FCD electronic coupling calculations complement our previous results on the effects of the two-*versus* multi-state treatment on the PSC systems. In this work we observed, that the multi-state FCD electronic couplings seem to be stabilized by including the dispersion corrections in the OT-LRC functional, *i.e.* relatively constant ED and CR couplings are predicted with both the two- and multi-state treatments. While more work would be required to confirm the effect of dispersion corrections on the electronic couplings in other NF

PSC systems, these findings complement our and other's previous statements for the importance of the combined effect of the dispersion corrections and tuned LRC functional when describing the local interfacial characteristics of PSC systems.

The polymer–SMA systems are predicted to have smaller inner reorganization energies for the ED process, which could be one factor explaining their higher efficiencies with respect to the polymer–polymer system. However, the Gibbs free energies for ED are smaller for the polymer–SMA systems than for the polymer–polymer system, which could explain, why no clear trends in ED rates are observed between the studied NF PSC systems. Nevertheless, the calculated ED rates are faster than the CR rates in all systems, which is desirable for working devices. In addition, the CR rates in the polymer–SMA systems are generally slower than in the polymer–polymer system, which could contribute to the higher power conversion efficiencies in the SMA containing systems. The magnitudes of the ED rates are rather constant regardless of the external reorganization energy, which affects the CR rates more pronouncedly. The vanishingly small CR rates associated with the smaller external reorganization energies indicate that comparing the applicability of an alternative CT rate model, *e.g.* the Marcus–Levich–Jortner, could be beneficial, when calculating the CR rates for these types of NF PSC systems.

This work provides more insight into the interplay between the structural, optoelectronic, and CT characteristics of the NF PSC compounds with high PCEs demonstrated in devices. Furthermore, important information about the structural and CT characteristics in both the APC and polymer-SMA type NF PSC systems has been revealed. Overall, the dispersion corrected OT-LRC functional is concluded to be a suitable choice for modeling of the NF PSC systems, especially for calculating the FCD electronic couplings. The findings of this work are beneficial for understanding the working principles of the studied systems and can help in designing and developing more efficient NF PSCs.

Conflicts of interest

The authors declare no competing financial interest.

Acknowledgements

References

1 Z. He, C. Zhong, S. Su, M. Xu, H. Wu and Y. Cao, *Nat. Photonics*, 2012, **6**, 591–595.

2 G. Li, R. Zhu and Y. Yang, *Nat. Photonics*, 2012, **6**, 153–161.

3 J. Zhao, Y. Li, G. Yang, K. Jiang, H. Lin, H. Ade, W. Ma and H. Yan, *Nat. Energy*, 2016, **1**, 15027.

4 Y. Jin, Z. Chen, M. Xiao, J. Peng, B. Fan, L. Ying, G. Zhang, X.-F. Jiang, Q. Yin, Z. Liang, F. Huang and Y. Cao, *Adv. Energy Mater.*, 2017, **7**, 1700944.

5 H. Kang, W. Lee, J. Oh, T. Kim, C. Lee and B. J. Kim, *Acc. Chem. Res.*, 2016, **49**, 2424–2434.

6 S. Chen, Y. An, G. K. Dutta, Y. Kim, Z.-G. Zhang, Y. Li and C. Yang, *Adv. Funct. Mater.*, 2017, **27**, 1603564.

7 F. Shen, J. Xu, X. Li and C. Zhan, *J. Mater. Chem. A*, 2018, **6**, 15433–15455.

8 Z.-H. Zhou, T. Maruyama, T. Kanbara, T. Ikeda, K. Ichimura, T. Yamamoto and K. Tokuda, *J. Chem. Soc., Chem. Commun.*, 1991, 1210–1212.

9 E. E. Havinga, W. ten Hoeve and H. Wynberg, *Polym. Bull.*, 1992, **29**, 119–126.

10 H. Zhou, L. Yang and W. You, *Macromolecules*, 2012, **45**, 607–632.

11 F. Würthner and M. Stolte, *Chem. Commun.*, 2011, **47**, 5109–5115.

12 G. Wang, F. S. Melkonyan, A. Facchetti and T. J. Marks, *Angew. Chem., Int. Ed.*, 2019, **58**, 4129–4142.

13 Z. Li, L. Ying, P. Zhu, W. Zhong, N. Li, F. Liu, F. Huang and Y. Cao, *Energy Environ. Sci.*, 2019, **12**, 157–163.

14 L. Zhu, W. Zhong, C. Qiu, B. Lyu, Z. Zhou, M. Zhang, J. Song, J. Xu, J. Wang, J. Ali, W. Feng, Z. Shi, X. Gu, L. Ying, Y. Zhang and F. Liu, *Adv. Mater.*, 2019, **31**, 1902899.

15 X. Guo and M. D. Watson, *Org. Lett.*, 2008, **10**, 5333–5336.

16 T. Jia, J. Zhang, W. Zhong, Y. Liang, K. Zhang, S. Dong, L. Ying, F. Liu, X. Wang, F. Huang and Y. Cao, *Nano Energy*, 2020, **72**, 104718.

17 Y. Lin, J. Wang, Z.-G. Zhang, H. Bai, Y. Li, D. Zhu and X. Zhan, *Adv. Mater.*, 2015, **27**, 1170–1174.

18 G. Zhang, J. Zhao, P. C. Y. Chow, K. Jiang, J. Zhang, Z. Zhu, J. Zhang, F. Huang and H. Yan, *Chem. Rev.*, 2018, **118**, 3447–3507.

19 J. Hou, O. Inganäs, R. H. Friend and F. Gao, *Nat. Mater.*, 2018, **17**, 119–128.

20 H. Sun, F. Chen and Z. K. Chen, *Mater. Today*, 2019, **24**, 94–118.

21 Z. Zheng, Q. Hu, S. Zhang, D. Zhang, J. Wang, S. Xie, R. Wang, Y. Qin, W. Li, L. Hong, N. Liang, F. Liu, Y. Zhang, Z. Wei, Z. Tang, T. P. Russell, J. Hou and H. Zhou, *Adv. Mater.*, 2018, **30**, 1801801.

22 Y. Cui, H. Yao, L. Hong, T. Zhang, Y. Xu, K. Xian, B. Gao, J. Qin, J. Zhang, Z. Wei and J. Hou, *Adv. Mater.*, 2019, **31**, 1808356.

23 H. Yao, Y. Cui, D. Qian, C. S. Ponseca, A. Honarfar, Y. Xu, J. Xin, Z. Chen, L. Hong, B. Gao, R. Yu, Y. Zu, W. Ma, P. Chabera, T. Pullerits, A. Yartsev, F. Gao and J. Hou, *J. Am. Chem. Soc.*, 2019, **141**, 7743–7750.

24 Q. Liu, Y. Jiang, K. Jin, J. Qin, J. Xu, W. Li, J. Xiong, J. Liu, Z. Xiao, K. Sun, S. Yang, X. Zhang and L. Ding, *Sci. Bull.*, 2020, **65**, 272–275.

25 J. Yuan, Y. Zhang, L. Zhou, G. Zhang, H. L. Yip, T. K. Lau, X. Lu, C. Zhu, H. Peng, P. A. Johnson, M. Leclerc, Y. Cao, J. Ulanski, Y. Li and Y. Zou, *Joule*, 2019, **3**, 1140–1151.

26 P. Cheng, G. Li, X. Zhan and Y. Yang, *Nat. Photonics*, 2018, **12**, 131–142.

27 B. Fan, L. Ying, Z. Wang, B. He, X. F. Jiang, F. Huang and Y. Cao, *Energy Environ. Sci.*, 2017, **10**, 1243–1251.

28 L. Lan, Z. Chen, Q. Hu, L. Ying, R. Zhu, F. Liu, T. P. Russell, F. Huang and Y. Cao, *Adv. Sci.*, 2016, **3**, 1600032.

29 S. Li, L. Ye, W. Zhao, H. Yan, B. Yang, D. Liu, W. Li, H. Ade and J. Hou, *J. Am. Chem. Soc.*, 2018, **140**, 7159–7167.

30 L. Zhan, S. Li, S. Zhang, X. Chen, T. K. Lau, X. Lu, M. Shi, C. Z. Li and H. Chen, *ACS Appl. Mater. Interfaces*, 2018, **10**, 42444–42452.

31 M. Zhang, X. Guo, W. Ma, H. Ade and J. Hou, *Adv. Mater.*, 2015, **27**, 4655–4660.

32 Poly[(4,8-bis[5-(2-ethylhexyl)-4-fluoro-2-thienyl)benzo[1,2-*b*:4,5-*b'*]dithiophene-2,6-diyl]-2,5-thiophenediyl(5,7-bis(2-ethylhexyl)-4,8-dioxo-4*H*,8*H*-benzo[1,2-*c*:4,5-*c'*]dithiophene-1,3-diyl)-2,5-thiophenediyl], **PBDB-T-2F** at Sigma-Aldrich, available at: https://www.sigmaaldrich.com/catalog/product/aldrich/906336?lang=fi&region=FI, accessed 20/05/2020.

33 H. Zhang, H. Yao, J. Hou, J. Zhu, J. Zhang, W. Li, R. Yu, B. Gao, S. Zhang and J. Hou, *Adv. Mater.*, 2018, **30**, 1800613.

34 Y. Ie, J. Huang, Y. Uetani, M. Karakawa and Y. Aso, *Macromolecules*, 2012, **45**, 4564–4571.

35 D. Qian, L. Ye, M. Zhang, Y. Liang, L. Li, Y. Huang, X. Guo, S. Zhang, Z. Tan and J. Hou, *Macromolecules*, 2012, **45**, 9611–9617.

36 D. Gedefaw, M. Tessarolo, W. Zhuang, R. Kroon, E. Wang, M. Bolognesi, M. Seri, M. Muccini and M. R. Andersson, *Polym. Chem.*, 2014, **5**, 2083–2093.

37 C. Lee, S. Lee, G.-U. Kim, W. Lee and B. J. Kim, *Chem. Rev.*, 2019, **119**, 8028–8086.

38 Q. Zhang, M. A. Kelly, N. Bauer and W. You, *Acc. Chem. Res.*, 2017, **50**, 2401–2409.

39 L. Benatto and M. Koehler, *J. Phys. Chem. C*, 2019, **123**, 6395–6406.

40 L. Benatto, C. F. N. Marchiori, C. Moyses Araujo and M. Koehler, *J. Mater. Chem. C*, 2019, **7**, 12180–12193.

41 Q. Wang, Y. Li, P. Song, R. Su, F. Ma, Y. Yang, Q. Wang, Y. Li, P. Song, R. Su, F. Ma and Y. Yang, *Polymers*, 2017, **9**, 692.

42 Y. Cui, H. Yao, J. Zhang, T. Zhang, Y. Wang, L. Hong, K. Xian, B. Xu, S. Zhang, J. Peng, Z. Wei, F. Gao and J. Hou, *Nat. Commun.*, 2019, **10**, 1–8.

43 L. Benatto and M. Koehler, *J. Phys. Chem. C*, 2019, **123**, 6395–6406.

44 G. Han, Y. Guo, X. Ma and Y. Yi, *Sol. RRL*, 2018, **2**, 1800190.

45 G. Han and Y. Yi, *Adv. Theory Simul.*, 2018, **1**, 1800091.

46 J. Lee, E. M. Go, S. Dharmapurikar, J. Xu, S. M. Lee, M. Jeong, K. C. Lee, J. Oh, Y. Cho, C. Zhang, M. Xiao, S. K. Kwak and C. Yang, *J. Mater. Chem. A*, 2019, **7**, 18468–18479.

47 Q.-Q. Pan, S.-B. Li, Y.-C. Duan, Y. Wu, J. Zhang, Y. Geng, L. Zhao and Z.-M. Su, *Phys. Chem. Chem. Phys.*, 2017, **19**, 31227–31235.

48 Q.-Q. Pan, S.-B. Li, Y. Wu, Y. Geng, M. Zhang and Z.-M. Su, *Org. Electron.*, 2018, **53**, 308–314.

49 T. Wang and J.-L. Brédas, *Matter*, 2020, **2**, 119–135.

50 G. Han, Y. Guo, X. Song, Y. Wang and Y. Yi, *J. Mater. Chem. C*, 2017, **5**, 4852–4857.

51 J.-L. Brédas, V. Coropceanu, C. Doiron, Y. T. Fu, T. Körzdörfer, L. Pandey, C. Risko, J. Sears, B. Yang, Y. Yi and C. Zhang, Modeling the electronic and optical processes in organic solar cells: density functional theory and beyond, in *Organic Solar Cells: Fundamentals, Devices, and Upscaling*, ed. B. P. Rand and H. Richter, CRC Press, Taylor & Francis Group, LLC, Boca Raton, 2014, pp. 537–588.

52 V. Coropceanu, J. Cornil, D. A. da Silva Filho, Y. Olivier, R. Silbey and J.-L. Brédas, *Chem. Rev.*, 2007, **107**, 926–952.

53 C.-P. Hsu, *Acc. Chem. Res.*, 2009, **42**, 509–518.

54 H. Oberhofer, K. Reuter and J. Blumberger, *Chem. Rev.*, 2017, **117**, 10319–10357.

55 P. Song, Y. Li, F. Ma, T. Pullerits and M. Sun, *Chem. Rec.*, 2016, **16**, 734–753.

56 A. A. Voityuk and N. Rösch, *J. Chem. Phys.*, 2002, **117**, 5607–5616.

57 R. J. Cave and M. D. Newton, *Chem. Phys. Lett.*, 1996, **249**, 15–19.

58 R. J. Cave and M. D. Newton, *J. Chem. Phys.*, 1997, **106**, 9213–9226.

59 Y. Li, T. Pullerits, M. Zhao and M. Sun, *J. Phys. Chem. C*, 2011, **115**, 21865–21873.

60 Y. Li, Y. Feng and M. Sun, *Sci. Rep.*, 2015, **5**, 13970.

61 D. Qian, Z. Zheng, H. Yao, W. Tress, T. R. Hopper, S. Chen, S. Li, J. Liu, S. Chen, J. Zhang, X.-K. Liu, B. Gao, L. Ouyang, Y. Jin, G. Pozina, I. A. Buyanova, W. M. Chen, O. Inganäs, V. Coropceanu, J.-L. Brédas, H. Yan, J. Hou, F. Zhang, A. A. Bakulin and F. Gao, *Nat. Mater.*, 2018, **17**, 703–709.

62 T. Wang, X.-K. Chen, A. Ashokan, Z. Zheng, M. K. Ravva and J.-L. Brédas, *Adv. Funct. Mater.*, 2018, **28**, 1705868.

63 M. Rust, J. Lappe and R. J. Cave, *J. Phys. Chem. A*, 2002, **106**, 3930–3940.

64 C.-H. Yang and C.-P. Hsu, *J. Chem. Phys.*, 2013, **139**, 154104.

65 T. Kastinen, M. Niskanen, C. Risko, O. Cramariuc and T. I. Hukka, *Phys. Chem. Chem. Phys.*, 2016, **18**, 27654–27670.

66 T. Kastinen, D. A. Da Silva Filho, L. Paunonen, M. Linares, L. A. Ribeiro Junior, O. Cramariuc and T. I. Hukka, *Phys. Chem. Chem. Phys.*, 2019, **21**, 25606–25625.

67 T. Kim, J. H. Kim, T. E. Kang, C. Lee, H. Kang, M. Shin, C. Wang, B. Ma, U. Jeong, T. S. Kim and B. J. Kim, *Nat. Commun.*, 2015, **6**, 8547.

68 K. Do, M. K. Ravva, T. Wang and J.-L. Brédas, *Chem. Mater.*, 2017, **29**, 346–354.

69 C.-R. Zhang, J. S. Sears, B. Yang, S. G. Aziz, V. Coropceanu and J.-L. Brédas, *J. Chem. Theory Comput.*, 2014, **10**, 2379–2388.

70 L. Pandey, C. Doiron, J. S. Sears and J.-L. Brédas, *Phys. Chem. Chem. Phys.*, 2012, **14**, 14243–14248.

71 M. Niskanen and T. I. Hukka, *Phys. Chem. Chem. Phys.*, 2014, **16**, 13294–13305.

72 J.-D. Chai and M. Head-Gordon, *Phys. Chem. Chem. Phys.*, 2008, **10**, 6615–6620.

73 J. P. Perdew, K. Burke and M. Ernzerhof, *Phys. Rev. Lett.*, 1996, **77**, 3865–3868.

74 C. Adamo and V. Barone, *J. Chem. Phys.*, 1999, **110**, 6158–6170.

75 J. P. Perdew, K. Burke and M. Ernzerhof, *Phys. Rev. Lett.*, 1997, **78**, 1396.

76 D. Niedzialek, I. Duchemin, T. B. De Queiroz, S. Osella, A. Rao, R. Friend, X. Blase, S. Kümmel and D. Beljonne, *Adv. Funct. Mater.*, 2015, **25**, 1972–1984.

77 M. J. Frisch, G. W. Trucks, H. B. Schlegel, G. E. Scuseria, M. A. Robb, J. R. Cheeseman, G. Scalmani, V. Barone, G. A. Petersson, H. Nakatsuji, X. Li, M. Caricato, A. V. Marenich, J. Bloino, B. G. Janesko, R. Gomperts, B. Mennucci, H. P. Hratchian, J. V. Ortiz, A. F. Izmaylov, J. L. Sonnenberg, D. Williams-Young, F. Ding, F. Lipparini, F. Egidi, J. Goings, B. Peng, A. Petrone, T. Henderson, D. Ranasinghe, V. G. Zakrzewski, J. Gao, N. Rega, G. Zheng, W. Liang, M. Hada, M. Ehara, K. Toyota, R. Fukuda, J. Hasegawa, M. Ishida, T. Nakajima, Y. Honda, O. Kitao, H. Nakai, T. Vreven, K. Throssell, J. A. Montgomery Jr, J. E. Peralta, F. Ogliaro, M. J. Bearpark, J. J. Heyd, E. N. Brothers, K. N. Kudin, V. N. Staroverov, T. A. Keith, R. Kobayashi, J. Normand, K. Raghavachari, A. P. Rendell, J. C. Burant, S. S. Iyengar, J. Tomasi, M. Cossi, J. M. Millam, M. Klene, C. Adamo, R. Cammi, J. W. Ochterski, R. L. Martin, K. Morokuma, O. Farkas, J. B. Foresman and D. J. Fox, *Gaussian 16, Revision B.01*, Gaussian, Inc., Wallingford CT, 2016.

78 Y. Shao, Z. Gan, E. Epifanovsky, A. T. B. Gilbert, M. Wormit, J. Kussmann, A. W. Lange, A. Behn, J. Deng, X. Feng, D. Ghosh, M. Goldey, P. R. Horn, L. D. Jacobson, I. Kaliman, R. Z. Khaliullin, T. Kuś, A. Landau, J. Liu, E. I. Proynov, Y. M. Rhee, R. M. Richard, M. A. Rohrdanz, R. P. Steele, E. J. Sundstrom, H. L. Woodcock III, P. M. Zimmerman, D. Zuev, B. Albrecht, E. Alguire, B. Austin, G. J. O. Beran, Y. A. Bernard, E. Berquist, K. Brandhorst, K. B. Bravaya, S. T. Brown, D. Casanova, C.-M. Chang, Y. Chen, S. H. Chien, K. D. Closser, D. L. Crittenden, M. Diedenhofen, R. A. DiStasio, H. Do, A. D. Dutoi, R. G. Edgar, S. Fatehi, L. Fusti-Molnar, A. Ghysels, A. Golubeva-Zadorozhnaya, J. Gomes, M. W. D. Hanson-Heine, P. H. P. Harbach, A. W. Hauser, E. G. Hohenstein, Z. C. Holden, T.-C. Jagau, H. Ji, B. Kaduk, K. Khistyaev, J. Kim, J. Kim, R. A. King, P. Klunzinger, D. Kosenkov, T. Kowalczyk, C. M. Krauter, K. U. Lao, A. D. Laurent, K. V. Lawler, S. V. Levchenko, C. Y. Lin, F. Liu, E. Livshits, R. C. Lochan, A. Luenser, P. Manohar, S. F. Manzer, S.-P. Mao, N. Mardirossian, A. V. Marenich, S. A. Maurer, N. J. Mayhall, E. Neuscamman, C. M. Oana, R. Olivares-Amaya, D. P. O'Neill, J. A. Parkhill, T. M. Perrine, R. Peverati,

A. Prociuk, D. R. Rehn, E. Rosta, N. J. Russ, S. M. Sharada, S. Sharma, D. W. Small, A. Sodt, T. Stein, D. Stück, Y.-C. Su, A. J. W. Thom, T. Tsuchimochi, V. Vanovschi, L. Vogt, O. Vydrov, T. Wang, M. A. Watson, J. Wenzel, A. White, C. F. Williams, J. Yang, S. Yeganeh, S. R. Yost, Z.-Q. You, I. Y. Zhang, X. Zhang, Y. Zhao, B. R. Brooks, G. K. L. Chan, D. M. Chipman, C. J. Cramer, W. A. Goddard III, M. S. Gordon, W. J. Hehre, A. Klamt, H. F. Schaefer III, M. W. Schmidt, C. D. Sherrill, D. G. Truhlar, A. Warshel, X. Xu, A. Aspuru-Guzik, R. Baer, A. T. Bell, N. A. Besley, J.-D. Chai, A. Dreuw, B. D. Dunietz, T. R. Furlani, S. R. Gwaltney, C.-P. Hsu, Y. Jung, J. Kong, D. S. Lambrecht, W. Liang, C. Ochsenfeld, V. A. Rassolov, L. V. Slipchenko, J. E. Subotnik, T. Van Voorhis, J. M. Herbert, A. I. Krylov, P. M. W. Gill and M. Head-Gordon, *Mol. Phys.*, 2015, **113**, 184–215.

79 L. Kronik, T. Stein, S. Refaely-Abramson and R. Baer, *J. Chem. Theory Comput.*, 2012, **8**, 1515–1531.

80 T. Stein, L. Kronik and R. Baer, *J. Am. Chem. Soc.*, 2009, **131**, 2818–2820.

81 B. Yang, Y. Yi, C.-R. Zhang, S. G. Aziz, V. Coropceanu and J.-L. Brédas, *J. Phys. Chem. C*, 2014, **118**, 27648–27656.

82 V. Barone and M. Cossi, *J. Phys. Chem. A*, 1998, **102**, 1995–2001.

83 M. Cossi, N. Rega, G. Scalmani and V. Barone, *J. Comput. Chem.*, 2003, **24**, 669–681.

84 X.-K. Chen, M. K. Ravva, H. Li, S. M. Ryno and J.-L. Brédas, *Adv. Energy Mater.*, 2016, **6**, 1601325.

85 G. Han and Y. Yi, *J. Phys. Chem. Lett.*, 2019, **10**, 2911–2918.

86 R. L. Martin, *J. Chem. Phys.*, 2003, **118**, 4775–4777.

87 A. Dreuw and M. Head-Gordon, *Chem. Rev.*, 2005, **105**, 4009–4037.

88 P. Ros and G. C. A. Schuit, *Theor. Chim. Acta*, 1966, **4**, 1–12.

89 Multiwfn 3.6, available at: http://sobereva.com/multiwfn/, accessed 05/01/2020.

90 T. Lu and F. Chen, *J. Comput. Chem.*, 2012, **33**, 580–592.

91 T. Lu and F. Chen, *Acta Chim. Sin.*, 2011, **69**, 2393–2406.

92 G. A. Zhurko, Chemcraft - graphical program for visualization of quantum chemistry computations, Ivanovo, Russia, 2005, available at: http://www.chemcraftprog.com, accessed 24/05/2020.

93 R. A. Marcus, *J. Chem. Phys.*, 1956, **24**, 966–978.

94 R. A. Marcus and N. Sutin, *Biochim. Biophys. Acta, Rev. Bioenerg.*, 1985, **811**, 265–322.

95 R. A. Marcus, *Rev. Mod. Phys.*, 1993, **65**, 599–610.

96 M. D. Newton, *Chem. Rev.*, 1991, **91**, 767–792.

97 C. F. Huang, S. L. Wu, Y. F. Huang, Y. C. Chen, S. T. Chang, T. Y. Wu, K. Y. Wu, W. T. Chuang and C. L. Wang, *Chem. Mater.*, 2016, **28**, 5175–5190.

98 A. Wadsworth, M. Moser, A. Marks, M. S. Little, N. Gasparini, C. J. Brabec, D. Baran and I. McCulloch, *Chem. Soc. Rev.*, 2019, **48**, 1596–1625.

99 N. E. Jackson, B. M. Savoie, K. L. Kohlstedt, M. Olvera de la Cruz, G. C. Schatz, L. X. Chen and M. A. Ratner, *J. Am. Chem. Soc.*, 2013, **135**, 10475–10483.

100 T. Kastinen, M. Niskanen, C. Risko, O. Cramariuc and T. I. Hukka, *J. Phys. Chem. A*, 2016, **120**, 1051–1064.

101 I. Osaka, T. Abe, S. Shinamura and K. Takimiya, *J. Am. Chem. Soc.*, 2011, **133**, 6852–6860.

102 E. Giussani, D. Fazzi, L. Brambilla, M. Caironi and C. Castiglioni, *Macromolecules*, 2013, **46**, 2658–2670.

103 D. Fazzi, M. Caironi and C. Castiglioni, *J. Am. Chem. Soc.*, 2011, **133**, 19056–19059.

104 T. Schuettfort, S. Huettner, S. Lilliu, J. E. MacDonald, L. Thomsen and C. R. McNeill, *Macromolecules*, 2011, **44**, 1530–1539.

105 V. Lemaur, L. Muccioli, C. Zannoni, D. Beljonne, R. Lazzaroni, J. Cornil and Y. Olivier, *Macromolecules*, 2013, **46**, 8171–8178.

106 T. J. Aldrich, M. Matta, W. Zhu, S. M. Swick, C. L. Stern, G. C. Schatz, A. Facchetti, F. S. Melkonyan and T. J. Marks, *J. Am. Chem. Soc.*, 2019, **141**, 3274–3287.

107 Z. Zhang, J. Yu, X. Yin, Z. Hu, Y. Jiang, J. Sun, J. Zhou, F. Zhang, T. P. Russell, F. Liu and W. Tang, *Adv. Funct. Mater.*, 2018, **28**, 1705095.

108 C. Van Dyck, T. J. Marks and M. A. Ratner, *ACS Nano*, 2017, **11**, 5970–5981.

109 J. Casado, *Top. Curr. Chem.*, 2017, **375**, 1–40.

110 S. Suramitr, W. Meeto, P. Wolschann and S. Hannongbua, *Theor. Chem. Acc.*, 2010, **125**, 35–44.

111 T. Körzdörfer, R. M. Parrish, J. S. Sears, C. D. Sherrill and J.-L. Brédas, *J. Chem. Phys.*, 2012, **137**, 124305.

112 W. Porzio, G. Scavia, L. Barba, G. Arrighetti and C. R. McNeill, *Eur. Polym. J.*, 2014, **61**, 172–185.

113 Y. Olivier, D. Niedzialek, V. Lemaur, W. Pisula, K. Müllen, U. Koldemir, J. R. Reynolds, R. Lazzaroni, J. Cornil and D. Beljonne, *Adv. Mater.*, 2014, **26**, 2119–2136.

114 N. E. Jackson, K. L. Kohlstedt, B. M. Savoie, M. Olvera de la Cruz, G. C. Schatz, L. X. Chen and M. A. Ratner, *J. Am. Chem. Soc.*, 2015, **137**, 6254–6262.

115 W. Zhao, S. Li, H. Yao, S. Zhang, Y. Zhang, B. Yang and J. Hou, *J. Am. Chem. Soc.*, 2017, **139**, 7148–7151.

116 M. Caironi, M. Bird, D. Fazzi, Z. Chen, R. Di Pietro, C. Newman, A. Facchetti and H. Sirringhaus, *Adv. Funct. Mater.*, 2011, **21**, 3371–3381.

117 E. F. Oliveira and F. C. Lavarda, *Polymer*, 2016, **99**, 105–111.

118 C. Risko, M. D. McGehee and J.-L. Brédas, *Chem. Sci.*, 2011, **2**, 1200–1218.

119 B. Fan, L. Ying, P. Zhu, F. Pan, F. Liu, J. Chen, F. Huang and Y. Cao, *Adv. Mater.*, 2017, **29**, 1703906.

120 A. Yin, D. Zhang, S. H. Cheung, S. K. So, Z. Fu, L. Ying, F. Huang, H. Zhou and Y. Zhang, *J. Mater. Chem. C*, 2018, **6**, 7855–7863.

121 G. Han, Y. Guo, X. Ma and Y. Yi, *Sol. RRL*, 2018, **2**, 1800190.

122 D. M. Stoltzfus, J. E. Donaghey, A. Armin, P. E. Shaw, P. L. Burn and P. Meredith, *Chem. Rev.*, 2016, **116**, 12920–12955.

123 A. A. Bakulin, A. Rao, V. G. Pavelyev, P. H. M. Van Loosdrecht, M. S. Pshenichnikov, D. Niedzialek, J. Cornil, D. Beljonne and R. H. Friend, *Science*, 2012, **335**, 1340–1344.

124 S. Chen, S. M. Lee, J. Xu, J. Lee, K. C. Lee, T. Hou, Y. Yang, M. Jeong, B. Lee, Y. Cho, S. Jung, J. Oh, Z. G. Zhang, C. Zhang, M. Xiao, Y. Li and C. Yang, *Energy Environ. Sci.*, 2018, **11**, 2569–2580.

125 L. Pandey, PhD thesis, Georgia Institute of Technology, 2013.

126 J. L. Brédas, D. Beljonne, V. Coropceanu and J. Cornil, *Chem. Rev.*, 2004, **104**, 4971–5003.

127 X.-K. Chen, M. K. Ravva, H. Li, S. M. Ryno and J.-L. Brédas, *Adv. Energy Mater.*, 2016, **6**, 1601325.

128 Y. Yi, V. Coropceanu and J.-L. Brédas, *J. Mater. Chem.*, 2011, **21**, 1479–1486.

129 W. Li, L. Ye, S. Li, H. Yao, H. Ade and J. Hou, *Adv. Mater.*, 2018, **30**, 1707170.

130 V. Lemaur, M. Steel, D. Beljonne, J.-L. Brédas and J. Cornil, *J. Am. Chem. Soc.*, 2005, **127**, 6077–6086.

131 T. Unger, S. Wedler, F.-J. Kahle, U. Scherf, H. Bässler and A. Köhler, *J. Phys. Chem. C*, 2017, **121**, 22739–22752.

132 J. Jortner, *J. Chem. Phys.*, 1976, **64**, 4860–4867.